COMMUNICATION OF TUMOR-IMMUNE CELLS IN 3D BIOPRINTED LYMPH NODE ENVIRONMENT

by

Müge Kasım Kıraç

B.S., Chemical Engineering, Boğaziçi University, 2017

M.S., Chemical Engineering, Boğaziçi University, 2019

Submitted to the Institute for Graduate Studies in
Science and Engineering in partial fulfillment of
the requirements for the degree of
Doctor of Philosophy

Graduate Program in Chemical Engineering

Boğaziçi University

2025

ACKNOWLEDGEMENTS

Fourteen years at Boğaziçi University... At times miserable, at times joyful. I have seen countless sunrises and sunsets on these campuses and experienced moments of deep frustration as well as immense happiness. This journey, with all its ups and downs, has finally come to an end. I am happy that I have successfully completed my PhD. I am proud and grateful to myself for enduring and cherishing every step of the way.

First and foremost, I would like to express my deepest gratitude and respect to my thesis advisor, Prof. Kutlu Ülgen. From my undergraduate project to my master's and throughout my PhD, she has always been there for me — guiding, supporting, encouraging, and showing the way. Her patience, wisdom, and faith in me have played a major role in shaping the researcher and person I am today. I feel incredibly fortunate to have walked this long road with her.

I also extend my sincere thanks to my co-advisor, Prof. Tuna Tuğcu, for his guidance and support. I would like to express my sincere appreciation to my thesis defense jury members: Assoc. Prof. Cansu Canbek Özdil, for her continuous support and constructive input throughout my doctoral journey; Prof. Sezen Soyer, Prof. Hilal Taymaz Nikerel, and Prof. Zeynep Petek Çakar. Their time, insightful feedback, and valuable contributions have greatly enriched this work.

My heartfelt thanks go to my family, who have always believed in me and lifted me up whenever I fell. I am grateful to my mother, who has always supported me unconditionally behind the scenes; to my father, who listens and encourages; and to my sister, who never hesitates to brainstorm with me and share her ideas. And, of course, to my dearest husband, my anchor and best friend, who has stood by me at every step, turning this demanding journey into a shared adventure full of laughter and strength. Without their love and support, this thesis would not have been possible.

I am truly lucky to have lifelong friends who have shared this path with me. Elif Esvap and Özlem Özbek have been with me since our undergraduate years — my partners in work, laughter, gossip, travels, tears, and late-night panic. Their presence has made the hardest times lighter and the best times even more meaningful. I also thank all the other KB 440 lab members — Şafak, Ezgi, Sena and İrem — for their companionship and for keeping the true lab spirit alive. I would like to thank Elif Gençtürk, who patiently taught me the fundamentals of experimental work and lab coordination — the very foundations on which this thesis stands. Her guidance, energy, and friendship have been truly invaluable throughout this journey. I would also like to thank members of Chemical Engineering Department, for being a part of this thesis and their support and companionship. I also want to thank Yakup Bal, his kind and helpful technical support. He always comes up with a quick solution and helps without any hesitation when I have a problem in the laboratory.

My warm thanks also go to Begüm and Yusuf, whose friendship and unwavering support have been invaluable sources of strength and joy throughout this journey.

Finally, I acknowledge the financial support of the Boğaziçi University Research Fund through projects 19764D and 20161P, which made this work possible.

ABSTRACT

COMMUNICATION OF TUMOR-IMMUNE CELLS IN 3D BIOPRINTED LYMPH NODE ENVIRONMENT

Melanoma is a very aggressive type of skin cancer that develops when melanocytes undergo malignant transformation. The aim of this thesis is to examine how gold nanoparticles (AuNPs), the mTOR inhibitor temsirolimus, and selected phytochemicals affect human A375 melanoma cells, with a particular focus on how immune cell-tumor communication shapes treatment outcomes. Experiments are carried out in both 2D cultures and 3D models, to better reflect the complex tumor microenvironment. The 3D systems incorporated extracellular matrix (ECM)-like material. Temsirolimus shows a more potent effect in 3D than in 2D cultures, though its effects are delayed, reflecting the slower penetration and altered uptake in ECM-rich conditions. Curcumin induces viability reduction in both 2D and 3D rapidly, which can be linked to inhibition of NK-κB, PI3K/Akt, and MAPK pathways. Stronger effects are shown when delivered with AuNPs, likely driven by elevated ROS and loss of mitochondrial membrane potential. On the other hand, M0 macrophages responded differently to treatments. AuNPs alone are well-tolerated, but high-dose temsirolimus (500 nM) and curcumin (40 μM) reduced their viability, especially after bioprinting, which creates mechanical stress. Co-culture experiments revealed that the presence of macrophages could alter drug responses mainly by accelerating but sometimes slowing cell death, underscoring the importance of cell-cell interactions. By integrating these in vitro findings with physiologically-based pharmacokinetic (PBPK) modeling of curcumin, this work bridges experimental results with potential in vivo outcomes. Overall, the study highlights the value of combining immune-tumor cocultures with 3D bioprinted models for more predictive drug testing and points toward the promise of nano-particle-drug-phytochemical combinations in melanoma therapy.

ÖZET

ÜÇ BOYUTLU BİYO BASILMIŞ LENF DÜĞÜMÜ MİKROSİSTEMİNDE TÜMÖR VE BAĞIŞIKLIK HÜCRELERİNİN İLETİŞİMİ

Melanom, melanositlerin dönüşüme uğramasıyla gelişen agresif bir cilt kanseri türüdür. Bu tezde, altın nanoparçacıkların (AuNP'ler), temsirolimus ilacının ve bazı fitokimyasalların insan A375 melanoma hücreleri üzerindeki etkileri incelenmiştir. Çalışma, tümör-bağışıklık hücresi iletişiminin tedavi sonuçlarını nasıl ilişkilendirdiğine odaklanmaktadır. Deneyler, tümör mikroçerçevesinin yapısını daha iyi yansıtmak amacıyla 2D kültürlerde ve 3D modellerde gerçekleştirilmiştir. 3D sistemlere, hücre dışı matriks (ECM) benzeri materyaller eklenmiştir. Temsirolimus, 2D kültüre kıyasla 3D'de daha güçlü bir etki sergilemiş, ancak bu etki ECM açısından zengin ortamlarda daha gecikmeli olmuştur. Kurkumin, 2D ve 3D sistemlerde hücre canlılığını azaltmış, bu durumun NK-κB, PI3K/Akt, ve MAPK yollarının inhibisyonuyla ilişkili olduğu düşünülmektedir. AuNP'lerle birlikte uygulandıklarında daha güçlü etkiler gözlemlenmiş, bu etki artan reaktif oksijen türleri (ROS) üretimi ve mitokondriyal membran potansiyeli kaybından kaynaklanmıştır. M0 makrofajlar AuNP'lere tek başına iyi tolere ederken, yüksek doz temsirolimus (500 nM) ve kurkumin (40 μM) biyobasım işleminden sonra hücre canlılıklarını azaltmıştır. Kokültür deneyleri, makrofajların varlığının, ilaç yanıtlarını değiştirebildiğini göstermiş ve bu da hücre-hücre etkileşimlerinin önemini vurgulamıştır. Bu çalışma, in vitro bulguları kurkumin için fizyolojik temelli farmakokinetik (PBPK) modelleme ile bütünleştirerek, deneysel sonuçları potansiyel in vivo sonuçlarla ilişkilendirmektedir. Bu çalışma, ilaç testleri için bağışıklık-tümör kokültürlerinin 3D biyobasım modelleriyle birleştirilmesinin değerini vurgulamakta ve melanoma tedavisinde nanoparçaçık-ilaç-fitokimyasal kombinasyonlarının potansiyeline işaret etmektedir.

TABLE OF CONTENTS

ACKNOWLEDGEMENTS iii
ABSTRACT v
ÖZET vi
LIST OF FIGURES xi
LIST OF TABLES xix
LIST OF SYMBOLS xxi
LIST OF ACRONYMS/ABBREVIATIONS xxii
1. INTRODUCTION 1
2. THEORETICAL BACKGROUND 7
2.1. Melanoma and Treatment Strategies 7
2.2. Monocytes and Macrophages 11
2.3. Cell-to-Cell Communication 13
2.4. 3D Bioprinting 16
2.4.1. Methods of 3D Bioprinting 17
2.4.2. Hydrogels as Bioink 21
2.4.3. Crosslinking Methods 24
2.5. Bioprinted Studies with Cells 26
2.5.1. 3D Bioprinted Models for Melanoma Cell Studies 27
2.5.2. Exploring THP-1 Cells Through 3D Bioprinting 28
2.5.3. Cell-to-Cell Communication Studies in Innovative 3D Bioprinting Platforms 30
2.6. Physiologically-Based Pharmacokinetic (PBPK) Modelling 32
3. MATERIALS AND METHODS 37
3.1. Melanoma Cell Culturing 37
3.2. THP-1 Monocytes Cell Culturing 39
3.3. Differentiation and Polarization of THP-1 Cells 41
3.3.1. Differentiation to M0 42
3.3.2. Polarization to M1 and M2 43

3.4. Analysis of Polarization Status Of Macrophages by Flow Cytometer . . 46
3.5. Viability Assessment with Alamar Blue and Acridin 47
3.5.1. Alamar Blue Assay 47
3.5.2. Acridine Orange/Propidium Iodide Method 49
3.6. ROS analysis with 2'7' Dichlorodihydrofluorescein Diacetate 50
3.7. IL-4 Cytokine Treatment 51
3.8. Analysis of IL-4 Cytokine Secretion by ELISA 51
3.8.1. ELISA (Human IL-4, Sandwich ELISA; Invitrogen IL-4 Human ELISA Kit) 51
3.9. Hydrogel Preparation 54
3.9.1. Gelatin-Alginate 54
3.9.2. Matrigel-Alginate & Matrigel Collagen 55
3.10. Characterization of Hydrogel 56
3.10.1. FTIR 56
3.10.2. Porosity 58
3.11. AuNP Production and Characterization 58
3.12. Viscosity and Mechanical Characterization of Gelatin-Alginate and Alginate - Matrigel Hydrogels 61
4. UNDERSTANDING THE BEHAVIOR OF A375 MELANOMA CELLS IN 2D SYSTEM 63
4.1. A375 Melanoma Cells Interacting with Macrophage-Like M0 Cells - 2D Coculturing 63
4.2. Therapeutic Strategies and Cytotoxicity Experiments: Nanoparticles (AuNPs) and Chemotherapeutic Agents Doxorubicin (DOX) and Temsirolimus 65
4.2.1. AuNP and DOX Concentration Effects on A375-GFP Cells . . . 65
4.2.2. AuNP and temsirolimus concentration effects on A375-GFP cells 68
4.2.3. Metabolic Activity Assessment on A375-WT Cells by Using Alamar Blue on 2D 75
4.3. Effects of IL-4 on A375-WT Melanoma Cells by Using AO/PI - Visually Observed on 2D 80

4.4. Secretion of IL-4 on A375-WT and M0-WT on 2D by ELISA 81
4.5. Phytochemical Effects on A375-WT 86
4.5.1. Results of Phytochemicals, AuNP, and Temsirolimus Treatment on A375-WT 88
4.5.2. Synergistic Effect of Phytochemicals and Temsirolimus Given with AuNP on A375-WT 93
4.5.3. Results of Phytochemicals Conjugated with AuNP on A375-WT 96
4.5.4. Synergistic Effect of Phytochemicals Given with Temsirolimus and AuNP on A375-WT 98
5. 3D EXPERIMENTS FOR OPTIMIZATION 102
5.1. Optimization Experiments with Different Hydrogels 102
5.1.1. 3D Bioprinting Process Parameters Optimization without Cell Loading 102
5.2. Optimization with Cell-Laden Hydrogels 104
5.2.1. A375-GFP Cell-Laden Gelatin-Alginate by Using a Bioprinter . 104
5.2.2. A375-GFP Cell-Laden Collagen-Matrigel by Using Bioprinter . 106
5.3. Cell-to-Cell Communication Experiments 111
5.3.1. Coculturing (GFP-tagged A375 cells and mcherry-tagged M0 cells) on 3D (8G4A Scaffold) with RPMI-1640 Medium 111
5.3.2. Coculturing (GFP-tagged A375 Cells and Nondifferentiated and Differentiated mCherry-tagged THP-1 Cells) on 3D (8G4A scaffold) with DMEM Medium 116
6. TREATMENT STRATEGIES 122
6.1. Treatment In Hydrogel (3D in 96-well plates) 122
6.1.1. A375 in Matrigel-Alginate Hydrogel in 96 Well-Plates 123
6.1.2. M0 in Matrigel-Alginate Hydrogel in 96 Well Plates 128
6.1.3. ROS Analysis 131
6.2. Treatment in 3D-Bioprinted Scaffold 136
6.2.1. A375 in 8G4A Hydrogel 136
6.2.2. A375-WT in Matrigel-Alginate Hydrogel 148
6.2.3. M0 in 8G4A Hydrogel - 3D Bioprinted 152

6.3. Coculture Treatments (Viability/Rhodamine Analyses – Day 1,2,3) . . 158
7. PBPK MODELLING 165
7.1. Model Structure 165
7.2. Sensitivity Analysis 174
8. CONCLUSIONS AND RECOMMENDATIONS 181
8.1. Conclusions 181
8.1.1. Monoculture Studies (2D vs 3D) 182
8.1.1.1. Impact of AuNP and Temsirolimus Treatment on A375 Cell Viability 182
8.1.1.2. Treatment of A375-WT Cells with Curcumin and Other Phytochemicals 183
8.1.1.3. Treatment (AuNP, Temsirolimus and curcumin) Effects on M0 macrophages 185
8.1.2. Impact of Coculture Compared to Monoculture Conditions . . . 186
8.1.3. PBPK Model 187
8.2. Limitations and Recommendations 187
REFERENCES 190
APPENDIX A: BIOPRINTING OPTIMIZATION 231
APPENDIX B: PERMISSIONS FOR REUSED FIGURES 232

LIST OF FIGURES

Figure 2.1. Macrophage activation. 12

Figure 2.2. Communication mechanism between melanoma cells and TAMs. . 15

Figure 2.3. 2D vs 3D cell culture [108]. 17

Figure 2.4. Laser-assisted bioprinting [111]. 18

Figure 2.5. Stereolithography [111]. 19

Figure 2.6. Printer-based bioprinting system [111]. 20

Figure 2.7. Extrusion-based bioprinting [111]. 20

Figure 2.8. dECM from human skin [115]. 21

Figure 2.9. Thermally induced entanglement for crosslinking. 25

Figure 2.10. Physical crosslinking. 25

Figure 2.11. Chemical crosslinking. 26

Figure 2.12. Transwell-plate setup for co-culturing [142]. 29

Figure 2.13. PBPK model [156]. 34

Figure 2.14. PBPK model with lymphatic system [157]. 35

Figure 2.15. Minimal PBPK model [159]. 35

Figure 3.1. A375-GFP melanoma cell line. 37

Figure 3.2. Cell counting on Eve automated cell counter. 39

Figure 3.3. Agglomeration of M0 cells at high density polarization. 44

Figure 3.4. Polarization experiment. 44

Figure 3.5. Polarization experiment for obtaining more viable cells. 45

Figure 3.6. Flow cytometer results. 47

Figure 3.7. FTIR results of hydrogel. 57

Figure 3.8. (a) SA, (b) G, (c) SA+G. 57

Figure 3.9. Porosity of gelatin–alginate. 58

Figure 3.10. UV–Vis data of various AuNPs. 59

Figure 3.11. DLS characterization of AuNP solutions. 61

Figure 4.1. Different concentrations of co-culturing in 2D. 64

Figure 4.2. Fluorescence change in A375-GFP cells. 67

Figure 4.3. Average fluorescence intensity of all treatments. 71

Figure 4.4. Fluorescence intensity of A375-GFP cells treated with AuNP-1 and temsirolimus. 72

Figure 4.5. Fluorescence intensity of A375-GFP cells treated with different concentrations of different AuNPs. 73

Figure 4.6. Fluorescence intensity of A375 cells treated with different concentrations of different AuNPs and temsirolimus. 74

Figure 4.7. Viability measurement with Alamar Blue on day 1: (a) viability according to the cell fluorescence intensity, (b) % reduction of Alamar Blue. 78

Figure 4.8. Experiment visualization. 81

Figure 4.9. IL-4 effects on A375-WT cells. 82

Figure 4.10. Standard curve of IL-4. 84

Figure 4.11. IL-4 concentration of the samples. 84

Figure 4.12. Viability of the top three concentrations day by day. 89

Figure 4.13. Viability after 24h of phytochemicals, AuNP, and temsirolimus treatment. 89

Figure 4.14. Viability after 48h of phytochemicals, AuNP, and temsirolimus treatment. 91

Figure 4.15. Viability after 72h of phytochemicals, AuNP, and temsirolimus treatment. 92

Figure 4.16. Viability of the top three concentrations day by day. 93

Figure 4.17. Viability after 24 h of phytochemicals and temsirolimus given with AuNP. 94

Figure 4.18. Viability after 48 h of phytochemicals and temsirolimus given with AuNP. 95

Figure 4.19. Viability after 72 h of phytochemicals and temsirolimus given with AuNP. 95

Figure 4.20. Viability of the top three concentrations of phytochemicals conjugated with AuNP treatments day by day. 96

Figure 4.21. Viability after 24h of phytochemicals conjugated with AuNP. . . . 97

Figure 4.22. Viability after 48h of phytochemicals conjugated with AuNP. . . . 98

Figure 4.23. Viability after 72h of phytochemicals conjugated with AuNP. . . . 98

Figure 4.24. Viability of the top three concentrations of phytochemicals given with temsirolimus and AuNP day by day. 99

Figure 4.25. Viability after 24h phytochemicals given with temsirolimus and AuNP. 100

Figure 4.26. Viability after 48h phytochemicals given with temsirolimus and AuNP. 100

Figure 4.27. Viability after 72h phytochemicals given with temsirolimus and AuNP. 101

Figure 5.1. Hydrogel scaffold for the initial experiments. (a) Top view, (b) side view. 103

Figure 5.2. (a) 8G4A hydrogel scaffold, (b) Matrigel scaffold. 103

Figure 5.3. Scaffolds after printing. 107

Figure 5.4. Progress of cells in Matrigel/collagen hydrogel over the 7 days. . . 108

Figure 5.5. Viability of A375-GFP cells in Matrigel-collagen bioink after two days. 110

Figure 5.6. Viability of A375-GFP cells in Matrigel-collagen bioink after seven days. 111

Figure 5.7. Growth of cells within gelatin-based vs Matrigel-based hydrogel. . 112

Figure 5.8. Comparison of gelatin–alginate and Matrigel–alginate hydrogels showing how A375 cells interact differently with gelatin–alginate vs. Matrigel–alginate. 120

Figure 6.1. Viability of A375–WT cells with respect to time for all treatments. 124

Figure 6.2. Viability with respect to treatment types for each day analysis. . . 125

Figure 6.3. Cell count-based viability results of M0 cells in Matrigel-alginate hydrogel. 129

Figure 6.4. Fluorescence signal positive cells ratio to all cells in 3D - 96 well plates. 132

Figure 6.5. Mean ROS intensity of all cells in Matrigel-alginate hydrogel in a 96-well plate. 134

Figure 6.6. Mean ROS intensity of signal-positive cells in Matrigel-alginate in a 96-well plate (3D). 135

Figure 6.7. Viability results of A375-WT in 8G4A scaffold - single treatments. 138

Figure 6.8. Viability results of A375-WT in 8G4A scaffold for treatments with AuNP 138

Figure 6.9. Viability of untreated & AuNP treated A375-WT - 8G4A scaffold. 139

Figure 6.10. ROS and Rhodamine analysis of untreated A375-WT and AuNP-treated in 8G4A scaffold. 140

Figure 6.11. Viability of A375-WT cells with curcumin-based treatments in 8G4A scaffold. 141

Figure 6.12. ROS and Rhodamine analysis of curcumin-based treated A375-WT in 8G4A scaffold. 142

Figure 6.13. Viability of A375-WT cells with temsirolimus-based treatments in 8G4A scaffold. 143

Figure 6.14. ROS and Rhodamine analysis of temsirolimus-based treated A375-WT in 8G4A scaffold. 144

Figure 6.15. Viability of A375-WT cells with TQ-based treatments in 8G4A scaffold. 145

Figure 6.16. ROS and Rhodamine analysis of TQ-based treated A375-WT in 8G4A scaffold. 146

Figure 6.17. Viability results of A375-WT in Matrigel-alginate scaffold. 149

Figure 6.18. ROS and Rhodamine analysis of A375-WT in Matrigel-alginate scaffold. 151

Figure 6.19. Viability results of M0-WT in 8G4A scaffold. 153

Figure 6.20. ROS and Rhodamine analysis of M0-WT in 8G4A scaffold. 155

Figure 6.21. Viability results of A375-WT and M0-WT cells in coculture. . . . 160

Figure 6.22. Rhodamine analysis of coculture. 162

Figure 6.23. A375 and M0 of non-treated coculture. 163

Figure 6.24. (a) Placement of the wells, (b) M0 cells on membrane. 164

Figure 7.1. PBPK model for curcumin. 167

Figure 7.2. Amount of curcumin in the gut with respect to time. 170

Figure 7.3. Curcumin concentration in all compartments. 170

Figure 7.4. Curcumin concentration in (a) lymph, (b) tight and leaky compartments. 172

Figure 7.5. (a) Experimental vs (b) PBPK model curcumin plasma concentration (experimental figure is obtained from Fança-Berthon et al., and the standard turmeric extract (STE) is the yellow line. 174

Figure 7.6. Concentration over time when varying $k_{a,\text{blood}}$, (a) plasma compartment, (b) tight and leaky compartments, (c) lymph compartment. 176

Figure 7.7. Concentration over time when varying $k_{a,\text{lymph}}$, (a) plasma compartment, (b) tight and leaky compartments, (c) lymph compartment. 178

Figure 7.8. Concentration over time when varied σ_1 and σ_2 179

Figure B.1. Permission for Figure 2.3 232

Figure B.2. Permission for Figures 2.4 to 2.7 233

Figure B.3. Permission for Figure 2.8 234

Figure B.4. Permission for Figure 2.13 234

Figure B.5. Permission for Figure 2.14 235

Figure B.6. Permission for Figure 2.15 236

LIST OF TABLES

Table 2.1. Phytochemicals vs melanoma. 10

Table 3.1. Passaging and cell counting of A375 cells. 38

Table 3.2. Passaging of THP1 and cell counting. 40

Table 3.3. Medium optimization viability test results. 46

Table 3.4. Concentration and size of AuNP solutions. 60

Table 4.1. Concentration of AuNP and DOX treatment on A375-GFP cells. . 67

Table 4.2. Dilution concentration of AuNPs and Temsirolimus (nM). 68

Table 4.3. Average fluorescence of cells against ½ dilution of AuNP treatment. 69

Table 4.4. Average fluorescence of cells against 1/5 dilution - AuNP treatment. 70

Table 4.5. Average fluorescence of cells against ½ dilution of Temsirolimus and combined treatment. 70

Table 4.6. Concentrations of treatments AuNP1–2–3, Temsirolimus and DOX. 76

Table 4.7. Viability of cells against AuNP. 77

Table 4.8. Viability of cells against Temsirolimus and DOX. 77

Table 4.9. Effect of the diameter of AuNPs on viability. 80

Table 4.10. Sets of experiments for IL-4 secretion. 83

Table 4.11. Initial concentrations of treatments. 87

Table 5.1. 3D Experiments performed with A375-GFP cell-laden bioink. . . . 105

Table 5.2. Co-culturing Experiments of A375-GFP with differentiated M0-mCherry cells in RPMI. 114

Table 5.3. Coculture experiments by using DMEM medium for scaffold incubation. 117

Table 5.4. Cell counting for THP-1 cells. 118

Table 5.5. Comparison of gelatin–alginate and Matrigel–alginate hydrogels. . 121

Table 6.1. Mechanistic effects of drug and phytochemical applications. 147

Table 6.2. Effect of treatments on cell death mechanism. 159

Table 7.1. Physiological and pharmacokinetic parameters used in the PBPK model. 168

Table 7.2. $C_{\max}$, $T_{\max}$ and AUC when varied $k_{a,\text{blood}}$ and constant $k_{a,\text{lymph}} = 0.131\ \text{h}^{-1}$. 177

Table 7.3. $C_{\max}$, $T_{\max}$, and AUC when varied $k_{a,\text{lymph}}$, and constant $k_{a,\text{blood}} = 1.05\ \text{h}^{-1}$. 179

Table 7.4. $C_{\max}$, $T_{\max}$ and AUC when varied σ_1 and σ_2. 180

LIST OF SYMBOLS

A_{gut}	Amount of curcumin in the gastrointestinal tract
AUC	Area under the concentration–time curve
C_l	Curcumin concentration in leaky tissues
C_{ly}	Curcumin concentration in systemic lymph
$C_{\max}$	Maximum concentration of drug
C_p	Curcumin concentration in plasma
C_t	Curcumin concentration in tight tissues
CL_p	Plasma clearance
G'	Storage modulus
G''	Loss modulus
ISF	Interstitial fluid volume
$k_{a,\text{blood}}$	Absorption rate constant from gut to plasma
$k_{a,\text{lymph}}$	Absorption rate constant from gut to lymph
L_1	Lymphatic flow rate to tight tissues
L_2	Lymphatic flow rate to leaky tissues
$T_{\max}$	Time to reach maximum concentration
V_p	Plasma volume
V_{gut}	Gut compartment volume
V_{leaky}	Volume of leaky tissues
V_{lymph}	Lymphatic system volume
V_{tight}	Volume of tight tissues
η	Steady-sheat viscosity
σ_1	Reflection coefficient for tight tissues
σ_2	Reflection coefficient for leaky tissues
σ_L	Reflection coefficient for lymphatic return

LIST OF ACRONYMS/ABBREVIATIONS

2D	Two-dimensional (cell culture system)
3D	Three-dimensional (cell culture system)
AB	Alamar Blue
ADME	Absorption, Distribution, Metabolism, Elimination
AO	Acridine Orange
AuNP(s)	Gold Nanoparticle(s)
Bet	Betulin, naturally occurring triterpene phytochemical
Curc	Curcumin
DMEM	Dulbecco's Modified Eagle Medium
DMSO	Dimethyl Sulfoxide
DOX	Doxorubicin
ECM	Extracellular Matrix
EGCG	Epigallocatechin Gallate
ELISA	Enzyme-Linked Immunosorbent Assay
Fl. Int.	Fluorescence Intensity
GFP	Green Fluorescent Protein
IL-4	Interleukin-4
M0	Undifferentiated macrophage phenotype derived from THP-1
M-CSF	Macrophage Colony-Stimulating Factor
mTOR	Mammalian Target of Rapamycin
ODE(s)	Ordinary Differential Equation(s)
Pa	Pascal
PBS	Phosphate Buffered Saline
PBPK	Physiologically Based Pharmacokinetic (modeling)
PI	Propidium Iodide
ROS	Reactive Oxygen Species
STAT6	Signal Transducer and Activator of Transcription 6
Tems	Temsirolimus

Thymq, TQ	Thymoquinone
TME	Tumor Microenvironment
WT	Wild Type

1. INTRODUCTION

Melanoma stands as a highly aggressive form of skin cancer, originating from the malignant transformation of melanocytes. This malignancy is particularly challenging due to its marked metastatic potential and its inherent resistance to various therapeutic interventions [1]. The global incidence of melanoma continues to rise [2], underscoring the urgent need for more effective treatment strategies. Its progression is fundamentally driven by the dysregulation and overactivation of crucial intracellular signaling pathways. Prominent among these are the Mitogen-Activated Protein Kinase/Extracellular Signal-Regulated Kinase (MAPK/ERK), Phosphoinositide 3-Kinase/Protein Kinase B (PI3K/Akt), and mammalian Target of Rapamycin (mTOR) pathways. When aberrantly active, these pathways collectively orchestrate key oncogenic processes. These include uncontrolled cell proliferation, enhanced cellular invasion, and evasion of programmed cell death (apoptosis) [3]. Given these complex underlying mechanisms and the significant clinical challenges, melanoma has become an intensive focus of research. Research in this field is mainly focused on developing novel therapeutic strategies, particularly targeted therapies [4]. There is also a strong emphasis on innovative combination treatments aimed at overcoming resistance and improving patient outcomes [5].

The A375 cell line serves as a widely recognized and invaluable model in the research landscape. Derived from human melanoma, this cell line is specifically characterized by the presence of the BRAF V600E mutation. This particular mutation is a pivotal oncogenic driver, leading to the constitutive activation of the MAPK signaling pathway. Ultimately, this promotes rapid cell proliferation and robust tumor development. Consequently, A375 cells are frequently used in in vitro studies. They provide a reliable platform for evaluating the efficacy of a range of therapeutic agents, including established targeted inhibitors such as BRAF and MEK inhibitors. Furthermore, A375 cells are used to explore the potential of novel compounds, particularly natural compounds and phytochemicals, in counteracting melanoma progression [6, 7].

THP-1 is a human monocytic leukemia cell line derived from the peripheral blood of a 1-year-old male patient with acute monocytic leukemia. It is widely used as an in vitro model for monocyte and macrophage biology, due to its ability to differentiate into macrophage-like cells upon stimulation (e.g., with phorbol 12-myristate 13-acetate, PMA). Once differentiated, THP-1 cells exhibit adherent morphology and express surface markers and cytokines characteristic of primary macrophages, making them a valuable tool for studying immune responses, inflammation, and host–pathogen or tumor–immune interactions [8].

Traditional two-dimensional (2D) monolayer cell culture has long been a successful technique in cell biology studies. The simplicity of growing cells as a single layer on rigid plastic or glass substrates offers practical advantages, particularly for straightforward microscopic observations and high-throughput drug screening applications. However, despite its widespread use, the 2D culture system presents several fundamental limitations that compromise its biological relevance. These major disadvantages stem primarily from the significantly restricted cell-cell and cell-extracellular matrix (ECM) interactions. Such interactions are critically different from the complex three-dimensional environment found in vivo. Consequently, cells grown in 2D often exhibit altered morphology, proliferation rates, gene expression profiles, and drug responses compared to their physiological counterparts. This divergence from in vivo conditions is particularly pronounced when attempting to replicate the intricate and dynamic interactions that occur within complex biological systems like the tumor microenvironment. Specifically, 2D systems prove biologically distant from reality in their inability to fully mimic the complex interplay between tumor cells and various immune cells, which is crucial for understanding cancer progression, metastasis, and the efficacy of immunotherapies. Therefore, while 2D cultures remain valuable for initial insights, their limitations necessitate the exploration of more physiologically relevant in vitro models to advance the understanding of complex cellular processes and disease mechanisms [9–11].

In this context, three-dimensional (3D) cell culture systems have recently gained significant attention, especially in tissue engineering and drug development studies. These advanced models offer a more physiologically relevant environment than traditional monolayers. In 3D culture systems, cells are encouraged to grow in multi-layered, spherical clusters, often within an ECM-like scaffold or hydrogel. This configuration allows for cell-cell and cell-matrix interactions, which are crucial for replicating the complex cellular communications and structural support in vivo. Furthermore, a key feature of 3D cultures, especially larger aggregates, is the development of gradients for oxygen and nutrients, with concentrations decreasing from the outer surface towards the center of the cellular cluster. This gradient phenomenon better mimics the microenvironmental conditions experienced by cells within actual tissues and tumors in vivo. Consequently, cells grown in 3D models exhibit behaviors that more closely resemble in in vivo tumor growth, including more accurate patterns of proliferation, differentiated gene and protein expression, and relevant metabolic activity [9–12].

To establish 3D cell culture, various bioinks such as hydrogels, microcarriers, and tissue-like structures are used. Hydrogels, in particular, are among the most suitable candidates for mimicking the ECM environment due to their high water retention capacity and biocompatibility. In this study, gelatin and alginate mixtures were also created, and the stability and ability of these hydrogels to support cell viability were investigated. Gelatin, a denatured form of collagen, is widely recognized for its excellent biocompatibility and cell adhesion properties, while alginate offers adjustable mechanical properties and forms stable hydrogels under mild conditions. Similarly, other common ECM-mimicking hydrogels, such as matrigel-alginate or collagen mixtures, are also frequently utilized in 3D cell culture to achieve diverse biological characteristics, serving as benchmarks or alternatives. The porous structure of the hydrogels chosen for this thesis allowed both cell migration and diffusion-based nutrient and gas exchange [13–15].

Building upon 3D cell culture techniques, 3D bioprinting represents a powerful advancement, enabling precise, layer-by-layer creation of complex, tissue-like structures

by directly depositing cells suspended within bioinks. In bioprinting, the distinction is that live cells are carefully protected within bioink throughout the entire printing process, ensuring their viability and functionality. While ensuring the mechanical stability and structural integrity of bioprinted constructs remains a significant challenge, this technique offers unparalleled advantages. Specifically, it allows cells to adapt to and interact within their natural microenvironment in the closest possible way to in vivo conditions [16–19].

In this thesis, we specifically investigated the interplay between A375 melanoma cells and THP-1 monocytes, including macrophages differentiated from them, within a physiologically relevant 3D culture environment. This advanced model was chosen to address the limitations of 2D systems in mimicking complex biological interactions. The inherently high proliferative capacity of A375 melanoma cells, as discussed previously, readily enables their self-assembly into compact, tumoroid-like structures when cultured in 3D. Concurrently, the differentiation of THP-1 monocytes into macrophages is demonstrably better supported and more realistically triggered within 3D environments compared to 2D cultures. This fosters a more in vivo-like immune cell phenotype and function. This establishment of a realistic microenvironment within 3D constructs significantly enhances crucial cell-cell and cell-ECM interactions. Therefore, it allows a more accurate reflection of the intricate communication dynamics between tumor cells and various immune cells. Furthermore, a critical advantage for translational relevance is that drug penetration and distribution within these complex 3D structures more closely recapitulate the conditions found in actual tumors in vivo. Consequently, the cellular responses to therapeutic agents obtained from such 3D models are expected to yield results that are substantially closer to clinical reality and better predict in vivo outcomes. This approach provides a robust platform for evaluating novel melanoma therapies in a highly relevant context [20–22].

In recent years, phytochemicals and gold nanoparticles (AuNPs) have emerged as promising alternative or complementary strategies in cancer treatment. Phytochemicals such as curcumin, epigallocatechin gallate (EGCG), betulin, and thymo-

quinone can play a role in suppressing cancer cell growth due to their antioxidant, anti-inflammatory, and pro-apoptotic properties. These compounds slow cell proliferation and trigger apoptotic processes, particularly by inhibiting signaling pathways such as mTOR and NF-κB. Meanwhile, AuNPs are widely used in drug delivery systems and photothermal therapy platforms, due to their biocompatibility and ease of surface functionalization. The easy uptake of AuNPs by cells and their ability to sensitize cancer cells by increasing reactive oxygen species (ROS) production make them a potential tool with synergistic effects when combined with phytochemicals or chemotherapeutic agents [23–29].

The efficacy and cytotoxicity of these agents used in cancer treatment are generally evaluated through dose-response relationships. In this approach, biomarkers such as cell viability, the percentages of apoptotic cells, ROS production, and mitochondrial membrane potential are examined at different dose levels in Chapter 3. The IC50 value is a critical indicator of therapeutic effectiveness and varies depending on the cell type, dose range, and treatment duration for both phytochemical and AuNP-based treatments.

Crucially, for successful fabrication of the 3D constructs utilized in this study, optimization of bioprinting parameters is essential. These parameters, such as extrusion pressure, hydrogel concentration, needle size, and printhead speed, were investigated. The influence of the parameters on the printed structure stability, viability, and distribution of encapsulated cells post-printing is mentioned in Chapter 4.

Moreover, it is well-established that dose-response profiles in conventional 2D monolayer cultures often differ substantially from those obtained in 3D cultures. 3D structures, by virtue of their enhanced cell-cell interactions, more complex ECM-like architecture, and inherent transport limitations, frequently exhibit a more resistant phenotype to therapeutic agents. Therefore, evaluating the combined effects of AuNPs and phytochemicals within these advanced 3D cell models provides a significantly stronger foundation for translational research. It better reflects the intricate physi-

ological barriers and cellular responses encountered in clinical reality. In chapter 5, dose-response effects were comprehensively observed on 3D platforms. The multidimensional evaluation of cell responses was further enhanced through the simultaneous analysis of parameters such as viability, oxidative stress, and mitochondrial membrane potential [30, 31]. Within this comprehensive assessment, ROS levels served as a critical indicator, providing crucial insights into both the mechanisms of cell death and the cellular antioxidant responses [32].

In conclusion, this thesis aimed to understand the stimulatory effects of melanoma cells on immune system cells and investigate these interactions through 3D co-culture systems. By applying phytochemicals to the coculture, the effects on cell viability and mitochondrial membrane stability were evaluated. As a result of these studies, the responses of cancer and immune cells to treatment in both 2D and 3D environments were compared, contributing data to the literature that better reflects clinical reality. This approach also enabled a more accurate interpretation of cell death mechanisms (apoptosis/necrosis) and cellular stress responses.

In addition to experimental studies, physiologically based pharmacokinetic (PBPK) modeling was used to predict the distribution of phytochemical agents in the body and their organ-level exposure [33]. PBPK models mathematically describe the pharmacokinetic behavior of drugs (absorption, distribution, metabolism, and elimination – ADME [34]). They serve as a powerful tool to calculate both plasma concentration-time curves and drug levels in target organs. In this study, the distribution of curcumin was estimated based on five compartments (gut, plasma, lymph, leaky and tight tissues). Assuming that curcumin is absorbed only from the gut, its transport to the lymphatic system and organs was modeled. In this context, the pharmacokinetic profiles of therapeutic agents at their sites of action and their systemic distribution were predicted, combining in vitro observations with in silico predictions.

2. THEORETICAL BACKGROUND

2.1. Melanoma and Treatment Strategies

Melanoma is a type of skin cancer that arises from melanocytes, pigment-producing cells in the epidermis. It can spread to the lymph nodes, liver, lungs, and central nervous system. Melanoma can grow deep into the skin and spread to other parts of the body. Despite accounting for 1% of skin cancer cases, melanoma is responsible for most skin cancer-related deaths due to its high metastatic potential and resistance to conventional therapies [35, 36]. The progression of melanoma is largely driven by dysregulation of intracellular signaling pathways that control cell growth, survival, and migration.

The MAPK/ERK pathway (mitogen-activated protein kinase/extracellular signal-regulated kinase) plays a central role in transmitting mitogenic signals from cell surface receptors to the nucleus. It is frequently hyperactivated in melanoma due to mutations in the *BRAF* gene, which encodes a serine/threonine kinase that acts as a switch on/off for the MAPK/ERK pathway. The most common mutation in melanoma is BRAFV600E (valine replaced by glutamic acid at position 600), and it leads to constitutive activation of the MAPK pathway independent of upstream signals [37, 38]. This promotes uncontrolled proliferation and survival.

To address these molecular drivers, targeted therapies that transiently suppress tumor growth in BRAF-mutant melanoma have been developed. BRAF inhibitors like vemurafenib, dabrafenib, and MEK inhibitors like trametinib are successful therapies. However, drug resistance commonly develops through second mutations, pathway reactivation or activation of alternative signaling routes [39]. As a result, combination therapies targeting multiple pathways, as well as novel delivery systems, are under investigation to overcome resistance and enhance efficacy [5]. Studies show that dabrafenib and trametinib, which target both BRAF and MEK pathways, increase the

overall survival rate [40,41]. Also, the combination of vemurafenib and cobimetinib significantly prolonged progression-free survival, although the treatment-related toxicity increased [42].

Another critical pathway is the PI3K/Akt/mTOR signaling pathway, which governs cell metabolism, growth, and apoptosis. Alterations in this pathway, such as PTEN loss or PI3K mutations, contribute to therapy resistance targeting the MAPK pathway, enhance melanoma cell survival under stress and metastatic progression [43, 44]. Temsirolimus, an inhibitor of the mammalian target of rapamycin (mTOR), has emerged as a promising agent in the treatment of various malignancies, including melanoma. It exerts its antitumor effects by inhibiting mTOR complex 1 (mTORC1) and reducing protein synthesis and inducing cell cycle arrest in the G1 phase [45, 46]. While the drug temsirolimus has demonstrated limited efficacy as a monotherapy in melanoma, its use in combination therapies, such as with BRAF or MEK inhibitors, has shown potential to overcome resistance mechanisms and enhance antitumor activity [45, 47]. Also, immunotherapy combinations suggest a promising therapy since mTOR inhibition is linked to modulation of the tumor microenvironment, including immune responses [48].

Phytochemicals, bioactive compounds derived from plants, attracted considerable interest as potential adjuvants or alternatives to conventional cancer therapies due to their multitargeted mechanisms, low toxicity profiles, and ability to modulate key signaling pathways involved in tumor progression [49]. Many phytochemicals, such as fisetin, EGCG, resveratrol, curcumin, capsaicin, luteolin, etc., are promising in melanoma since they have a role in cell growth inhibition, cell cycle arrest, and apoptosis. Curcumin, the principal polyphenol in *Curcuma longa*, exerts antiproliferative and pro-apoptotic effects through the inhibition of multiple pathways, including NF-κB [50] and PI3K/Akt/mTOR [51], while also inducing oxidative stress and cell cycle arrest in melanoma cells. However, its clinical translation has been limited by poor solubility and bioavailability. Thus, delivery via nanoparticles or various combinations with other therapies is promoted. Epigallocatechin-3-gallate (EGCG), a major

ingredient in green tea, inhibits melanoma cell growth and metastasis by suppressing VEGF expression [52], MMP activity, and inflammatory cytokines [53], as well as promoting apoptosis through the mitochondrial pathway. Betulin has shown the ability to induce apoptosis in melanoma cells via the mitochondrial intrinsic pathway, including caspase-9 activation, while also exhibiting antioxidant and anti-inflammatory properties [54]. Thymoquinone, the active constituent of black seed, exerts cytotoxic effects against melanoma by modulating ROS levels, downregulating STAT3, and enhancing apoptotic signaling through caspase-3 activation [55]. The effects of phytochemicals on melanoma cells are summarized in Table 2.1.

There are several types of melanoma cells widely used in studies. A375 (ATCC CRL-1619) is a cell line exhibiting epithelial morphology that was isolated from the skin of a 54-year-old female patient with malignant melanoma. MeWo (ATCC HTB-65) is a cell line exhibiting fibroblast morphology that was isolated from the skin of a 78-year-old, white male patient with malignant melanoma. UACC-62 (Accegen ABC-TC534S) is a melanoma cell line from the NCI-60 panel, which was developed for screening compounds and molecular target discoveries against common human cancers. The A375 melanoma cell line was used for this study due to its well-characterized BRAFV600E mutation, which is present in approximately 50 of melanomas and drives MAPK/ERK pathway activation. This makes A375 a relevant model for studying targeted therapies and drug resistance mechanisms. Its stable growth, reproducibility, and responsiveness to treatments also support its use in evaluating novel therapeutic strategies.

Table 2.1. Phytochemicals vs melanoma.

Phytochemical	**Source (plant)**	**Representative IC_{50}/ effective conc. (A375)**	**Key mechanisms (melanoma-relevant)**	**Ref.**
Curcumin	*Curcuma longa*	Reported IC_{50} values vary widely (≈10–80 μM at 24–48 h, assay-dependent).	ROS ↑; mitochondrial apoptosis; NF-κB ↓; PI3K/Akt & MAPK modulation.	[56–58]
Betulinic acid (betulin)	*Betula* spp.	$IC_{50} \approx 16.9$ μM (24 h, one report); broader ranges across derivatives/assays.	Mitochondrial membrane permeabilization; ROS ↑; melanoma-selective cytotoxicity.	[59–62]
EGCG (epigallocatechin-3-gallate)	*Camellia sinensis* (green tea)	Effective concentrations ∼10–50 μg/mL (≈22–110 μM) in single-agent and combo studies.	Inhibits proliferation/migration; STAT3/ERK modulation; anti-angiogenic; ubiquitin ligase/TRAF6 effects.	[63–65]
Resveratrol	Grapes, berries	$IC_{50} \approx 23$ μM (48 h) in A375 (at least one report).	Cell-cycle arrest; mitochondrial apoptosis; downregulates MMPs and metastatic traits.	[66–69]
Quercetin	Onions, apples, etc.	Anti-proliferative at tens of μM; exact IC_{50} varies by derivative (often 20–100 μM).	Cell-cycle arrest; ERK/MAPK modulation; apoptosis; may sensitize to other drugs.	[70–73]
Sulforaphane (SFN)	Cruciferous vegetables (e.g., broccoli)	Effective at low-to-mid μM in melanoma lines; often combined with epigenetic drugs.	HDAC inhibition; cell-cycle arrest; apoptosis; targets melanoma stem-like cells.	[74,75]
Artemisinin / derivatives (e.g., artemisone)	*Artemisia annua*	Derivative activities vary (e.g., artemisone $IC_{50} \approx 95.7$ μM vs. A375); enhanced in combinations.	ROS generation (iron-dependent); apoptosis; anti-metastatic activity in preclinical models.	[76–78]

Table 2.1. Phytochemicals vs melanoma. (cont.)

Phytochemical	**Source (plant)**	**Representative IC_{50}/ effective conc. (A375)**	**Key mechanisms (melanoma-relevant)**	**Ref.**
Berberine	*Berberis* spp.	Anti-proliferative / migration inhibition typically at tens of μM; study-dependent IC_{50}.	AMPK activation; cell-cycle arrest; apoptosis; anti-migration/invasion.	[79–82]

2.2. Monocytes and Macrophages

Monocytes are a type of white blood cells (leukocyte) and an essential component of the innate immune system. They are produced in the bone marrow from hematopoietic stem cells and circulate in the bloodstream, representing about 5-10% of total leukocytes in peripheral blood. Monocytes are highly versatile cells that serve as precursors to macrophages and dendritic cells when they migrate from the bloodstream into tissues [83].

Macrophages are differentiated, tissue-resident immune cells derived primarily from circulating monocytes. When an infection or injury occurs, monocytes are recruited to the affected tissue, where they undergo a process of differentiation and maturation into macrophages. These macrophages are highly versatile cells that reside in tissues throughout the body and act as the body's primary "guardians" and "clean-up crew". Their main function is phagocytosis, the process of destroying pathogens, dead cells, and cellular debris. Macrophages are also crucial for presenting antigens to T-cells, thereby bridging the innate and adaptive immune response. Additionally, they secrete a wide range of signaling molecules, such as cytokines and chemokines, which orchestrate the inflammatory response and promote tissue repair. The delicate balance and dynamic functions of monocytes and macrophages are critical for maintaining tissue homeostasis and defending against a variety of diseases [83, 84].

Macrophages exhibit remarkable functional plasticity and can adopt different phenotypes depending on microenvironmental cues: classically activated M1 macrophages, induced by IFN-κ and LPS, display pro-inflammatory, antimicrobial, and tumoricidal properties, whereas alternatively activated M2 macrophages, induced by IL-4 and IL-13, are associated with anti-inflammatory functions, tissue remodeling, and in some cases, tumor progression (Figure 2.1). The resting, non-polarized M0 state serves as the precursor from which either phenotype can develop. This phenotypic diversity allows monocytes and macrophages to serve as both protectors against disease and, under certain pathological conditions such as cancer, facilitators of disease progression [85–87].

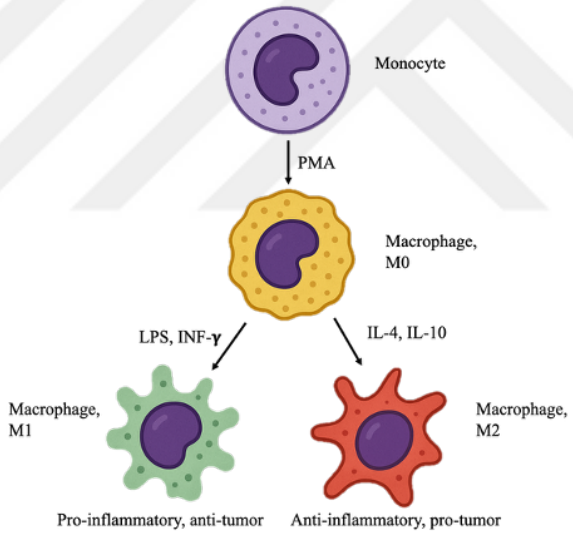


Figure 2.1. Macrophage activation.

THP-1 is a monocytic cell obtained from a 1-year-old male child with acute monocytic leukemia. As a suspension cell line, THP-1 exhibits phenotypic and functional properties similar to human blood monocytes. These are widely used as a model system for studying monocyte-macrophage biology, inflammation, and immune modulation. It is a long-lived (nearly immortal) cell line that is desirable for in vitro studies due to reproducibility. But also, it has the disadvantage of being less sensitive to some stimuli (e.g., lipopolysaccharide, LPS). THP-1 monocytic cells can be differentiated into dif-

ferent types of macrophages depending on the environment. This cell line can be used in in vitro cancer research, modelling of monocyte-macrophage response, and other applications.

2.3. Cell-to-Cell Communication

Cell-to-cell communication is fundamental to the function and survival of all multicellular organisms, orchestrating complex processes such as tissue development, immune response, and homeostasis. It allows cells to sense and respond to their environment, coordinating their activities to maintain a stable internal state. This communication is facilitated by a variety of signaling molecules, including hormones, neurotransmitters, and growth factors. These molecules bind to specific receptors in or on the cell and trigger the intracellular events [88, 89]. For example, the immune system's ability to identify and destroy pathogens or cancerous cells relies heavily on cell-to-cell communication. Immune cells, such as macrophages and T-cells, use signaling molecules to communicate with each other and with infected or abnormal cells, coordinating a precise and effective response [90, 91].

Studying solo cells causes a loss of context by removing the cell from its native tissue microenvironment, like the ECM and neighboring cells. This deprives the cell of critical physical and biochemical cues that regulate its behavior. For instance, a cancer cell in isolation might behave very differently from one embedded within a tumor, where it is influenced by fibroblasts, immune cells, and the signaling landscape. Also, phenotypic alterations can occur without natural ECM [92, 93].

Studying the communication between melanoma and immune cells, particularly macrophages, is important because this interaction is a major determinant of tumor progression, metastasis, and the effectiveness of immunotherapy. A key reason to focus on this crosstalk in this study is to understand the mechanisms by which melanoma cells manipulate the immune system for their own survival.

Monocytes and macrophages play a dual role in melanoma, both promoting and inhibiting tumor growth depending on their polarization state. This makes them a critical subject of study. Research has shown that macrophages are heavily involved in all stages of melanomagenesis. In the early stages, they can exhibit an M1 (pro-inflammatory) phenotype, which is associated with an anti-tumor response. These macrophages kill cancer cells through phagocytosis and by secreting pro-inflammatory cytokines like IFN-γ [94–96].

In established tumors, the tumor microenvironment (TME) can reprogram these macrophages to an M2 (anti-inflammatory) phenotype, transforming them into tumor-associated macrophages (TAMs). TAMs are a hallmark of advanced melanoma and are associated with a poor prognosis [97, 98]. Within TME, these cells exert multiple pro-tumor factors, including immune suppression through the secretion of immuno-suppressive cytokines such as IL-10, which inhibits T-cell activation and facilitates immune evasion by melanoma cells [99]. They also promote angiogenesis by releasing growth factors, notably vascular endothelial growth factor (VEGF), thereby enhancing the formation of new blood vessels to supply the tumor with essential nutrients and oxygen [97]. In addition, TAMs contribute to metastasis by facilitating melanoma cell migration, invasion and colonization of distant tissues [96].

Macrophages and melanoma cells engage in a dynamic and bidirectional crosstalk that profoundly influences tumor progression, immune evasion, and therapeutic resistance. This communication occurs through multiple mechanisms, including the secretion of soluble mediators [100], exchange of extracellular vesicles [101], direct cell-cell contact [102], and extracellular matrix remodeling [103]. Melanoma cells secrete colony-stimulating factor-1 (CSF-1), chemokines such as CCL2 and CCL5, and immunomodulatory cytokines including IL-10 and TGF-β, which recruit circulating monocytes and polarize them toward an M2-like, tumor-promoting phenotype [100]. In turn, macrophages release pro-inflammatory mediators such as TNF-*alpha* and IL-1β, as well as pro-angiogenic factors including VEGF, EGF, and FGF, which support melanoma cell proliferation, migration, and vascularization [103, 104]. Additionally,

macrophage-derived CCL18 and IL-10 contribute epithelial-mesenchymal transition (EMT)-like changes in melanoma cells, enhancing their invasive potential [105]. Extracellular vesicles from both cell types shuttle microRNAs, proteins, and metabolites that reprogram the phenotype of the recipient cell [101]. Direct membrane interactions, including integrin-mediated adhesion and Notch signaling, further sustain this pro-tumoral dialogue [102]. Collectively, these interactions establish an immunosuppressive tumor microenvironment, promote metastatic dissemination, and diminish the efficacy of conventional and targeted therapies. Figure 2.2 shows the communication dynamics between melanoma and macrophage.

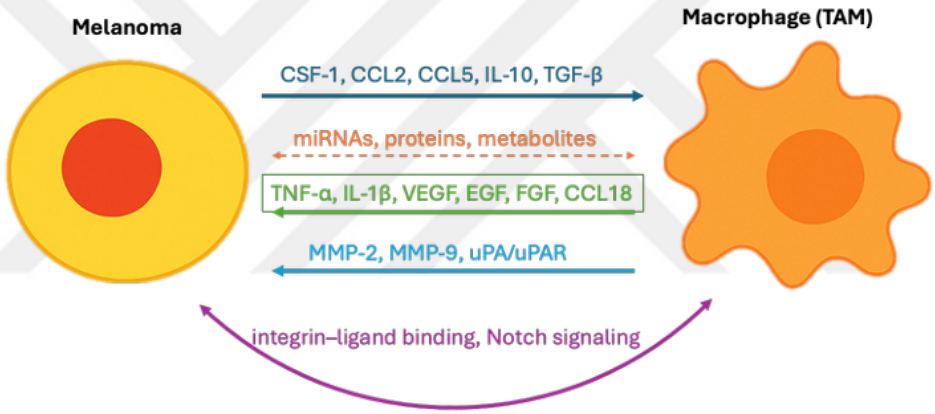


Figure 2.2. Communication mechanism between melanoma cells and TAMs.

Mahmoud Hussein examined the complex role of TAMs in melanoma progression. The study investigated how TAMs can exert both tumor-suppressive and tumor-promoting effects through their interactions with melanoma cells. The research focused on the exchange of soluble factors between TAMs and melanoma cells, which can either inhibit or facilitate tumor growth [106, 107].

Traditional 2D cultures fail to capture the dynamic interaction between monocytes/macrophages and other cells within complex TME. 3D bioprinting offers a solution by enabling the fabrication of biomimetic models that more accurately represent in vivo conditions. Researchers are using 3D bioprinting to create multi-cellular melanoma

models. For example, Pizzurro et al. have combined melanoma cells with fibroblasts and macrophages within a 3D collagen-based hydrogel. These models have been used to observe how direct cell-to-cell interactions and the 3D environment influence the polarization of monocytes into tumor-promoting TAMs. These models allow for a more realistic study of the mechanisms behind immune suppression and a platform for testing new immunotherapies [107]. Further literature studies are summarized in section 2.5.3. Cell-to-cell communication in 3D bioprinted systems.

2.4. 3D Bioprinting

Bioprinting, as a form of three-dimensional (3D) cell culture, represents a significant paradigm shift from traditional two-dimensional (2D) cell culture systems. 2D systems, in which cells are grown in a flat monolayer on a rigid plastic surface, have been the gold standard for decades due to their simplicity and low cost. However, they have fundamental limitations that restrict their ability to accurately model in vivo biological processes. The primary advantage of 3D bioprinting is its capacity to create complex, multi-cellular structures that more closely mimic the physiological microenvironment of native tissues and organs. In contrast to 2D cultures where cells have unnatural, unconstrained access to nutrients and uniform gene expression, 3D models allow for the formation of concentration gradients, realistic cell-to-cell and cell-extracellular matrix (ECM) interactions, and more accurate cell morphology and function (Figure 2.3). This enhanced biological relevance makes 3D bioprinted models superior for a wide range of applications, from drug delivery and toxicity screening to the study of complex diseases like cancer, where the tumor's 3D architecture and its interactions with the surrounding microenvironment are critical determinants of progression and treatment response [9–12, 108].

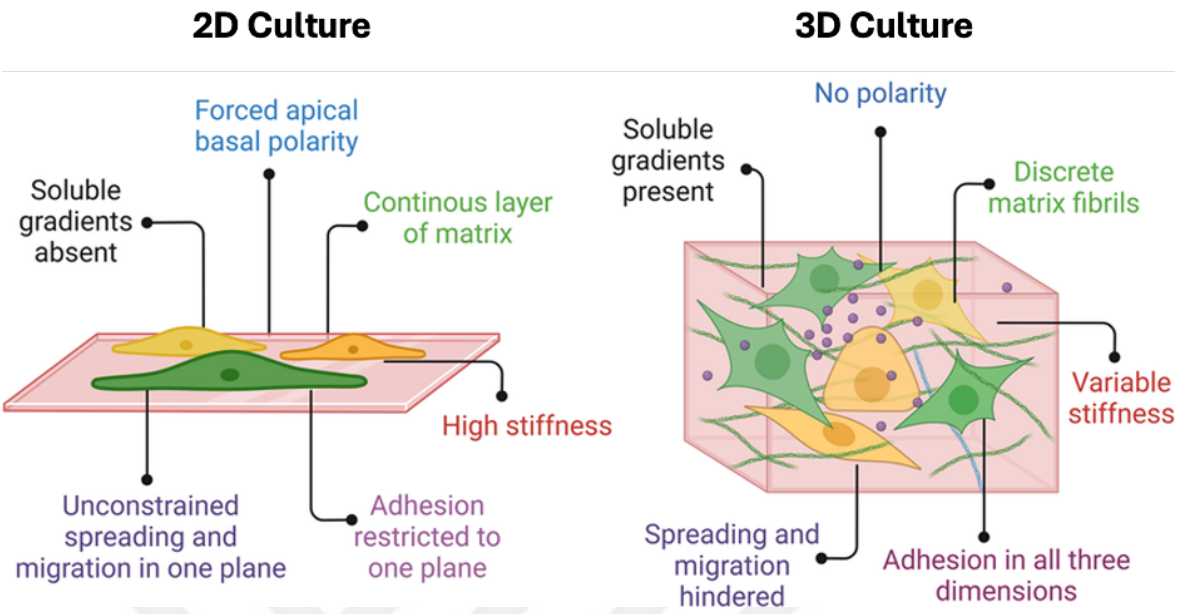


Figure 2.3. 2D vs 3D cell culture [108].

2.4.1. Methods of 3D Bioprinting

Biofabrication is a multidisciplinary field of research. It is 3D fabrication that expands the scope of studies in the laboratory setting by placing cells in tissue scaffolds that mimic the extracellular matrix. By changing parameters such as scaffold design, biomaterial selection, and cell selection, living systems can be simulated in 3 dimensions [109].

In rapid prototyping, rapid 3D production, the scaffold is fabricated layer by layer under computer control. The 3D design of the scaffold is modeled using CAD software or created using imaging data such as CT or MRI. In this way, a scaffold with complex geometry to be studied, such as an organ or tissue system simulating a specific situation for a person or patient, is created in a sensitive and controlled manner. The advantages of rapid prototyping include the presence of scaffold connections, the combination of different materials, a faster and less stepwise production process thanks to automation, and greater cost efficiency [110].

There are more than 30 rapid prototyping techniques worldwide, and most of these techniques can be used in biomedical fields, but only a few are compatible with the use of hydrogels. Among these techniques, there are 3 main topics: Laser-based, Inkjet-based and Extrusion-based.

Laser-based systems crosslink the hydrogel using light energy for the scaffold. There are several techniques such as stereolithography, micro-stereolithography, and solid-substrate curing. The advantages of laser-based systems generally include high resolution and workability with viscous materials. However, this system is often expensive and thermal damage to the material is possible. The long production time can also be counted among the disadvantages [110].

In laser-assisted bioprinting, a cell-laden hydrogel is applied to the metal film, which is vaporized by the laser light, leading to the removal of bioink droplets (Figure 2.4). The main problem with this technique is that the cells are exposed to high temperatures, and the viability of the cells decreases. Ultrafast lasers can be used to prevent this, but they also increase the cost of manufacturing [111].

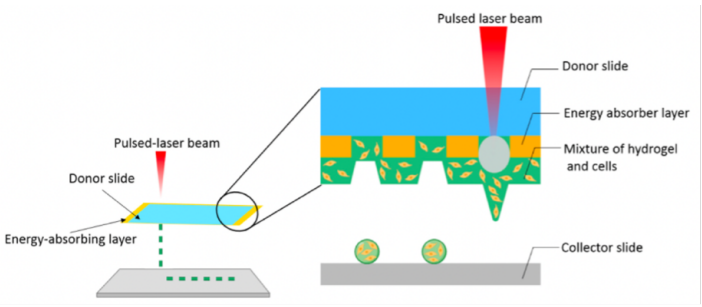


Figure 2.4. Laser-assisted bioprinting [111].

Stereolithography is a laser-based 3D bioprinting technique that uses a UV laser and a directional mirror. The mirror reflects the light beam onto to the hydrogel and crosslinks it (Figure 2.5). With this technique, a precise and high-resolution scaffold can be fabricated. The disadvantage of this technique is that the laser has a destructive effect on the cells and causes skin cancer [111].

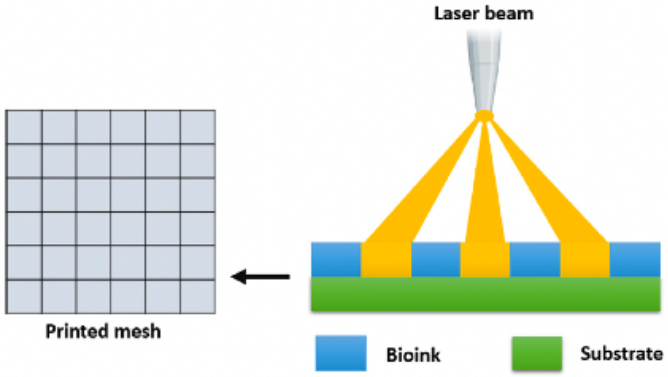


Figure 2.5. Stereolithography [111].

Inkjet-based systems are divided into drop-on-demand or continuous-jet systems. In continuous-jet systems, ink emerges continuously from a nozzle under pressure. The jet then splits into a series of droplets whose direction is controlled by electrical signals. In the drop-on system, the ejection of the hydrogel is controlled by an electrical signal. They are the least compatible printer systems with hydrogels and are difficult to use with highly viscous materials. A clogging problem arises when working with high density cells, and it is a system that can generate thermal and tensile stresses. However, it is an advantageous system because the bio-inks can be easily replaced, production is fast and inexpensive, and high resolution is achieved [111, 112].

Piezoelectric inkjet printing uses voltage pulses between a printing plate and an electrode to create droplets. This voltage is generated by a piezoelectric actuator around the hydrogel chamber [111].

Thermal inkjet uses a thermal actuator and heat used to generate the pressure pulse in the hydrogel chamber [111] (Figure 2.6).

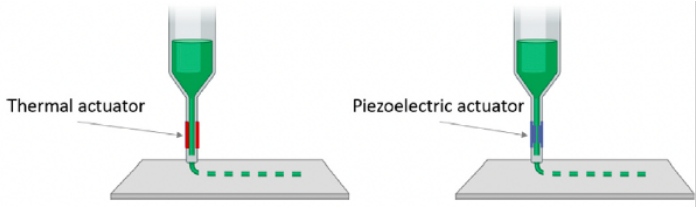


Figure 2.6. Printer-based bioprinting system [111].

Extrusion-based bioprinting is the widely used method due to its compatibility with a broad range of bioinks and high cell density (Figure 2.7). It offers ease of use and low-cost, disposable syringes (for mechanical) and cartridges (for pneumatic). Various printable materials (hydrogels) can be used in this system, and it is the most suitable technique for tissue engineering. A disadvantage can be the high shear stress, which can affect the viability of the cells [111, 112].

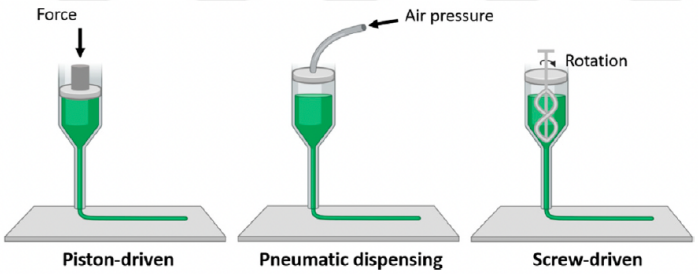


Figure 2.7. Extrusion-based bioprinting [111].

There are several key parameters that influence print success, cell viability, and structural stability. Nozzle diameter affects the resolution of the scaffold and shear stress. Smaller diameters (100-200 mum = 33-27 gauge) can improve the precision, but can damage the cells due to higher shear stress. Printing pressure must be balanced to ensure continuous extrusion without damaging cells. Higher viscosity inks like alginate require increased pressure, which also damages cells. Printing speed affects the filament consistency and structural integrity. Very high speed may lead to filament breakage, while very low speed may cause over-deposition. Every hydrogel requires different temperature control, so the printhead or the print surface temperature should be set accordingly [113].

A study created a tri-layered 3D bioprinted model of melanoma using patient-derived cancer stem cells, fibroblasts and other healthy cells embedded in a collagen-based hydrogel. This model was used to screen chemotherapy drugs and identify which patients were susceptible or resistant to specific treatments [114].

Researchers have bioprinted melanoma models using decellularized ECM (dECM) from human skin as a bioink. This allows them to create a biomolecule-rich matrix that more accurately reflects the native tissue (Figure 2.8). These models have been used to study the initial stages of metastatic disease by observing melanoma cell migration through the basement membrane [115].

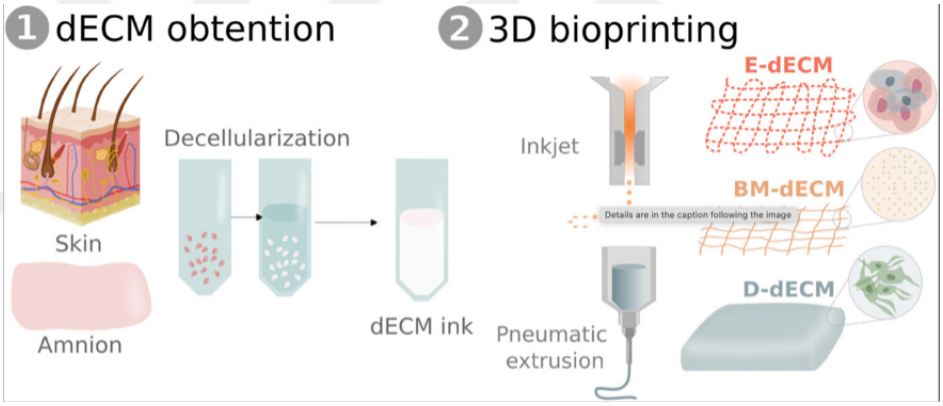


Figure 2.8. dECM from human skin [115].

Some studies incorporate endothelial cells to bioprint a microvascular network within the melanoma model. This allows for a more accurate simulation of how tumors acquire nutrients and how cancer cells might spread through the vascular system, providing a platform to study anti-angiogenic therapies [116].

2.4.2. Hydrogels as Bioink

Hydrogels are divided into two as their generation methods. Natural hydrogels are the ones obtained from nature by extracting the essence with chemical or physical processes. Alginate, gelatin, hyaluronic acid, etc., are examples of natural hydrogels,

and these natural polymeric hydrogels are widely used in studies due to their biocompatibility, degradation, and low cost. However, they show very poor mechanical strengths and stability for bioprinting. On the other hand, synthetic hydrogels, which are generated by humans, have better mechanical properties than natural hydrogels, but they show worse biological properties. PEG and PEG-derivatives are widely used in the studies due to their hydrophilic properties, which allow the diffusion of the nutrients and waste [117].

Alginate is a biocompatible, cheap, and fast gelating natural polymer that is widely used in bioprinting [118]. Among the natural hydrogels, alginate is the most stable and have good rheological properties. Alginate at a concentration between 2-4%(w/v) is easily extrudable, provides sufficient structural integrity, and is biocompatible. Upon exposure to a crosslinking agent, it quickly undergoes gelation and retains its 3D structure [118]. However, cell adhesion and cell communication in alginate are poor, especially at higher concentrations, due to the strong hydrophilic characteristics of alginate. To overcome these issues, several modifications and/or combinations, such as Matrigel or gelatin, were studied [112, 117, 119].

Oxidized alginate and the combination of various cross-linkers such as Ca2+, semicarbazone, oxime, and hydrazone were studied, where the oxidized alginate cross-linked with the semicarbazone or hydrazone showed good viscoelasticity and adhesion in terms of bioprintability [120]. Another group studied methacrylated alginate (MeAlg), which was polymerized with light. MeAlg showed shear-thinning behavior, which requires more pressure to create a more concentrated matrix [121].

Gelatin is another biocompatible and cheap natural polymer for the use of bioprinting purposes. In addition, gelatin has advantages for bioprinting in terms of high adsorption of water, good cell adhesion, and being non-immunogenic. However, since gelatin is highly soluble at physiological temperatures, the mechanical stability is low after printing [112, 122]. Since it shows poor rheological characteristics, it is usually used in combination with another hydrogel like alginate to improve its stability [123].

GelMA is the most widely used synthetic hydrogel. Methacrylated groups are chemically added to gelatin, and gelatin characteristics have improved, showing great stability and printability [124, 125]. Different cell densities within the GelMA have been studied, and it was seen that HepG2 cells can live within the hydrogel up to 8 days [125]. The bioprintability of the GelMA hydrogel depends on the elastic modulus of the hydrogel. The pore architecture of GelMA scaffold was studied by changing the needle gauge, pressure, and flow rate [124]. In another study, 10% GelMA in FBS solution was bioprinted for the primary human chondrocyte growth. The cell-laden scaffold was crosslinked with ultraviolet light, and these conditions provided great printability and cell viability [126].

Hyaluronic acid (HA) is a natural polymer, which exists in all connective tissues, such as skin, cartilage, and articular joints. It is a fast gelated hydrogel and it promotes proliferation. Self-healing, injectability and shear thinning characteristics were investigated after modifying HA with hydrazide or aldehyde groups. The results showed that 3T3 fibroblasts can live 14 days when the hydrogel concentration is 1.5% [127].

Matrigel is a hydrogel that has the advantage of contributing to cell differentiation. However, slow gelation and gelation above 4°C make this hydrogel disadvantageous for use in 3D bioprinting. Because gelation occurs at low temperatures, the extrusion head requires a cooling system, which increases the cost of cooling the hydrogel [128]. Despite these disadvantages, the Matrigel scaffold provides good cell viability. To overcome challenges to provide rheological stability, the combination of Matrigel and agarose is studied [129].

Collagen is another natural bioink commonly used to make scaffolds for cell cultivation. It is biocompatible and promotes cell proliferation. It exhibits high cell adherence, which makes it desirable for in situ studies. However, it has poor mechanical properties that make the scaffold unstable. Its slow gelation also makes it less stable. Polyethylene glycol (PEG) is a synthetic hydrogel that is biocompatible and supports cell viability. It has high porosity, which makes it desirable for the extracel-

lular matrix. However, it is resistant to cell adhesion and protein adsorption, which are necessary for cell growth in a 3D-printed scaffold.

Chitosan is a biodegradable and antibacterial natural polymer generally used in artificial tissue engineering for bone and skin. It has a low gelation rate, which is a limitation for its use in 3D bioprinting. However, this limitation can be reduced by combining it with other hydrogels, which have a higher viscosity and thus increase stability.

Different types of hydrogels are combined to improve their rheological and mechanical properties. Berg et al. used 2% alginate and 3% gelatin to study the effect of influenza A virus on human alveolar cells [130]. It was found that low concentration of GelMA (less than 2%) and combination with alginate can support cell viability and proliferation. Ding et al. investigated the alginate-gelatin combination to study cell distribution in a planar scaffold [131]. They examined a ratio of 2% alginate and up to 20% gelatin and found that most cells aggregated around the cross region of the scaffold. 10% GelMA and 1% alginate showed the best stress-strain curve, and scaffold stability lasted up to 96 hours [132].

Different cell types in different hydrogels are also investigated in many studies. Chondrocytes are 93% viable in alginate, while they are 88% viable in GelMA after 21 days. HUVECs are 57% viable in gelatin for 3 days, while they are 90% viable in GelMA for up to 21 days. L929 (mouse fibroblasts) are 97% viable in alginate, whereas they are only 60% viable in the alginate-gelatin combination. BMSCs are 90% viable in GelMA, but only 78% viable in the alginate-GelMA combination within 21 days [117].

2.4.3. Crosslinking Methods

Crosslinking is a procedure that hardens the hydrogel scaffold after it is produced. There are three methods (thermal, chemical, and physical crosslinking methods) that can be applied to the scaffold depending on the hydrogel composition [117].

Thermal crosslinking is a method in which temperature changes control the crosslinking reaction. Thermal crosslinking at room temperature or 37℃ is the most commonly used temperature to harden the scaffold (Figure 2.9).

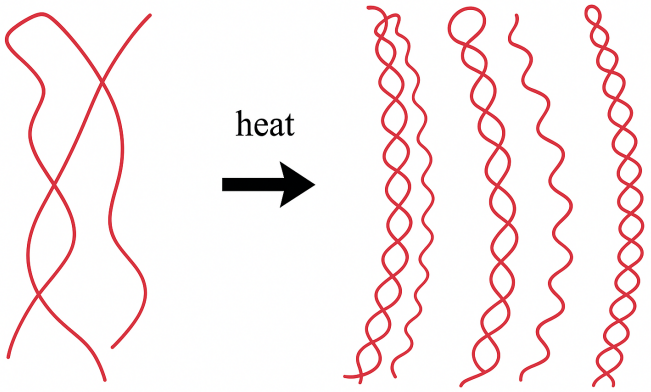


Figure 2.9. Thermally induced entanglement for crosslinking.

Physical crosslinking is generally applied to the hydrogel by exposing the scaffold to UV light (Figure 2.10). Methacrylated groups like GelMA, HAMA, AlgMA etc., are treated by the UV light to harden and stabilize the scaffold.

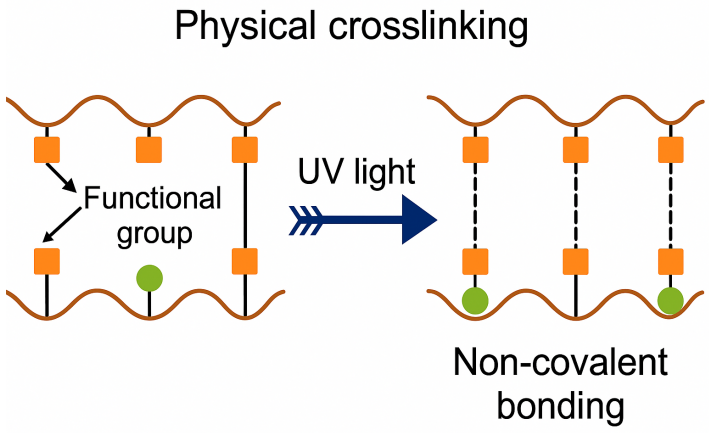


Figure 2.10. Physical crosslinking.

Chemical crosslinking is a method in which reaction agents are added to the hydrogel to harden the material (Figure 2.11). Ionic interactions help to link the polymers and harden it. Generally, Ca^{2+} ions are used for this chemical bonding. $CaSO_4$, NaCl, $CaCO_3$, and $CaCl_2$ are commonly used for this process, and Ca^{2+} cations trigger the crosslinking reaction. Various concentrations of $CaCl_2$ have been investigated in the literature; combinations with chemical and physical crosslinking have also been studied.

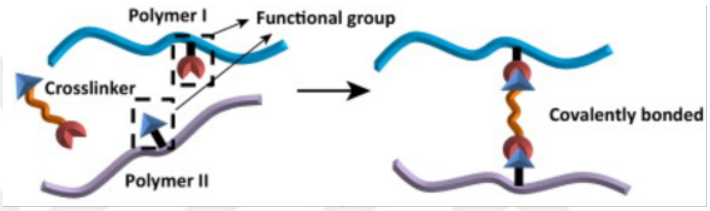


Figure 2.11. Chemical crosslinking.

2.5. Bioprinted Studies with Cells

3D bioprinting has emerged as a powerful biofabrication technology that enables the precise spatial deposition of living cells, biomaterials, and bioactive molecules to create tissue-like scaffolds that closely mimic the architecture and microenvironment of native tissues [109, 118]. Unlike traditional 2D cultures, 3D bioprinting allows the incorporation of multiple cell types within biomimetic scaffolds, facilitating cell-cell and cell-ECM interactions in a physiologically manner [133]. This approach has been widely applied in cancer research, regenerative medicine, and immunology [134], where patient-derived or model cell lines can be combined with hydrogels such as alginate, gelatin, collagen or Matrigel to recapitulate tissue-specific microenvironments. In cancer modeling, 3D bioprinted constructs allow for the coculture of tumor cells with stromal and immune cells, allowing the investigation of tumor growth dynamics [135], drug resistance [136], and immune modulation [134, 137] under conditions that more accurately reflect in vivo physiology.

2.5.1. 3D Bioprinted Models for Melanoma Cell Studies

Multi-layered models of the tumor and its surrounding microenvironment, researchers can gain a deeper understanding of the disease and test new therapies in a more accurate setting. A study published a 3D bioprinted model of metastatic melanoma that is suitable for drug screening. This model incorporates melanoma cells and dermal fibroblasts within different layers to mimic the skin's structure. By tracking the cells, researchers were able to model the initial stages of metastasis and better understand how melanoma cells behave and respond to drugs [115].

Researchers have developed a 3D bioprinted model of malignant melanoma that can identify a patient's resistance to chemotherapy. This model, which incorporates patient-derived cancer stem cells and healthy cells from the surrounding environment, accurately reproduces the tumor microenvironment. This breakthrough could lead to the development of personalized therapies fot patients, as the model showed different responses to a drug called vemurafenib compared to traditional 2D cultures [114].

Schmid et al. developed a new bioink composed of alginate, hyaluronic acid and gelatin (Alg-HA-Gel) optimized for 3D bioprinting applications. The formulation was tuned to achieve favorable rheological properties, enabling precise extrusion printing with high shape fidelity while maintaining a cytocompatible environment. They demonstrated that the bioink supports the encapsulation and growth of various human cell types, including skin-derived fibroblasts and melanoma cells, with high post-printing viability. The constructs maintained structural stability during culture, and the inclusion of hyaluronic acid enhanced cell spreading and proliferation. This study highlights Alg-HA-Gel as a versatile, printable hydrogel suitable for creating melanoma-containing 3D tissue models for disease modeling and therapeutic testing [138].

There is another study that presents a novel 3D bioprinting strategy to fabricate biomimetic melanoma models using patient-derived melanoma cells within a customized hydrogel matrix. The hydrogel formulation was optimized for printability,

mechanical stability, and biocompatibility, incorporating components such as gelatin, alginate, and bioactive additives to mimic the tumor microenvironment. The printed constructs maintained high cell viability and supported melanoma cell proliferation, invasion, and formation of tumor-like aggregates over time. Importantly, the model recapitulated key features of melanoma pathology [105], including heterogeneity and invasive behavior, and was responsive to standard melanoma therapies, enabling drug screening and personalized medicine approaches. This work demonstrates the potential of 3D bioprinted melanoma models as physiologically relevant platforms for studying tumor biology and evaluating therapeutic responses [139].

The study by Duan et al. successfully created a melanoma model by using a GelMA/PEGDA composite scaffold. The researchers wanted to establish an in vitro model that mimics the tumor microenvironment to help with cancer treatment and drug research. The study found that melanoma cells, specifically A375 cells, showed higher levels of aggregation and proliferation on the 3D bioprinted scaffold compared to traditional 2D cultures. Furthermore, the 3D environment caused the cells to become more aggressive and differentiate more, as shown by higher expression MMP-9 protein, which is involved in extracellular matrix degradation and is a marker for tumor aggressiveness. The study also evaluated the effect of the natural compound luteolin on the melanoma cells. It was found that luteolin's anti-cancer effects were both time- and dose-dependent. However, the melanoma cells grown in the 3D model were more resistant to luteolin than those in the 2D culture system, which is believed to be a more accurate reflection of how a drug would work in the body [140].

2.5.2. Exploring THP-1 Cells Through 3D Bioprinting

THP-1 is commonly used in hydrogels for tissue engineering studies. Barthes et al. studied THP-1 cells as monocytes and macrophages (differentiated THP-1) encapsulated in gelatin hydrogel (Figure 2.12). Cytokine detection by ELISA was performed for coculture systems containing monocytes/macrophages and HUVECs or fibroblasts to determine the effects of the microenvironment on growth or secretion.

Cells were viable for 13 days [141].

Coburn et al. investigated using THP-1-derived macrophages and vocal fold fibroblasts (VFFs) within the glycol-chitosan hydrogel. For cross-linking the hydrogel, glyoxal was used as a cross-linking agent at different concentrations (0.005, 0.01, and 0.02%). It was observed that the stiffness of the hydrogel increased with increasing concentration of the crosslinking agent. Transwell plates were used for the cocultivation experiments. VFF cells encapsulated with the hydrogel were placed in the transwell plate, while macrophages were placed at the bottom of the plate. The cytokine secretion, TNF-α as a pro-inflammatory cytokine, and IL-10, as an anti-inflammatory cytokine, were examined by ELISA, and it can be seen that as the stiffness of the hydrogel increases, the anti-inflammatory activity increases [142].

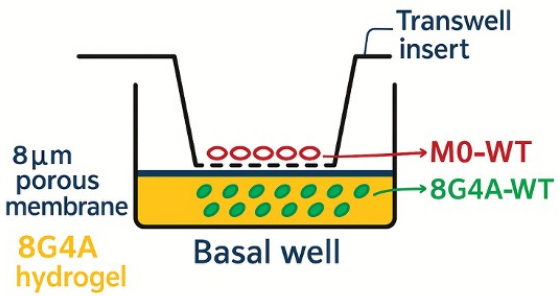


Figure 2.12. Transwell-plate setup for co-culturing [142].

Raveendran et al. explore the use of 3D bioprinting to create a macrophage model for investigating inflammatory responses. Researchers differentiated THP-1 cells into macrophages within a 3D environment and observed an elevated pro-inflammatory response when exposed to bacterial endotoxin (LPS). This demonstrates that 3D bioprinting is a promising tool for modeling inflammation and drug responses in a more physiologically relevant setting than traditional 2D cultures [143].

A study of Aldrich et al. describes a 3D bioprinted bone scaffold both antibiotics and viable macrophages to treat infections following craniotomy. The study found that incorporating live macrophages into the antibiotic-delivering scaffold significantly

improved bacterial clearance of Staphylococcus aureus compared to using antibiotics alone. This research highlights the potential of using bioprinting to create targeted scaffolds that augment the body's immune response [144].

2.5.3. Cell-to-Cell Communication Studies in Innovative 3D Bioprinting Platforms

Cancer cells, including melanoma cells, A375 and others, communicate with stromal cells (fibroblasts, endothelial cells), immune cells (macrophages, T cells, NK cells) and keratinocytes and melanocytes in the tumor microenvironment (TME). Cell-to-cell communication occurs through different mechanisms like direct cell–cell contact via adhesion molecules (N-cadherin, ICAM-1, integrins) [145] or gap junctions (connexins) [146] for direct cytoplasmic exchange of ions/small molecules, paracrine signaling (cytokines, chemokines, and growth factors secreted into the TME) [147], extracellular vesicles (exosomes and microvesicles), tunneling nanotubes (e.g., actin-based cellular bridges, exchange of organelles (like mitochondria) and signaling molecules) [148].

Bioprinted melanoma models with integrated macrophages are used to study how these immune cells contribute to drug resistance. By introducing monocytes into a bioprinted tumor, Madsen et al. observed how different melanoma cell lines influence their differentiation and subsequent phenotype, which in turn can affect the efficacy of a drug. This allows for a better understanding of how immunotherapeutic compounds function in a complex environment [94].

Different types of cells are cocultured in 3D bioprinted systems. Desigaux et al. have engineered a 3D breast cancer model that more accurately replicates the tumor microenvironment. This platform incorporated cancer cells, cancer-associated fibroblasts (CAFs), and endothelial cells. The model is created with a collagen-hyaluronic acid bioink and spontaneously develops key characteristics of a tumor, which is a hypoxic core (an area with low oxygen) surrounded by a proliferative outer layer. The CAFs dynamically remodel the extracellular matrix, increasing the tissue's stiffness, which

is a known feature of aggressive tumors. Furthermore, they secrete pro-angiogenic and radio-resistance-associated cytokines, chemical signals that stimulate blood vessel growth and, reduce the cancer cells' sensitivity to radiotherapy. This innovative model provides an invaluable tool for exploring the complex, dynamic interactions between the tumor and its stroma, offering a powerful platform for testing stroma-targeted therapies aimed at overcoming resistance to conventional treatments [149].

Liu et al. created a 3D bioprinted model of breast tumor tissue with embedded lymphatic vessels. This model was built by using GelMA containing breast tumor cells, with a microchannel lined with lymphatic endothelial cells (LECs) to mimic a lymphatic vessel. The research found that this 3D platform is a functional tool for studying the interactions between lymphatic vessels and breast tumor cells. It also confirms that VEGF promotes the growth of LECs and attracts breast tumor cells to migrate towards the lymphatic vessel [150].

The paper published by Wang et al. details a 3D bioprinting method to create breast cancer models that incorporate adipose-derived mesenchymal stem/stromal cells (ADMSC) to study drug resistance. The study found that breast cancer cells in these 3D models were more resistant to the chemotherapy drug doxurubicin compared to 2D cultures, and this resistance was more pronounced in models with a thicker ADMSC layer bioprinted. The researchers also discovered that a lysyl oxidase (LOX) inhibitor could reduce this drug resistance, highlighting the value of this 3D bioprinted model for studying breast cancer and drug screening [151].

Another group studied the effects of stromal cells on cholangiocarcinoma (CCA) cells in a 3D bioprinting model. The researchers created 3D models using tumor cells (RBE) and different types of stromal cells, including tumor-assıciated endothelial cells (TEC), tumor-associated fibroblasts (TAF) and tumor-associated macrophages (TAM). This study found that cells in the 3D bioprinted models showed better proliferation, higher expression of tumor-related genes, and increased resistance to drugs compared to cells grown in a traditional 2D culture. The presence of TAF and TAM stromal cells

specifically boosted the proliferation and malignancy of the CCA cells, while TEC did not have a similar effect. The 3D model was also shown to promote the epithelial-mesenchymal transition (EMT) of CCA cells, possibly by activating the Wnt/β-catenin signaling pathway. Overall, the paper concludes that this 3D bioprinted model is an effective tool for studying the effects of stromal cells on CCA cells and could serve as a valuable platform for preclinical research and drug testing [152].

There is research creating 3D bioprinted glioblastoma microenvironments with astrocytes and neural precursor cells, with and without macrophages. The study found that these 3D models, particularly those including macrophages, more accurately mimic the gene expression and biological characteristics of real glioblastoma tumors compared to traditional 2D cultures. This platform is presented as a valuable and scalable tool for future research on glioblastoma, including drug testing and the identification of new therapeutic targets [153].

2.6. Physiologically-Based Pharmacokinetic (PBPK) Modelling

Physiologically based pharmacokinetic modelling is a mathematical modelling used for ADME (absorption-distribution-metabolism-excretion) of substances in living organisms. This method is generally used in drug development and pharmaceutical research. It is a multicomponent model; the components are generally organs or tissues. To build a PBPK model, principles of mass transfer, fluid dynamics, and biochemistry are used, and basic differential equations (reaction rate, diffusion, perfusion, flow, etc.) are defined for the compartments. These organs/tissues are predefined based on their similarity and are assumed to be well mixed for this modelling approach [154].

PBPK model is used for predicting the concentration of a substance in plasma. There are static and dynamic models for PBPK modelling. Static modelling is used to predict metabolic clearance, transporter-mediated clearance, and drug-drug interactions. This is a good method for total exposure, but it does not provide a concentration-time curve because it is based on the steady-state assumption. On the other hand, the

dynamic model is used to predict the time profile of substances such as drugs, metabolites, enzymes, etc. Absorption kinetics, maximum concentration and distribution kinetics can be determined by dynamic PBPK models [155].

Whole body models or reduced body models can be created by dividing tissue compartments into small or large groups. For example, in a small model, the compartments are lungs, liver, brain, kidney, and the remaining organs. In a large whole body model, each organ and tissue is assumed to be a separate compartment, which gives more accurate results, while it is much more difficult to define differential equations based on mass balance (Figure 2.13).

PBPK modeling can also incorporate the lymphatic system to characterize the plasma and simulate the distribution of therapeutic agents and their interaction within the lymphatic system.

In the literature, the processes of discovery and development of mAbs (monoclonal antibodies) are usually studied [157–159]. mAbs differ from small substances in terms of their permeability. Therefore, the differential equations and pharmacokinetic (PK) parameters differ from PBPK modeling for whole plasmas. The model works for the mechanism of antibody movement, i.e., from plasma to tissue, from tissue to interstitial fluid (lymph), from lymph to lymph node, and from lymph node to venous blood (Figure 2.14).

The disposition of mAbs in the brain was studied by PBPK modeling [158]. Pharmacokinetic data were obtained from the literature and also estimated in-house. Model equations were established for blood (plasma and blood cells, lymph nodes), brain (plasma, unbound and bound mAb in the endosomal compartment at the brain-blood barrier (BBB), unbound mAb in the brain ISF compartment, blood cell compartment), CSF (unbound and bound mAb in endosomal compartment at brain CSF barrier, lateral ventricle, third fourth ventricle, cisterna magna, subarachnoid space), a typical tissue ”i” (blood cell compartment, plasma compartment), and the liver compartment.

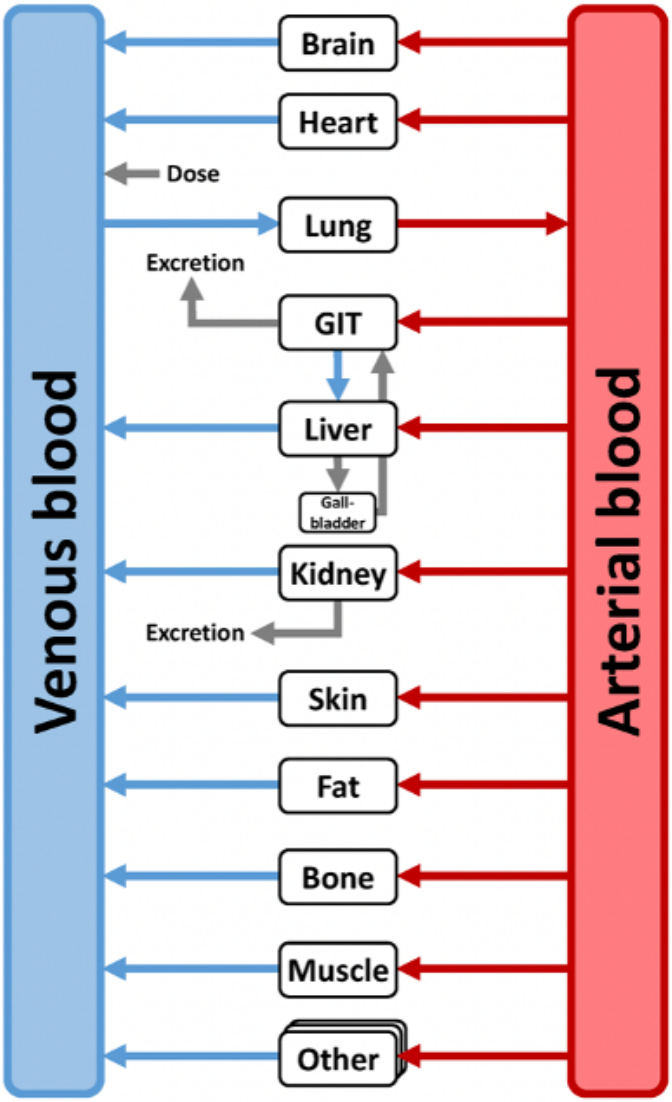


Figure 2.13. PBPK model [156].

A mPBPK (minimal PBPK) model was used to understand the similarities in tissue distribution of mAb in different species [159]. For this modeling, allometric scaling is used, which assumes that different species have similar anatomy, physiology, and biochemistry. For this model, a simple structure is built that includes two compartments: Vtight (muscle, skin, adipose tissue, brain) and Vleaky (liver, kidney, heart, all other tissues). Twelve mAbs were studied and pharmacokinetic profiles were established as a function of time for four species (human, mouse, monkey, rat), (Figure 2.15).

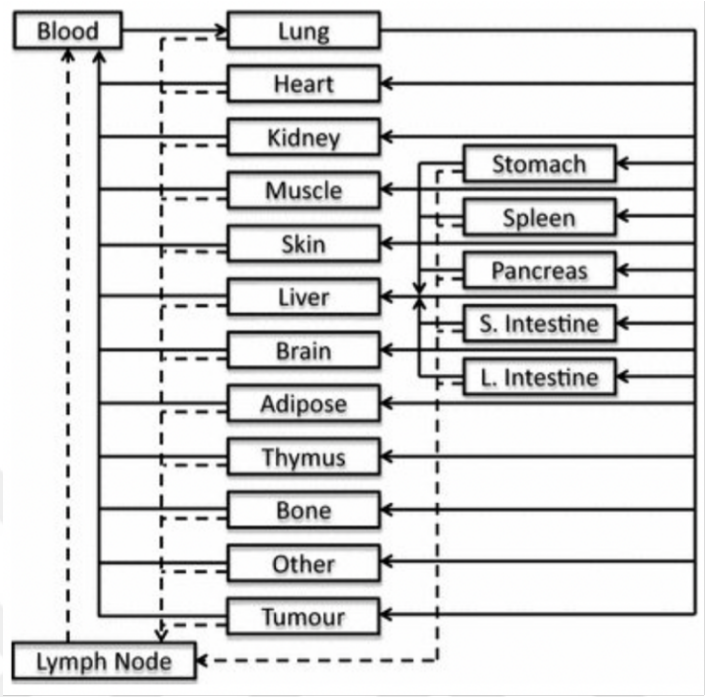


Figure 2.14. PBPK model with lymphatic system [157].

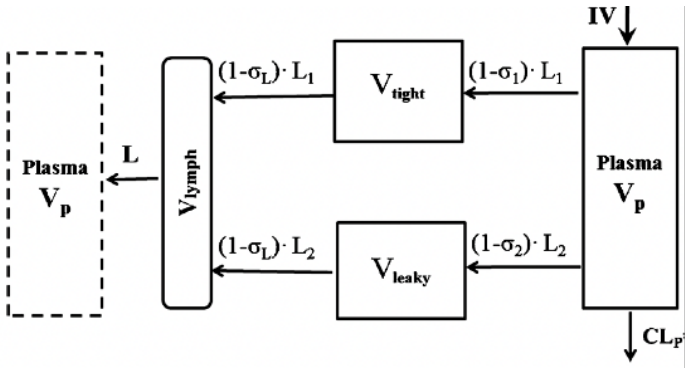


Figure 2.15. Minimal PBPK model [159].

A very comprehensive PBPK model was constructed for characterizing plasma and tissue pharmacokinetics of mAbs in wild-type, FcRn-knockout, tumor-bearing, and nontumor-bearing mice [155]. The researchers also investigated the scale-up potential of the model by exemplifying mouse, human, monkey, and rat plasma. The unknown parameters (C_{FcRn} concentration, CL_{up} (rate of pinocytosis per unit of endosomal space),

K_{deg}, and C_{LNLF} (proportionality constant)) were estimated using 820 equations from 8 different data sets. Thus, this study is able to comprehensively characterize the disposition of mAb in different preclinical species and in humans.

3. MATERIALS AND METHODS

3.1. Melanoma Cell Culturing

For the experiments, GFP-tagged A375 (A375-GFP, Figure 3.1) cell line and wild-type A375 (A375-WT, w/o GFP tag) are used to investigate viability in 2D and 3D platforms. They are kindly provided by the Department of Molecular Biology and Genetics at Bogazici University. These cells are adherent (i.e., they grow attached to the surface of the cell culture flask) with an epithelial morphology (phenotypic responses of individual cells).

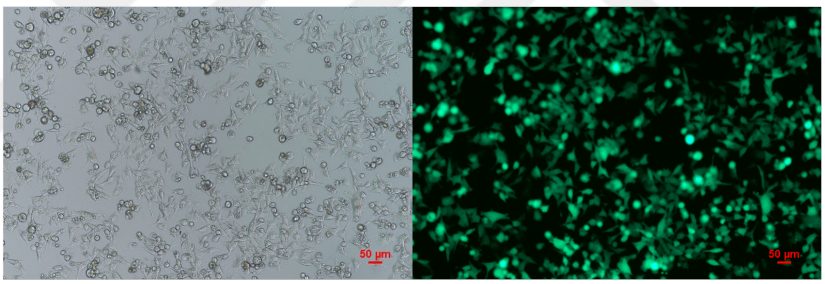


Figure 3.1. A375-GFP melanoma cell line.

Both A375-GFP and A375-WT cells are grown in a DMEM complete medium, which contains 10% fetal bovine serum (FBS) and 1% Penicillin-Streptomycin (Pen-Strep). First, stock cells were thawed and mixed with 7 mL complete DMEM medium and centrifuged at 500 g for 2 minutes to remove the DMSO within the cells. After removing the waste, 5 mL of complete medium is mixed into the cell pellet. Then the cells are transferred to the T25 flask. After 2-3 days, when the confluency of the cells reaches about 80%, the cells need to be passaged. To passage the cells, first, the cell waste is removed from the flask, and the cells are washed with PBS. Then, 1 mL of trypsin is added to the flask to detach the cells from the flask bottom, and they are waited in the incubator for 3 minutes. After the cells are detached, they are mixed with 3 mL of complete medium, and ½ (according to the cell density, it can be 1/3) of

the mixture is transferred to a clean T75 flask, which has 10 mL of complete medium in it. Then the flask was put into the incubator. Passaging was repeated every 2-3 days (Table 3.1).

Table 3.1. Passaging and cell counting of A375 cells.

Passaging Time	**Experimental Procedure**	**Total Cells/mL**	**Viable Cells**	**Viability (%)**
Day 0 (10% complete medium)	Frozen stock + 5 mL medium; T25 flask (incubation in 5 mL DMEM)	1.5×10^6	1.4×10^6	97
Day 3 (10% complete medium)	1 mL trypsinized cells + 2 mL medium; T75 flask (incubation in 10 mL DMEM)	2.1×10^6	1.9×10^6	92
Day 6 (10% complete medium)	2 mL trypsinized cells + 2 mL medium; T75 flask (incubation in 10 mL DMEM)	4.1×10^6	3.9×10^6	97
Day 9 (10% complete medium)	2 mL trypsinized cells + 2 mL medium; T75 flask (incubation in 10 mL DMEM)	4.0×10^6	3.7×10^6	92
Day 9 (20% FBS + 10% DMSO)	1 cryogenic vial for stock (1 mL)	3.7×10^6	3.6×10^6	96

The viability of the cultured cells in a petri dish is investigated using EVE Automated Cell Counter (NanoEntek). Eve cell counter slides are filled with 5 μL of cell sample and 5 μL of Trypan blue. The cell counter distinguishes dead cells from live cells when cells appear black on the screen. Trypan blue provides dead cells that appear black on the screen (Figure 3.2).

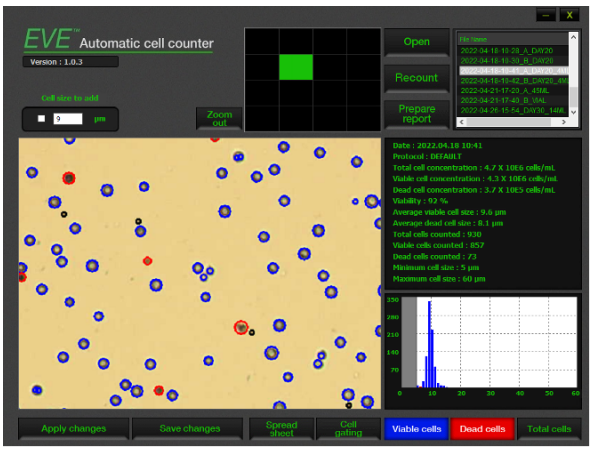


Figure 3.2. Cell counting on Eve automated cell counter.

3.2. THP-1 Monocytes Cell Culturing

THP-1 cells are a human monocytic leukemia cell line originally derived from the peripheral blood of a one-year-old male with acute monocytic leukemia. They are widely used as an in vitro model for studying monocyte and macrophage biology due to their ability to differentiate macrophage-like cells upon stimulation. For the experiments, mCherry-tagged THP-1 (mCherry-THP-1) cell line and wild-type THP-1 (WT-WT, w/o mCherry tag) are used to investigate viability in 2D and 3D platforms. They are kindly provided by the Molecular Biology and Genetics Department at Bogazici University. THP-1 cells normally grow in suspension, but as macrophages (after differentiating into macrophage-like cells), the cells become adherent to the cell culture vessel.

THP-1 cells are grown in RPMI-1640 complete medium (10% FBS included). All equipment is autoclaved and UV sterilized before all cell culturing processes to prevent contamination. RPMI complete medium is prepared with 500 mL RPMI-1640, 10% FBS, 1% MEM-Nea, and 1% Pen/Strep. The frozen stock of THP-1 is passaged in RPMI medium containing 20%, 15%, and 10% FBS, 3 days apart. Table 3.2 shows the number of viable THP-1 cells after they were passaged.

Table 3.2. Passaging of THP1 and cell counting.

Passaging Time	**Experimental Procedure**	**Total Cells/mL**	**Viable Cells**	**Viability (%)**
Day 0 (20% complete medium)	Frozen stock + 1 mL medium + 50% trypan blue	1.7×10^6	1.36×10^6	80
Day 3 (15% complete medium)	Centrifuged cells + 2 mL medium + 50% trypan blue	3.9×10^5	1.95×10^5	50
Day 6 (10% complete medium)	Centrifuged cells + 2 mL medium + 50% trypan blue	2.9×10^6	2.3×10^6	80
Day 9 (10% complete medium)	Centrifuged cells + 2 mL medium + 50% trypan blue (Separated into two plates finally)	4.0×10^6	3.7×10^6	92
Day 12 (10% complete medium)	Plate 1 — Centrifuged cells + 2 mL medium + 50% trypan blue (Separated into two plates finally)	4.1×10^6	3.7×10^6	91
	Plate 2 — Centrifuged cells + 2 mL medium + 50% trypan blue (Separated into two plates finally)	3.2×10^6	2.9×10^6	89
Day 15 (10% complete medium)	Plates 1 and 2 combined; Centrifuged cells + 4 mL medium + 50% trypan blue (Separated into four plates finally)	3.4×10^6	3.0×10^6	89
	Plates 3 and 4 combined ($\sim$14 mL) + 50% trypan blue (Prepared frozen stock)	1.3×10^6	1.2×10^6	88

Table 3.2. Passaging of THP1 and cell counting. (cont.)

Passaging Time	**Experimental Procedure**	**Total Cells/mL**	**Viable Cells**	**Viability (%)**
Day 20 (10% complete medium)	Plates 1 and 2 combined (A) (∼14 mL) + 50% trypan blue	2.1×10^6	1.9×10^6	91
	Plates 3 and 4 combined (B) (∼14 mL) + 50% trypan blue	1.7×10^6	1.6×10^6	94
	Centrifuged cells (A) + 4 mL medium + 50% trypan blue (Separated into four plates finally)	4.7×10^6	4.3×10^6	92
	Centrifuged cells (B) + 4 mL medium + 50% trypan blue (Separated into four plates finally)	6.6×10^6	6.1×10^6	93
Day 23 (10% complete medium)	7 plates combined (∼45 mL) + 50% trypan blue (Prepared frozen stock)	1.7×10^6	1.5×10^6	88
	1 cryogenic vial for stock	8.9×10^6	8.5×10^6	96

3.3. Differentiation and Polarization of THP-1 Cells

Macrophages are highly plastic immune cells that play critical roles in both innate and adaptive immunity. The basic, undifferentiated state of macrophages is referred to as M0 macrophages. M0 macrophages are undifferentiated macrophages that serve as a baseline or "resting" state in experimental models. They are primarily used in research as a starting point to study macrophage polarization under different stimuli. Since M0 macrophages have not yet been committed to a specific phenotype (such as M1 or M2), they offer a neutral background to investigate the effects of various biological, chemical, or physical factors on macrophage behavior [160]. In vitro, M0 macrophages are frequently used to model the initiation of immune response, the effects of drugs

or nanoparticles on macrophage polarization, disease models involving dysregulated macrophage activation, such as cancer, or chronic inflammation [161, 162].

M0 macrophages can polarize into two main functional phenotypes: M1 and M2. M1 macrophages, also known as classically activated macrophages, are typically induced by stimuli such as lipopolysaccharide (LPS) and interferon-gamma (IFN-γ). They are associated with pro-inflammatory responses and are essential for pathogen clearance and antitumor immunity [87]. In contrast, M2 macrophages are induced by cytokines like interleukin-4 (IL-4) and interleukin-14 (IL-13). M2 macrophages contribute to anti-inflammatory responses, tissue remodeling, and wound healing processes [163]. Due to their distinct functional profiles, M1 and M2 macrophages are widely used in in vitro studies to model inflammatory diseases, cancer, and regenerative medicine applications [164].

3.3.1. Differentiation to M0

Phorbol 12-myristate 13-acetate (PMA) is commonly used to differentiate THP-1 monocytes into M0 macrophages, with typical treatment concentrations ranging from 5-100 ng/mL [165]. In this study, a concentration of 20 ng/mL PMA is selected to induce differentiation. A 1000x PMA stock solution is prepared by dissolving 20 μg of PMA in 1 mL of DMSO. For the working solution, 1 μL of the 1000x PMA stock is added to every 1 mL of complete THP-1 culture medium (RPMI-1640 supplemented with 3% FBS and 1% Pen/Strep) to achieve the desired 20 ng/mL concentration. THP-1 cells are treated with the PMA-containing medium for 24 hours to allow differentiation into M0 macrophage-like cells. With this treatment, THP-1 cells become adherent. After the treatment period, cells are incubated in PMA-free complete medium for an additional 48 hours to stabilize their differentiated phenotype. After the resting period, THP-1 cells were differentiated into M0 and are ready to be used in the experiments.

To collect M0 macrophages for downstream experiments, the culture medium is first removed, and the cells are gently washed with ice-cold PBS. The plate is then incu-

bated with fresh ice-cold PBS for 30 minutes to loosen the cells. After incubation, the attached cells are carefully detached using a cell scraper, taking care to minimize mechanical stress to preserve cell viability and integrity. In case of macrophage-like cells, prolonged trypsinization has a negative effect on cell viability (damages the membrane proteins and may even kill the cells), and the detachment efficiency with cell scrapers depends highly on the skill of the researcher.

3.3.2. Polarization to M1 and M2

Several protocols have been developed for the differentiation and polarization of the THP-1 cells. There are five trials to polarize the M0 cells into M1 and M2.

Ready-to-use Macrophage Generation Media XF (PromoCell, C-28055 and C-28056) is initially tested on 6-well plates. The manufacturer (Promocell) suggested that M0 cells wait in macrophage generation media for 6 days. These experiments are done in 6-well plates, which should contain 1.5 million cells per well. When this protocol was applied to M0 cells, all of them were dead after 6 days.

Since 6 days is too long for the cells to polarize, 24-hour treatment is tested in a 6-well plate. 2 wells are kept for M0 control, two wells are treated with M1 generation media, and 2 wells are treated with M2 generation media. Unfortunately, since the cell density in a well is a little bit high (higher than 1.5 million/well), cells agglomerated (Figure 3.3), and the test is unsuccessful.

The same procedure (trial number 2) is applied to M0 cells, but this time, 1.5 million cells are used per well. At the end of 24 hours of M1 and M2 treatment, polarized cells are not attached to the plate, which indicates these cells are dead.

Yet, a flow cytometer test is done to prove whether these cells are polarized or not. Unfortunately, since the number of live cells is insufficient, the flow cytometer did not give reasonable results.

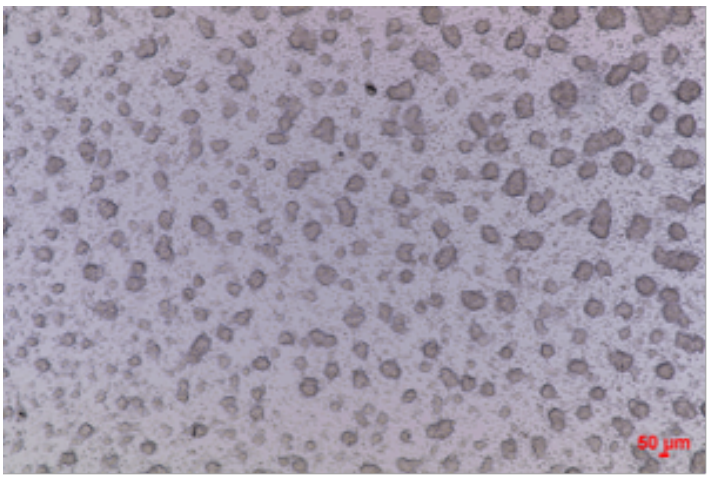


Figure 3.3. Agglomeration of M0 cells at high density polarization.

Since the ready-to-use media does not work successfully as expected, the conventional methods are then used to polarize the cells.

For M1 polarization, M0 macrophages are stimulated with 100 ng/mL lipopolysaccharide (LPS) and 100 ng/mL interferon-gamma (IFN-γ) for 6 hours. Following this activation period, cells are incubated in complete growth medium without stimuli for an additional 18 hours to allow for polarization. For M2 polarization, cells are treated with 100 ng/mL interleukin-4 (IL-4) and 100 ng/ mL interleukin-10 (IL-10) for 24 hours. These cytokine-based protocols are widely used to induce pro-inflammatory M1 and anti-inflammatory M2 phenotypes in vitro. These chemicals are dissolved in a complete medium.

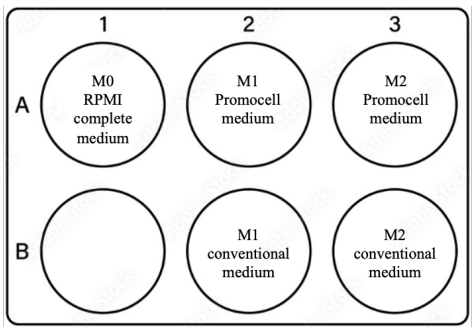


Figure 3.4. Polarization experiment.

Cells are treated with four different media, as shown in Figure 3.4 (2 for M1 polarization and 2 for M2 polarization). After 24 hours, a flow cytometer test is performed for these cells; however, because of the insufficient number of live cells, results could not be obtained. To increase the number of viable cells, the number of wells is doubled, and the previous protocol is applied (Figure 3.5).

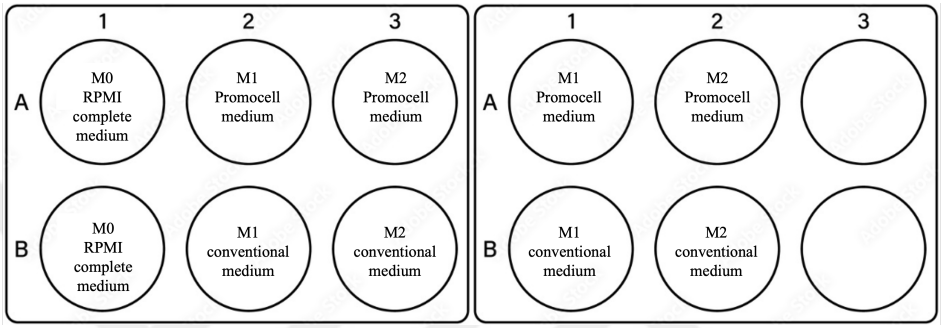


Figure 3.5. Polarization experiment for obtaining more viable cells.

Medium optimization experiments are conducted for polarizing THP-1 cells. Viability tests for different conditions are made to increase the viability and polarization of the M0 cells. Tests are run in 6-well plates, and each well contains 1.5×10^6 cells. The tests were:

- M1 – conventional protocol – 36h
- M1 – conventional protocol within M1 generation medium – 24h
- M1 – conventional protocol within M1 generation medium – 36h
- M2 – conventional protocol – 36h
- M2 – conventional protocol within M2 generation medium – 24h
- M2 – conventional protocol within M2 generation medium – 36

The viability test results are given in the following Table 3.3. The most successful protocol for M1 and M2 polarization is obtained by using the conventional protocol for 36 hours.

Table 3.3. Medium optimization viability test results.

Phenotype	**Protocol**	**Medium**	**Duration**	**Viable cells**	**Viability (%)**
M1	Conventional	M1 generation medium	24 h	4.5×10^5	25
M2	Conventional	M2 generation medium	24 h	3.4×10^5	24
M1	Conventional	M1 generation medium	36 h	3.0×10^5	27
M1	Conventional	Complete RPMI-1640 medium	36 h	6.0×10^5	56
M2	Conventional	M2 generation medium	36 h	4.3×10^5	27
M2	Conventional	Complete RPMI-1640 medium	36 h	4.7×10^5	47

3.4. Analysis of Polarization Status Of Macrophages by Flow Cytometer

The polarization status of macrophages is evaluated by flow cytometry using CD80, CD86, CD163, and CD206 antibodies, which are established markers for M1 and M2 macrophage phenotypes, respectively [166]. CD80 and CD86 expression indicate M1 polarization, while CD163 and CD206 expression are associated with M2 polarization. M0 macrophages are not expected to express these markers at significant levels.

The flow cytometry results (Figure 3.6) confirmed that M0 cells remained non-polarized, as they do not express any tested markers. Upon treatment with Promocell M1 generation medium, only 0.19% of the cells expressed CD80 and 0.86% expressed CD86, indicating minimal M1 polarization. In contrast, the conventional M1 polarizing protocol led to higher polarization, with 28.1% of the cells expressing CD80 and 7.89% CD86 (Figure 3.6).

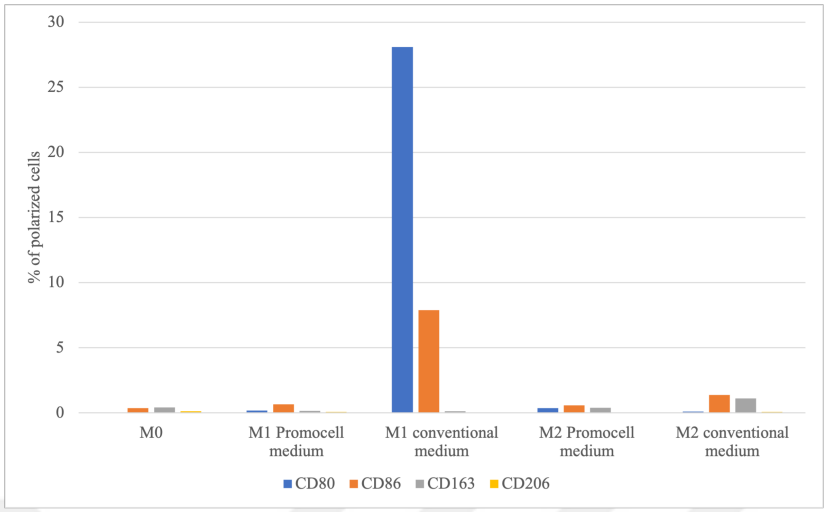


Figure 3.6. Flow cytometer results.

Regarding M2 polarization, neither the Promocell M2 medium nor the conventional M2 protocol induced significant marker expression. Only 0.40% of the cells expressed CD163 and 0.048% expressed CD206, suggesting that M2 polarization is not achieved under the tested conditions (Figure 3.6).

In summary, while M1 polarization is partially achieved using the conventional protocol, M2 polarization could not be induced with either method. Since the amount of M1 cells (30% polarized to M1 cells) are not enough to run an experiment, the study will be based on the M0 macrophages.

3.5. Viability Assessment with Alamar Blue and Acridin

3.5.1. Alamar Blue Assay

Alamar blue is a cell viability reagent that measures the metabolic activity of living cells. It contains resazurin, a non-fluorescent, cell-permeable compound that is reduced to highly fluorescent resofurin by mitochondrial and cytoplasmic oxidoreductase in metabolically active cells. The degree of resazurin reduction is directly proportional to the number of viable cells and can be quantified either by absorbance

or fluorescence measurements [167]. In this study, the Alamar blue assay is used to evaluate the cytotoxic effects of various treatments on A375-WT and M0-WT cells by assessing both viability and metabolic function.

Cells are seeded in 96-well plates at a density of 10000 cells per well and allowed to adhere overnight under standard culture conditions (37°C, 5% CO_2). Following treatment with various agents, 10% (v/v) Alamar blue reagent is added directly to the culture medium in each well. Cells are incubated with the reagent for 4 hours at 37°C, protected from light, to allow sufficient reduction of resazurin. After incubation, both absorbance and fluorescence are measured using a microplate reader. Absorbance readings are recorded at 570 nm and 600 nm, while fluorescence is measured using excitation at 540 nm and emission at 590 nm.

The percentage of cell viability is calculated by normalizing the fluorescence or absorbance values of treated cells against those of untreated control cells. Percentage reduction is determined based on absorbance differences between treated wells and negative control wells (medium + Alamar blue without cells), as described in previous studies and manufacturers' guidelines [167]. Resazurin reduction is calculated as

$$\text{Alamar Blue reduction } (\%) = \frac{\left(O_2 A_1 - O_1 A_2\right)}{\left(R_1 N_2 - R_2 N_1\right)} \times 100 \tag{3.1}$$

where O_1: molar extinction coefficient (E) of oxidized Alamar Blue at 570 nm, O_2: E of oxidized Alamar Blue at 600 nm, R_1: E of reduced Alamar Blue at 570 nm, R_2: E of reduced Alamar Blue at 600 nm, A_1: absorbance of test wells at 570 nm, A_2: absorbance of test wells at 600 nm, N_1: absorbance of the negative control well (medium + Alamar Blue, no cells) at 570 nm, N_2: absorbance of the negative control well (medium + Alamar Blue, no cells) at 600 nm. Viability is calculated as

$$\text{Viability } (\%) = \frac{FI_{590,\ \text{test agent}}}{FI_{590,\ \text{untreated control}}} \times 100 \tag{3.2}$$

where FI_{590} is the fluorescence intensity at 590 nm emission (560 nm excitation).

3.5.2. Acridine Orange/Propidium Iodide Method

Cell viability is a critical parameter for evaluating the effects of drug treatments on cellular health. Live/dead staining using acridine orange (AO) and propidium iodide (PI) is a widely used method to distinguish between live, proliferating, and dead cells. AO is a nucleic acid-selective fluorescent dye that permeates all cells and stains green. PI is impermeable to live cells and selectively stains dead cells with compromised membranes red [168, 169]. The combination of AO and PI provides a reliable, rapid assessment of cell viability and membrane integrity in response to various treatments.

Acridine orange stock is prepared by dissolving 5 mg AO in 1 mL ethanol (5 mg/mL) while propidium iodide stock is prepared by dissolving 3 mg PI in 1 mL ethanol (3 mg/mL).

After treatment, cells are washed once with PBS to remove residual medium and unattached cells. A staining solution containing 1 μg/mL acridine orange [170] and 3 μg/mL propidium iodide [171] in PBS is freshly prepared. Cells are incubated with the AO/PI solution for 5 minutes for 2D platforms and 20-30 minutes for 3D platforms in an incubator, protected from light. Following staining, cells are washed with PBS and fresh PBS is added onto the cells, before they are immediately imaged using a fluorescence microscope. Live cells exhibited green fluorecence due to AO uptake, whereas dead cells display red fluorescence as a redult of PI binding to nuclear DNA. At least 4 random fields are captured per sample to ensure representative quantification of live and dead cells.

Following imaging, pictures are analyzed by using ImageJ. Number of all cells and dead cells are measured and the viability is calculated as

$$\text{Viability } (\%) = \frac{N_{\text{total}} - N_{\text{dead}}}{N_{\text{total}}} \times 100 = \frac{I_{\text{AO}} - I_{\text{PI}}}{I_{\text{AO}}} \times 100 \tag{3.3}$$

where N_{total} is the total number of cells, N_{dead} is the number of dead cells, I_{AO} is the green fluorescence intensity from acridine orange (all cells), and I_{PI} is the red

fluorescence intensity from propidium iodide (dead cells).

3.6. ROS analysis with 2'7' Dichlorodihydrofluorescein Diacetate

Reactive oxygen species (ROS) are chemically reactive molecules containing oxygen, such as superoxide anions, hydrogen peroxide, and hydroxyl radicals. They are naturally produced as byproducts of normal cellular mechanisms and play critical roles in cell signaling and homeostasis. However, excessive ROS production can lead to oxidative stress, causing cellular damage and apoptosis. Monitoring ROS generation is crucial to understanding the cellular responses to treatments, particularly those involving cytotoxicity, apoptosis, or stress-related pathways. In this study, intracellular ROS production is assessed using a fluorescence-based assay (2',7'-dichlorodihydrofluorescein diacetate, H_2DCFDA) after various treatments applied to A375-WT and M0-WT cells on both 2D and 3D platforms.

A 10 mM stock solution of H_2DCFDA is prepared by dissolving 48.7 mg H_2DCFDA in 10 mL DMSO; the stock is then aliquoted into small vials to avoid multiple freeze–thaw cycles.

Intracellular ROS levels are measured using H_2DCFDA. After treatment, cells (or scaffolds) are washed once with PBS to remove residual medium. H_2DCFDA is diluted in PBS to a final concentration of 100 μM and added to the cells. Cells are incubated at 37°C for 30 min. Following incubation, cells are washed twice with PBS and fresh PBS is added at the end. Then, fluorescence is immediately measured using a fluorescence microscope. The fluorescence intensity correlates with the amount of ROS produced within the cells.

The fluorescence intensity corresponding to intracellular ROS levels is background-corrected by subtracting the fluorescence values of blank wells (containing only medium and H_2DCFDA). ROS levels in treated samples are then normalized to the fluorescence intensity of untreated control cells, which is set as 100%. The relative ROS production

for each treatment group is expressed as

$$\text{Relative ROS (\%)} = \frac{F_{\text{corr, sample}}}{F_{\text{corr, control}}} \times 100 \tag{3.4}$$

where the corrected fluorescence is $F_{\text{corr}} = F_{\text{raw}} - F_{\text{background}}$.

3.7. IL-4 Cytokine Treatment

Interleukin-4 (IL-4) is a key anti-inflammatory cytokine primarily involved in Th2-mediated immune responses and macrophage polarization toward the M2 phenotype. Although its effects are well-characterized in immune cells, studies have suggested that IL-4 may also influence tumor cell behavior. In melanoma, including A375 cells, IL-4 has been reported to inhibit proliferation, promote apoptosis, and impair tumorigenic potential through modulation of signaling pathways such as STAT6 and PI3K/Akt [172, 173].

1000x recombinant human IL-4 stock is prepared by dissolving 5μg lyophilized IL-4 in 250 mL ultra-pure water. Then it is aliquoted into small vials to avoid multiple freeze-thaw cycles. To prepare working concentrations of 20, 40, and 60 ng/mL, the stock solution is diluted directly into the complete cell medium (DMEM or RPMI-1640 supplemented with 10% FBS and 1% Pens/Strep). Specifically, 1 μL, 2 μL, and 3 μL of the stock solution are added per 1 mL of the medium to obtain the final concentrations of 20, 40, and 60 ng/mL, respectively. Freshly prepared IL-4 containing media are used immediately for cell treatment to maintain cytokine activity.

3.8. Analysis of IL-4 Cytokine Secretion by ELISA

3.8.1. ELISA (Human IL-4, Sandwich ELISA; Invitrogen IL-4 Human ELISA Kit)

ELISA test (Invitrogen, IL-4 Human ELISA kit) is conducted to determine the presence of IL-4 amount in the samples. This test uses the Sandwich ELISA format.

The protocol as the kit suggested is followed. Briefly, the procedure is

(i) Preparation of materials

- *Decide sample count and set duplicates.* Each sample is measured in duplicate to increase precision.
- *Prepare Human IL-4 standard.* Total standard used per experiment is 200 μL (duplicate wells). Dissolve 1 vial in 1250 μL distilled water (reconstituted standard). It should not be stored at -80°C; however, storing is preferable to discarding if necessary. Prepare at least 225 μL for an experiment to buffer pipetting error. The well concentrations will be: 500, 250, 125, 62.5, 31.2, 15.6, 7.8 pg/mL.
- *Prepare Wash Buffer* in a Schott bottle. The kit provides a 20× stock; dilute with deionized water to 1×. Wash buffer is used between steps to clean wells. Use 400 μL per well each wash.
  - Wash each well 2 times before starting the test.
  - Wash 3 times after biotin–sample incubation.
  - Wash 3 times after streptavidin–HRP incubation.

  Calculate the total wash buffer volume accordingly.
- *Prepare Assay Buffer* in a 15 mL conical tube. The kit provides a 20× stock; dilute with distilled water to 1×. Assay buffer maintains pH, stabilizes proteins, and supports specific interactions between samples and plate-bound antibodies. Use 100 μL in *standard* wells and 50 μL in sample wells. It is also used to prepare Biotin Conjugate and Streptavidin–HRP; include these in the total volume calculation.
- *Prepare Biotin Conjugate* in a conical tube. Provided at 100×; dilute with 1× assay buffer. Use 50 μL per well (once).
- *Prepare Streptavidin–HRP.* Provided at 200×; dilute with 1× assay buffer. Use 100 μL per well.
- *Excess volume.* Prepare all solutions at least 25 μL more than the calculated need to minimize pipetting error.

(ii) Procedure

- Pour the wash buffer into a reservoir.
- Prepare standard serial dilutions in 1.5 mL microtubes labeled S1–S7. Add 225 μL assay buffer to each tube. Add 225 μL reconstituted standard only to S1 and mix. Transfer 225 μL from S1 to S2, mix; then 225 μL from S2 to S3, and so on until S7 (serial 1:2 dilutions).
- Wash the strips twice with 400 μL wash buffer per well using a multichannel pipette. Wait 10–15 s, then empty into the sink. Tap strips on paper towel to remove residual liquid.
- Add 100 μL of prepared standard dilutions to the standard wells (in vial order).
- Add 100 μL assay buffer to *blank* wells. Do not pipette to mix.
- Add 50 μL assay buffer to sample wells. Do not pipette to mix.
- Add 50 μL of samples to the sample wells. Do not pipette to mix.
- Add 50 μL Biotin Conjugate to all wells. Gentle pipetting may be used here to mix; avoid touching the well bottoms at all steps.
- Cover with adhesive film and incubate 2 h at room temperature in the dark. Gently shake occasionally.
- Remove film, empty wells, and tap strips on paper towel. Ensure well bottoms are dry.
- Wash wells 3 times with wash buffer. After the final wash, tap firmly to remove all buffer.
- Add 100 μL Streptavidin–HRP to all wells, including blanks.
- Cover and incubate 1 h at room temperature in the dark; gently shake occasionally (or use a shaker in the dark, if available).
- Remove film and wash all wells 3 times with wash buffer.
- Add 100 μL TMB substrate solution to all wells. Incubate 10 min at room temperature, shaking occasionally. Perform this step with lights off; color development should be visible.
- Stop the reaction by adding 100 μL stop solution when the highest standard turns dark blue. After adding stop solution, wells turn yellow. Note: not

shaking during incubation may yield lower-than-expected OD values.

- Read the plate at 450 nm on a plate reader within 30 min after adding the stop solution.

(iii) Plate reader setup (Gen5)

- Insert the plate into the reader and open Gen5.
- Create a new protocol.
- Select *Absorbance* and set wavelength to 450 nm. Click *OK*.
- Open *Layout*. Assign controls, samples, and blanks. Click *Next*.
- Set blanks as duplicates. Click *Next*.
- Enter standard concentrations and units; choose duplicate. Click *Next*.
- Set samples as duplicates.
- On the layout grid, select each category on the left and click the corresponding well positions; duplicates will populate simultaneously.

3.9. Hydrogel Preparation

3.9.1. Gelatin-Alginate

The hydrogels are prepared at least one day prior to bioprinting. Both gelatin and alginate are dissolved in 1x PBS at a defined weight/weight (w/w) ratio. For example, in the case of 8G4A hydrogel, 8 g of gelatin and 4 g of alginate are dissolved in 100 mL of PBS. First, the required volume of PBS solution is poured into a beaker and placed on a magnetic stirrer. Half of the total gelatin is added and stirred until fully dissolved. After 30 minutes, the remaining gelatin is added. Alginate is added gradually in four portions, with a 1-2 hour interval between each addition, depending on the mixing status of the solution. After all components are added, the beaker is covered to prevent evaporation, and the solution is left stirring to ensure full dissolution and homogeneity.

3.9.2. Matrigel-Alginate & Matrigel Collagen

Matrigel (GFR, membrane matrix, Corning, cat:354230) is widely used biologically active scaffold for cell cultures. It contains extracellular proteins such as laminin, collagen, entactin, etc., and mimics the in vivo microenvironment by promoting cell attachment, proliferation, and differentiation. However, while Matrigel provides biological advantages, its mechanical stability is limited, especially under long-term culture or in 3D bioprinting applications. Therefore, it is often mixed with structurally supportive biomaterials like collagen or alginate. These combinations help improve the hydrogel's mechanical integrity, printability, and stability.

Matrigel is stored at -20 °C in a 1.5 mL Falcon tube and is liquified for 2 hours at 4 °C. Liquified Matrigel is taken from the Falcon tube using a precooled pipette and put into the standard 2 mL precooled bioprinter syringe to prevent gelation when it is transferred. Then, Matrigel is incubated at 37 °C for 15 minutes for gelation.

A collagen-matrigel hydrogel is prepared to create a biocompatible scaffold that supports cell adhesion and proliferation, making it suitable for in situ cell culture applications. The final hydrogel composition consisted of 65% collagen type 1, 20% Matrigel and 15% complete medium containing A375-GFP cells at a density of 1×10^6cells/mL. Collagen stock solution (5 mg/mL) is diluted to 4 mg/mL using 0.1M acetic acid, and its pH is adjusted to 7.2-7.4 by adding 1M NaOH, as the manufacturer suggests. After pH adjustment, the collagen is aliquoted and stored at 4 °C.

Hydrogel preparation is carried out in a precooled environment. Matrigel is liquified at 4 °C and mixed with diluted collagen (1.4 mL collagen + 0.43 mL Matrigel) in a cold Falcon tube. Then, 0.323 mL of cell-containing medium is added, and the bioink is gently mixed and loaded into a precooled syringe. Gelation is induced by incubating the syringe at 37 °C for 15 minutes.

Alginate is mixed with Matrigel to increase the scaffold stability [174, 175]. Alginate is prepared in 1x PBS solution, 1% by weight, at room temperature. The preparation of bioink, consisting of Matrigel and alginate, is conducted in a precooled environment. Matrigel is liquified at +4°C. After the Matrigel is liquified, 0.50 ml alginate and 1.5 ml Matrigel are mixed in a precooled Falcon tube. A cell culture consisting of $2 \times 10^6 6$ cells is centrifuged, and the supernatant is removed. The hydrogel is added to the cells and mixed gently. Then, the hydrogel is transferred to a bioprinter syringe via a pipette and a precooled tip. The syringe is put into the incubator at 37°C for 15 minutes to let the gelation occur. This is the first step of the crosslinking.

3.10. Characterization of Hydrogel

3.10.1. FTIR

The Bruker brand FT-IR device was employed to analyze different types and proportions of hydrogels used for scaffolding. In the analysis, pure alginate and pure gelatin (Figure 3.7) peaked at 3250 cm^2. This means that hydrogels have O-H bonds inside them (Figure 3.8). Pure alginate also peaked at 1400 cm^2, indicating moderate C-H bending. The alginate peaked again at about 1040 cm^2, indicating a strong CO-O-CO bond. Pure gelatin peaked at approximately 1650 and 1580 cm^2, indicating moderate N-H bending (Figure 3.7).

When these two materials were mixed with water and each other in different proportions, they showed very similar characteristics. Since the O-H bond naturally increases in these materials that combine with water, a prominent peak was observed at approximately 3350 cm^2. The second largest peak, which comes from the combination of these two materials, is observed at approximately 1650 cm^2 and this peak indicates the presence of two strong bonds. This double bond also contains the N-H effect (Figure 3.7). Water evaporation from the hydrogel may have occurred as 10G6A waited a week until the FTIR analysis was complete. So, 10G6A shows a slightly lower absorbance value, but the peaks are similar to the other hydrogels (Figure 3.7).

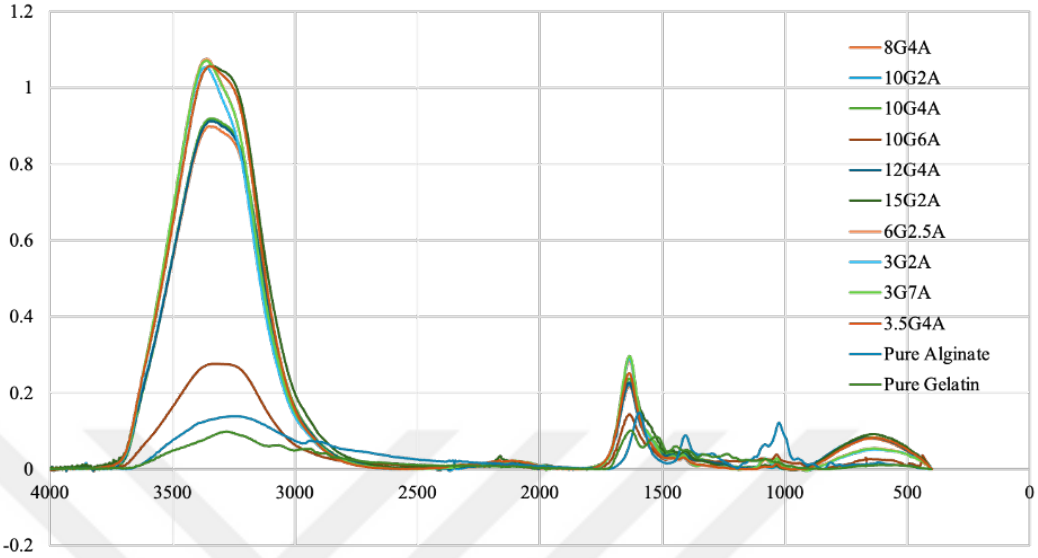


Figure 3.7. FTIR results of hydrogel.

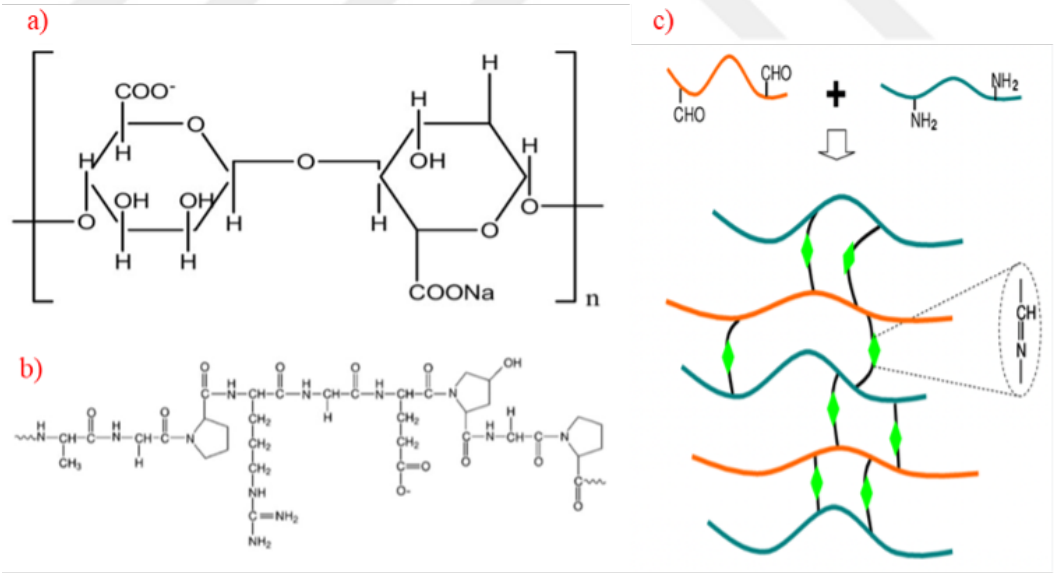


Figure 3.8. (a) SA, (b) G, (c) SA+G.

3.10.2. Porosity

The porosity in the hydrogel scaffold was first tried to be measured by immersion in the ethanol method; however, as with the crosslinking material, the hydrogel was deconstructed and dispersed as soon as it was combined with ethanol. Consequently, porosity could not be measured.

As an alternative method, the hydrogel scaffolds are examined under the microscope, and the porosity was estimated by dividing the area of the pores by the entire hydrogel (Figure 3.9). Round red areas indicate voids in the hydrogel. The division of the sum of these areas over the entire image area gives us porosity by

$$\text{Porosity } (\%) = \frac{A_1 + A_2 + A_3 + A_4 + A_5 + A_6 + A_7}{A_{\text{total}}} \times 100 = 5.94. \tag{3.5}$$

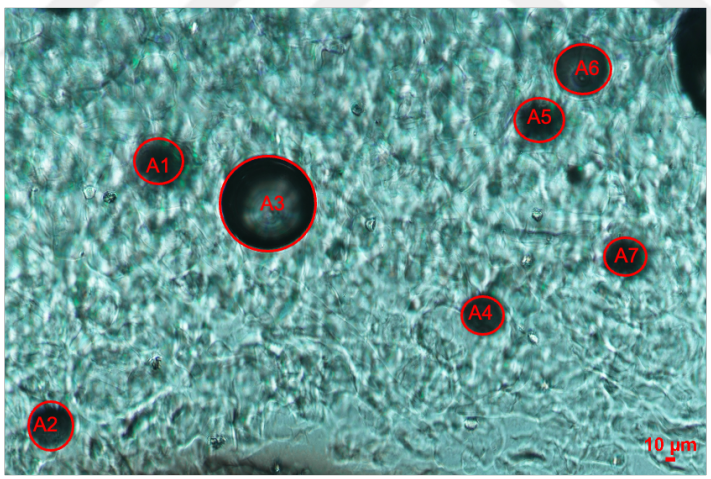


Figure 3.9. Porosity of gelatin–alginate.

3.11. AuNP Production and Characterization

Gold nanoparticle (AuNP) solutions were prepared using the Turkevich method. Aqueous hydrogen tetrachloroaurate ($HAuCl_4$) was treated with citric acid in boiling water, whereby Au^{3+} ions were reduced to Au^0. According to the reaction temperature and the duration of $HAuCl_4$ treatment, nanoparticle size and polydispersity varied.

AuNPs with various diameters and concentrations were kindly provided by Assoc. Prof. Cansu Canbek Özdil and Barış Bilge.

The size distribution of the particles was determined from DLS data, while the solution absorbance was obtained from UV–Vis measurements (Figure 3.10).

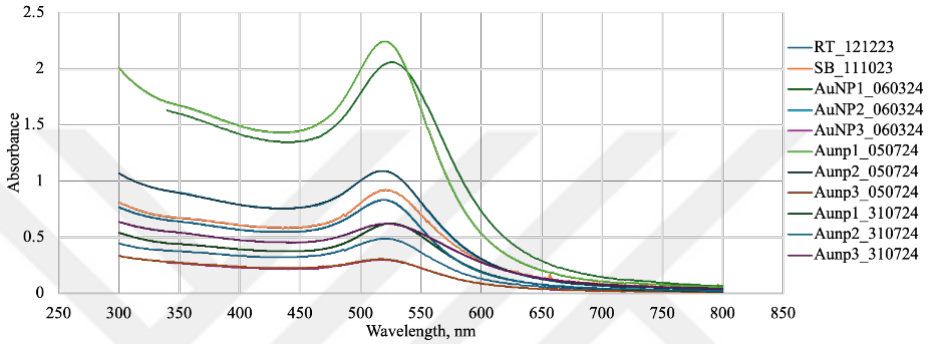


Figure 3.10. UV–Vis data of various AuNPs.

Around the ∼525 nm region the solutions exhibit an absorbance peak, which is attributed to residual Au^{3+} ions. In contrast, Au nanoparticles themselves are ion-free; therefore, to estimate the nanoparticle-related absorbance, the signal at 400 nm is used. The corresponding UV–Vis values are listed in Table 3.4.

Once the DLS and UV–Vis data are available, the concentration of the nanoparticle solution can be obtained from the Beer–Lambert law as

$$A = \varepsilon\, b\, c \tag{3.6}$$

where A is the absorbance (dimensionless), ε is the molar extinction coefficient ($M^{-1}\,cm^{-1}$), b is the optical path length (cm), and c is the molar concentration (M).

The value of ε is taken from literature and assumed identical across the nanoparticle solutions. The absorbance A is read at $\lambda = 400$ nm from the UV–Vis spectra, and the path length is $b = 1$ cm (standard cuvette). Solving the Beer-Lambert equation for

c gives the working expression used in this study as

$$c = \frac{A_{400}}{\varepsilon\, b} \quad \text{with} \quad b = 1 \text{ cm}. \tag{3.7}$$

The calculated nanoparticle concentrations are reported below (see Table 3.4).

Table 3.4. Concentration and size of AuNP solutions.

AuNP Name	**Absorbance A**	**Epsilon, ε ($M^{-1}\,cm^{-1}$)**	**Concentration, c (M)**	**Concentration, c (nM)**	**Size (nm)**
RT_121223	0.334	3.67×10^8	9.1249×10^{-10}	0.912	11.7
SB_111023	0.607	3.67×10^8	1.6558×10^{-9}	1.655	43.8
AuNP1_060324	1.417	3.67×10^8	3.861×10^{-9}	3.861	8.5
AuNP2_060324	0.789	3.67×10^8	2.1499×10^{-9}	2.149	9.0
AuNP3_060324	0.230	3.67×10^8	6.267×10^{-10}	0.626	10.5
AuNP1_050724	1.491	3.67×10^8	4.0627×10^{-9}	4.062	13.5
AuNP2_050724	0.790	3.67×10^8	2.1526×10^{-9}	2.152	13.5
AuNP3_050724	0.239	3.67×10^8	6.5123×10^{-10}	0.651	11.7
AuNP1_310724	0.394	3.67×10^8	1.0736×10^{-9}	1.073	15.7
AuNP2_310724	0.567	3.67×10^8	1.545×10^{-9}	1.544	11.7
AuNP3_310724	0.476	3.67×10^8	1.297×10^{-9}	1.297	13.5

The size distribution obtained from dynamic light scattering (DLS). The data for each sample is obtained in triplicates. The average values of the distribution of the particles are given in the following Figure 3.11, and the average diameter of the AuNP samples is given in Table 3.4.

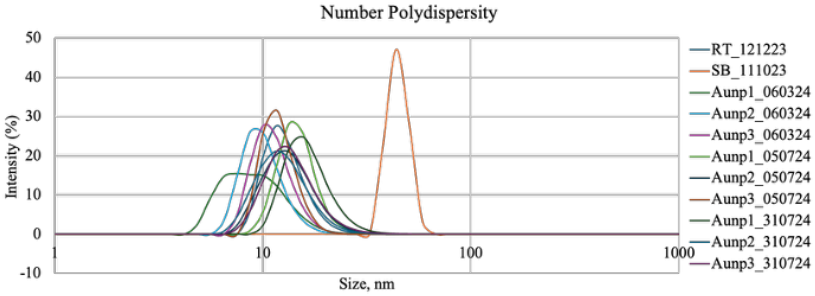


Figure 3.11. DLS characterization of AuNP solutions.

3.12. Viscosity and Mechanical Characterization of Gelatin-Alginate and Alginate - Matrigel Hydrogels

The successful extrusion-based 3D bioprinting of cell-laden constructs requires the bioink to exhibit a balance of rheological and mechanical properties. These properties govern the material's printability, the shear stress experienced by encapsulated cells, and the post-printing structural integrity and biological responsiveness of the construct. The two composite bioinks used in this study, Gelatin-Alginate and Matrigel-Alginate, are formulated to meet these criteria.

For an extrusion-based system, a bioink must exhibit shear-thinning behavior—a decrease in viscosity under the shear stress of extrusion, followed by rapid viscosity recovery post-extrusion to maintain shape fidelity.

To characterize these properties, steady-shear viscosity (η) and oscillatory rheology are measured using a rotational rheometer with a parallel-plate geometry. The resulting data confirm the desired shear-thinning profile, showing a viscosity decrease as the shear rate increases, which is beneficial for extrusion while ensuring shape maintenance at low shear rates. Furthermore, small-amplitude oscillatory shear (SAOS) testing provides the essential viscoelastic parameters: the storage modulus, G', (storage modulus, elastic-solid part of response) and the loss modulus G'' (loss modulus, viscous-liquid part of response), along with the loss tangent ($\tan(\delta) = G''/G'$). These parameters are the established academic standards for defining a material's printabil-

ity and filament stability, with their optimization directly correlating to the resulting construct fidelity and cell viability [176].

Literature suggests that gelatin-alginate hydrogels formulated within a specific viscosity range (typically corresponding to a storage modulus, G', of 100 to 10000 Pa and a loss tangent $\tan(\delta)=G''/G'$ between 0.25 and 0.45) exhibit an optimal compromise between high print resolution and low cell-damaging shear stress during extrusion [177, 178]. The 8% Gelatin+/4% Alginate formulation is designed to possess a sufficiently high initial viscosity and a yield stress to prevent collapse immediately after printing yet retain the shear-thinning capability required for smooth extrusion.

The Matrigel-alginate formulation was developed to mimic complex tissue microenvironments. Here, the stiffness of the matrix is primarily tuned by adjusting the alginate content and calcium dose, while the Matrigel component serves to enrich adhesivity and provide biochemical cues. The final formulations were specifically tuned to achieve marrow-like moduli (≈0.5–40 kPa), a range that is critical for enabling disease-relevant mechanobiology assays [179].

Matrix rheology and mechanics govern diffusion, spreading, migration, proliferation, and treatment response. In general, as viscosity and G' increase, pore space and effective mesh size decrease, limiting cell spreading and migration, slowing diffusion of nutrients/drugs, and favoring spheroid/cluster formation in some cell types; conversely, lower viscosity/softer gels promote spreading and motility but may compromise construct stability. These trends are documented across alginate/gelatin systems and cancer models, including melanoma [180–182].

Based on the above, we selected gelatin-alginate and Matrigel-alginate formulations that (i) exhibit shear-thinning for gentle extrusion, (ii) recover G' rapidly post-shear for shape retention, and (iii) fall within biologically relevant moduli for lymph-node–like and tumor-adjacent tissues.

4. UNDERSTANDING THE BEHAVIOR OF A375 MELANOMA CELLS IN 2D SYSTEM

4.1. A375 Melanoma Cells Interacting with Macrophage-Like M0 Cells - 2D Coculturing

In order to study the interactions between immune cells and cancer cells, THP-1 cells, a human monocytic cell line, are frequently co-cultured with A375 melanoma cells. The ability of THP-1 cells to develop into cells that resemble macrophages makes them important components of the tumor microenvironment. Researchers can better understand how melanoma cells affect immune cell activity by co-culturing differentiated THP-1 cells with A375 melanoma cells. Numerous cytokines and chemokines may be secreted as a result of the interaction between THP-1 cells and A375 cells. Understanding the interactions between immune and cancer cells, which can affect tumor growth and immune evasion, is made easier by researching these secretions. The effectiveness of anticancer medications in the presence of immune cells can be evaluated using co-culture systems. THP-1 cells have the ability to affect A375 cells' capacity for invasion and metastasis. Researchers can find elements that either encourage or prevent melanoma cell invasion and metastasis by examining these interactions.

Different concentrations of A375-GFP cells and M0-mCherry cells are co-cultured in a 6-well plate to determine the optimum cell viability in a coculture. The cell densities of the wells are given below, and the viability of the cells after 2 days is tabulated in Figure 4.1.

- Well #1 – M0 (2M cells)
- Well #2 – M0 (2M cells) + A375 (1M cells)
- Well #3 – M0 (2M cells) + A375 (500k cells)
- Well #5 – M0 (2M cells) + A375 (200k cells)
- Well #6 – M0 (2M cells) + A375 (100k cells)

THP-1-mCherry cells are differentiated by using the protocol mentioned in Chapter 3. Once the THP-1 cells are differentiated, they lose their ability to proliferate so that the density of the M0-mCherry cells is kept constant while A375-GFP cells are changed. Although the standard cell seeding density in a 6-well plate is 300 000 cells per well, they are seeded at 2M per well since not all seeded THP-1 cells will differentiate into M0.

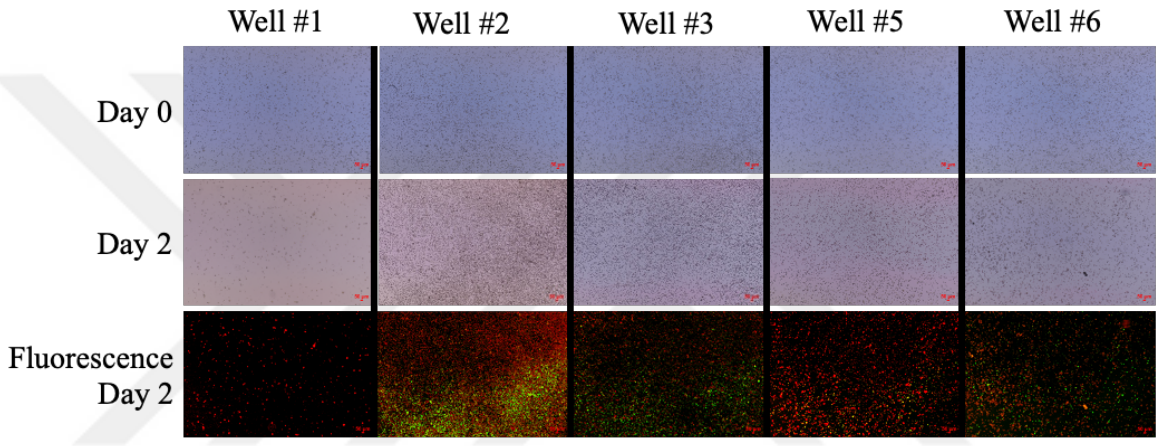


Figure 4.1. Different concentrations of co-culturing in 2D.

In monoculture conditions, M0-mCherry macrophages exhibit negligible proliferation, as evidenced in well 1, whereas A375-GFP melanoma cells demonstrate significant proliferation by the end of the second day in wells 2 and 3, rendering M0-mCherry cells indistinct. Seeding A375-GFP cells at densities of 1×10^5 or 2×10^5 per well achieves a balanced M0-mCherry/A375-GFP co-culture by day 3, as observed in wells 5 and 6. The viability of both M0-mCherry and A375-GFP cells is confirmed through their respective fluorescence signals after 2 days of co-culturing.

However, due to the limited proliferative capacity and viability of M0, M1, and M2 macrophages in vitro, the duration of co-culture experiments is not extended. Macrophages are traditionally considered terminally differentiated cells with minimal proliferative potential under standard culture conditions. While certain stimuli, such as macrophage colony-stimulating factor like M-CDF (macrophage colony-stimulating factor), can induce proliferation in specific macrophage subsets [183–185], this effect

is not universally observed across all macrophage phenotypes [186]. To avoid introducing phenotypic variability and to maintain experimental consistency, M-CSF supplementation was deliberately omitted in this study. M-CSF is known to promote monocyte-to-macrophage differentiation and can skew macrophages toward an M2-like anti-inflammatory phenotype, potentially altering their behavior and responsiveness to therapeutic agents [187, 188]. Furthermore, M-CSF has been reported to influence macrophage proliferation and polarization, which may introduce confounding variables in co-culture models or during cytotoxicity assays [185]. Therefore, excluding M-CSF ensured the preservation of the unpolarized M0 phenotype throughout the experimental timeline and allowed more physiologically relevant evaluation of treatment responses without interference from external differentiation signals.

Nevertheless, since the 3D scaffold environment better mimics in vivo conditions, it is decided to perform a limited set of co-culture experiments in a 3D platform. These trials are kept short, only up to two days, given the well-known limitations in the viability and proliferative capacity of M0 macrophages. This approach is based on the hypothesis that a supportive, biomimetic microenvironment could temporarily sustain macrophage viability. Even short-term maintenance would allow early interaction with melanoma cells and observation of initial treatment in the co-culture system.

4.2. Therapeutic Strategies and Cytotoxicity Experiments: Nanoparticles (AuNPs) and Chemotherapeutic Agents Doxorubicin (DOX) and Temsirolimus

4.2.1. AuNP and DOX Concentration Effects on A375-GFP Cells

Gold nanoparticles and DOX (doxorubicin) treatments are applied to A375-GFP cells with eight concentrations at 96-well plates. There are two concentrations of AuNP solutions (RT121223: 0.912 nM and SB111023: 1.63 nM). AuNPs called RT121223 and SB111023 have 11.7 nm and 43.8 nm diameters, respectively. Doxorubicin (DOX) is a potent anthracycline chemotherapeutic agent widely used in cancer treatment and

research. Its primary mechanism involves intercalation into DNA and inhibition of topoisomerase II, leading to DNA double-strand breaks and apoptosis. Additionally, DOX undergoes redox cycling, producing reactive oxygen species (ROS) that contribute to oxidative damage and cytotoxicity [189]. Because of its well-characterized mechanism, fluorescence properties, and broad anticancer activity, DOX is frequently used as a model drug in drug delivery studies, cytotoxicity assays, and combination therapy research. According to the manufacturer's prospectus, the stock concentration of doxorubicin (DOX) is typically 2 mg/mL (3.44 mM). In the literature, a working concentration of 40 ng/mL DOX was used for experiments on A375 melanoma cells [190]. To achieve this target concentration, the stock solution was first diluted to 172.4 µM and then subjected to eight successive 1:2 serial dilutions.

All wells are filled with 15 000 A375-GFP cells in a 150 μL complete medium, and the cells are cultured for one day in an incubator at 37 °C. The concentration of both RT121223 and SB111023 is diluted to one-tenth of its concentration, and it takes two repeats. Also, it is diluted to half of its concentration and takes two repeats. DOX concentration is diluted by half in both plates. Finally, AuNP and DOX are mixed and diluted to half. These solutions are mixed with the cells and then left for 72 hours in the incubator to investigate the fluorescence of the cells, which indicates the viability of the cells after treatment. The concentrations of the treatments are given in Table 4.1.

The fluorescence of the cells in the control group varies between 2-7 and is shown in Figure 4.2. as an orange dot. The fluorescence intensity of A375-GFP cells mixed with AuNP varies from 1-6, and this variation is not proportional to concentration. It means AuNP lower than 8 nM doesn't have a positive or negative effect on A375-GFP cells, and thus not cytotoxic. On the contrary, the fluorescence of the cells exposed to DOX varies between 5 and 35, showing a positive correlation with both DOX concentration and cell viability. However, these results are misleading, as the highest fluorescence intensity corresponds to the highest DOX concentration, suggesting increased viability. This misinterpretation arises from the strong autofluorescence of DOX [191], which interferes with accurate viability assessments. DOX experiments are abandoned due to

Table 4.1. Concentration of AuNP and DOX treatment on A375-GFP cells.

SB111023					**RT121223**				
			AuNP+DOX 1:2 dilution (AuNP, nM)					**AuNP+DOX 1:2 dilution (AuNP, nM)**	
AuNP 1:10 dilution (nM)	**AuNP 1:2 dilution (nM)**	**DOX 1:2 dilution (mM)**	**AuNP 1:2 dltn (nM)**	**DOX 1:2 dltn (nM)**	**AuNP 1:10 dltn (nM)**	**AuNP 1:2 dltn (nM)**	**DOX 1:2 diltn (mM)**	**AuNP 1:2 dltn (nM)**	**DOX 1:2 dltn (nM)**
1.63E-01	8.150	86.200	4.075	43.10	9.12E-02	0.456	86.200	0.228	43.10
1.63E-02	4.075	43.100	2.038	21.55	9.12E-03	0.228	43.100	0.114	21.55
1.63E-03	2.038	21.550	1.019	10.78	9.12E-04	0.114	21.550	0.057	10.77
1.63E-04	1.019	10.775	0.509	5.388	9.12E-05	0.057	10.775	0.029	5.388
1.63E-05	0.509	5.388	0.255	2.694	9.12E-06	0.029	5.388	0.014	2.694
1.63E-06	0.255	2.694	0.127	1.347	9.12E-07	0.014	2.694	0.007	1.347
1.63E-07	0.127	1.347	0.064	0.673	9.12E-08	0.007	1.347	0.004	0.673
1.63E-08	0.064	0.673	0.032	0.337	9.12E-09	0.004	0.673	0.002	0.337

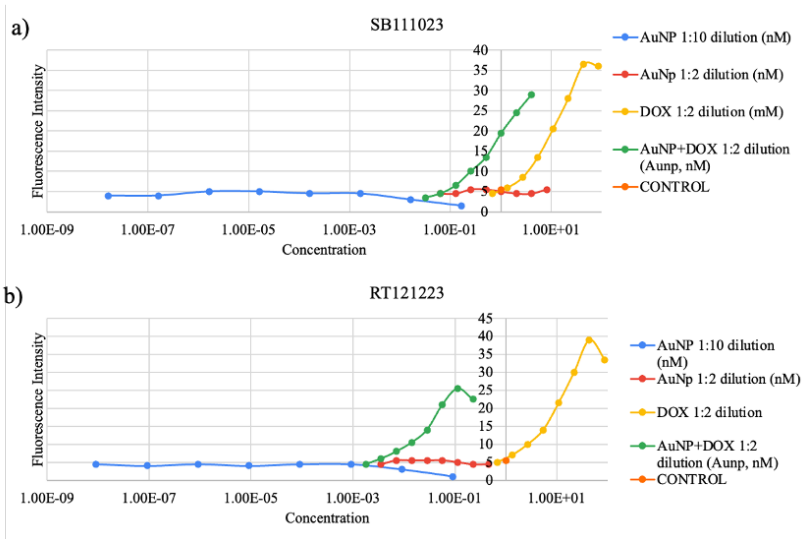


Figure 4.2. Fluorescence change in A375-GFP cells.

DOX's autofluorescence property.

4.2.2. AuNP and temsirolimus concentration effects on A375-GFP cells

Another batch of AuNP is prepared (called 060324), including AuNP1, AuNP2, and AuNP3, and has diameters of 8.5 nm, 9 nm, and 10.5 nm, respectively. A375-GFP cells are next treated with another chemotherapeutic agent temsirolimus as a positive control. 500 nM [192], temsirolimus is given to the cells initially and diluted 1:2 ratio. Additionally, these drugs are administered to AuNP-treated cells at a ratio of 1:2 with 2 repeats, and viability is measured by looking at the fluorescence intensity of the cells using a plate reader. Temsirolimus is given to the cells simply by mixing with the AuNPs instead of conjugating with them. Also, a duplicate of the control group is prepared with no treatment. A375-GFP cells are treated with AuNPs with 1/2 and 1/5 dilutions. 10,000 cells/well are placed in a 96-well plate. AuNP dilutions are given below Table 4.2.

Table 4.2. Dilution concentration of AuNPs and Temsirolimus (nM).

AuNP1 (8.5 nm) (1:2)	**AuNP1 (8.5 nm) (1:5)**	**AuNP2 (9 nm) (1:2)**	**AuNP2 (9 nm) (1:5)**	**AuNP3 (10.5 nm) (1:2)**	**AuNP3 (10.5 nm) (1:5)**	**Temsirolimus (1:2)**
1.9306	0.7722	1.0750	0.4300	0.3134	0.1253	500
0.9653	0.1544	0.5375	0.0860	0.1567	0.0251	250
0.4826	0.0309	0.2688	0.0172	0.0783	0.0050	125
0.2413	0.0062	0.1344	0.0034	0.0392	0.0010	62.5
0.1207	0.0012	0.0672	0.0007	0.0196	2.01E-04	31.25
0.0603	2.47E-04	0.0336	1.38E-04	0.0098	4.01E-05	15.63
0.0302	4.94E-05	0.0168	2.75E-05	0.0049	8.02E-06	7.81
0.0151	9.88E-06	0.0084	5.50E-06	0.0024	1.60E-06	3.91

According to these dilutions, the viability of the cells is measured by investigating the fluorescence intensity of the cells in the wells using a microplate reader (Biotek

Synergy HTX). It can be said that a high concentration of AuNP decreases the growth of A375-GFP cells. The results were given in both Tables 4.3-4.5 and Figures 4.3 and 4.4.

Table 4.3. Average fluorescence of cells against ½ dilution of AuNP treatment.

AuNP-1 8.5 nm (nM)	**Fl. Int.**	**AuNP-2 9 nm (nM)**	**Fl. Int.**	**AuNP-3 10.5 nm (nM)**	**Fl. Int.**
1.9306	2				
0.9653	3	1.0750	3.5		
0.4826	4	0.5375	4.5		
0.2413	4	0.2688	4.5	0.3134	2.5
0.1207	5	0.1344	4	0.1567	3.5
0.0603	4.5	0.0672	4.5	0.0783	5
0.0302	5	0.0336	4.5	0.0392	5
0.0151	4.5	0.0168	4.5	0.0196	5
		0.0084	4	0.0098	5
				0.0049	5
				0.0024	4.5
Control group (non-treated A375-GFP cells)					5.25

The fluorescence intensity of non-treated cells ranges from 4 to 7, with an average of 5.25. In the figures, the fluctuation of the fluorescence intensity of the control cells is shown along the concentration axis, even if these cells are not treated. Both the temsirolimus and AuNP treatment responses are below this range in general. The trend of the fluorescence intensity is increasing as the concentration of the treatment agent decreases.

The experimental data demonstrate that increasing concentrations of AuNP-1 result in a progressive decline in the fluorescence intensity of A375-GFP melanoma cells, indicating a concentration-dependent reduction in cell viability. This effect is

Table 4.4. Average fluorescence cells against 1/5 dilution - AuNP treatment.

AuNP-1 (nM)	**Fl. Int.**	**AuNP-2 (nM)**	**Fl. Int.**	**AuNP-3 (nM)**	**Fl. Int.**
0.77222	3	0.43	1.5	0.12534	4.5
0.154444	3.5	0.086	2	0.025068	5
0.0308888	5	0.0172	3	0.0050136	5.5
0.00617776	4	0.00344	4	0.00100272	5.5
0.00123555	5	0.000688	4	0.00020054	6
0.00024711	4	0.0001376	4	4.0109E-05	6
4.9422E-05	3.5	0.00002752	5	8.0218E-06	5.5
9.8844E-06	4.5	5.504E-06	5	1.6044E-06	5
Control group (non-treated A375-GFP cells)					5.25

Table 4.5. Average fluorescence of cells against ½ dilution of Temsirolimus and combined treatment.

Tems (nM)	**Fl. Int.**	**Tems (nM)**	**AuNP-1 (nM)**	**Fl. Int.**	**Tems (nM)**	**AuNP-2 (nM)**	**Fl. Int.**	**Tems (nM)**	**AuNP-3 (nM)**	**Fl. Int.**
500	3.5	500	1.9306	1.5						
250	4.5	250	0.9653	2	500	1.075	2			
125	4.5	125	0.4826	3	250	0.5375	3			
62.5	4	62.5	0.2413	4	125	0.2688	4	500	0.3134	3
31.25	4.5	31.25	0.1207	4	62.5	0.1344	4	250	0.1567	4
15.63	4.5	15.63	0.0603	4	31.25	0.0672	5	125	0.0783	4
7.81	4.5	7.81	0.0302	5	15.63	0.0336	4.5	62.5	0.0392	4.5
3.91	4	3.91	0.0151	5	7.81	0.0168	5	31.25	0.0196	5
					3.91	0.0084	4.5	15.63	0.0098	5
								7.81	0.0049	5
								3.91	0.0024	4.5
Control group (non-treated A375-GFP cells)										5.25

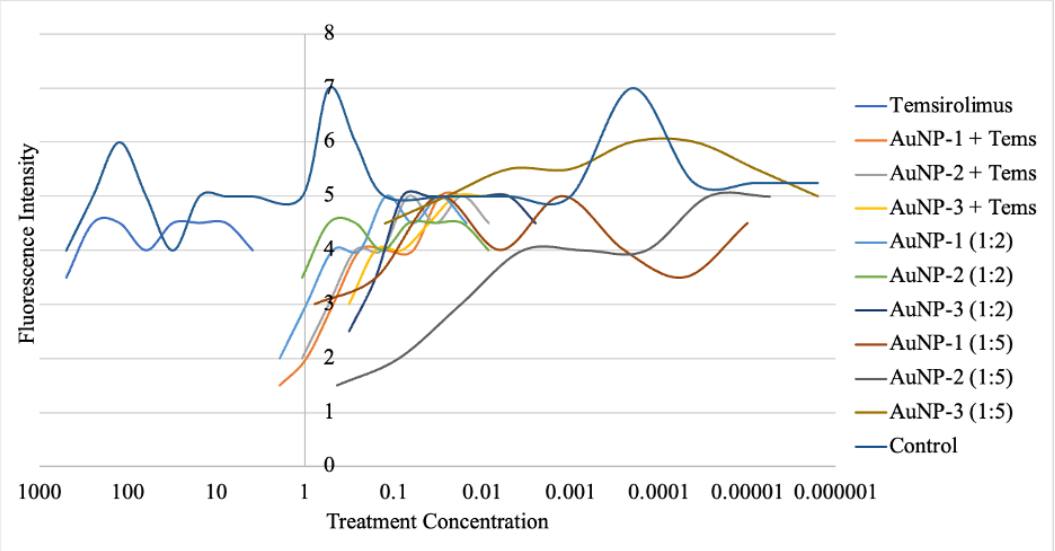


Figure 4.3. Average fluorescence intensity of all treatments.

more pronounced when AuNP-1 is combined with temsirolimus, particularly at higher concentrations (1.93 nM AuNP-1 and 500 nM temsirolimus), as shown in Figure 4.3a. Cells treated solely with temsirolimus exhibit higher viability compared to those treated with AuNP-1, implying that AuNP-1 possesses inherent cytotoxic properties, especially at concentrations exceeding 0.24 nM. This toxicity is likely an artifact of the measurement, as metal nanoparticles can quench nearby fluorophores through energy transfer or plasmonic effects, thus lowering the signal without actually inducing cell [193]. On the other hand, A375-WT cells tolerated AuNPs up to 2 nM without evident toxicity.

The enhanced cytotoxicity observed with the combination of AuNP-1 and temsirolimus may be attributed to several synergistic mechanisms. Positively charged AuNPs can disrupt cellular membranes, increasing permeability and facilitating greater intracellular accumulation of temsirolimus [194, 195]. Additionally, AuNPs are known to induce oxidative stress by generating reactive oxygen species (ROS), leading to mitochondrial dysfunction and apoptosis [196–198]. Temsirolimus, an mTOR inhibitor, can also promote oxidative stress and autophagy. The concurrent induction of oxidative stress by both agents may amplify apoptotic pathways in melanoma [199, 200]. Furthermore, AuNPs may interfere with lysosomal function, potentially enhancing the cytotoxic effects of temsirolimus by disrupting cellular homeostasis and promoting cell

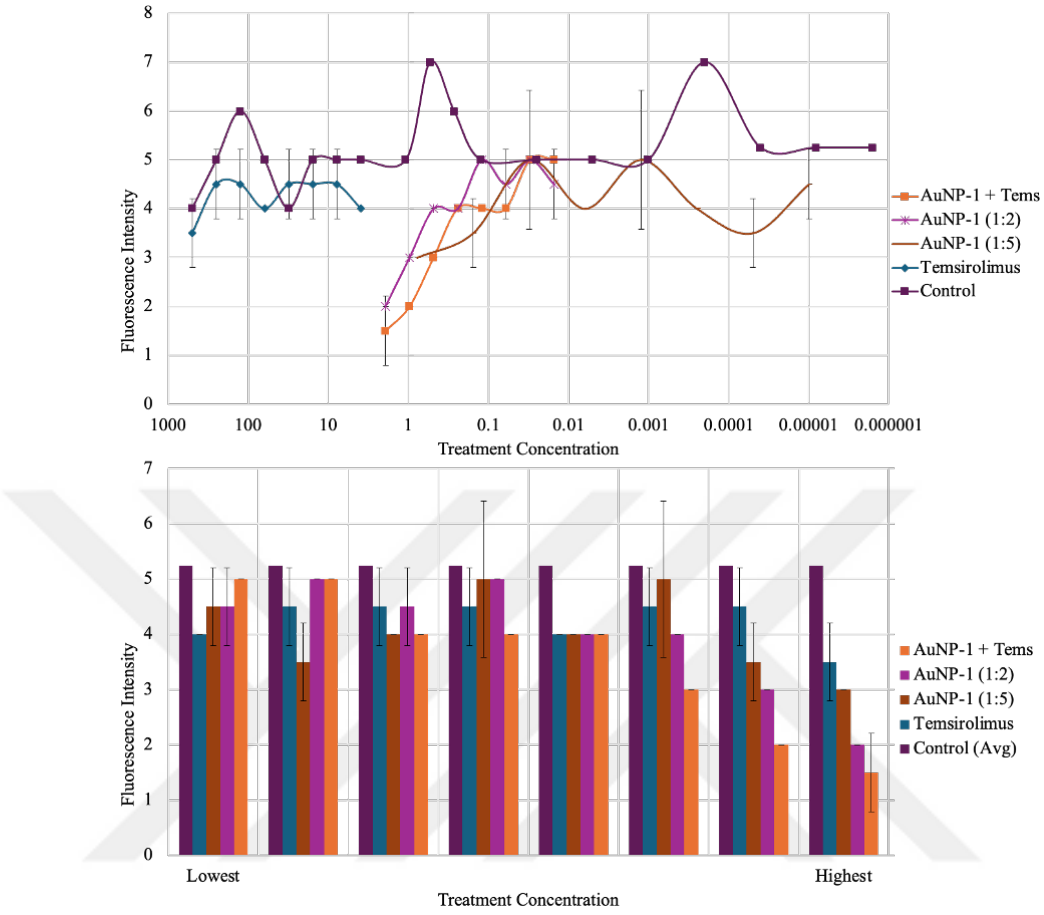


Figure 4.4. Fluorescence intensity of A375-GFP cells treated with AuNP-1 and temsirolimus.

death [195, 198].

These findings align with previous studies demonstrating that nanoparticles like AuNPs can enhance the efficacy of chemotherapeutic agents by modulating cellular pathways and increasing drug retention within the tumor microenvironment. The combination of AuNPs with mTOR inhibitors like temsirolimus represents a promising strategy for enhancing anticancer effects through multiple mechanisms, including drug uptake, oxidative stress induction, and interference with survival pathways.

In Figure 4.5, the cytotoxic effects of three differently sized gold-nanoparticle (AuNP-1, AuNP-2, and AuNP-3) on A375-GFP melanoma cells were assessed. The ini-

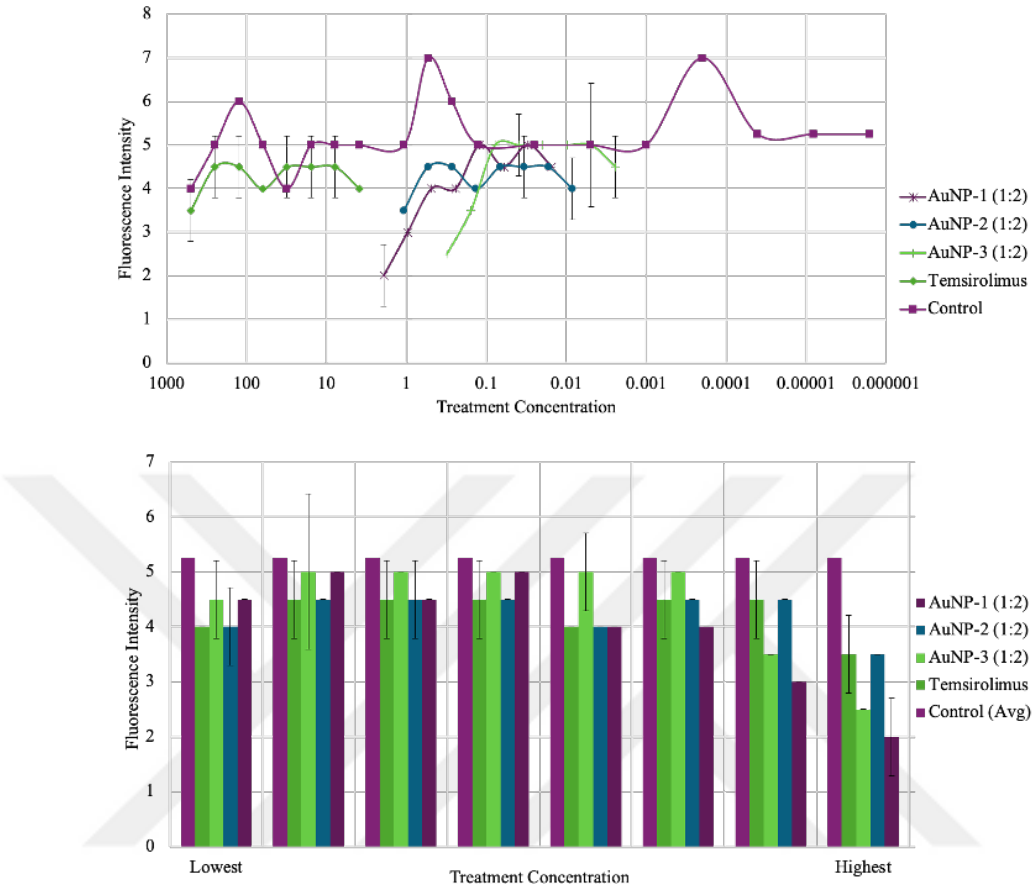


Figure 4.5. Fluorescence intensity of A375-GFP cells treated with different concentrations of different AuNPs.

tial concentrations for AuNP-1, AuNP-2, and AuNP-3 are 1.93 nM, 1.07 nM, and 0.31 nM, respectively. At concentrations above 0.25 nM, both AuNP-1 and AuNP-2 exhibit a consistent trend of decreasing fluorescence intensity with increasing concentration, indicating reduced cell viability (Figure 4.5and Table 4.5). However, at concentrations below 0.25 nM, the fluorescence intensity fluctuates, making it challenging to discern a clear size-dependent effect. Notably, the cellular response at these lower concentrations resembled the effects observed with temsirolimus treatment below 50 nM. Overall, an inverse relationship between treatment concentration and cell viability is observed as depicted in Figure 4.5.

These observations are in line with previous studies suggesting that smaller gold nanoparticals exhibit greater cytotoxicity due to their higher surface area-to-volume

ratio and more efficient cellular uptake. Increased ROS production and enhanced activation of apoptotic pathways have been commonly reported in response to smaller-sized AuNPs. For instance, enhanced cytotoxic effects have been observed in melanoma and liver cancer cells exposed to AuNPs with diameters below 15 nm, primarily due to increased oxidative stress and cell death mechanisms [201–203].

In conclusion, both the size and concentration of AuNPs affect their cytotoxicity in A375-GFP cells. Smaller particles show more substantial toxic effects, especially at higher doses. These findings highlight the need to carefully adjust nanoparticle size and dose when developing AuNP-based therapies for melanoma.

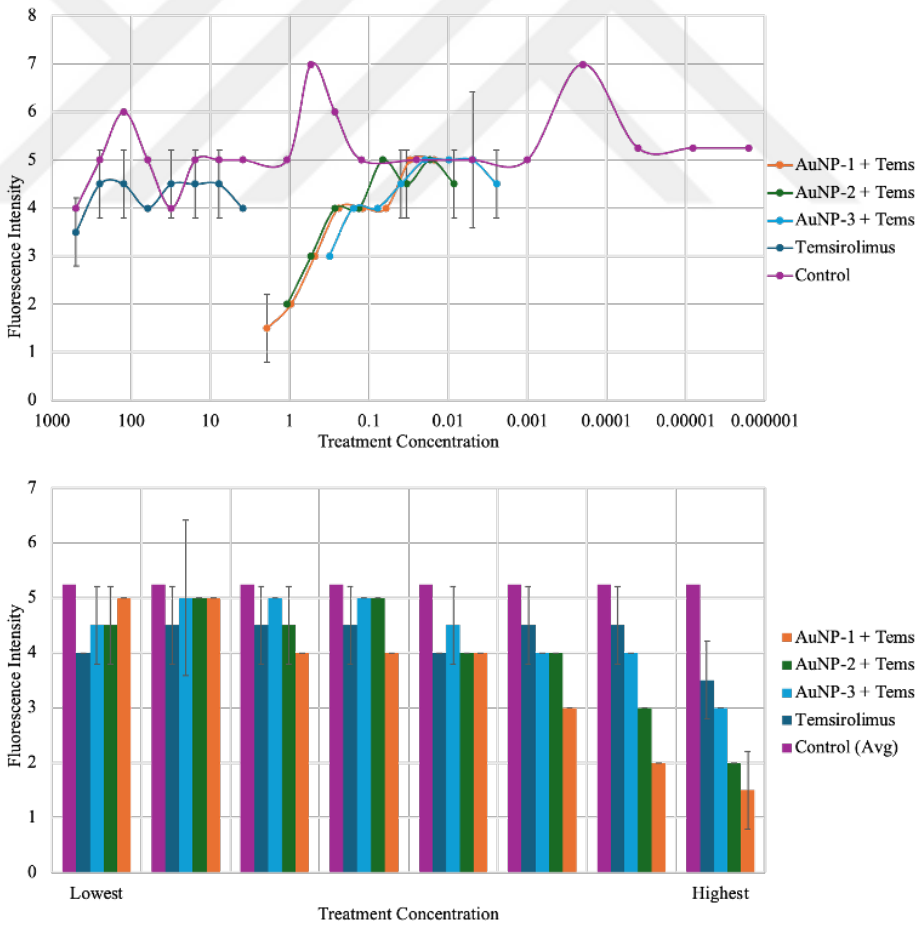


Figure 4.6. Fluorescence intensity of A375 cells treated with different concentrations of different AuNPs and temsirolimus.

Three types of AuNPs with different diameters are combined with temsirolimus at a 1:2 dilution ratio and administered to A375-GFP cells. As shown in Figure 4.6 all three AuNP-temsirolimus combinations exhibit comparable levels of cytotoxicity across equivalent concentrations, and these are notably more toxic than temsirolimus alone. This suggests that AuNPs potentiate the cytotoxic effects of temsirolimus.

Furthermore, Figure 4.5 indicates that increased concentrations of both agents result in a gradual reduction in cell viability, supporting the possibility of a dose-dependent synergistic effect. Interestingly, the size of the AuNPs does not significantly alter the combined cytotoxic effect, implying that when co-administered with temsirolimus, nanoparticle diameter plays a less prominent role in determining overall toxicity.

These findings are consistent with previous studies suggesting that AuNPs can enhance the efficacy of chemo-therapeutic agents by increasing cellular uptake, altering endosomal escape, and disrupting key survival pathways such as mTOR signaling. The lack of a strong size-dependent effect in the combined treatments may be due to the dominating influence of temsirolimus on mTOR inhibition, which could overshadow the subtler effects of nanoparticle size on cellular interaction and internalization [204].

4.2.3. Metabolic Activity Assessment on A375-WT Cells by Using Alamar Blue on 2D

Another batch of AuNP is prepared (called 050724), including AuNP-1, AuNP-2, and AuNP-3, and has diameters of 13.5 nm, 13.5 nm, and 11.7 nm, respectively. AuNP-1 and AuNP-2 have the same diameter, while they have different concentrations of 4.062 nM and 2.152 nM, while AuNP-3 is 0.651 nM. A375-WT (w/o GFP tag) cells are treated with AuNP-1, AuNP-2, AuNP-3, temsirolimus and DOX with 1/2 dilutions on a 96-well plate (Table 4.6). When the AuNPs are given to the cells, they are mixed with the complete medium to provide nutrients to the cells. Thus, AuNP concentrations are halved when AuNPs are given to the cells. The concentrations of

the treatments are given in the following table.

A375-WT cells are seeded in a 96-well plate at a density of 10,000 cells per well and incubated for 24 hours. Following incubation, treatments are applied to the cells. After 1 day of treatment, cell viability is assessed by using Alamar blue. For this, 20 μL of Alamar blue is added to each well and incubated for 4 hours. The absorbance and fluorescence values are measured by using a plate reader, and the reduction of Alamar blue, as well as cell viability, are calculated according to the methodology in the Section 3.5.1.

Table 4.6. Concentrations of treatments AuNP1–2–3, Temsirolimus and DOX.

AuNP1, nM (13.5 nm)	**AuNP2, nM (13.5 nm)**	**AuNP3, nM (11.7 nm)**	**Temsirolimus, nM**	**DOX, ng/mL**
2.031			500	100
1.015	1.076		250	50
0.507	0.538	0.325	125	25
0.258	0.269	0.250	62.5	12.5
0.126	0.135	0.162	31.25	6.2
0.0634	0.067		15.63	3.125
0.0317	0.034		7.81	1.5625
0.0158	0.017		3.91	0.78125
	0.008			

Since the concentration of AuNP-3 is already low, it is only diluted twice. To facilitate the comparison of results, AuNP concentrations similar to each other are presented in the same row. The reduction of Alamar Blue (AB), cell viability based on absorbance values of AB, and viability based on fluorescence intensity of the cells are summarized in Table 4.7 and 4.8.

Percent (%) viability based on fluorescence data is calculated by referencing the metabolic activity of test cells against control cells, so it is considered an indicator

Table 4.7. Viability of cells against AuNP.

AuNP conc.	**% Reduction of Alamar Blue**			**% Viability (absorbance of AB)**			**% Viability (fluorescence of cells)**		
	AuNP-1 (13.5 nm)	AuNP-2 (13.5 nm)	AuNP-3 (11.7 nm)	AuNP-1 (13.5 nm)	AuNP-2 (13.5 nm)	AuNP-3 (11.7 nm)	AuNP-1 (13.5 nm)	AuNP-2 (13.5 nm)	AuNP-3 (11.7 nm)
2.031	50.24			89.54			134.12		
1.015	53.90	45.10		96.06	80.38		77.22	200.93	
0.507	52.02	49.82	38.81	92.71	88.78	69.17	57.79	83.46	243.06
0.258	54.36	50.49	50.00	96.89	89.98	89.11	56.80	59.87	136.30
0.126	55.65	54.76	46.96	99.18	97.60	83.70	43.32	63.84	75.04
0.0634	52.80	54.74		94.09	97.55		51.55	56.01	
0.0317	50.80	53.47		90.54	95.30		70.97	51.74	
0.0158		51.20		91.25			71.17		

Table 4.8. Viability of cells against Temsirolimus and DOX.

Concentration		**% Reduction of Alamar Blue**		**% Viability (absorbance of AB)**		**% Viability (fluorescence of cells)**	
Tems (nM)	**DOX (ng/mL)**	**Tems**	**DOX**	**Tems**	**DOX**	**Tems**	**DOX**
500.0	100.0	56.97	59.86	81.05	101.53	49.27	54.62
250.0	50.0	50.64	55.41	93.77	90.26	65.13	38.76
125.0	25.0	51.73	51.31	87.83	92.20	54.72	38.66
62.5	12.5	54.04	49.27	98.76	96.32	46.29	33.70
31.3	6.3	52.19	49.83	96.22	93.01	41.04	33.31
15.6	3.1	51.36	49.66	96.15	91.54	43.12	32.61
7.8	1.6	52.16	50.22	94.04	98.84	61.16	34.10

of cell viability. On the other hand, percent (%) reduction is determined using the measurements from negative control wells (containing only medium and Alamar blue) as a reference. It indicates the percentage of Alamar Blue dye that has been reduced

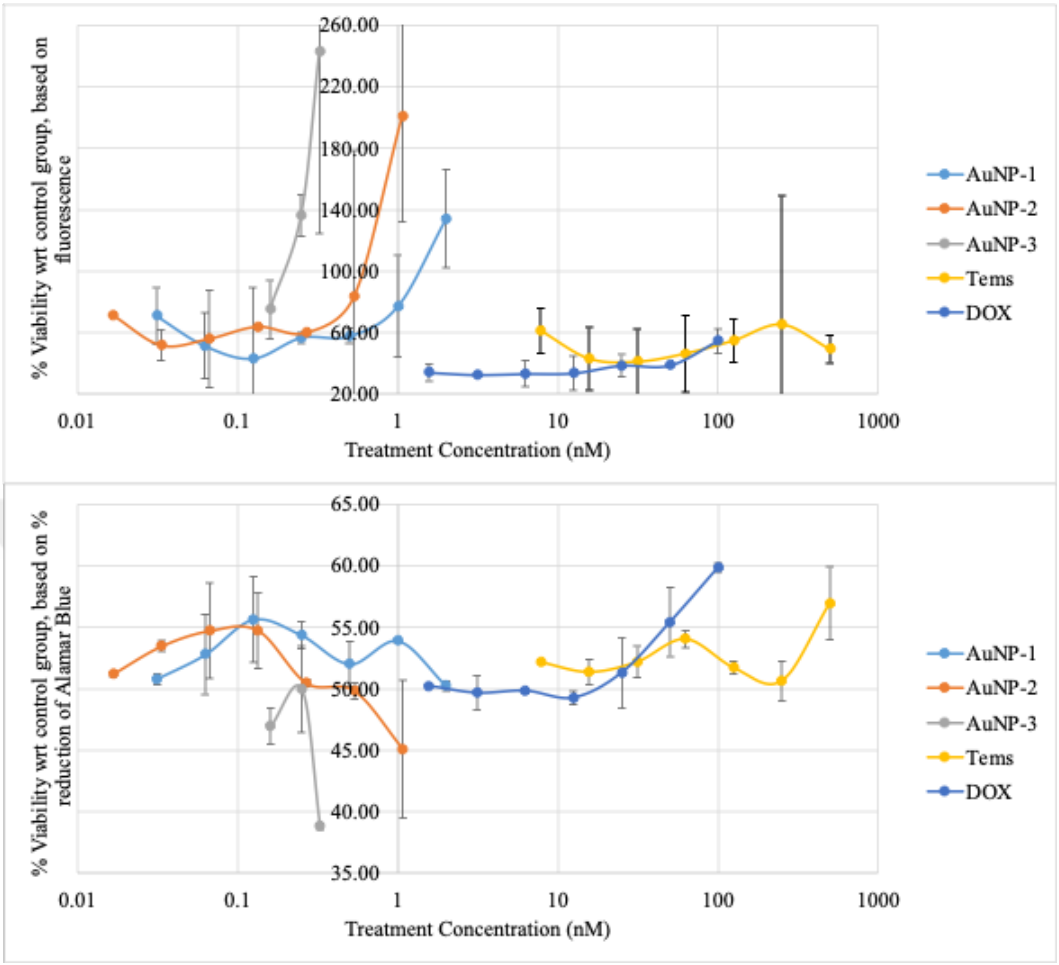


Figure 4.7. Viability measurement with Alamar Blue on day 1: (a) viability according to the cell fluorescence intensity, (b) % reduction of Alamar Blue.

by the cells in each well. It reflects the extent to which the initially blue dye has been converted to pink. Since reduction calculations do not involve normalization to a control group, reduction values cannot be directly equated with viability; they only provide indirect insight into cell viability. Also, the reduced amount of alamar blue is unknown; the results may misdirect the interpretation.

Figure 4.7a represents the fluorescence-based viability measurements. AuNP-1 and AuNP-2 (both 13.5 nm) follow a similar trend, viability decreases at concentrations below 500 nM, but unexpectedly increases at higher concentrations. Also, the viability of cells administered with AuNP-3 (11.7 nm) increases when the concentration is higher than 200 nM. This may be attributed to the stimulatory or hormetic effect

of AuNPs [205]. The increase in reduction at higher treatment concentrations should be double-checked with the % viability results (covered in Section 3.5). Cells treated with temsirolimus exhibit less than 60% viability, with the lowest viability observed at the highest drug concentration-consistent with its cytostatic mechanism as an mTOR inhibitor. In contrast, DOX treatment reduces viability below 60%. However, higher concentrations unexpectedly result in increased fluorescence. This anomaly aligns with the autofluorescence feature of the DOX mentioned in the previous sections [191].

Figure 4.7b illustrates the cellular metabolic activity through the reduction of resazurin to resofurin, which is used to evaluate the redox state of treated melanoma cells. AuNP-3 causes the most substantial reduction in dye conversion at higher concentrations, indicating metabolic inhibition. AuNP-2 shows a similar but less pronounced trend, while AuNP-1 maintains moderate activity. Cells treated with temsirolimus and DOX exhibit less than 60% metabolic activity; however, the highest temsirolimus concentration provides the highest viability, which is inconsistent with the literature.

As the graphs show, the measurements based on absorbance values and viability calculations based on Alamar blue reduction give unreliable results. Similarly, an excessive increase in fluorescence in AuNP-administered cells should be double-checked with other viability measurement methods. The summary of size and initial concentration of AuNP used in melanoma cells are given in Table 4.9.

To sum up, in this section, various batches of AuNPs are administered to both A375-WT and A375-GFP cells, and depending on the cell line, viability is investigated with two different methods: fluorescence intensity and alamar blue reduction. Based on the viability results analyzed by fluorescence intensity, a higher concentration of AuNP administration on cells leads to viability loss, independent of the AuNP size. Alamar blue assay indicates the reverse result, where a higher concentration of AuNP leads to higher viability. These results are conflicting, and it would be better if they are repeated and validated.

Table 4.9. Effect of the diameter of AuNPs on viability.

AuNPs	**Size (nm)**	**Concentration (nM)**	**Cell Type**
RT121223	11.7	0.912	A375–GFP
SB111023	43.8	1.650	A375–GFP
AuNP 1–060324	8.5	3.861	A375–GFP
AuNP 2–060324	9.0	2.149	A375–GFP
AuNP 3–060324	10.5	0.626	A375–GFP
AuNP 1–050724	13.5	4.062	A375–WT
AuNP 2–050724	13.5	2.152	A375–WT
AuNP 3–050724	11.7	0.651	A375–WT
AuNP 1_310724	15.7	1.073	A375–WT
AuNP 2_310724	11.7	1.544	A375–GFP
AuNP 3_310724	13.5	1.297	A375–GFP
AuNP used in Section 4.5	10.0	2.000	A375–WT

4.3. Effects of IL-4 on A375-WT Melanoma Cells by Using AO/PI - Visually Observed on 2D

It is reported that IL-4 inhibits melanoma cell growth and viability [206, 207]. To assess how IL-4 affects melanoma cell viability, different concentrations of IL-4 (20ng/mL, 40ng/mL, and 60 ng/mL) are applied to A375-WT cells (w/o GFP tag) as another treatment strategy. On a 6-well plate, 100 000 cells per well are seeded and incubated overnight. Then, different concentrations of IL-4 are given to the cells in the DMEM complete medium. After 24 hours, a viability test is done on the A375-WT cells by using acridine orange (AO) and propidium iodide (PI) stains. Acridine orange enters all cells, and cells emit green fluorescence light when they are exposed to AO. On the other hand, propidium iodide enters only the dead cells, and the dead cells that face PI emit red fluorescence light. Both bright field and fluorescence field images are taken and processed using the ImageJ program to count the dead and live cells. 6 μL propidium iodide and 6 μL acridine orange are mixed with 6 mL PBS to do the

viability test (1 mL/well).

In the 6-well plate, the first three wells are control groups, which means they are not treated with IL-4; the 4th, 5th, and 6th wells were treated with 20, 40, and 60 ng/mL IL-4, respectively (Figure 4.8).

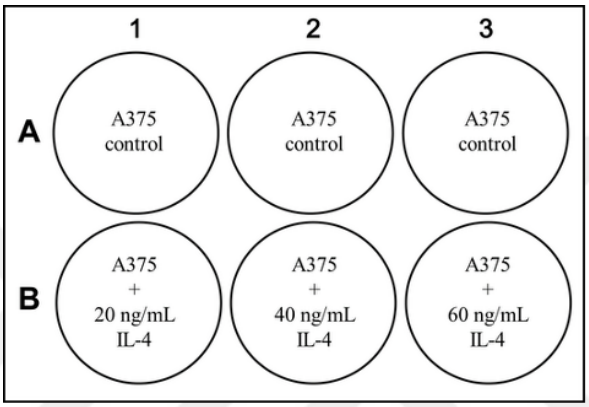


Figure 4.8. Experiment visualization.

The viability results are given with the fluorescence images in Figure 4.9. All the cells fluoresced green, while only the dead cells fluoresced red. Non-treated cells have roughly 60% viability on average, while the cells treated with 20 ng/mL, 40 ng/mL, and 60 ng/mL IL-4 have 57.1%, 62.6%, and 51.1%, respectively. 60 ng/mL IL-4 has a more toxic effect on A375-WT cells (Figure 4.9). These results are consistent with the literature [207, 208].

4.4. Secretion of IL-4 on A375-WT and M0-WT on 2D by ELISA

Melanoma cells may secrete interleukin-4 (IL-4) as a protective response to drug-induced stress. This secretion can be triggered by cytotoxic stimuli, including chemotherapeutics and nanoparticles, and serves as a compensatory mechanism to support cell survival. IL-4 has been shown to enhance tumor cell proliferation and survival by activating key pathways like STAT6 and PI3K/Akt, which contribute to resistance against apoptosis and cytotoxicity [209]. Temsirolimus, an mTOR inhibitor, may elicit such

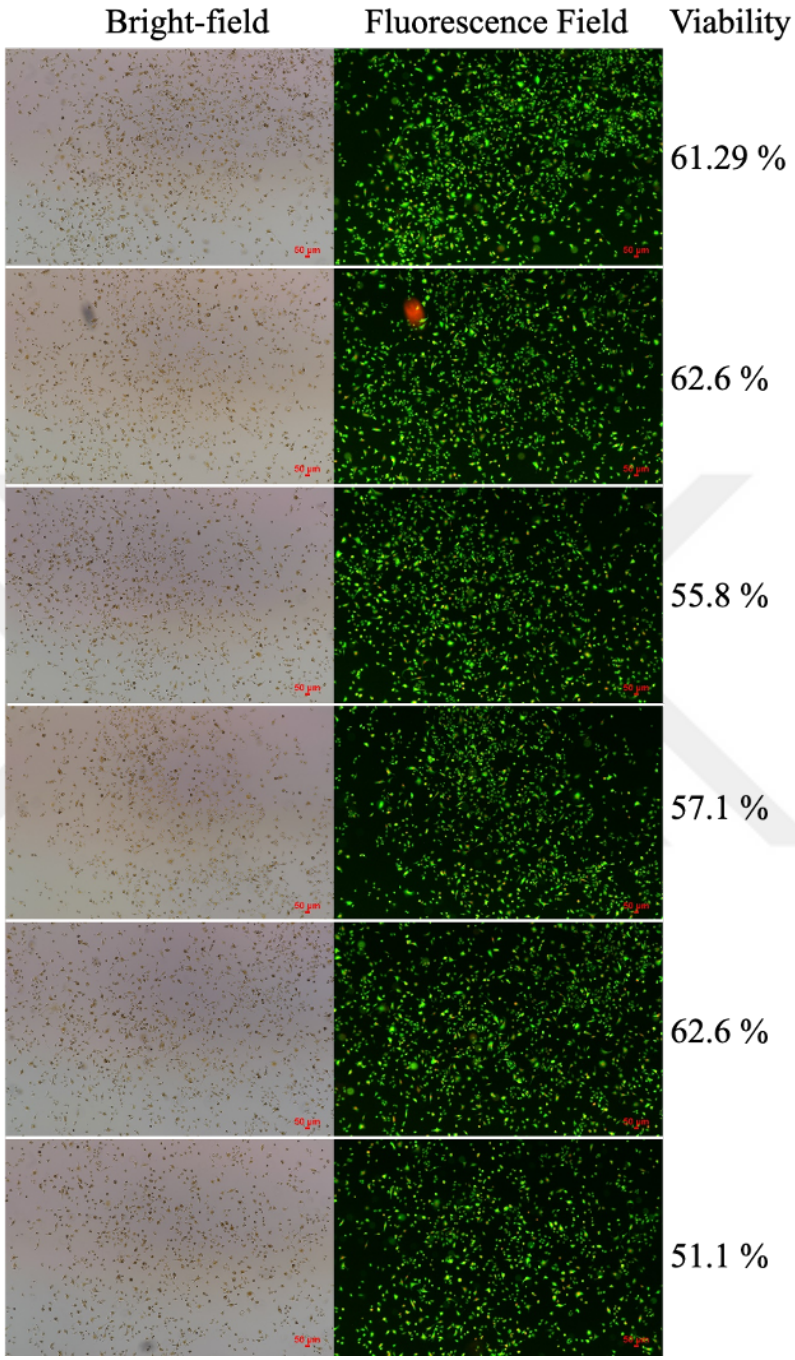


Figure 4.9. IL-4 effects on A375-WT cells.

responses by interfering with metabolic signaling, whereas AuNPs are known to stimulate cytokine release through oxidative stress and membrane interaction [210, 211]. Additionally, nanoparticle-cell interactions can lead to immune-like signaling in tumor cells, resulting in the upregulation or downregulation of inflammatory cytokines such

as IL-4, IL-6 and TNF-α [212].

These mechanisms highlight the possibility that both temsirolimus and AuNP treatments could induce IL-4 secretion in A375-WT cells (w/o GFP tag). In macrophages, such as M0-WT, cytokine expression profiles are inherently sensitive to environmental changes, and exposure to therapeutic agents may alter their polarization status and cytokine output. A375 cells may secrete IL-4 in response to drug-induced stress as a way to counteract cytotoxic effects by several mechanisms related to cellular stress, immune modulation, or survival responses. The secretion of IL-4 from A375-WT and M0-WT is analyzed when they are treated with AuNP, temsirolimus, and IL-4, and their combinations, which are given in Table 4.10. M0-WT and A375-WT cells are seeded in 6-well plates and incubated overnight. AuNPs, temsirolimus, and IL-4 are given to the cells and incubated for 24 hours. The set of treatments is given in Table 4.10.

After the treatments, supernatants of the cells in the wells are collected and centrifuged at 1000g for 5 minutes to eliminate the dead cells in the supernatant. Each supernatant is divided into three and kept at -80°C for further analysis. Cells are also removed from the plate and kept in PBS and put at -80°C for possible western blot analysis.

Table 4.10. Sets of experiments for IL-4 secretion.

Set-1	**Set-2**	**Set-3**
M0	M0	A375
M0+Temsirolimus	M0+IL-4	A375+Temsirolimus
M0+AuNP1	M0+IL-4+Temsirolimus	A375+AuNP1
M0+AuNP2	M0+IL-4+AuNP1	A375+AuNP2
M0+AuNP3	M0+IL-4+AuNP2	A375+AuNP3
	M0+IL-4+AuNP3	

An ELISA test (Invitrogen, IL-4 Human ELISA kit) is conducted to determine the amount of IL-4 in the samples. This test uses the Sandwich ELISA format. The protocol, as the kit suggested, is followed. The procedure is given in the methods section. The standard curve for the concentration of IL-4 from the absorbance levels is created by the analysis, and it is given in the following figure. The results are given in Figure 4.10.

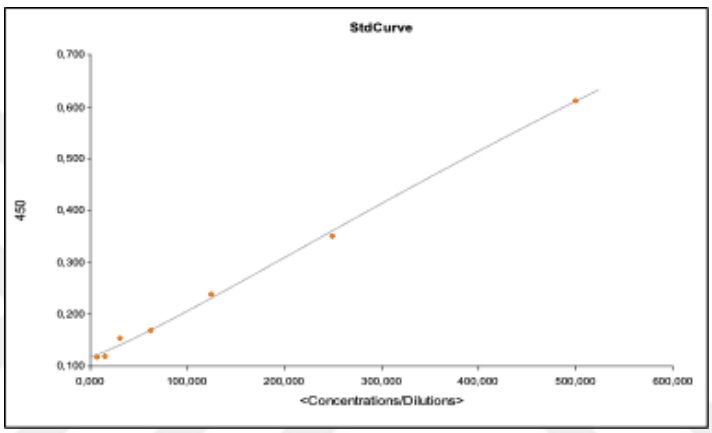


Figure 4.10. Standard curve of IL-4.

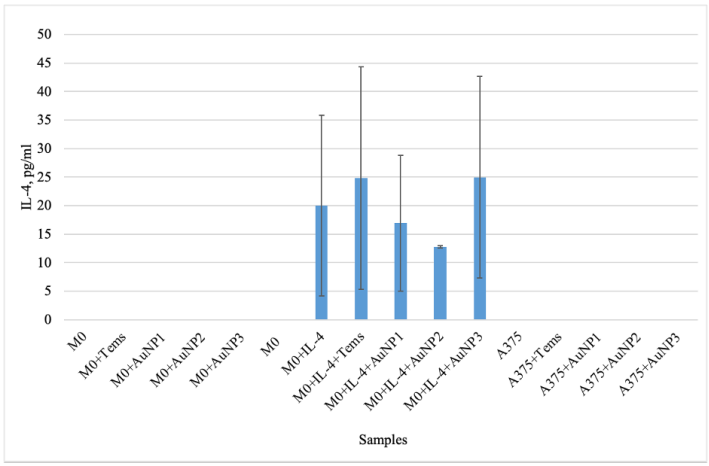


Figure 4.11. IL-4 concentration of the samples.

As shown in Figure 4.11, IL-4 secretion is not detectable in either A375-WT (w/o GFP tag) melanoma cells or M0-WT macrophages following the treatment with

temsirolimus or AuNPs. This indicates that neither treatment alone induces a cytokine-mediated immunoregulatory response in these mono-cultures. In contrast, only M0-WT macrophages stimulated with exogenous IL-4 show measurable IL-4 levels in the supernatant, which confirms the assay's reliability.

Interestingly, M0-WT macrophages treated with IL-4 and AuNP-2 exhibited the lowest extracellular IL-4 levels, suggesting possible enhanced uptake or intracellular retention of IL-4. Previous studies have demonstrated that nanoparticle properties such as size and surface chemistry influence absorption and trafficking in immune cells, particularly macrophages [213]. This could indicate that AuNP-2 facilitates increased internalization of IL-4 or alters its receptor recycling dynamics.

While mTOR pathway inhibition by temsirolimus is known to modulate immune responses and cytokine expression, particularly through PI3K/Akt/mTOR pathway, IL-4 secretion is not induced in this setting. Feedback activation of immune signaling following mTOR inhibition has been observed under certain conditions [214], but it likely requires a complex immune microenvironment or co-culture with other cell types. This could explain the lack of IL-4 secretion in A375-WT cells.

Moreover, A375-WT cells do not secrete IL-4 even under stress conditions induced by temsirolimus or AuNPs. This suggests that these treatments do not promote a shift toward an immune-modulatory or cytokine-secreting phenotype. This finding is consistent with previous studies indicating that IL-4 production in tumors is mainly associated with immune cell infiltration, particularly by Th2 cells or activated macrophages, rather than being produced by tumor cells themselves.

In conclusion, these findings suggest that neither temsirolimus nor AuNPs alone is sufficient to induce IL-4-mediated immunomodulation in M0-WT or A375-WT cells under 2D monoculture conditions. The immune-neutral response may reflect the need for cellular crosstalk, 3D microenvironmental cues, or additional pro-inflammatory stimulation to trigger IL-4 signaling. Also, the secretion of IL-4 can be investigated with

a coculture system of A375 cells and M0 cells, since the cell-to-cell communications induce the chemokine and cytokine secretion [100].

4.5. Phytochemical Effects on A375-WT

Phytochemicals, naturally occurring bioactive compounds derived from plants, have gained increasing attention for their therapeutic potential in cancer treatment due to their anti-inflammatory, antioxidant, and anti-proliferative properties. In this study, the effects of several phytochemicals – curcumin, Epigallocatechin gallate (EGCG, green tea base), Betulin, and thymoquinone – are investigated on A375-WT melanoma cells cultured in a 2D environment. These agents are tested both individually and in combination with AuNPs, which serve as drug delivery platforms due to their biocompatibility and ability to enhance cellular uptake. Additionally, the mTOR inhibitor temsirolimus is included to evaluate potential synergistic or additive effects when combined with phytochemicals and AuNPs. DMSO is used as the solvent control. This section aims to explore how these phytochemicals, alone or in conjugation with AuNPs and/or temsirolimus, influence melanoma cell viability, highlighting their potential in combinatorial therapies.

To evaluate the concentration-dependent effects of each individual agent and their combinations, serial dilutions were prepared starting from the initial concentrations listed in Table 4.11. The working concentrations for the phytochemicals were selected based on values reported in the literature [56, 65, 215, 216]. For each phytochemical, a stock solution corresponding to four times the target concentration was prepared, and then six sequential 1:2 serial dilutions were performed. This procedure generated a series of six concentrations for each compound, enabling the systematic investigation of dose–response relationships on A375-WT cells. The final treatment concentrations were selected by comparing the IC_{50} values reported in the literature with those obtained from our serial dilution experiments.

Stock solutions of temsirolimus, curcumin, EGCG, betulin, and thymoquinone are prepared in DMSO. So, DMSO is also given to the cells to eliminate the toxic effect on the cells and detect the treatment effect. The amount of DMSO in treatments varies, so the maximum concentration of DMSO is selected according to the treatment with the highest amount of DMSO, which is the combined treatment of AuNP+Tems+Betulin.

Table 4.11. Initial concentrations of treatments.

Initial concentrations of treatments	**AuNP (nM)**	**Tems (nM)**	**Phytochemical (μM)**	**AuNP/Phyt Cnjg (nM)**
AuNP	2			
Tems		500		
Curcumin			160	
EGCG			160	
Betulin			160	
Thymoquinone			160	
AuNP/Curc Cnjg				2
AuNP/EGCG Cnjg				2
AuNP/Thymq				2
AuNP+Tems	2	500		
AuNP+Curc	2		160	
AuNP+EGCG	2		160	
AuNP+Betulin	2		160	
AuNP+Thymq	2		160	
AuNP+Tems+Curc	2	500	160	
AuNP+Tems+EGCG	2	500	160	
AuNP+Tems+Betulin	2	500	160	

A total of 10000 A375-WT cells are seeded per well in 96-well plates. After an overnight incubation to allow for cell attachment, treatments are applied in duplicate wells at various concentrations. Cell viability is assessed on 24th, 48th, and 72nd hours following treatment using the Alamar Blue assay, according to the manufacturer's instructions, and it is mentioned in Chapter 2.

Measurements are performed using a microplate reader. For absorbance-based detection, readings are taken at 570 nm and 600 nm. For fluorescence-based detection, excitation is set at 540 nm and emission at 590 nm. The viability results rely on the fluorescence-based reduction of resazurin to resofurin, a proxy for cellular metabolic activity and thus cell viability, graphed and given in the following sections.

4.5.1. Results of Phytochemicals, AuNP, and Temsirolimus Treatment on A375-WT

The effects of curcumin, EGCG, betulin, AuNP, and temsirolimus are administered to A375-WT cells alone to investigate the single treatment effects on cells in a monolayer (2D) culture model. Treatments are administered to cells at concentrations given in Table xx, and diluted in half five more times. The single-agent and dose-dependent impact on cell viability and metabolic activity is investigated using fluorescence-based measurements. In the legend, c_AuNP, c_tems, and c_phyt indicate the concentration of AuNP, temsirolimus, and each phytochemical, respectively.

Figures 4.12, 4.13, 4.14 and 4.15 present the cellular viability percentages based on multiple drug treatments, dosages at three concentrations, and time points. The viability of all treatments is calculated by normalizing to the control group at the corresponding time point. Values exceeding 100% indicate proliferation or increased viability in the respective cell population relative to the control group at that time-point. Figure 4.12 comprises time-resolved data (24h, 48h, 72h) for individual compounds. Figures 4.13, 4.14 and 4.15 show the dosage effects without showing how the results change over time.

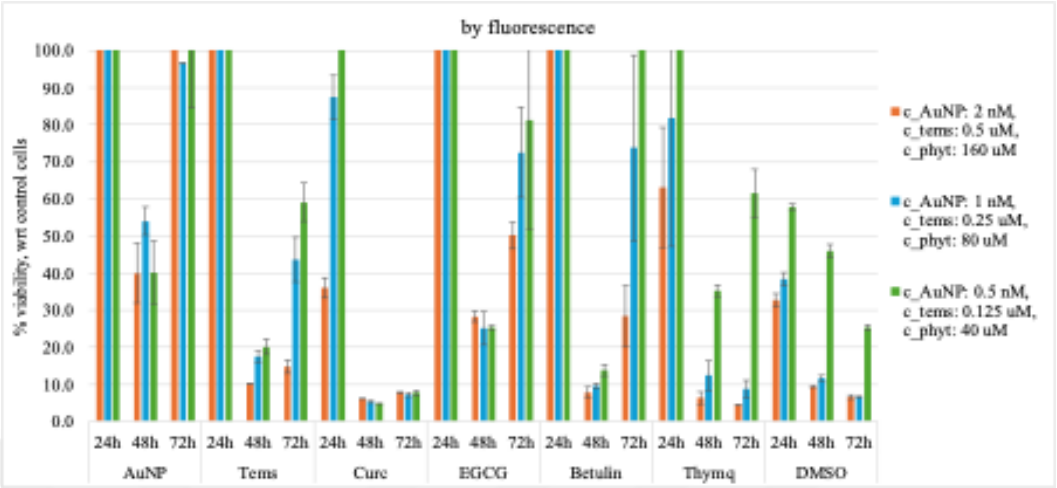


Figure 4.12. Viability of the top three concentrations day by day.

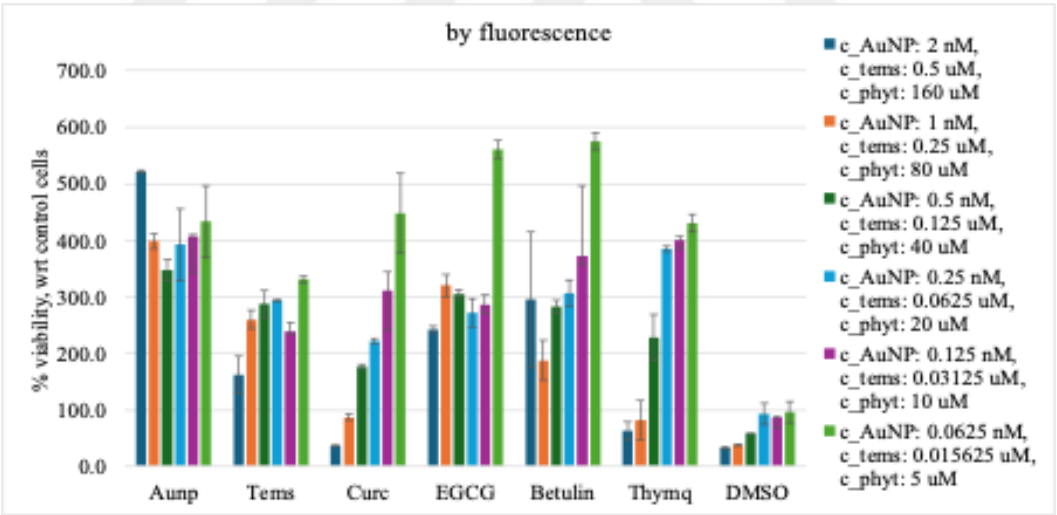


Figure 4.13. Viability after 24h of phytochemicals, AuNP, and temsirolimus treatment.

After 24 hours of treatment, all treated cells - except those exposed to curcumin and thymoquinone at high concentrations – exhibit a significant increase in metabolic activity, exceeding 200% at all tested concentrations. This result likely reflects a transient metabolic response or potential assay interference rather than an actual increase in cell proliferation. In some cases, early drug-induced stress can cause a compen-

satory rise in cellular metabolic activity [217], temporarily increasing the reduction of resazurin. The important point is that this elevated signal is not sustained as viability decreases by day 2 (Figure 4.12 and Figure 4.14), aligning with the cytotoxic effects of phytochemicals and temsirolimus. These findings emphasize the need to interpret fluorescence-based viability results with caution and investigate them deeper with complementary experiments, such as in 3D platforms.

AuNP treatment results in beyond normal physiological viability percentages, particularly at 24h and at low concentrations (Figure 4.13). While superficially indicative of increased proliferation, this signal likely represents a redox artifact due to mitochondrial or cytosolic stimulation. Nanoparticles are well-known to elicit ROS-dependent metabolic activation, redox cycling, which transiently elevates NADPH availability – the key cofactor reducing resazurin. This effect diminishes over time (Figure 4.12), with viability decreasing sharply by 48h and 72h. Such a pattern can be interpreted as hypermetabolism or hormetic responses rather than genuine proliferative effects [217, 218].

Temsirolimus shows a non-linear viability profile. At high concentrations (0.5uM), temsirolimus results in moderate viability at 24h, but severe metabolic suppression by 48h and 72h (Figure 4.12). Decreasing temsirolimus concentration is inversely proportional to increasing viability (Figures 4.13- 4.15). This suggests that high-dose temsirolimus suppresses cell growth via mTOR inhibition, while lower concentrations permit or even stimulate metabolic adaptation, possibly via activation of upstream survival signaling pathways [219].

Curcumin exhibits a classic dose-dependent cytotoxic effect (Figure 4.12). At 24h, even the highest dose yields only 36% viability, decreasing further over time to approximately 7% at 72h. This trend indicates strong pro-apoptotic or anti-proliferative activity. However, Figure 4.14 shows increasing viability with decreasing curcumin concentrations, suggesting a hormetic effect where low-dose curcumin mildly activates

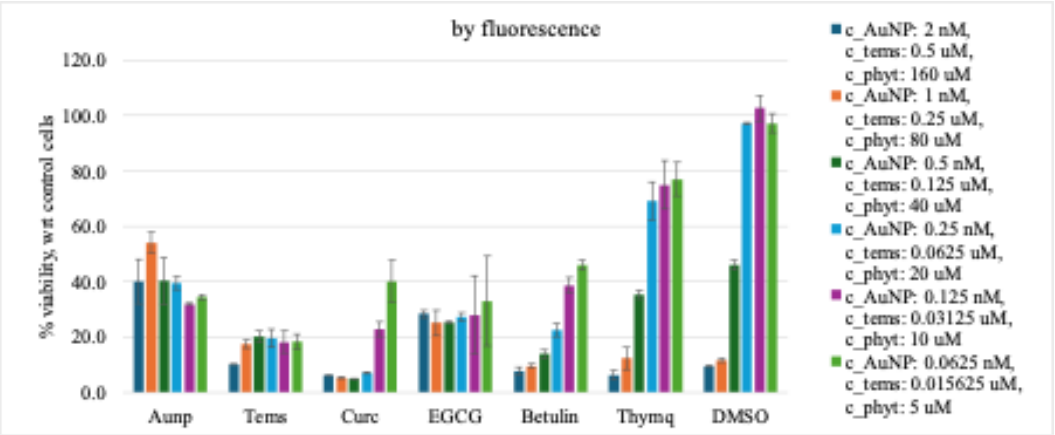


Figure 4.14. Viability after 48h of phytochemicals, AuNP, and temsirolimus treatment.

metabolic pathways without triggering apoptosis. Such duality in curcumin's activity has been reported, with low doses supporting redox balance and higher doses inducing oxidative stress [56].

EGCG consistently yields high viability readings, which may not reflect actual cell proliferation but instead EGCG's potent antioxidant activity, which enhances cellular redox capacity and thus resazurin reduction. Notably, EGCG has been documented to chemically reduce resazurin even in the absence of cells, further complicating its interpretation in viability assays [220].

Betulin exhibits moderate to strong increases in viability across all concentrations, particularly at low doses. Similar to EGCG, betulin is known to modulate mitochondrial respiration and has mild antioxidant properties. As seen in Figure 4.12, increasing viability over time suggests sustained metabolic activation rather than apoptosis.

Thymoquinone demonstrates a classic dose-dependent increase in viability across all concentrations. Viability increases from 63.1% at high concentrations to 430% at the lowest dose. This sharp upward trend suggests a pronounced hormetic response, where low concentrations of thymoquinone stimulate cellular metabolic activity, likely through the activation of antioxidant or stress adaptive pathways. Conversely, high

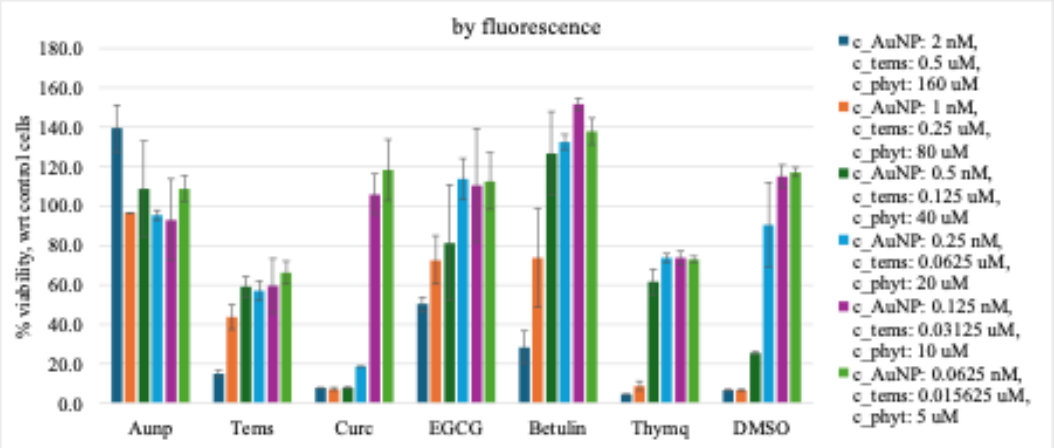


Figure 4.15. Viability after 72h of phytochemicals, AuNP, and temsirolimus treatment.

concentrations appear to exert cytotoxic effects, potentially via pro-oxidant mechanisms or the induction of apoptosis. These findings align with previous studies that describe thymoquinone's dual redox behavior – acting as a cytoprotective agent at low doses and as a cytotoxic compound at higher concentrations [55]. This hormetic profile underscores the importance of dose optimization when evaluating thymoquinone's biological activity in vitro models.

DMSO serves as the solvent control and shows a logical increase in viability with decreasing compound concentrations. The values reflect baseline metabolic activity in the absence of active cytotoxic compounds. Minor fluctuations likely result from cell density differences, evaporation, or mild DMSO-induced membrane permeability effects.

Notably, the DMSO control is designed to match the highest solvent concentration used across phytochemical treatments. However, due to solubilities and stock preparation, even the highest phytochemical doses do not contain as much DMSO as the control; in most individual phytochemical treatments, they corresponded to the DMSO levels present in only the fourth or fifth highest concentration groups (Figures 4.13- 4.15). Therefore, any cytotoxic effects observed in phytochemical treatments are unlikely to be attributed solely to DMSO and should be interpreted as compound-

specific responses.

4.5.2. Synergistic Effect of Phytochemicals and Temsirolimus Given with AuNP on A375-WT

The high dose combination reveals distinct patterns of cytotoxicity across all AuNP+compound pairings (Figure 4.16). Among the combinations, AuNP+temsirolimus exhibits a progressive viability decline over time (from 51.2 % to 24.3%, then 15.6%), consistent with mTOR pathway suppression and potential cumulative redox stress.

AuNP+curcumin shows rapid and sustained toxicity (from 24.5% to 5.7% then 4.6%), likely due to curcumin's known ability to destabilize mitochondrial membranes and induce apoptosis in oxidative environments (Figures 4.17- 4.19) [221]. When delivered with AuNPs, which enhance cellular uptake and bioavailability, these effects are magnified. The observed synergy aligns with literature showing that curcumin's cytotoxic effects are significantly enhanced.

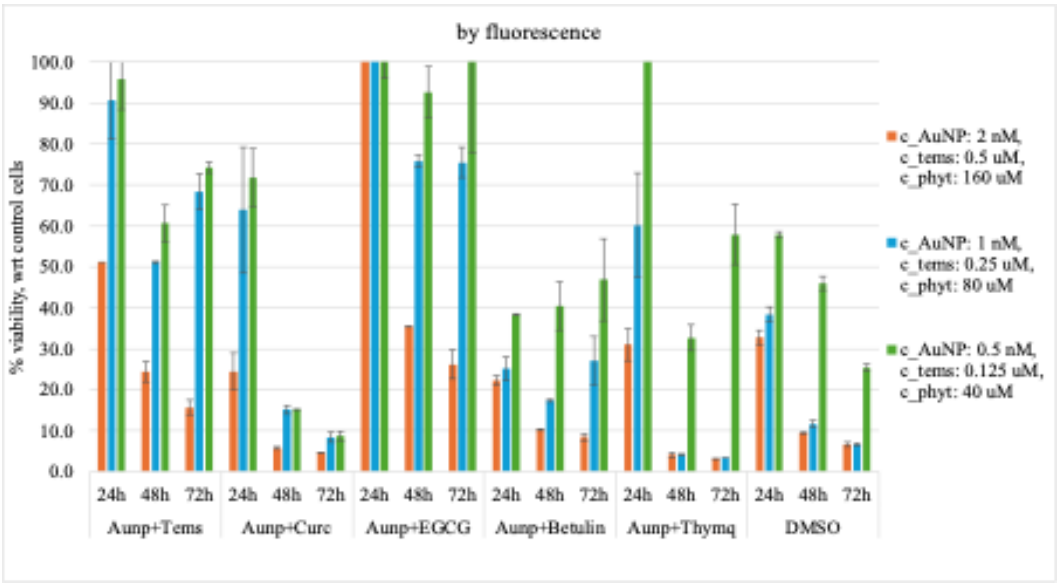


Figure 4.16. Viability of the top three concentrations day by day.

The AuNP+EGCG combination displayed a biphasic pattern: a transient increase in viability of 107.7% at 24 hours, followed by a decline to 26.2% by 72 hours (Figure 4.16). This is consistent with EGCG's redox duality. Initially, EGCG may act as an antioxidant, boosting NADPH-dependent resazurin reduction. However, in the presence of AuNP, EGCG can undergo auto-oxidation, generating hydrogen peroxide and inducing oxidative stress [222].

The betulin combination displayed steadily decreasing viability from 22.3% to 8.4% over 72 hours (Figures 4.16- 4.19). Betulin disrupts mitochondrial respiration and triggers intrinsic apoptosis through cytochrome c release and caspase activation [223]. The cytotoxic response may be enhanced in the presence of AuNP-induced stress, even if the initial impact is moderate.

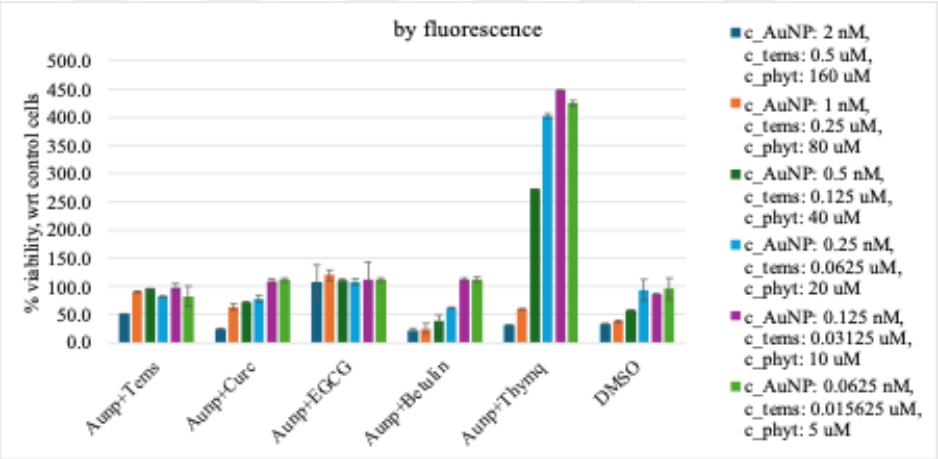


Figure 4.17. Viability after 24 h of phytochemicals and temsirolimus given with AuNP.

AuNP+thymoquinone demonstrated a dose- and time-dependent duality in combination with AuNPs. High doses are clearly cytotoxic and induce early apoptotic signals (Figure 4.17) [224]. Mid-range doses trigger transient metabolic spikes, potentially linked to short-term antioxidant compensation. Low doses induce sustained, elevated viability likely due to redox adaptation and hormetic stimulation 55. These findings align with the well-established biphasic behaviour of thymoquinone and un-

derscore the validation to distinguish between metabolic compensation and true cell survival.

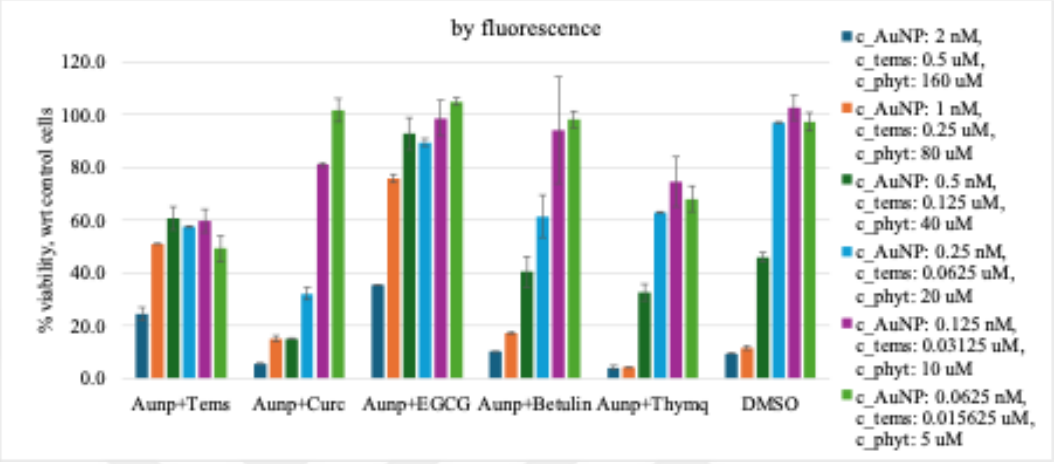


Figure 4.18. Viability after 48 h of phytochemicals and temsirolimus given with AuNP.

The DMSO control showed decreasing values, serving benchmark for solvent-related background toxicity. However, all combination treatments exhibited greater cytotoxicity than DMSO alone, confirming that observed effects stem primarily from drug-specific mechanisms rather than solvent artifacts.

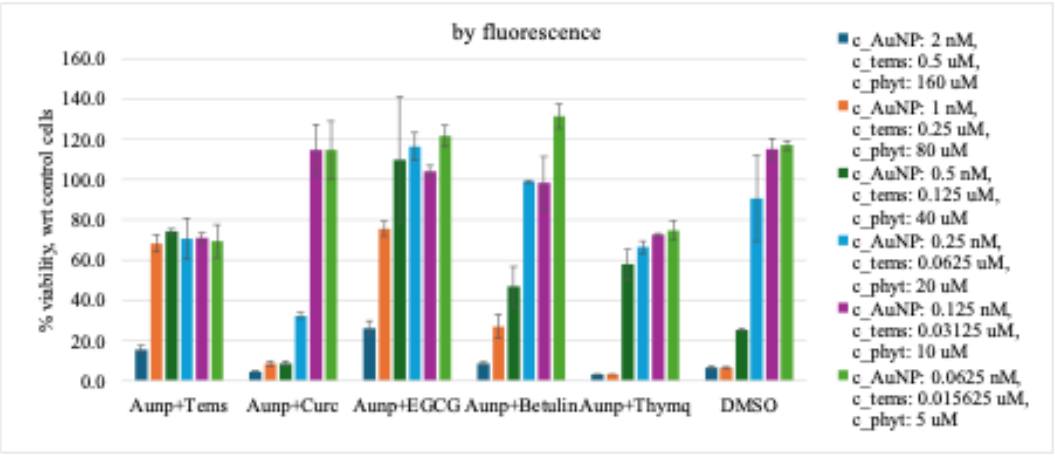


Figure 4.19. Viability after 72 h of phytochemicals and temsirolimus given with AuNP.

4.5.3. Results of Phytochemicals Conjugated with AuNP on A375-WT

This dataset shows the effects of increasing concentrations of AuNP-conjugated phytochemicals- curcumin conjugate 1, curcumin conjugate 2, EGCG conjugate, and thymoquinone conjugate- on cellular viability at 24h, 48h, and 72h. The results reveal compound-specific and dose-dependent viability trends, reflecting complex redox-modulating behaviors of phytochemicals and the enhanced delivery efficiency.

Curcumin conjugate 1 demonstrates a nonlinear viability response across concentrations and time points (Figures 4.20- 4.23). At 2 nM, a sharp drop in viability is observed (111.5% to 16.% while lower concentrations (1-0.125 nM maintain values between 100-135% throughout the assay. This indicates that high-dose exposure likely triggers mitochondrial disruption and ROS-mediated apoptosis effects associated with curcumin's pro-oxidant potential at cytotoxic doses [221]. The rapid cytotoxicity at 2 nM also suggests efficient intracellular delivery of curcumin by AuNPs, leading to early-onset apoptosis.

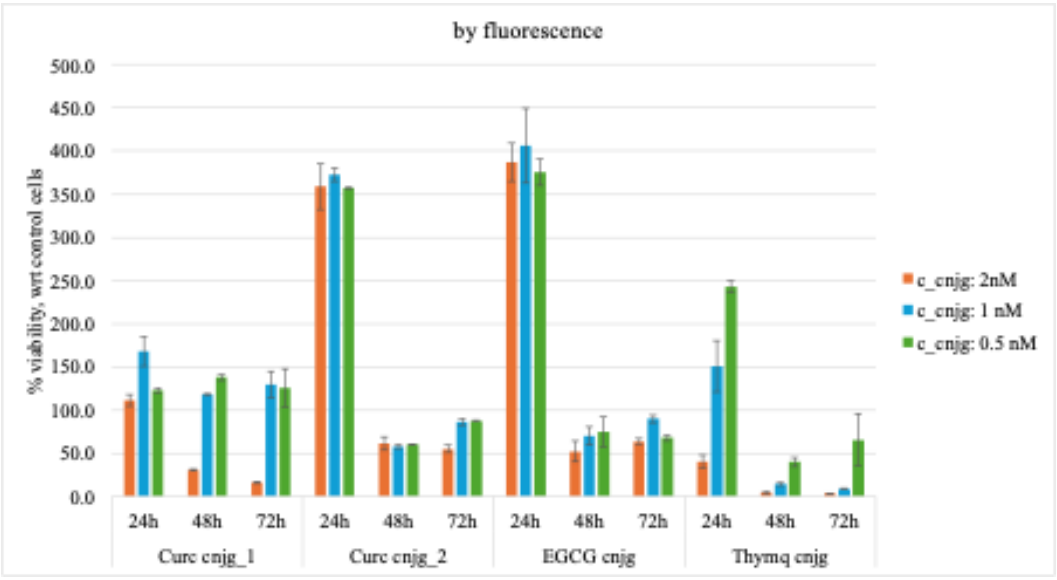


Figure 4.20. Viability of the top three concentrations of phytochemicals conjugated with AuNP treatments day by day.

Curcumin conjugate 2 presents a sharp increase in metabolic activity at 24h across all concentrations (Figure 4.21). Even at 2 nM, viability remains at 54.9% at 72h-far above the levels observed with curc cnjg_1. This discrepancy may be attributed to differences in conjugation chemistry that prolong curcumin release or alter intracellular trafficking. Yet, the slower decline implies reduced cytotoxicity and prolonged adaptation.

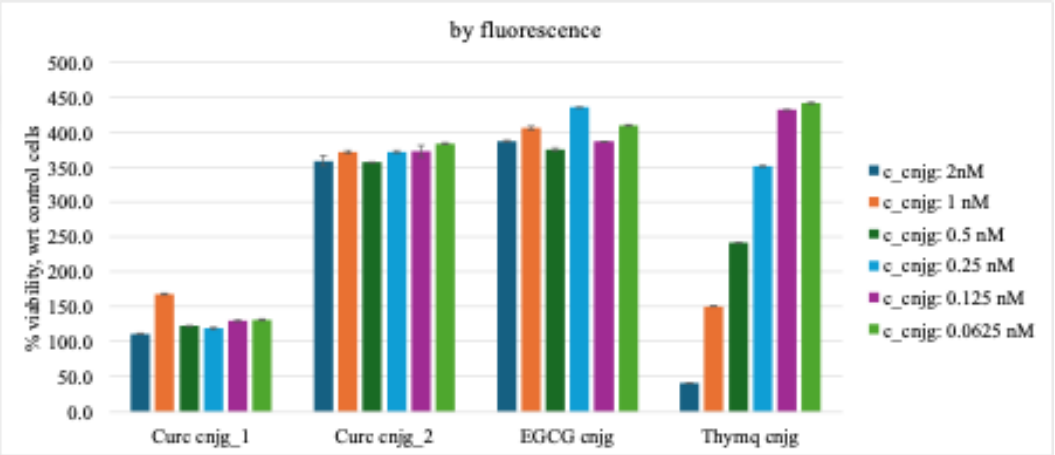


Figure 4.21. Viability after 24h of phytochemicals conjugated with AuNP.

The EGCG-AuNP conjugate induces consistently elevated viability at all concentrations at 24h. High values reflect enhanced mitochondrial output or potential assay interference. EGCG has been shown to chemically reduce resazurin, which may inflate viability readouts independent of cell proliferation [217].

Thymoquinone conjugate shows a classic dose-dependent response. At high concentration (2 nM and 1 nM), viability decreases from approximately 50% to under 20% - indicative of strong pro-oxidant stress and apoptosis induction. However, at 0.5 nM, delayed cytotoxicity is observed (viability rebounds to 65.7% by 72h) (Figure 4.23). The most interesting behavior occurs at 0.25-0.0625 nM, where viability rises over time, reaching 87.2% and 65.9%, respectively. These findings mirror the dual nature of thymoquinone, which is anti-inflammatory and antioxidant at low doses, but strongly cytotoxic via ROS generation and mitochondrial disruption at higher concen-

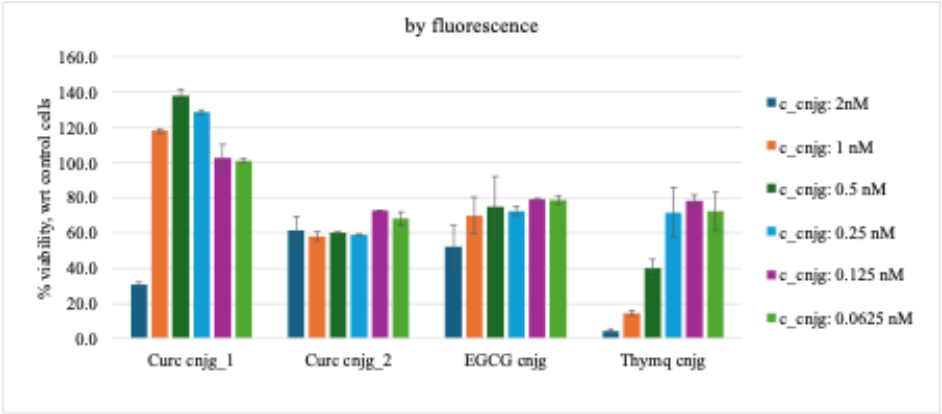


Figure 4.22. Viability after 48h of phytochemicals conjugated with AuNP.

trations [55].

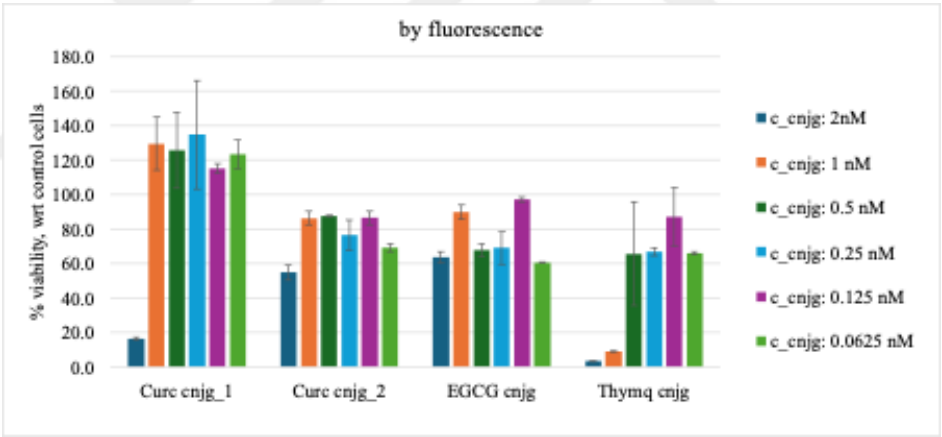


Figure 4.23. Viability after 72h of phytochemicals conjugated with AuNP.

4.5.4. Synergistic Effect of Phytochemicals Given with Temsirolimus and AuNP on A375-WT

This dataset captures the viability profiles of triple drug combinations composed of AuNPs, temsirolimus, and either curcumin, EGCG, or Betulin, across a dose range (2 nM to 0.0625 nM AuNPs and 160 μM to 5 μM phytochemicals). The results reflect a consistent pattern of dose-dependent cytotoxicity at high concentrations, with varied adaptation (Figures 4.24- 4.27).

In these treatment groups, the DMSO concentration is higher than in previous conditions; therefore, any observed decrease in viability may also reflect the cytotoxic contribution of DMSO.

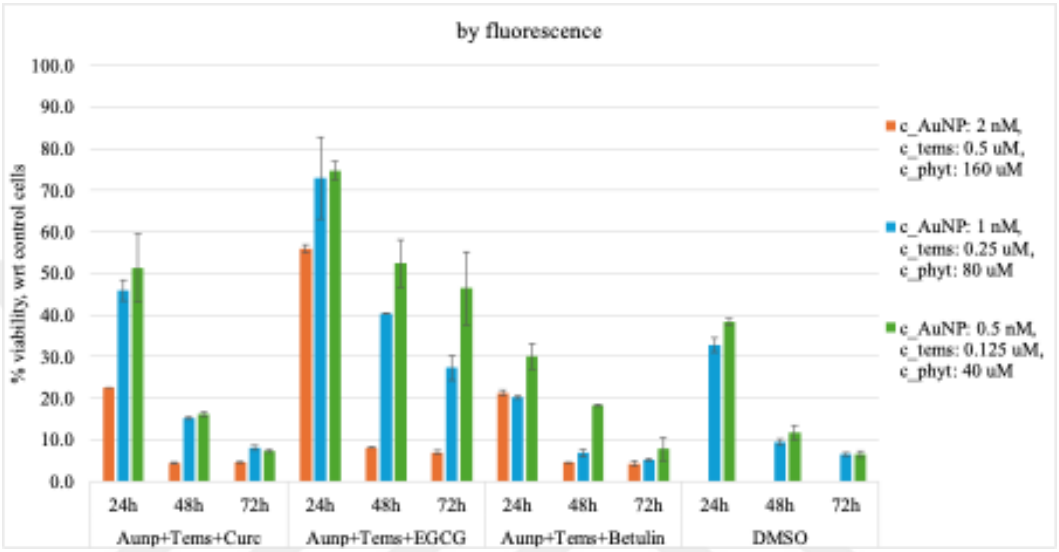


Figure 4.24. Viability of the top three concentrations of phytochemicals given with temsirolimus and AuNP day by day.

AuNP+temsirolimus+curcumin combination exhibits the strongest cytotoxicity across all concentrations and timepoints. At the highest dose (2 nM AuNP+0.5uM tems+160uM curc), viability decreased rapidly to 4.5% (Figure 4.24). Even at the moderate doses, the pattern is maintained. Curcumin is known for mitochondrial membrane disruption, ROS generation, and activation of caspase-dependent apoptotic pathways. Temsirolimus contributes by inhibiting mTORC1, limiting protein synthesis, and stress recovery. When delivered via AuNPs, curcumin bioavailability and intracellular accumulation increase, potentiating its effects. These combined mechanisms likely overwhelm cellular redox buffering and survival signaling, leading to rapid loss of viability.

The EGCG combination reveals a biphasic response. At high doses, viability declined moderately, but at mid and low concentrations, viability is substantially preserved. EGCG's dual antioxidant/pro-oxidant nature is well-established; while

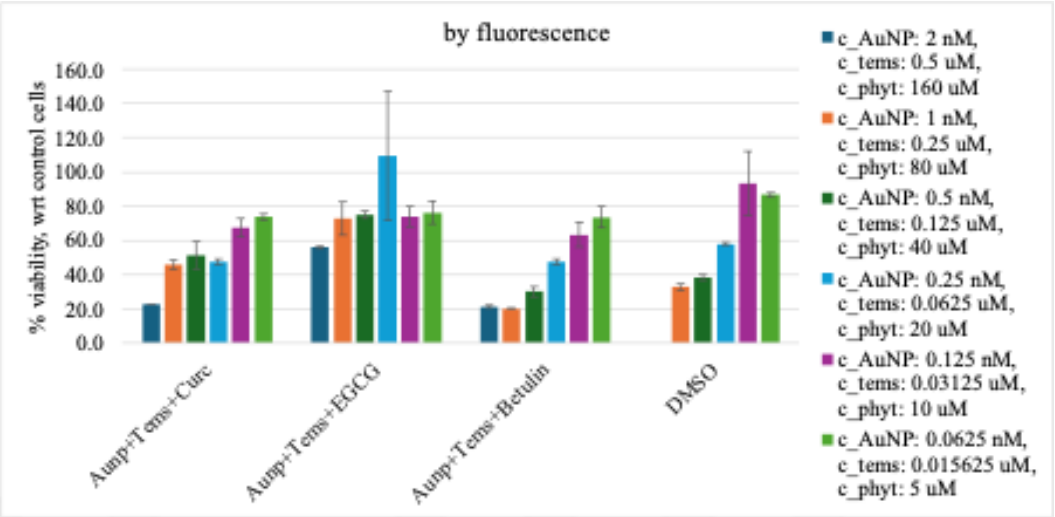


Figure 4.25. Viability after 24h phytochemicals given with temsirolimus and AuNP.

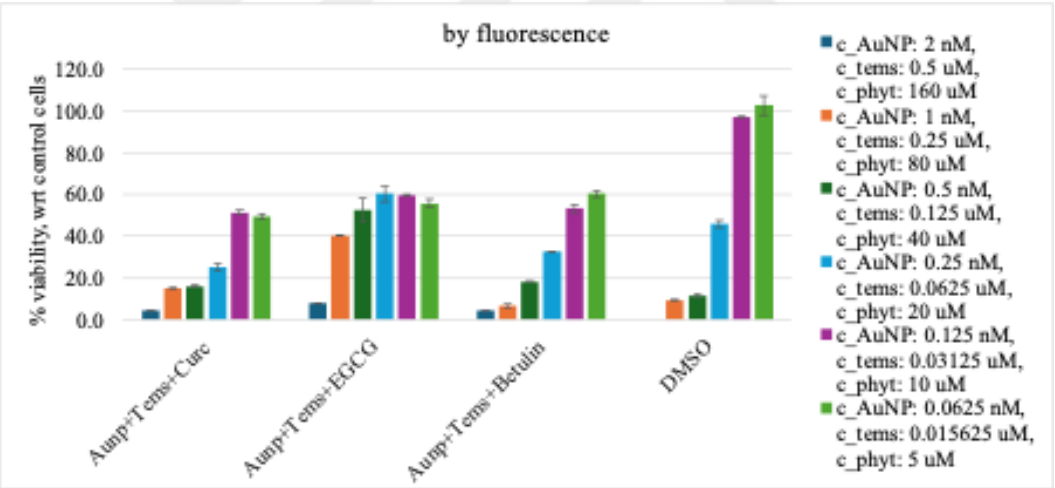


Figure 4.26. Viability after 48h phytochemicals given with temsirolimus and AuNP.

high doses induce oxidative stress and DNA fragmentation, low doses activate redox-adaptive pathways. The role of AuNPs in facilitating intracellular EGCG delivery could amplify these redox effects in both directions. Additionally, EGCG is known to chemically reduce resazurin, which could contribute to elevated fluorescence signals without actual proliferation. Nonetheless, the preservation of viability at lower doses suggests stress adaptation rather than pure assay interference.

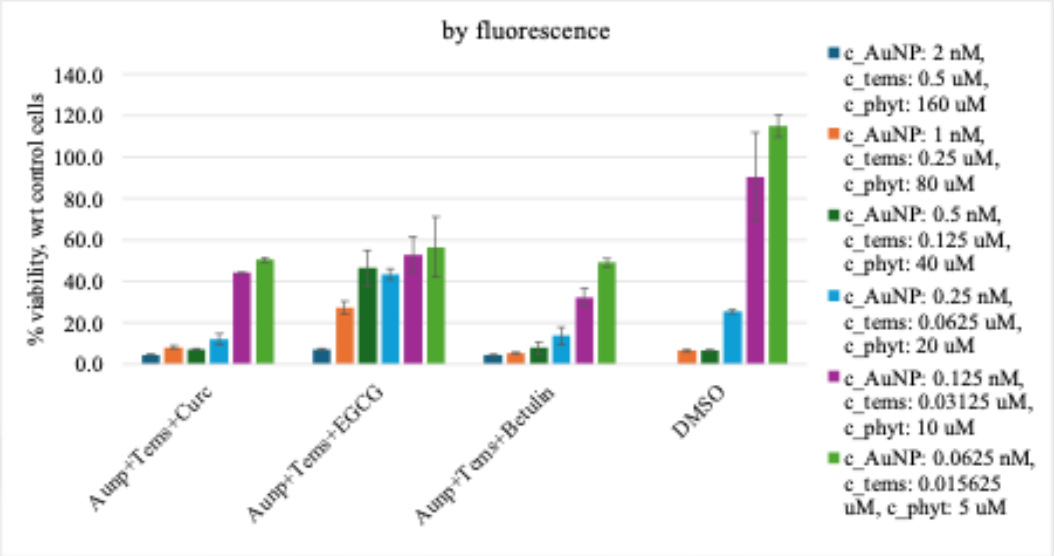


Figure 4.27. Viability after 72h phytochemicals given with temsirolimus and AuNP.

The betulin-containing triple combination demonstrated gradual recovery from cytotoxicity with decreasing concentration. At the highest dose, viability dropped to 4.3%, yet at the lowest dose, it recovered to 49.1% by 72h (Figure 4.27). Betulin is known to modulate mitochondrial respiration, induce intrinsic apoptosis via cytochrome c release, and inhibit NF-κB signaling. These effects may synergize with mTOR inhibition with tems and resox stress from AuNPs, particularly at high doses. However, at low doses, betulin's milder mitochondrial effects may promote metabolic stimulation or partial cytoprotection.

5. 3D EXPERIMENTS FOR OPTIMIZATION

5.1. Optimization Experiments with Different Hydrogels

Different types of hydrogels (gelatin, gelatin-alginate at different formulation ratios, Matrigel, collagen) are used as scaffolds for A375 melanoma cells and THP-1 monocyte cells.

5.1.1. 3D Bioprinting Process Parameters Optimization without Cell Loading

The custom-made 3D bioprinter (AXO-A1) was bought from Axolotl Biosystems. This bioprinter has two different heads which can work simultaneously. There are several printheads such as high-temperature printhead, UV curing toolhead, high-pressure printhead etc. Several trials have been made with different hydrogels, nozzles, pressures, and flow rates to understand how the bioprinter works.

As a start, we tried the Nivea crème as a hydrogel to understand how the bioprinter works. A simple but durable scaffold has been created. As for the cell incubation, different ratios of the gelatin-alginate mixture, such as 15% w/w gelatin + 2% w/w alginate (15G2A), 8% w/w gelatin+4% w/w alginate (8G4A), 10G2A, 10G4A, Matrigel, etc., are printed in the bioprinter. Different sizes of syringe nozzle (18-27 gauge), different speeds (2-15 mm/s) and pressure (0.5-25 psi) of the printhead, and different printhead temperatures (24°C and 37°C) are investigated for each different hydrogel.

Initially, a simple structure was selected as the scaffold shape (Figure 5.1) to understand the bioprinter parameters and how they work. It has a 1 cm x 1cm length and width and a 3 mm height. However, the height was changed to 1 mm due to the stability issues.

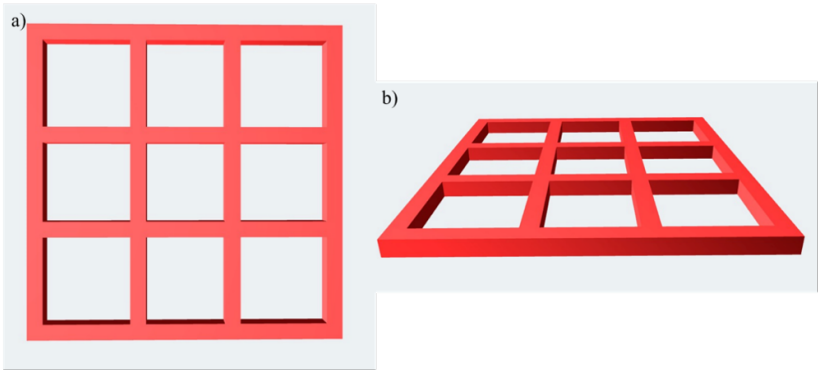


Figure 5.1. Hydrogel scaffold for the initial experiments. (a) Top view, (b) side view.

All the investigated parameters are given in the Appendix A with the results. At the end of the optimization experiments, the most stable gelatin-alginate mixture is obtained when the 8G4A gelatin-alginate mixture is printed with 20g blunt dispensing needle, and using 5 mm/s printhead speed, 2 psi pressure and 0.25 mm layer height (total 4 layers) as can be seen in Figure 5.2a. In every trial, the corners have more hydrogel, and the edges slightly get thinner.

Matrigel is investigated with different parameters as well. As the Matrigel is more difficult to keep in gel form, the final scaffold is always broken on one side. However, Matrigel printed with 22 gauge needle at 1-2 psi with a 5 mm/s printhead speed and 24°C printhead temperature stays stable (Figure 5.2b).

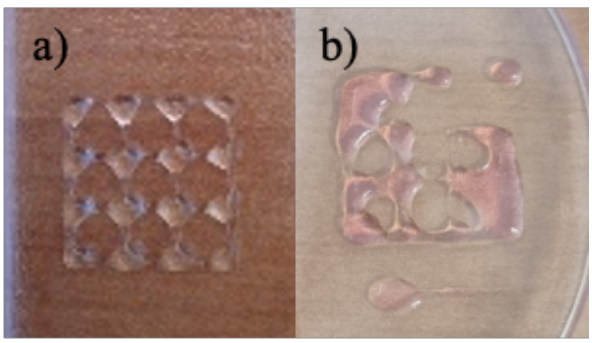


Figure 5.2. (a) 8G4A hydrogel scaffold, (b) Matrigel scaffold.

5.2. Optimization with Cell-Laden Hydrogels

Different types of hydrogels (gelatin, gelatin-alginate at different formulation ratios, Matrigel) are used as scaffolds for A375 melanoma cells, THP-1 monocyte cells (mentioned in Appendix A), and THP-1 differentiated M0 cells. Although the scaffolds are optimized without the cells, the dynamics of the hydrogel may change with the addition of the cells and cell medium, so, the experiments are done with different ratios of hydrogels as well.

5.2.1. A375-GFP Cell-Laden Gelatin-Alginate by Using a Bioprinter

A total of five different concentrations of hydrogels are mixed with melanoma A375-GFP cells with a 1:1 ratio (Table 5.1). 2 mL of hydrogel is mixed in a beaker with 2 mL of cells, which contains an average of 2×10^6 cells/mL, and the final cell density becomes 1×10^6 cells/mL in the hydrogel. Cells and the hydrogel are mixed in a beaker with a sterilized spoon manually for 2 minutes. Then, the mixture (which can be called bioink) is transferred to the syringe. Then the bioink is printed onto a plate according to identified parameters to create the scaffold. Different parameters are set for different concentrations of gelatin-alginate. Gelatin and alginate are prepared by dissolving in PBS by weight. For these experiments, the viability of A375-GFP cells is investigated in 10G2A, 8G4A, 10G4A, 10G6A, and 12G4A hydrogels.

After the printing is completed, the scaffold is crosslinked with 3 mL of crosslinker ($CaCl_2$) and waited 10 minutes in the incubator. After crosslinking, the $CaCl_2$ is removed, and the scaffold is washed with PBS. Then, 4 mL of complete medium was put on the scaffold. The medium was changed every three days to provide nutrition and remove the waste from the cell environment.

Cells in specific locations in the scaffold were monitored for up to 16 days. Each cell-laden hydrogel is printed twice. However, two of the hydrogels (10G6A and 12G4A) were contaminated within two days, and one other (10G2A) was contaminated after 6

days.

Table 5.1. 3D Experiments performed with A375-GFP cell-laden bioink.

Hydrogel	**Cell type**	**Mix ratio (hydrogel:cell medium)**	**Duration of experiment**	**Result (Viability)**
10% gelatin and 2% alginate	A375-GFP	1:1 (2 mL : 2 mL)	8 days	Viable; Contamination at 6th day
10% gelatin and 4% alginate	A375-GFP	1:1 (2 mL : 2 mL)	16 days	Viable; Cluster formation after 5th day
10% gelatin and 6% alginate	A375-GFP	1:1 (2 mL : 2 mL)	2 days	Viable; Contaminated at 2nd day
8% gelatin and 4% alginate	A375-GFP	1:1 (2 mL : 2 mL)	14 days	Viable; Cluster formation after 5th day; Migration of cells occurred between 5th–7th day
12% gelatin and 4% alginate	A375-GFP	1:1 (2 mL : 2 mL)	2 days	Contaminated at 2nd day

In the 8G4A hydrogel, cells show 12 days of viability. Cells behave as they are naturally, such as growing, proliferating, and migrating. They tend to accumulate, proving that cell communication is strong. A great migration was seen in this hydrogel (Appendix A). However, after 12 days, the scaffold is broken. The structure is broken off at the edges. Then, it becomes hard to identify the location of the identified cells.

On the other hand, the cells in the 10G4A hydrogel show the most prolonged viability. The scaffold is stable for 16 days. Cells behave as in their nature, and they tend to accumulate, which proves the communication between the cells is strong. Of all three successful experiments, the most successful one is the 10G4A hydrogel because it provides the longest viability and durability of the scaffold. 8G4A and 10G4A show similar physical characteristics and viability within the hydrogel. Since the cells have great mobility in 8G4A hydrogel, this hydrogel is selected for the following experiments.

5.2.2. A375-GFP Cell-Laden Collagen-Matrigel by Using Bioprinter

The preliminary experiments with Matrigel indicated a necessity to mix Matrigel with collagen to increase the scaffold stability. Collagen is another natural bioink commonly used to make scaffolds for cell cultivation. It is biocompatible and promotes cell proliferation. It exhibits high cell adherence, which makes it desirable for in situ studies. The hydrogel consists of 65% collagen type 1, 20% Matrigel, and 15% cells with a complete medium of DMEM.

Collagen is a viscous product when it is undiluted. Its density is 5 mg/ml, and it is used in experiments in the range of 1-4 mg/ml. It is diluted to 4 mg/ml using 0.1 M acetic acid as solvent. Also, the final pH needs to be 7.2-7.4 when the collagen is used in an experiment. The pH is arranged by using 1 M NaOH.

When 1 ml of collagen was combined with 0.25 ml of acetic acid, the pH of the solution was measured as 3.29. Upon the subsequent addition of 80 μl of NaOH to the same mixture, the pH increased to 7.2, indicating successful neutralization of the acidic medium. The collagen is aliquoted and stored at +4 °C after it is diluted, and the pH is adjusted.

The preparation of bioink, consisting of Matrigel and collagen, is conducted in the precooled environment. Matrigel is liquified at +4°C. The dilution of collagen is also conducted in ice at +4°C. After the Matrigel is liquified, 1.4 ml collagen and 0.430

ml Matrigel are mixed in a precooled falcon tube. A complete medium of 0.323 ml full of 1×10^6 A375-GFP cells is added to the hydrogel and mixed gently. Then, the hydrogel is transferred to a precooled syringe. The syringe is put into the incubator at 37°C for 15 minutes to let the gelation occur.

Needle size, pressure, and temperature are determined during the Matrigel optimization experiments. The printing condition is selected for 20 g needle size, 2psi pressure, and 37°C printhead temperature. Since the viscosity (gelation) of the bioink is low, the printer sometimes squirts the ink onto the scaffold. So, the scaffolds don't have unique heights (Figure 5.3).

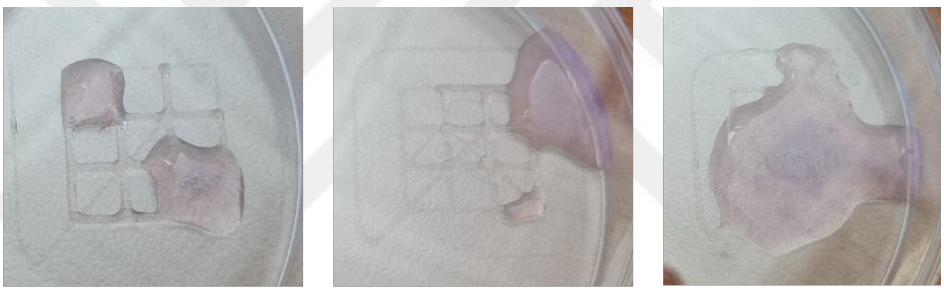


Figure 5.3. Scaffolds after printing.

After printing, the DMEM complete medium is put onto the scaffolds, and the plates are placed in the incubator. The medium of the scaffolds is changed every three days.

The progress of the cells is given in the following table (Figure 5.4), with both bright field and fluorescence pictures.

The viability of the A375-GFP cells on the 2^{nd} and 7^{th} days is investigated using propidium iodide dye. Propidium iodide is a membrane-impermeable fluorescent DNA stain and exhibits enhanced fluorescence upon binding to either DNA or RNA. When in an aqueous solution, PI has a fluorescent excitation maximum of 493 nm (blue-green)

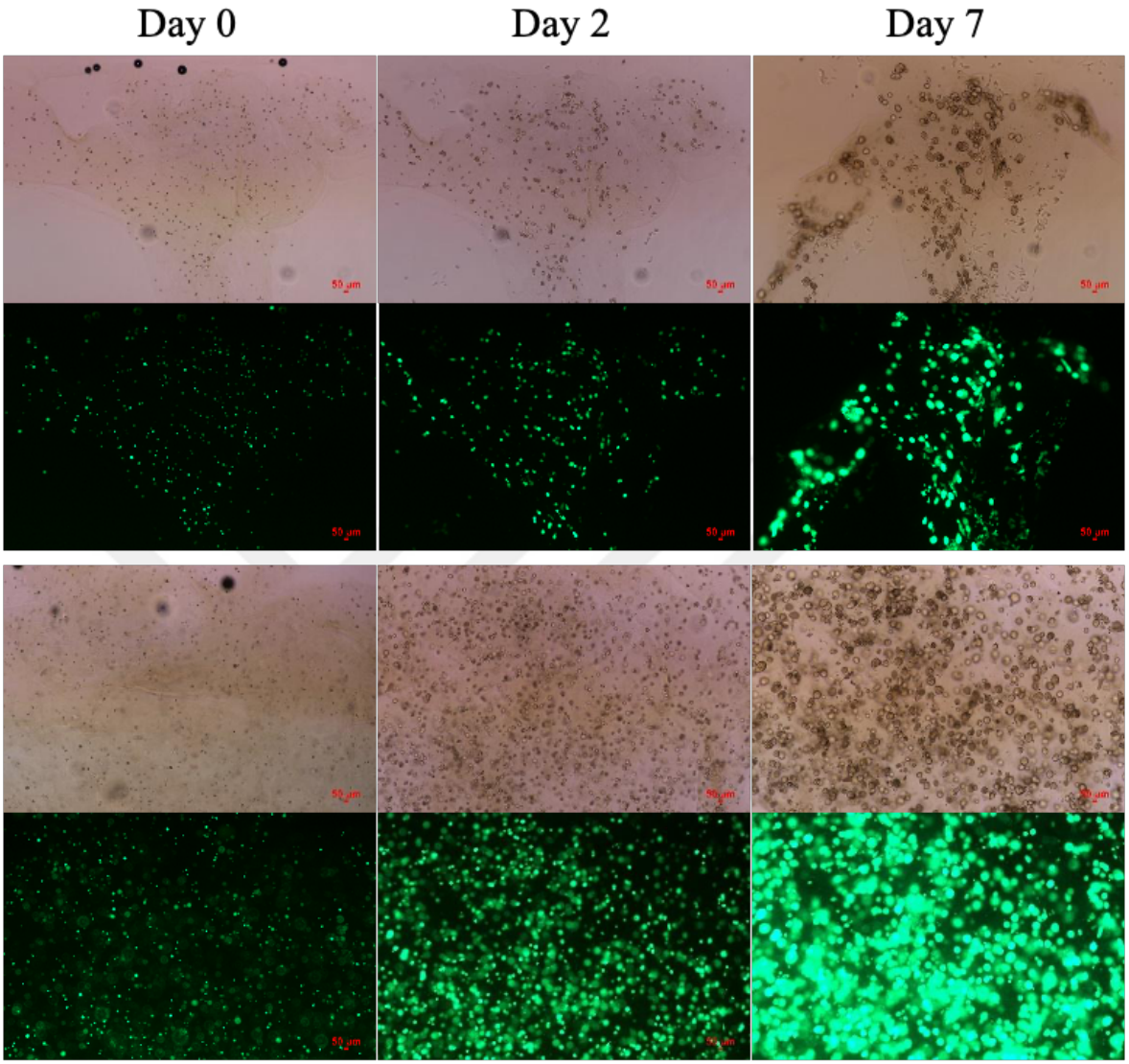


Figure 5.4. Progress of cells in Matrigel/collagen hydrogel over the 7 days.

and an emission maximum of 636 nm (red). So, when PI is used on cells, it only enters the dead cells, and the dead cells fluoresce red. PI stain is stocked by dissolving 3 mg of PI in 1 ml of absolute ethanol. In an experiment, 1 μL of stock PI is dissolved in 1 ml of PBS. The medium on the scaffold is removed, and the PBS solution is placed on the scaffold and allowed to wait for 2 minutes. This should be done in a dark place so as not to affect the PI. After 2 minutes, PBS consisting of PI is removed, and the scaffold is washed twice with PBS. After that, cells are monitored under 535 nm light.

A375-GFP cells fluoresce when the FITC light is emitted. An increase in fluorescence means cells grow, increasing in number and accumulating over the seven days. To ensure the cells are growing, viability assessment is done using PI staining 2 days and 7 days after bioprinting. Red fluoresced (dead cells) and green fluoresced (all cells) are monitored using fluorescence light, and the alive cells are calculated by subtracting them from each other. Pictures are processed using the ImageJ program. Viability analysis and the bright and fluorescence picture of the scaffolds on the second and seventh days are given in the following Figures 5.5,- 5.7.

On the second day of the culture in the Matrigel-collagen scaffold, cells increase their volume and number, as can be seen from Figure 5.5. All cells are fluoresced green since the A375-GFP cells are tagged by green fluorescent protein, while the dead cells fluoresce since the PI stain is applied. Both green and red fluorescence pictures are processed using ImageJ, and the numbers of live and dead cells are calculated. At the end of the second day, the viability of the cells is roughly 70% (Figure 5.5).

These results show that matrigel-collagen hydrogel is biocompatible for A375 cells. Further treatment strategies like anti-cancer drugs, phytochemicals, and nanoparticle effects on melanoma cells can be investigated by using this hydrogel.

A375-GFP cells agglomerate and create a greater volume of cell clusters after 7 days of incubation in the matrigel-collagen environment (Figure 5.6). Since all cells fluoresce green, the fluorescence of all cells amplifies each other in the picture. The outlines of the cells are unclear so it becomes harder to count the cells. On the other hand, the fluorescence of the dead cells is lower than the green fluorescence, and the outline of the cells is clearer. After 7 days, the scaffold is completely deteriorated, and the cells are moved outside of the hydrogel.

Both gelatin–alginate and Matrigel–alginate hydrogels are used as hybrid biomaterials to mimic aspects of the extracellular matrix (ECM), but they differ significantly in composition, biological signaling, and application relevance. Gelatin–alginate

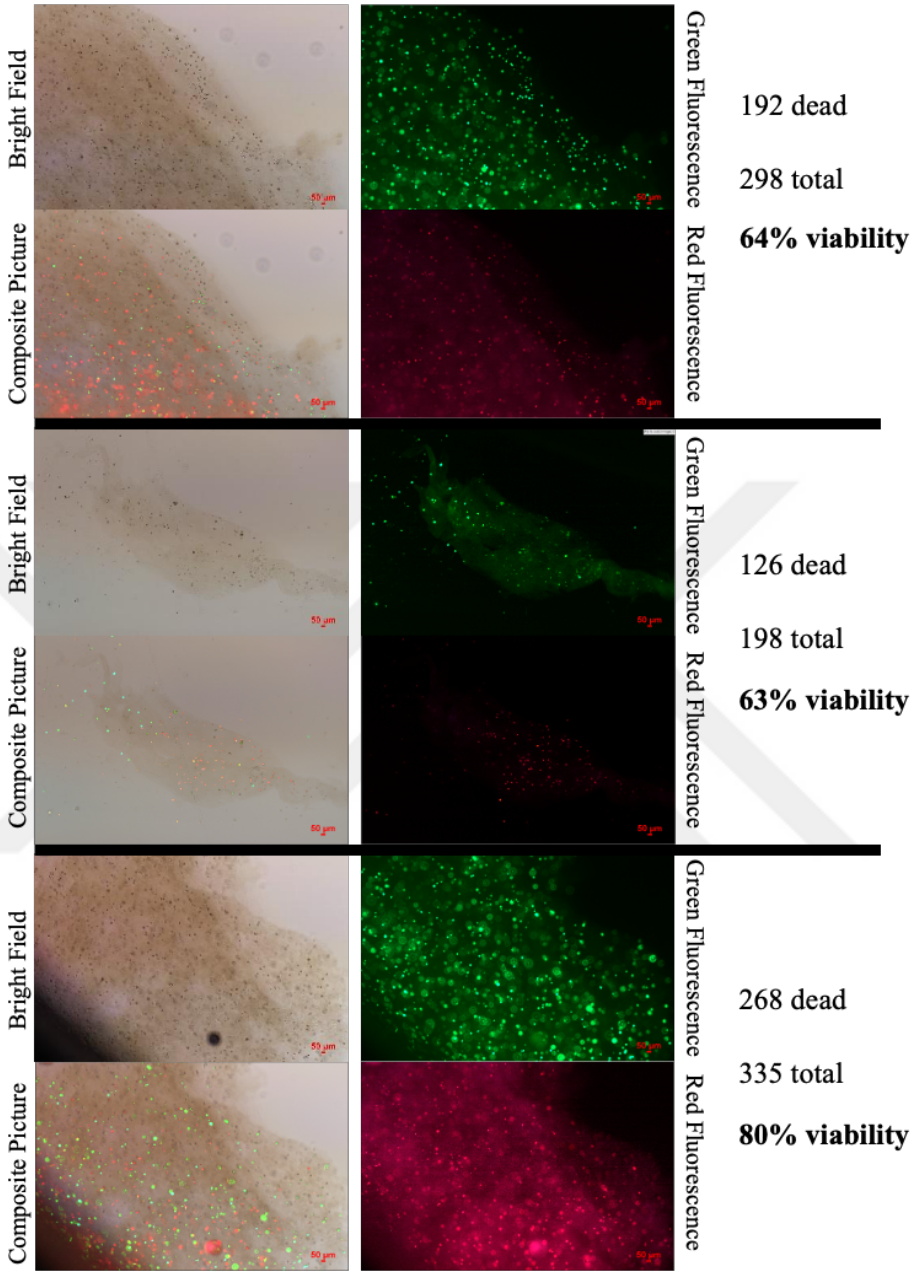


Figure 5.5. Viability of A375-GFP cells in Matrigel-collagen bioink after two days.

(denatured collagen, rich in Arg–Gly–Asp (RGD) motifs) is better for defined, tunable, reproducible systems, while Matrigel–alginate is better for tumor-like, growth factor–rich (EGF, TGF-β, bFGF, VEGF, etc.) environments with adhesion ligands (laminin, collagen IV) to study invasion and drug response in cells. Cell growth is supported better within a matrigel-based hydrogel, while migration is observed in a gelatin-based hydrogel (Figure 5.7).

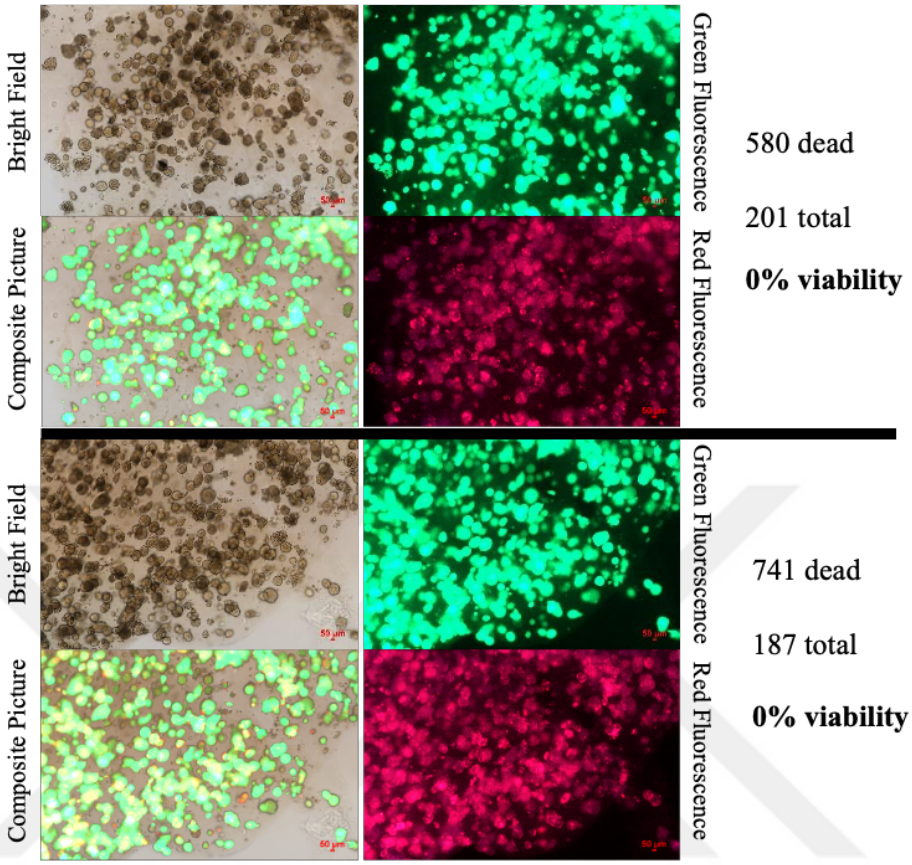


Figure 5.6. Viability of A375-GFP cells in Matrigel-collagen bioink after seven days.

5.3. Cell-to-Cell Communication Experiments

5.3.1. Coculturing (GFP-tagged A375 cells and mcherry-tagged M0 cells) on 3D (8G4A Scaffold) with RPMI-1640 Medium

Hydrogel containing 8% gelatin (w/w) and 4% alginate (w/w) is used according to the previous A375-GFP experiments. GFP-tagged A375 cells and mcherry-tagged M0 cells are cocultured (Table 5.2). The mobility and viability of the cells are observed using a Nikon Ti-E inverted microscope. Fluorescence images are analyzed by using ImageJ. Bioprinter specifications are set as follows for bioprinting.

- Nozzle size: 20G
- Nozzle speed: 5 mm/s

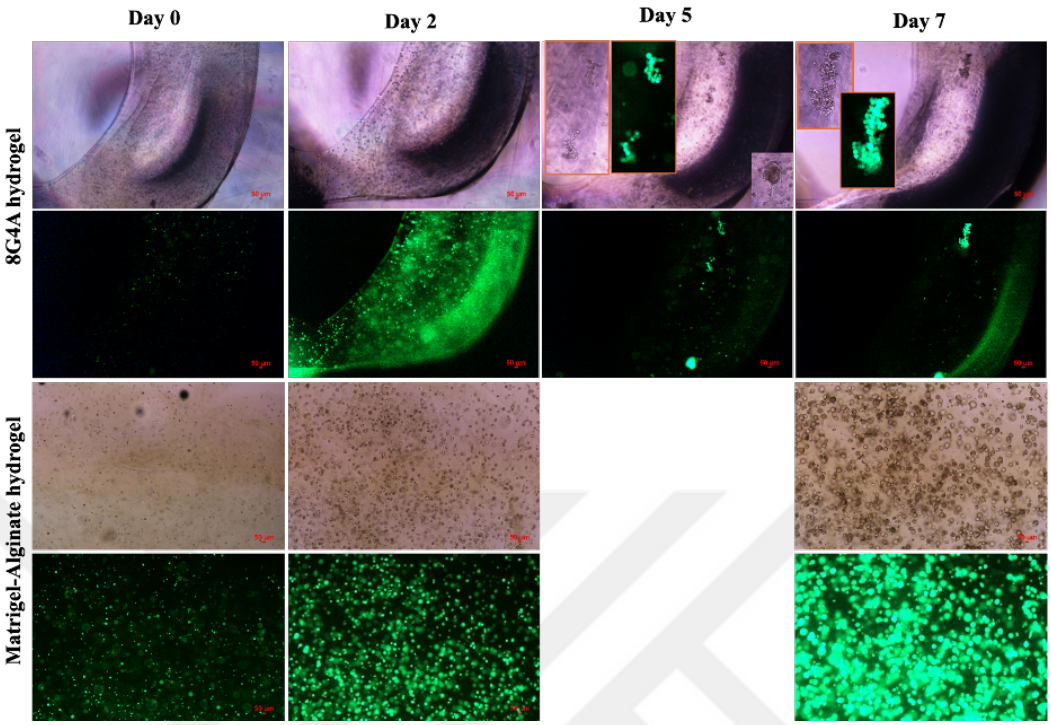


Figure 5.7. Growth of cells within gelatin-based vs Matrigel-based hydrogel.

- Pressure ≈ 2 psi
- Layer height: 0.25 mm
- Scaffold height: 1mm
- Hydrogel: 8% gelatin and 4% alginate

The same growth medium is chosen since they are cocultured in a scaffold. Both M0-mecherry cells and A375-GFP cells are grown in the RPMI-1640 medium.

M0-mcherry cells are removed from the plate by using PBS-EDTA and PBS. They are in ice-cold PBS-EDTA kept for half an hour. Then, the cells are collected by using a cell scraper. Several experiments are done to optimize the parameters and avoid contamination. Before each experiment, cell counting is done to arrange the cell density in the hydrogel. M0-cherry and A375-GFP cells are diluted to 1×10^6 viable cells, the medium is removed from the cells, and then mixed with hydrogel, resulting in 1×10^6viable cells per mL hydrogel (which can be said bioink). After the scaffold is printed, cells are crosslinked with $CaCl_2$ by incubating for 10 minutes in the incubator.

Then, the RPMI-1640 medium is put on the scaffold to grow the cells and is left for at least 3 days.

To sum up, all 7 experiments failed to observe the coculture of THP-1-mcherry, M0-mcherry and A375-GFP cells and their responses to each other. After that, the RPMI-1640 medium was changed to DMEM medium for both A375 and THP-1 cell growth. The reason for the deterioration is the RPMI-1640 medium, which doesn't contain $CaCl_2$ inside which helps to crosslink and provide stability to the gelatin-alginate hydrogel.

Table 5.2. Co-culturing Experiments of A375-GFP with differentiated M0-mCherry cells in RPMI.

Experiment	**M0-mCherry viability**	**A375-GFP viability**	**Result**
Exp. 1	4.6×10^5 viable cells, 65% viability	1×10^6 viable cells, 85% viability	All the scaffolds are contaminated. Contamination occurs due to $CaCl_2$. Fresh 0.1 M $CaCl_2$ is prepared and autoclaved. Another hydrogel is also prepared.
Exp. 2	9.5×10^5 viable cells, 63% viability	2×10^6 viable cells, 93% viability	All scaffolds are deteriorated after 3 days and contaminated after 5 days. Hydrogel has too many air bubbles, which may cause deterioration. The fresh hydrogel is prepared. PBS-EDTA and $CaCl_2$ solutions are filtered using a 0.22 μm sterile filter.
Exp. 3	–	–	To reduce contamination, bioink is printed in a $CaCl_2$ solution. However, the hydrogel cannot adhere to the plate and agglomerates during printing.
Exp. 4	3.1×10^5 viable cells, 31% viability	3.5×10^6 viable cells, 93% viability	Even on day 0, the scaffold began to crack from the outer sides. Contamination was not observed in this experiment. However, the scaffolds were completely deteriorated after 3 days. It was assumed that EDTA has a role in the deterioration of the scaffold. To reduce the EDTA effect, the cells were washed only with PBS before use.
Exp. 5	2.8×10^5 viable cells, 60% viability	3×10^6 viable cells, 95% viability	Even on day 0, the scaffold begins to crack from the outer sides. The fluorescence of M0 cells is difficult to identify even on day 0.

Table 5.2. Co-culturing Experiments of A375-GFP with differentiated M0-mCherry cells in RPMI. (cont.)

Experiment	**M0-mCherry viability**	**A375-GFP viability**	**Result**
Exp. 6	–	–	M0-mCherry cells were removed from the plate using only PBS solution. M0 cells were kept for half an hour in ice-cold PBS and then collected using a cell scraper. At the end of 3 days, the scaffolds were completely deteriorated. Contamination did not occur.
Exp. 7	THP-1, 2×10^6 viable cells, 80% viability	3×10^6 viable cells, 95% viability	Both A375-GFP and THP-1-mCherry cells increased their volume and proliferated. On day 0, cells were small and individually spread in hydrogel. Small cracks occurred on the hydrogel edges. By day 3, cells grew larger and proliferated, with increased fluorescence intensities. Cracks deepened, leading to deterioration. By day 6, A375-GFP cells accumulated and formed large clusters, whereas THP-1-mCherry cells created smaller clusters, suggesting differential cell behavior within the hydrogel. This difference may be attributed to the highly proliferative and invasive nature of A375 cells, enabling them to rapidly dominate the microenvironment, while THP-1-mCherry cells remained more localized. By day 6, the hydrogel was completely deteriorated.

5.3.2. Coculturing (GFP-tagged A375 Cells and Nondifferentiated and Differentiated mCherry-tagged THP-1 Cells) on 3D (8G4A scaffold) with DMEM Medium

Hydrogel containing 8% gelatin w/w and 4% alginate w/w is used for these experiments according to the previous A375-GFP experiments. GFP-tagged A375 cells and mcherry-tagged M0 cells are cocultured in these experiments. The mobility and viability of the cells are observed using a Nikon Ti-E inverted microscope. Fluorescence images are analyzed by using ImageJ.

5 different types of growth procedures are applied in these experiments, but at the end, a complete DMEM medium is put onto a scaffold for cells to use. These experiments are explained below:

- DMEM M0 + DMEM rest: In this procedure, THP-1-mcherry cells are differentiated with PMA in DMEM medium for 1 day, and the cells rest in complete DMEM medium again for 2 days. These cells are mixed with hydrogel and the scaffold is printed only with these M0-mcherry cells. The scaffold is incubated with DMEM complete medium.
- RPMI M0 + DMEM rest: In this procedure, THP-1-mcherry cells are differentiated with PMA in RPMI-1640 medium for 1 day, and the cells rest in complete DMEM medium again for 2 days to adjust the cells to DMEM medium. These cells are mixed with hydrogel, and the scaffold is printed only with these M0-mcherry cells. The scaffold is incubated with DMEM complete medium.
- RPMI M0 + RPMI rest + DMEM A375: In this procedure, THP-1-mcherry cells are differentiated with PMA in RPMI-1640 medium for 1 day, and the cells rest in complete RPMI-1640 medium again for 2 days, as the standard procedure. A375-GFP cells are cultured in their standard complete DMEM medium. These cells are mixed with hydrogel, the scaffold is printed with two different cells, and coculture is incubated with a complete DMEM medium.
- RPMI M0 + DMEM rest + DMEM A375: In this procedure, THP-1-mcherry cells

are differentiated with PMA in RPMI-1640 medium for 1 day, and the cells rest in complete DMEM medium again for 2 days to adjust the cells to DMEM medium. A375-GFP cells are cultured in their standard complete DMEM medium. These cells are mixed with hydrogel, the scaffold is printed with two different cells, and coculture is incubated with a complete DMEM medium.

- DMEM M0 + DMEM rest + DMEM A375: In this procedure, THP-1-mcherry cells are differentiated with PMA in DMEM medium for 1 day, and the cells rest in complete DMEM medium again for 2 days. A375-GFP cells are cultured in their standard complete DMEM medium. These cells are mixed with hydrogel, the scaffold is printed with two different cells, and coculture is incubated with a complete DMEM medium.

Results are summarized in Table 5.3.

Table 5.3. Coculture experiments by using DMEM medium for scaffold incubation.

Experiment	**Cell types**	**THP-1 differentiation medium**	**M0 rest medium**	**Scaffold medium**	**Results % Viability**
Exp. 1	M0	DMEM	DMEM	DMEM	0%
Exp. 2	M0	RPMI-1640	DMEM	DMEM	0%
Exp. 3	M0-mCherry + A375-GFP	RPMI-1640	RPMI-1640	DMEM	64.4%
Exp. 4	M0-mCherry + A375-GFP	RPMI-1640	DMEM	DMEM	30%
Exp. 5	M0-mCherry + A375-GFP	DMEM	DMEM	DMEM	28%

These experiments are run simultaneously. Cell counting for M0-mcherry and A375-GFP cells is done before the bioink is prepared. Bioprinter settings are the same as explained in Section 5.1.1. The scaffolds maintain their structure for at least 10 days.

Cell counting for differentiated THP-1 cells (M0-mCherry cells) in different media and for A375-GFP cells in complete DMEM medium is given in the table below (see Table 5.4).

Table 5.4. Cell counting for THP-1 cells.

Condition	**Viable cell number**	**Viability (%)**
RPMI M0 + RPMI rest	8.5×10^5	73
RPMI M0 + DMEM rest	5.9×10^5	54
DMEM M0 + DMEM rest	8.3×10^5	47
A375 (DMEM)	4.4×10^6	93

The viability of M0-mcherry cells is the least when THP-1-mcherry is differentiated in a DMEM medium, which is reasonable since differentiation in a DMEM medium is not the standard protocol for the THP-1 cells. The pictures of the progress of the incubation in scaffolds are given in the Appendix A. Experiment results are explained in the following paragraphs.

For all experiments, bright field and fluorescence pictures are taken for days 0, 2, 4, 7, 9, and 13. The hydrogel keeps its stability for more than 14 days. However, it starts to crack from the top of the hydrogel after 9 days. Cells are placed in 3 dimensions within the hydrogel, so there are different focuses to investigate the cells in the z-direction while investigating through the microscope.

M0-mcherry cells don't grow, so the fluorescence of M0 cells decreases over time, meaning the viability of cells decreases. Yet, several cells have red fluorescence, and they may be viable after 14 days (Appendix A) meaning gelatin-alginate hydrogel is biocompatible with M0 cells. However, the viability test shows 0% viability for M0 cells after 14 days.

At the end of 14 days of coculture, a cell viability test with Thermo-Fisher L3224 is applied to the scaffold. The kit contains calcein-AM for dyeing viable cells and ethidium homodimer-1 for dyeing dead cells. After waiting for the scaffold for 15 minutes in an incubator, viable cells fluoresce green while dead cells fluoresce red under a fluorescence microscope.

At the end of the 14 days of coculture in the hydrogel (8% gelatin w/w and 4% alginate scaffold), the fluorescence intensity of both A375-GFP and M0 cells are decreased. Previously, it was reported that the fluorescence intensity and the number of A375-GFP cells were increased when it was incubated for 10 days in a gelatin/alginate hydrogel. Contrarily, when A375-GFP cells are cocultured with M0 macrophage-like cells, the number of cells doesn't increase. So, it can be said that the presence of M0 cells blocks the increase in the number of A375 cells. The viability at the end of the experiment decreased for M0-mcherry and A375-GFP cells to roughly 30% (visually observed). Since the viability of M0 cells decreased to 0, the viable cells must be the A375 cells. Also, since both cell types are tagged with green or mCherry fluorescence protein, these results may be misleading.

Monoculture and coculture of A375 and M0 cells in 3D environment with different treatments are investigated within both 8G4A and matrigel-alginate hydrogels. Matrigel-only or matrigel-collagen are not chosen for these experiments due to the lack of stability of the scaffold; rather, alginate is added to the matrigel to increase the durability. The comparison of 8G4A and matrigel-alginate hydrogels is given in Table 5.5 and Figure 5.8.

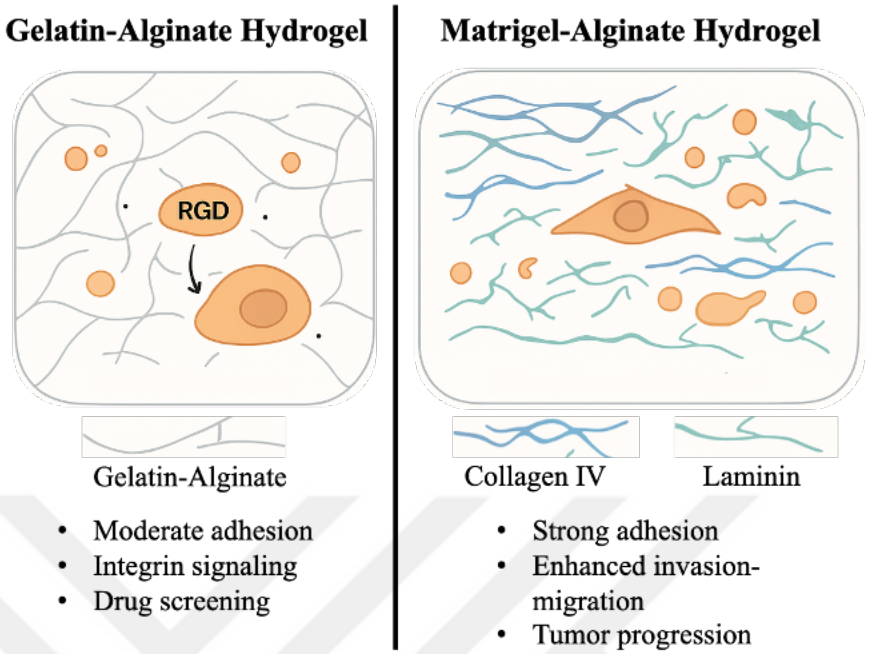


Figure 5.8. Comparison of gelatin–alginate and Matrigel–alginate hydrogels showing how A375 cells interact differently with gelatin–alginate vs. Matrigel–alginate.

Table 5.5. Comparison of gelatin–alginate and Matrigel–alginate hydrogels.

Feature	**Gelatin–Alginate**	**Matrigel–Alginate**
Composition	Gelatin (unfolded collagen with RGD motifs) + alginate (structural support)	Matrigel (laminin, collagen IV, entactin, growth factors) + alginate (structural support)
Cell adhesion	RGD motifs in gelatin provide moderate adhesion	Laminin and collagen IV integrin-binding domains provide strong adhesion
Growth factors	N/A	EGF, TGF-β, bFGF, VEGF
Biological complexity	Low (reproducible)	Complex (rich but variable biochemicals)
Tunable properties	High tunability of stiffness and degradability	Low tunability
Reproducibility	High, consistent batches	Low, variability in batches
Cost	Low	High
Advantages	Mechanobiology can be modeled; ECM stiffness effects can be observed; adhesion can be supported without overstimulation; suitable for high-throughput assays	More suitable to tumor microenvironment; invasion, spheroid formation, angiogenesis can be promoted; relevant for drug resistance and metastasis studies
Best application	Mechanistic studies of integrin signaling, stiffness response, controlled drug screening	Tumor progression models, invasion/migration assays, angiogenesis and drug resistance studies

6. TREATMENT STRATEGIES

To better understand the effects of phytochemicals, like curcumin, chemotherapeutic agents, like temsirolimus and AuNP, and their synergistic effects in a more physiologically similar environment, the study is extended from 2D cultures to 3D platforms. Based on optimization experiments, two hydrogel are selected for their ability to provide a stable and biologically supportive microenvironment: Matrigel-alginate (75% v/v Matrigel and 25% v/v alginate (prepared 1% w/w alginate in PBS solution)) and 8G4A (8% w/w gelatin and 4% w/w alginate in PBS solution). These hydrogels are used to encapsulate A375 melanoma cells (A375-GFP and A375-WT) and THP-1-derived M0 macrophages (M0-GFP and M0-WT) to simulate the immune component of tumors and their co-culture. They are tested in both well-based encapsulation and bioprinted scaffold formats to evaluate how structural organization influences cell behavior and treatment response.

6.1. Treatment In Hydrogel (3D in 96-well plates)

In this section, the impact of these treatments on A375 melanoma cells, M0 macrophages and their coculture within a 3D hydrogel matrix is investigated by creating 3D matrix in a 96-well plate. The hydrogel for encapsulation is selected as Matrigel-alginate composite (75% v/v Matrigel and 25% v/v alginate (prepared 1% w/w alginate in PBS solution)). This hydrogel is chosen to provide a biologically supportive extracellular matrix-like structure. Optimization experiments showed that Matrigel alone and Matrigel-collagen mix do not provide sufficient stabilization to the scaffold, so alginate is preferred to mix with Matrigel. After hydrogel preparation, cells are mixed with the hydrogel, hereafter called bioink, and seeded into a 96-well plate. Bioink in the wells is crosslinked using $CaCl_2$ incubation for 10 minutes to stabilize the alginate within the bioink and provide stability.

Following the crosslinking, different treatments are applied, including AuNP, temsirolimus, curcumin, thymoquinone and their conjugations and combinations.

- AuNP (1 nM),
- Temsirolimus (500 nM and 4 nM),
- AuNP (1 nM) + temsirolimus (500 nM),
- Curcumin (500 uM),
- Curcumin (500 uM) + temsirolimus (500 nM),
- Curcumin (500 uM) + AuNP (1 nM),
- Curcumin (500 uM) + temsirolimus (4 nM).

The cytotoxic and metabolic effects of these treatments are assessed on days 1, 3, 5, and 7 using AO/PI staining to evaluate cell viability and H_2DCFDA to evaluate ROS. This study aims to compare the drug responses in 3D cultures with previous 2D findings and to determine the influence of the hydrogel microenvironment on treatment efficacy.

6.1.1. A375 in Matrigel-Alginate Hydrogel in 96 Well-Plates

A375-WT cells (1×10^6 cells/mL, 93% viability) are mixed with Matrigel-alginate hydrogel (75% v/v Matrigel + 25% v/v alginate), and the bioink is placed in a 96-well plate and crosslinked with $CaCl_2$ for 10 minutes in the incubator. The medium mixed with various treatments is added to the wells on the hydrogel. The viability of the cells on the first, third, fifth, and seventh days of treatment is investigated by using the AO/PI viability test. The fluorescence pictures are processed by using ImageJ. The viability is assessed in two ways: cell count-based and fluorescence area-based, as explained in Chapter 2. Some of the data is missing because the hydrogel deteriorated during the experiments.

The fluorescence area-based results are more reliable for the control group and AuNP-treated groups since A375 cells proliferate and create clusters as time passes,

and they are counted as one cell by ImageJ, which leads to a loss of data. On the other hand, other treated cells can be counted as they do not create any clusters.

Viability is assessed using acridine orange and propidium iodide dual staining, as this assay reports membrane integrity as a proxy for cell survival. However, it is important to note that PI-positive cells include both necrotic and late-apoptotic populations. As such, this method detects undergoing apoptosis that are not yet completely degraded or metabolically inactive [225]. Conversely, AO-positive cells with intact membranes may still be in early stages of apoptosis or under sublethal stress. Therefore, AO/PI staining reflects a snapshot of membrane integrity rather than definitive live-dead classification, and some treatment groups may contain a significant proportion of transitional or pre-lethal cells.

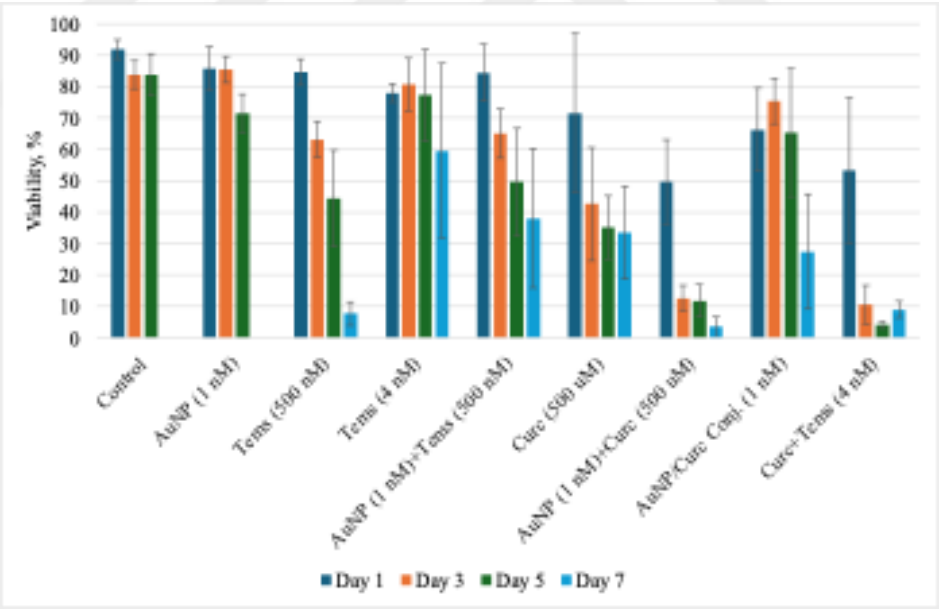


Figure 6.1. Viability of A375–WT cells with respect to time for all treatments.

Throughout the 5-day treatment period, the viability of the control group and the AuNP-treated (1 nM) A375-WT cells remained above 80% and 70% respectively, which suggests the Matrigel-alginate hydrogel provides a supportive and biocompatible environment for melanoma cells (Figure 6.1). These results are consistent with previous studies indicating the biocompatibility of low-concentration AuNP [226], the 1 nM

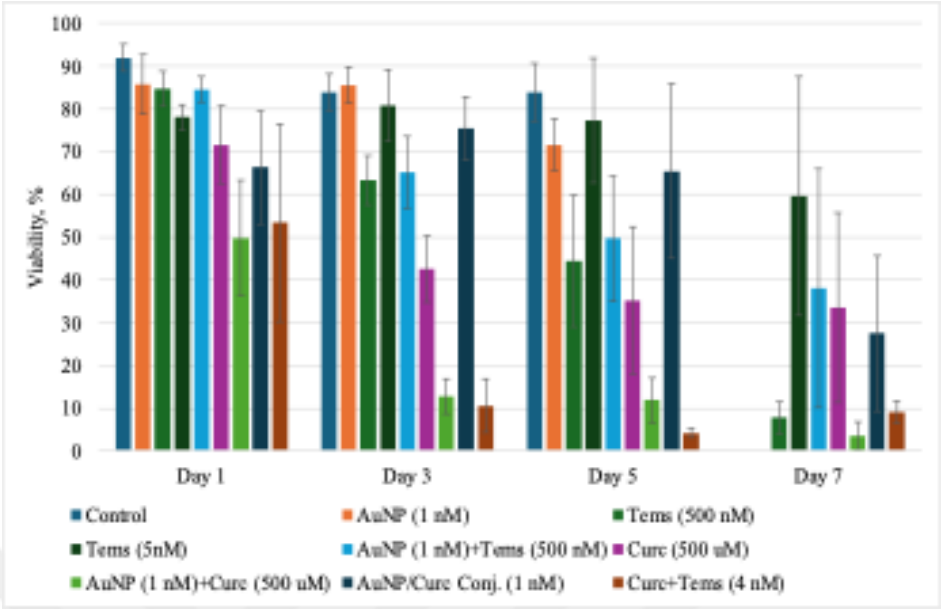


Figure 6.2. Viability with respect to treatment types for each day analysis.

AuNP treatment shows minimal cytotoxicity toward A375-WT cells.

High viability with AuNP treatment can be investigated through interconnected biological and physicochemical reasons. First of all, the surface chemistry and the ability to protein adsorption of AuNPs can enhance the viability through forming a protein corona within the medium, which can mimic the ECM components and/or growth factors, enhancing the cell adhesion, spreading, and survival [227, 228] (protein corona: a multilayer of proteins around AuNPs by adsorption and accumulation [229]). The positively charged surface of AuNPs can interact with negatively charged ECM components, like alginate, which modulate the stiffness and porosity of the hydrogel, indirectly promoting cell proliferation and migration [230]. AuNPs are efficiently internalized by cancer cells, including A375, via endocytosis [231]. Once inside the cell, AuNPs localize in the cytoplasm and may interact with organelles without causing acute toxicity [232]. These interactions can subtly influence gene expression, metabolic activity, and proliferation, especially in 3D environments where spatial constraints and matrix signaling shape cell behavior [233]. Also, in 3D matrices, AuNPs can facilitate the formation of more stable tumor spheroids or microtumor structures. The resulting spheroid architecture enhances cell-cell interactions and paracrine signaling, both of

which contribute to improved survival and proliferation in 3D culture systems [234,235].

In contrast, temsirolimus exhibits a cytotoxic effect during the treatment, reducing cell viability progressively. Temsirolimus is a well-known inhibitor of the mammalian target of rapamycin complex 1 (mTOR1), a key regulator of cellular growth, protein synthesis, and survival. It inhibits the hyperactive PI3K/Akt/mTOR signaling in melanoma cells, leading to reduced phosphorylation of S6 kinase and 4E-BP1, which are downstream targets of mTOR [236], and inducing the cell cycle arrest in G1 phase [237]. When temsirolimus is co-administered with AuNPs, the cytotoxic effect of temsirolimus does not change much until the 7th day of treatment. On the 7th day, co-administered cells have more viability. While AuNPs can serve as carriers or bioactive agents themselves, their combination with temsirolimus in this context appears to attenuate the drug's cytotoxic efficacy. This finding contradicts previous studies reporting that nanoparticle-based delivery systems can enhance the cellular uptake and therapeutic efficacy of mTOR [238]. One possible explanation is that AuNPs interact with temsirolimus altering the drug's availability or uptake. For example, the formation of protein corona or adsorption of temsirolimus onto the AuNP surface could reduce the free, bioactive concentration of the drug, so limiting its access to intracellular mTOR complexes. Additionally, since AuNP alone has mild prosurvival signaling on melanoma cells, it may transiently buffer cells against the full metabolic stress induced by mTOR inhibition on the 7th day.

Curcumin also demonstrates a notable inhibitory effect on A375-WT cells, with viability decreasing by 42% as early as day 3 and remaining relatively stable thereafter. A more drastic decrease in viability is observed when curcumin and AuNPs are administered simultaneously, reducing the cell viability to 12% by day 3 (Figure 6.1). These results are supported by the earlier studies showing that AuNPs can enhance the solubility and intracellular bioavailability of hydrophobic compounds like curcumin, thereby increasing their anticancer activity [226, 239].

Curcumin is a polyphenolic compound known to exert antiproliferative and pro-apoptotic effects in various cancer cells, including melanoma. In A375 cells, curcumin has been shown to suppress multiple oncogenic signaling pathways, notably the NF-κB, PI3k/Akt, and MAPK pathways [240, 241]. Inhibition of these pathways reduces transcription of survival-promoting genes such as Bcl-2, cyclin D1, and VEGF, while promoting ROS generation [56], mitochondrial dysfunction, and activation of intrinsic apoptosis [242]. The outcome is a significant reduction in cell viability, often in a dose- and time-dependent manner.

The combination of AuNPs and curcumin results in a more pronounced reduction in A375 cell viability compared to curcumin alone, suggesting an additive or synergistic cytotoxic effect. Curcumin exerts anticancer activity by inhibiting key pro-survival pathways such as PI3k/Akt, NF-κB, and MAPK, while promoting oxidative stress, mitochondrial dysfunction and apoptosis [240]. When co-administered with AuNPs, several factors may enhance curcumin's efficacy. AuNPs are known to increase cellular membrane permeability and facilitate endocytic uptake, potentially promoting intracellular accumulation of curcumin. Moreover, both AuNPs and curcumin independently induce ROS, and their combined treatment may amplify oxidative stress to cytotoxic levels. However, the interaction between curcumin and the protein corona formed on AuNP surfaces could also alter drug availability or release kinetics, possibly modulating the timing and magnitude of the intracellular response [227].

Treatment with curcumin-conjugated AuNP provides a similar cytotoxic response, reducing cell viability to approximately 30% by day 7, however it is not as effective as curcumin alone or co-administered with AuNP. When curcumin is conjugated to AuNPs (AuNP/Curc cnjg.), several factors may alter its biological effect. On one hand, AuNPs can enhance cellular uptake of curcumin due to increased membrane interaction and endocytosis [239]. On the other hand, the conjugation chemistry, released kinetics and protein corona formation may hinder the timely release of free curcumin inside the cell. If curcumin is bound too tightly to the nanoparticle surface or released too slowly, its intracellular bioactivity may be reduced compared to free curcumin [243]. Moreover,

AuNPs themselves can mildly affect redox balance or induce cell stress responses that may either synergize or counteract curcumin's cytotoxic effects, depending on concentration and exposure time.

The combination of curcumin and temsirolimus demonstrates the most rapid and potent cytotoxic response. Cell viability decreases to 52% within the first 24 hours and drops to 10% in the following days (Figure 6.1), indicating a potential synergistic interaction between the two agents. Such synergy has been investigated in previous studies, where curcumin is found to enhance the anticancer efficacy of various chemotherapeutic drugs, including mTOR inhibitors, through multiple mechanisms such as inhibition of NF-κB and PI3K/Akt signaling [244, 245].

Treatment with a lower concentration of temsirolimus alone does not result in a significant decrease in viability throughout the 7-day treatment period (Figure 6.1), reinforcing the notion that combination therapies are more effective in overcoming melanoma cells' resistance mechanisms.

Among all the treatment groups, AuNP+curcumin, including the conjugated ones, and curcumin+temsirolimus coadministration exhibit the strongest and fastest cytotoxic effects on A375-WT cells, highlighting their therapeutic potential (Figure 6.2).

6.1.2. M0 in Matrigel-Alginate Hydrogel in 96 Well Plates

M0-WT cells (1×10^6 cells/mL, 70% viability) are mixed with Matrigel-alginate hydrogel (75% v/v Matrigel + 25% v/v alginate), and the bioink is placed in a 96-well plate and crosslinked with $CaCl_2$ for 10 minutes in the incubator. The medium mixed with various treatments is added to the wells on the hydrogel. The viability of the cells on the first, third, fifth, and seventh days of treatment is investigated by using the AO/PI viability test. The fluorescence pictures are processed by using ImageJ. The viability is assessed in two ways: cell count-based and fluorescence area-based. Some of the data is missing because the hydrogel deteriorated during the experiments.

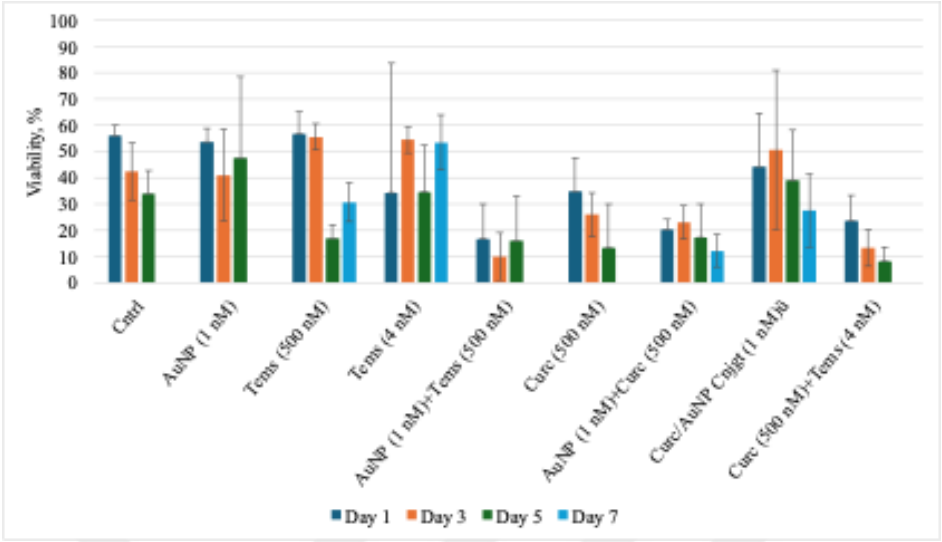


Figure 6.3. Cell count-based viability results of M0 cells in Matrigel-alginate hydrogel.

M0 macrophages are undifferentiated (naïve) macrophages and derived here from THP-1 Monocyte cell lines. Even with macrophage colony-stimulating factor (M-CSF), most macrophages will survive but not divide significantly in culture. Since M0-WT cells are non-proliferative and do not form clusters under culture conditions, cell count-based viability assessments are considered more robust and representative in evaluating cytotoxic effects.

In the control and AuNP-treated groups, viability decreased gradually over five days to 35% and 45%, respectively (Figure 6.3). Considering that the initial viability prior to hydrogel encapsulation is around 70%, this decrease corresponds to an approximate 50% reduction in viable cells by day 7. These findings indicate that the Matrigel-alginate hydrogel itself does not fully preserve long-term viability in M0 cells, and AuNPs at the low concentration do not exhibit significant cytotoxicity.

Temsirolimus (500 nM) treatment alone resulted in a substantial decrease in cell viability, reducing it to approximately 30% by day 7 (Figure 6.3). This aligns with previous findings showing that mTOR inhibition induces apoptosis in monocyte-derived macrophages (M0), particularly through mTOR1 pathway suppression [246]. When temsirolimus is co-administered with AuNPs, a rapid and enhanced cytotoxic

response is observed (Figure 6.3), viability dropped to 15% after just 24 hours, which suggests potential synergistic or delivery-enhancing effects of the nanoparticle. Low concentration of temsirolimus (4 nM) has a mild cytotoxic effect on M0 cells.

Curcumin exhibited pronounced toxicity toward M0-WT cells, decreasing viability to 35% within the first 24 hours of exposure. This supports prior studies that demonstrated curcumin's pro-apoptotic and anti-inflammatory effects in monocytes/macrophages via NF-κB and MAPK pathway inhibition [247]. The cytotoxicity becomes more severe when curcumin is co-administered with AuNPs, with viability decreasing to 20% after 24 hours and further 10% by day 3, indicating approximately 85% total reduction. This sharp decline suggests a potential additive and synergestic mechanism between curcumin and AuNPs, possibly due to the enhanced cellular uptake or reactive oxygen species (ROS) generation [248]. In conjugated form (Cu-AuNPs), the cell viability is slightly less than 30% on day 7. Interestingly, treatment with AuNP-conjugated curcumin resulted in a milder response, with viability ranging between 40–50% by day 5. This suggests that the release kinetics or bioavailability of curcumin may be altered when conjugated to nanoparticles, reducing its immediate cytotoxic potential. Curcumin has multiple functional groups (keto-enol, phenol, etc.) responsible for its bioactivity. When curcumin is covalently or strongly bound to the AuNP surface, these groups might be blocked or altered, reducing its ability to interact with biological targets (e.g., proteins, enzymes, cell membranes) or to enter cells through passive diffusion. In contrast, free curcumin retains all its reactive functionalities and can interact more freely with cellular components. Moreover, conjugated curcumin may experience reduced uptake due to steric effects, i.e., bulky AuNPs may limit curcumin's ability to penetrate the cell membrane. Surface charge or aggregation may be another obstacle. Conjugates alter the surface charge or induce aggregation, reducing cellular internalization. Free curcumin, especially when co-administered with AuNPs, might still benefit from membrane interaction enhancement by AuNPs without being hindered by them. In conjugated systems, curcumin may be tightly bound and not released efficiently inside the cell, especially if there's no stimuli-responsive linker (e.g., pH-sensitive or redox-cleavable). In co-administration, curcumin is freely

diffusible, and AuNPs might help destabilize the cell membrane or act synergistically in other ways. In conjugated systems, if the loading is low, the effective dose of curcumin may be much lower than its co-administered free form. In co-administration, both components are independently bioavailable, possibly achieving higher local concentrations. Conjugates might suffer from stability problems in physiological conditions (e.g., salt-induced aggregation). Aggregated Cur-AuNPs might be less bioavailable or more quickly cleared [249]. In conclusion, Curcumin conjugation may limit its bioavailability and interaction with targets, whereas co-administration allows both curcumin and AuNPs to act independently and possibly synergistically, leading to greater cytotoxicity or therapeutic effect [239].

Among all tested combinations, curcumin combined with 4 nM temsirolimus proved to be the most cytotoxic, completely eliminating most viable cells. Lower concentrations of temsirolimus, however, demonstrated variable and generally lower toxicity—an effect likely influenced by cellular resistance mechanisms and mTOR pathway dynamics in non-dividing M0 macrophages. Furthermore, curcumin either coadministered or conjugated with AUNPs seems to lessen viability.

6.1.3. ROS Analysis

To evaluate oxidative stress responses, intracellular reactive oxygen species (ROS) levels are assessed in both A375 melanoma cells and M0 macrophages following treatment with AuNP, temsirolimıs, curcumin, their binary combinations and curcumin-conjugated AuNP. The procedure for ROS staining and imaging is detailed in Section 3.6. ROS analysis is conducted on days 1, 3, 5, and 7 using fluorescence imaging within the hydrogel environment. However, technical challenges during washing steps, particularly the incomplete removal of ROS detection solution, compromised image quality, resulting in strong background signals, most notably on days 3 and 7. Similarly, imaging on days 1 and 5 is affected by residual background signal and limited hydrogel permeability, which may impact the reliability and quantifiability of the results. While the dataset offers preliminary insights into treatment-induced oxidative patterns, in-

terpretations should be made with caution due to these procedural constraints.

AuNP treatment on M0 cells results in relatively stable viability, indicating low inherent cytotoxicity. However, ROS analysis reveals a high percentage of ROS+ cells on day 1 (72%, Figure 6.4), and although this drops to 35% by day 5, the mean ROS intensity increased significantly (Figures 6.5 and **??**), implying that a smaller subset of cells experienced severe oxidative stress over time. This may reflect low-grade, sustained redox imbalance induced by AuNPs via endosomal accumulation and membrane interactions [250]. Despite this, most macrophages appear resilient to such stress, suggesting ROS levels are not sufficient to trigger widespread death.

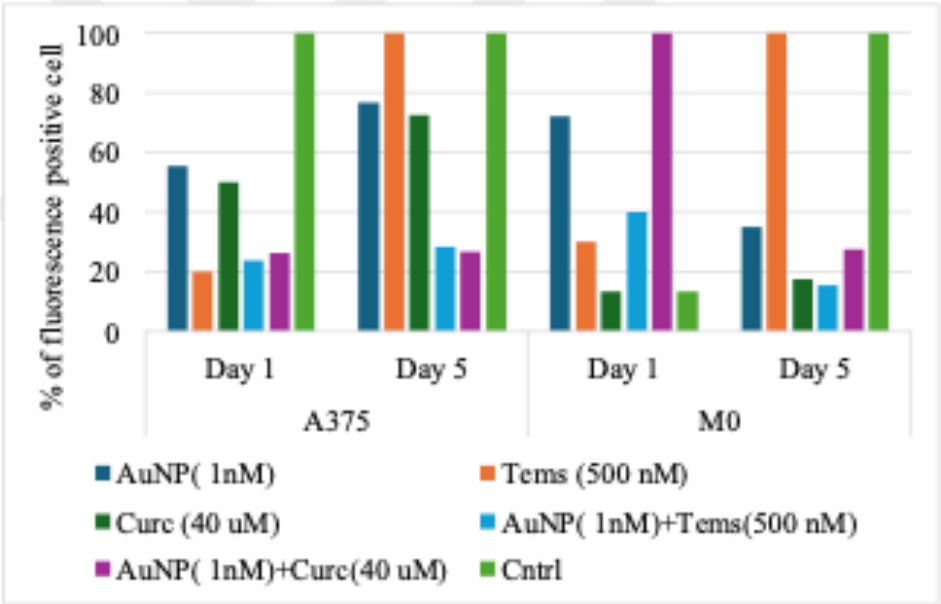


Figure 6.4. Fluorescence signal positive cells ratio to all cells in 3D - 96 well plates.

Temsirolimus-treated M0 cells maintain high viability on days 1 and 3, followed by a sharp decline on day 5 (Figure 6.3). ROS analysis shows a moderate increase on day 1 (30%ROS+ cells) and 100% ROS positivity by day 5 (Figure 6.4), suggesting that oxidative stress accumulates over time as a consequence of impaired mitochondrial function and mTOR-regulated antioxidant defenses. The strong ROS signal on day 5 corresponds well with the sharp drop in viability (Figure 6.5), indicating a ROS-associated cell death mechanism, likely via mitochondrial dysfunction and apoptosis

[251, 252]. On the other the combination with AuNP produced the most dramatic loss of viability (Figure 6.3). ROS data show moderate stress on day 1 (40% ROS+ cells, Figure 6.4) but low ROS levels on Day 5 (Figures 6.4- 6.6). This suggests that cells undergoing early oxidative stress likely died before day 5, leaving a surviving population with low ROS. The strong cytotoxic effect is likely due to synergistic disruption of mitochondrial and mTOR signaling, with early ROS acting as a trigger, followed by programmed cell death pathways, possibly independent of ongoing ROS by day 5. This fits known mechanisms where combined metabolic and oxidative stress overwhelms macrophage homeostasis.

Curcumin consistently reduced M0-WT viability from 35% to 13% until day 5, indicating a ROS-independent cytotoxic effect. Correspondingly, ROS levels are very low on both days (Figures 6.5 and 6.6) This supports curcumin's well-documented antioxidant role, especially in macrophages, where it scavenges ROS and suppresses NF-κB signaling, reducing inflammatory and survival responses [241, 253]. The decline in viability likely results from non-redox mechanisms, such as cell cycle arrest, inhibition of transcriptional survival pathways, or autophagy, rather than oxidative damage [240, 253].

Viability of M0-WT cells co-administered with AuNP and curcumin steadily declines and ROS data shows 100% ROS+ cells on day 1 but a sharp decrease by day 5 (Figure 6.4). This suggests early additive pro-oxidant activity, where AuNPs override curcumin's antioxidant capacity, leading to an initial ROS increase in all cells. As macrophages succumb to stress, or adapt the environment, fewer remain ROS+ on day 5, but viability also continues to drop. This indicates a delayed ROS-independent death mechanism, possibly via inflammatory or autophagy-mediated pathways triggered by the initial stress.

A375-WT melanoma cells maintain high viability throughout the experiment (Figure 6.1), despite displaying consistently high ROS levels (100% ROS+ cells and high mean intensity on both days, Figures 6.4- 6.6). This indicates A375 cells can tol-

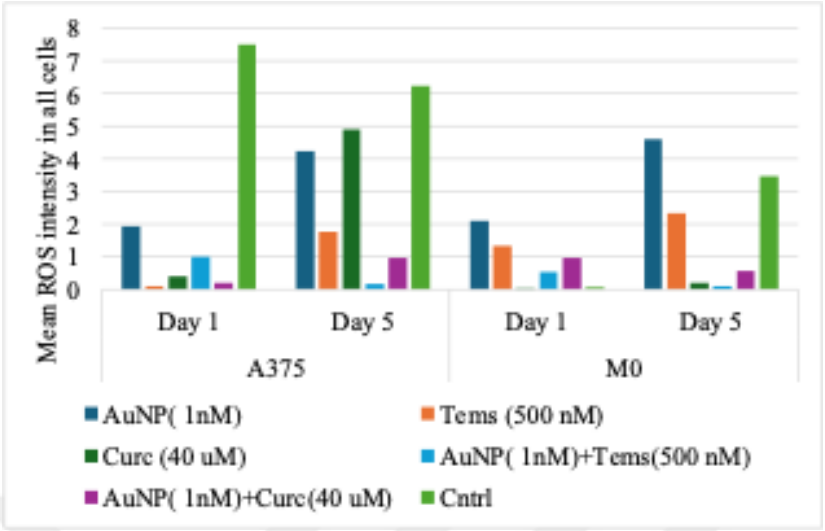


Figure 6.5. Mean ROS intensity of all cells in Matrigel-alginate hydrogel in a 96-well plate.

erate elevated endogenous oxidative stress, possibly through activation of antioxidant defense mechanisms such as Nrf2-mediated glutathione synthesis [254].

AuNP treatment alone on A375-WT induces a progressive increase in ROS intensity from day 1 to day 5, and a corresponding moderate decrease in viability. These findings are consistent with the ability of AuNPs to generate sub-lethal oxidative stress via intracellular accumulation and membrane interactions, which over time, may disrupt redox balance and initiate cell death pathways [250].

Temsirolimus treatment on A375 cells results in a delayed but profound decline in viability (Figure 6.1), coinciding with a shift from low initial ROS (both on ROS+ cells and intensity) to high ROS on day 5. This trend suggests that mTORC1 inhibition by temsirolimus may gradually impair mitochondrial homeostasis and redox regulation, eventually leading to ROS-associated apoptosis for the remained cells. In contrast, AuNP and temsirolimus co-administered cells show moderate cytotoxicity without substantial ROS induction. This suggests non-ROS-mediated cytotoxicity, likely involving metabolic stress or autophagy dysregulation without mitochondrial rupture.

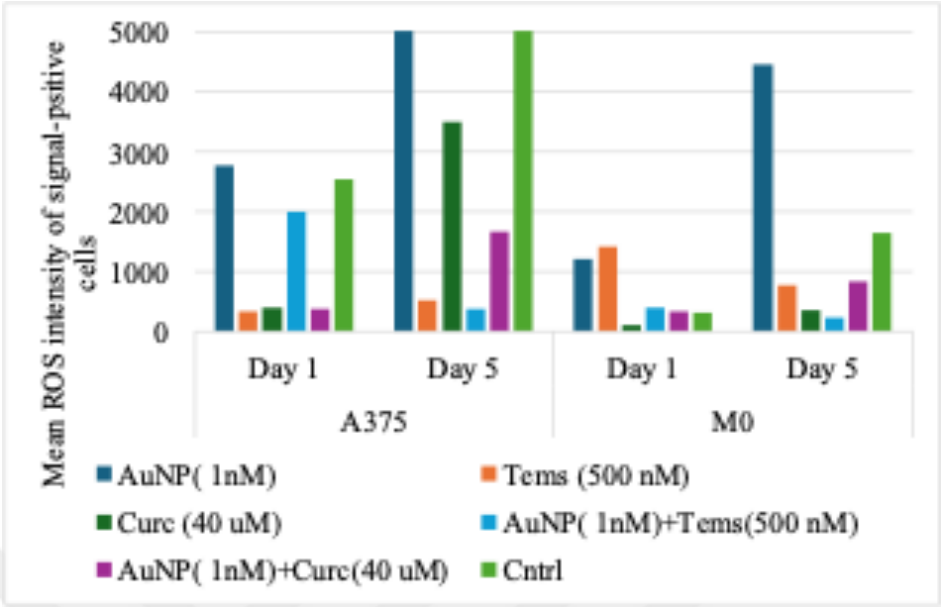


Figure 6.6. Mean ROS intensity of signal-positive cells in Matrigel-alginate in a 96-well plate (3D).

Curcumin treatment causes a marked drop in viability and is associated with a substantial increase in ROS intensity on day 5. These data support curcumin's context-dependent pro-oxidant role in cancer cells [240, 255, 256], likely mediated by mitochondrial destabilization and inhibition of survival pathways such as NF-κB.

Interestingly, co-administration of AuNP and curcumin leads to the most pronounced cytotoxicity (Figure 6.1), yet ROS positivity remains relatively low, with moderate intensity. This discrepancy suggests that curcumin and AuNPs induce an early ROS burst, followed by a rapid onset of apoptosis. The synergistic oxidative stress likely eliminates ROS-positive cells early, leaving behind a less active cell population by day 5 that is undergoing or committed apoptosis.

Overall, the data suggest that both A375 and M0 cell death is mediated by both ROS-dependent and independent mechanisms, with the severity and timing of oxidative stress playing a pivotal role. These findings will be further supported by upcoming experiments using 3D bioprinted scaffold environments, including cell-laden 8G4A and Matrigel-alginate hydrogels for both A375-WT and M0-WT.

6.2. Treatment in 3D-Bioprinted Scaffold

In this section, the time-dependent impact of these treatments on A375 melanoma cells and M0 macrophages within the 3D hydrogel matrix is investigated by creating a 3D scaffold by using a 3D bioprinter. The hydrogel for encapsulation is selected as 8G4A composite (8% w/w gelatine and 4% w/w in PBS solution), and Matrigel-alginate composite (75% v/v Matrigel and 25% v/v alginate (prepared 1% w/w alginate in PBS solution)). These hydrogels are chosen to provide a biologically supportive extracellular matrix-like structure, determined by the optimization experiments. Optimization experiments showed that Matrigel alone and Matrigel-collagen mix do not provide sufficient stabilization to the scaffold, so alginate is preferred to mix with Matrigel. Also, it is decided that 8G4A composition is more stable and supportive to cell viability than the other compositions to create 3D extracellular scaffolds.

After hydrogel preparation, cells are mixed with the hydrogel, hereafter called bioink, and transferred to the 3D bioprinter syringe. The printing parameters, such as nozzle speed, nozzle size, pressure etc., are set to previously defined values in Chapter 5. A grid-shaped scaffold is printed for each experiment. After bioprinting, the scaffolds are crosslinked using $CaCl_2$ incubation for 10 minutes to stabilize the alginate within the bioink and provide stability.

6.2.1. A375 in 8G4A Hydrogel

A375-WT cells (3.4×10^6 viable cells/mL, 92% viability) are mixed with 8G4A hydrogel as 0.5×10^6 cells per mL and loaded into a bioprinter syringe. Scaffolds are printed in petri dishes and subsequently crosslinked with $CaCl_2$ for 10 minutes in the incubator. Following crosslinking, the scaffolds are transferred into 6-well plates to reduce the medium consumption. The medium containing various treatments is added to each well, directly onto the scaffold. Cell viability is assessed on the first, third, fifth, and seventh day of incubation using AO/PI staining, and fluorescence images are analyzed using ImageJ for quantitative evaluation. ROS and rhodamine analysis are

performed and analyzed using ImageJ. The following treatments are administered to cells, mixed with the DMEM complete medium.

- AuNP (1 nM),
- Temsirolimus (500 nM)
- Temsirolimus (4 uM)
- AuNP (1 nM) + temsirolimus (500 nM)
- AuNP (1 nM) + Temsirolimus (4 uM)
- Curcumin (160 uM)
- Curcumin (40 uM)
- AuNP (1 nM) + Curcumin (160 uM)
- AuNP (1 nM) +Curcumin (40 uM)
- Thymoquinone (40 uM)
- AuNP (1 nM) + Thymoquinone (40 uM)
- Curcumin/AuNP conjugated (1 nM)
- Thymoquinone/AuNP conjugated (1 nM)
- Curcumin (160 uM) + Temsirolimus (500 nM)
- Control

The general viability results are given in Figures 6.7 and 6.8, to get early insights into the A375-WT response in the 8G4A scaffold. The results demonstrate distinct temporal patterns of cytotoxicity, reflecting the unique mechanisms of action and potential synergistic interactions among these treatments. Each treatment is explained in the following.

In untreated A375 cells cultured within the 3D-printed 8G4A scaffold, viability remains relatively stable over the course of 12 days, decreasing gradually from 88.7% (day 1) to 42% (day 12) (Figure 6.9). ROS activity is assessed by the percentage of ROS-positive cells, which stays low (18.6% by day 7, 8.1% by day 12), indicating limited oxidative stress. Rhodamine 123 fluorescence shows stable mitochondrial polarization,

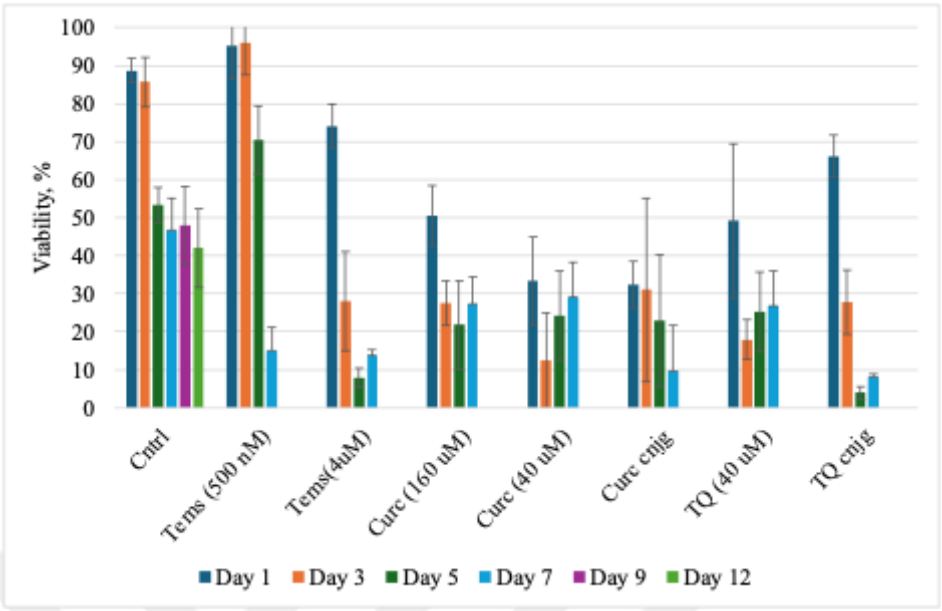


Figure 6.7. Viability results of A375-WT in 8G4A scaffold - single treatments.

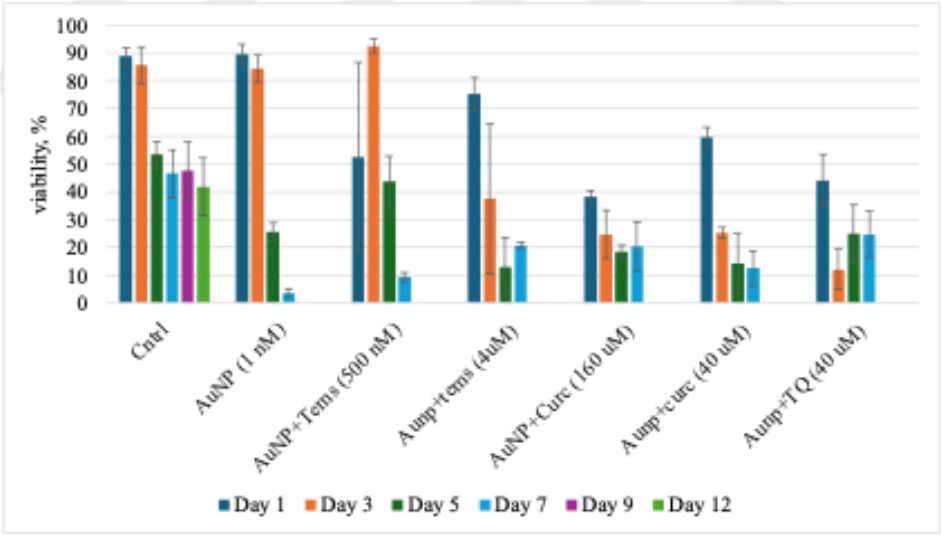


Figure 6.8. Viability results of A375-WT in 8G4A scaffold for treatments with AuNP

with signal-positive cells consistently present (Figure 6.10). These results confirm that the 8G4A scaffold provides a biocompatible 3D environment, but slow diffusion of oxygen and nutrients may contribute to progressive metabolic stress, as seen in the modest rise in ROS and gradual viability loss over time [257, 258].

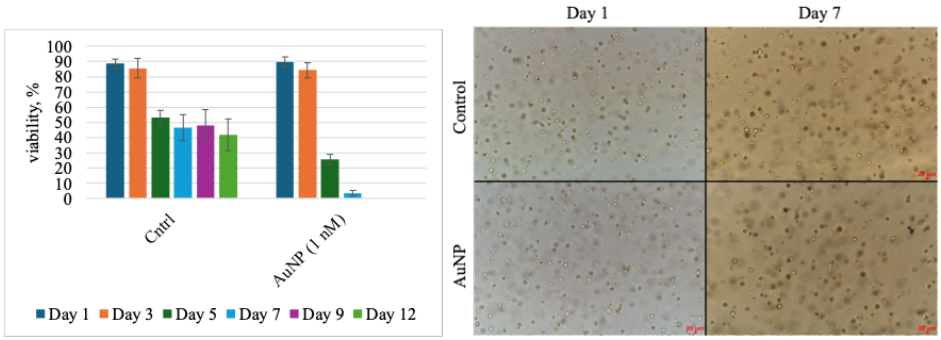


Figure 6.9. Viability of untreated & AuNP treated A375-WT in 8G4A scaffold.

AuNPs initially support viability (89% day 1), but a dramatic decline occurs by day 5 and day 7 (36%). This drop coincides with high ROS+ cell percentages on days 1 and 3 (83% and 55%, respectively), and intense rhodamine uptake at early time points, indicating strong mitochondrial polarization and subsequent dysfunction (Figure 6.10). AuNPs are known to disrupt mitochondrial homeostasis by promoting ROS generation through Fenton-like reactions and redox cycling on the particle surface, triggering apoptosis [259]. The temporal correlation between ROS burst, rhodamine signal spike, and viability collapse supports a model of early oxidative stress-induced apoptosis, particularly through mitochondrial pathways involving cytochrome c release and caspase-9 activation [260].

Free curcumin at 160 μM exhibits early cytotoxicity, with viability dropping from 50% (day 1) to 22% by day 5 (Figure 6.11). ROS levels are markedly high at all early time points, while rhodamine fluorescence peaks on day 1 and diminishes thereafter, indicating rapid mitochondrial depolarization (Figure 6.12) [261]. The lower dose (40 μM) followed a similar trend but with slightly stronger effects on day 1 and day 3.

When co-administered with AuNPs, curcumin's cytotoxicity intensifies: the Curc (160 μM) and AuNP group demonstrates higher ROS on day 1 and a corresponding viability decrease from 50% to 18.3% by day 5 (Figure 6.12), with rhodamine intensities indicating substantial mitochondrial disruption from day 3 to day 7 (since there are some technical problems, rhodamine intensities of day 1 and day 5 data cannot

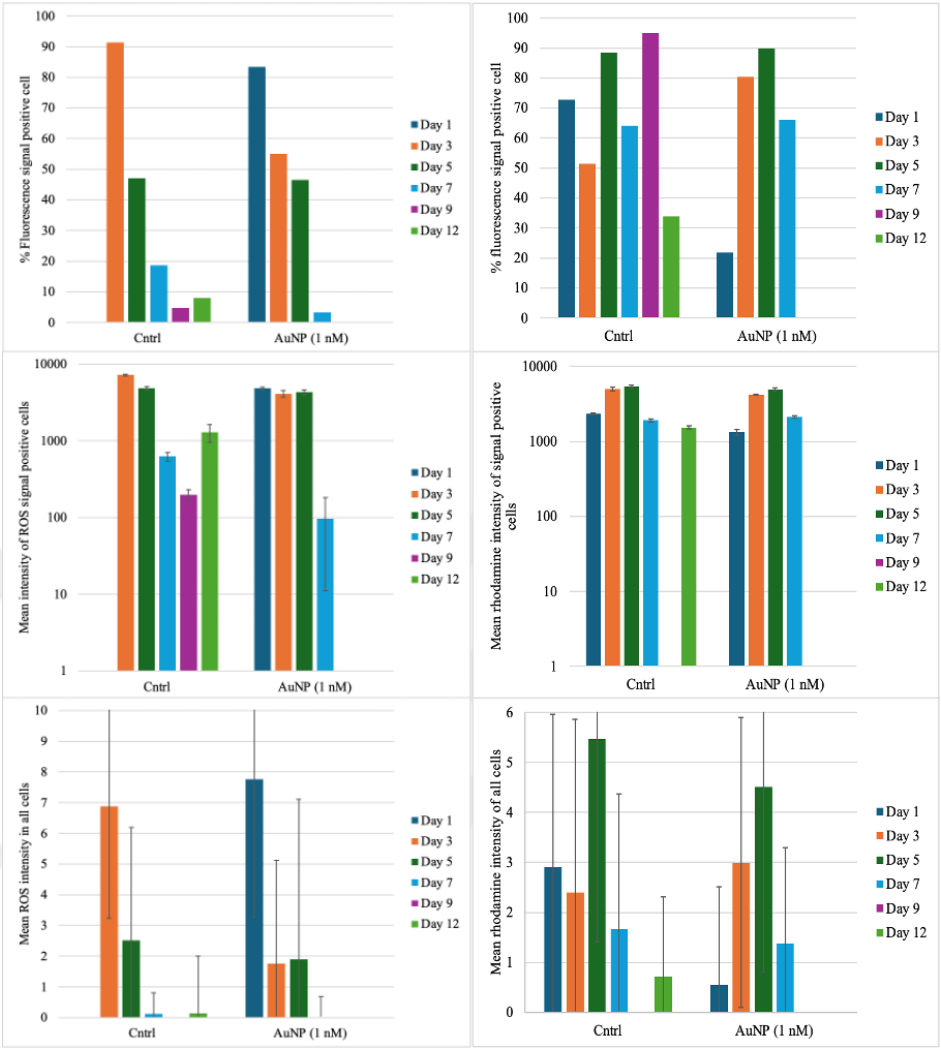


Figure 6.10. ROS and Rhodamine analysis of untreated A375-WT and AuNP-treated in 8G4A scaffold.

be obtained.). These results reflect synergistic effects where AuNPs enhance intracellular curcumin delivery and augment redox stress [262]. Compared to free curcumin, AuNP+curcumin shows less ROS, suggesting either slower cellular uptake or ROS-buffering effects of AuNPs.

Conjugated curcumin shows delayed cytotoxicity, likely due to slower release kinetics and less immediate ROS generation (Figure 6.12), indicating reduced oxidative stress (possibly due to antioxidant effect). Rhodamine uptake is more moderate and sustained, reflecting mitochondrial targeting with delayed depolarization, which is an

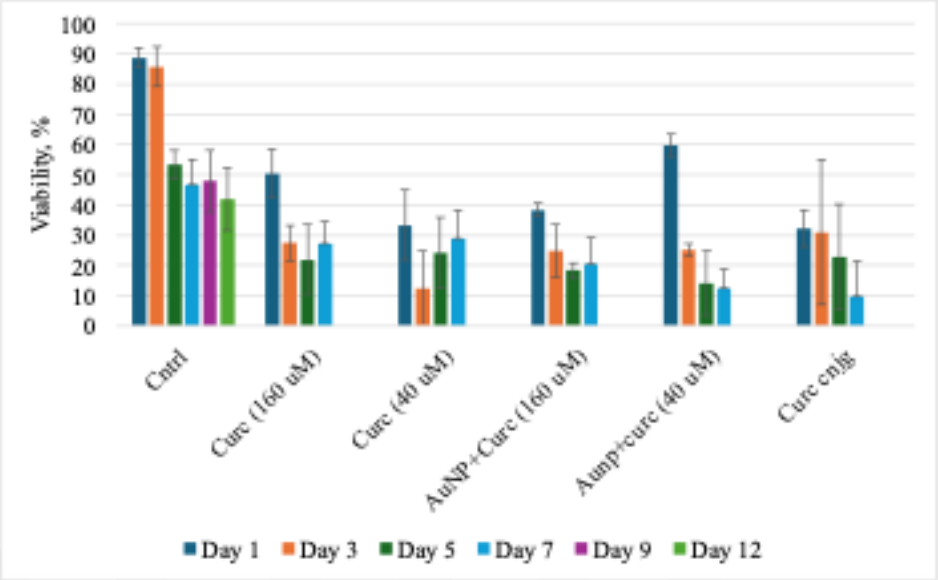


Figure 6.11. Viability of A375-WT cells with curcumin-based treatments in 8G4A scaffold.

advantage for controlled delivery strategies. Furthermore, curcumin-conjugated AuNPs preserve the Rhodamine signal better than free curcumin, suggesting less severe mitochondrial damage or delayed release of curcumin.

Temsirolimus-treated cells have high initial viability (day 1, 3), followed by a significant drop (day 5, 7), indicating a delayed cytotoxic effect (Figure 6.13) [263]. This is the characteristic of mTOR inhibitors, as their anti-proliferative effects might take longer to translate into overt cell death or the 8G4A hydrogel creates a barrier and leads to poor drug penetration. Higher concentration (4 μM) shows faster and more pronounced viability drop, as expected for a dose-dependent drug effect. Delayed and significant ROS induction (high on days 3 and 5) correlates with the delayed viability drop (Figure 6.14). Fluctuation in rhodamine+ cells with a decrease suggests mitochondrial depolarization, correlating with cell death.

A375 cells have an initial lower viability when co-administered with temsirolimus and AuNP on day 1 compared to temsirolimus alone, but then surprisingly have high viability on day 3. This suggests that while AuNPs might cause some initial stress,

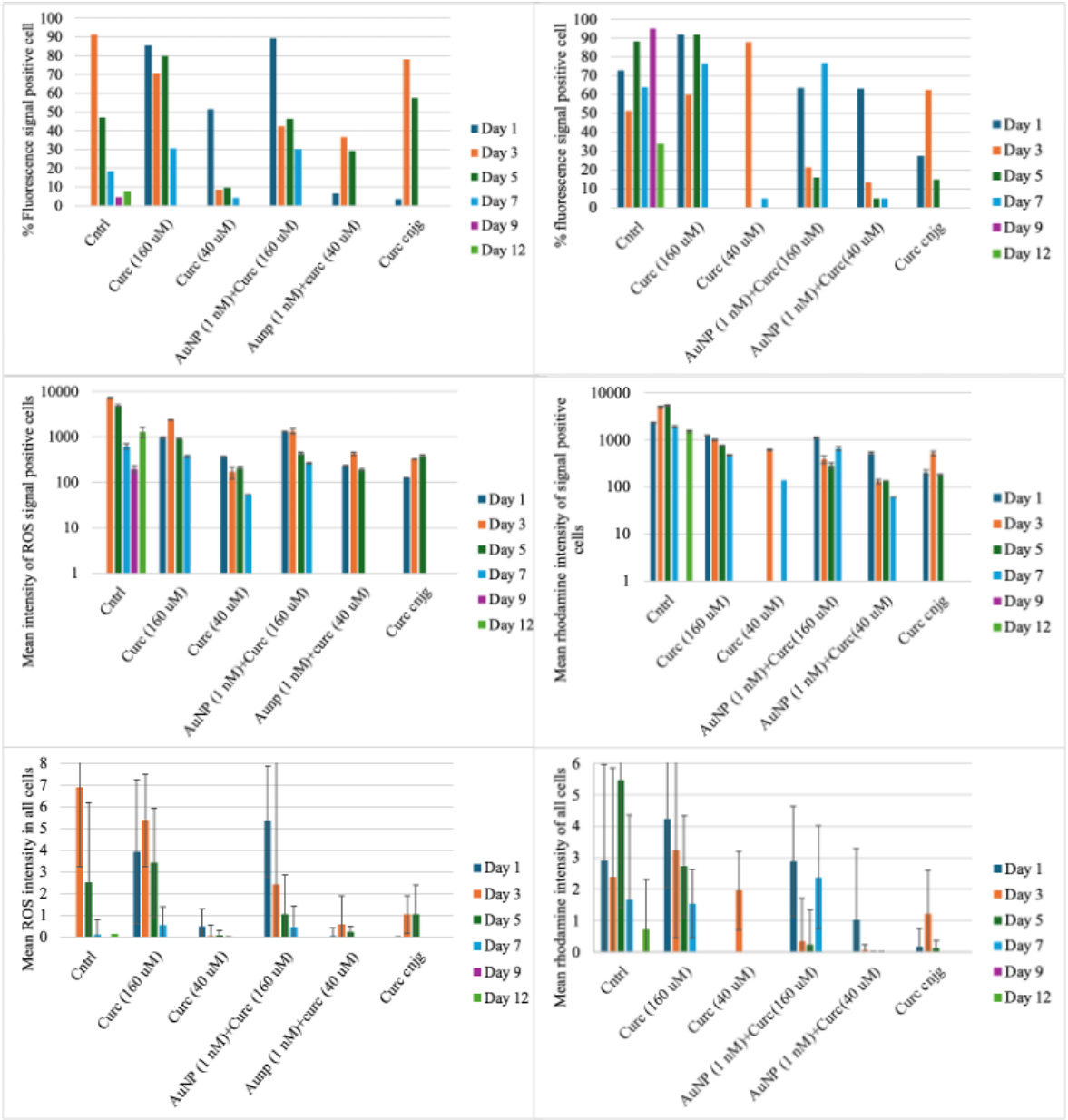


Figure 6.12. ROS and Rhodamine analysis of curcumin-based treated A375-WT in 8G4A scaffold.

their co-administration with temsirolimus at 500nM somehow improves or maintains viability compared to AuNPs alone, potentially by modulating temsirolimus delivery or cellular response. However, this effect is temporary, which raises a question of whether an error was made while image processing, as viability still drops significantly by day 5 and 7, indicating eventual combined toxicity (Figure 6.13). Higher concentration of co-administration of AuNP and temsirolimus (4 $|mu$M) has a similar but stronger and

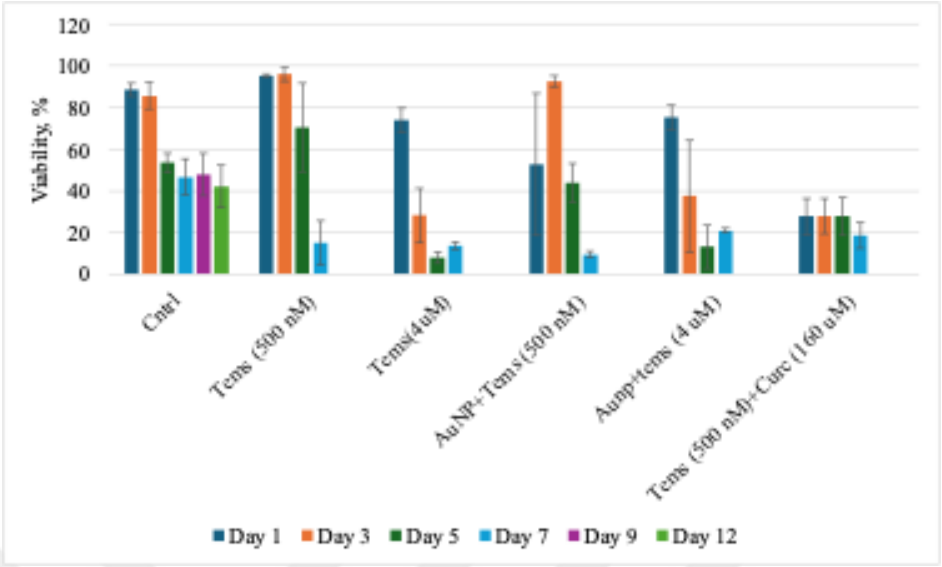


Figure 6.13. Viability of A375-WT cells with temsirolimus-based treatments in 8G4A scaffold.

rapid effect on A375 cells, except for day 3 behavior. Having very high ROS levels on days 3 and 5, significantly higher than temsirolimus alone, indicates the combination leads to profound oxidative stress, likely contributing to eventual cell death. This could be due to AuNP-induced stress, which combines with temsirolimus-induced metabolic changes. High rhodamine positivity on days 1 and 5, potentially indicating compensatory mitochondrial activity in surviving cells or a different pathway of cell death that does not immediately cause complete depolarization of all mitochondria (Figure 6.14). The overall decline in vitality, combined with high ROS, likely indicates severe mitochondrial dysfunction eventually.

Thymoquinone-treated A375 cells show rapid initial cytotoxicity (drop to 18% on day 3, Figure 6.15), and remain stable. This suggests sensitive cells are quickly killed, while a resistant population persists. Fluorescence of the cells on days 1 and 7 could not be detected, which may be either a technical problem or the cells behave unexpectedly opposite to their pro-oxidant activity [264]. It could imply that at this concentration, TQ induces cell death primarily through other mechanisms before significant DCFDA-detectable ROS accumulation, or that the ROS generated is rapidly scavenged/not persistent. The peak on day 5 might indicate a delayed ROS burst in a subset of cells

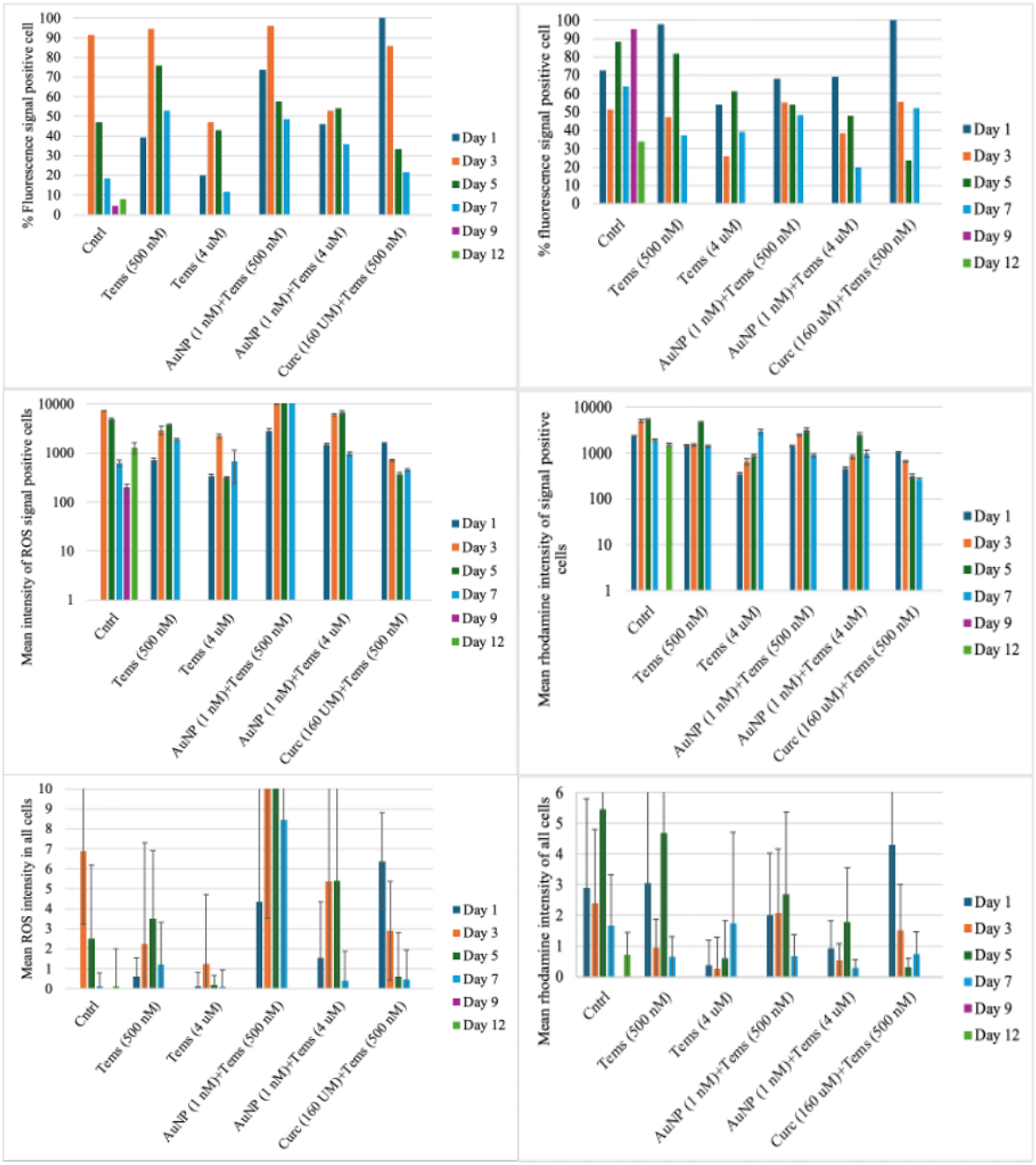


Figure 6.14. ROS and Rhodamine analysis of temsirolimus-based treated A375-WT in 8G4A scaffold.

(Figure 6.16). Rhodamine fluorescence cannot be detected on day 1 and day 7, but it is high on day 5, correlating with viability stability. This could suggest that the remaining viable cells maintain active mitochondria.

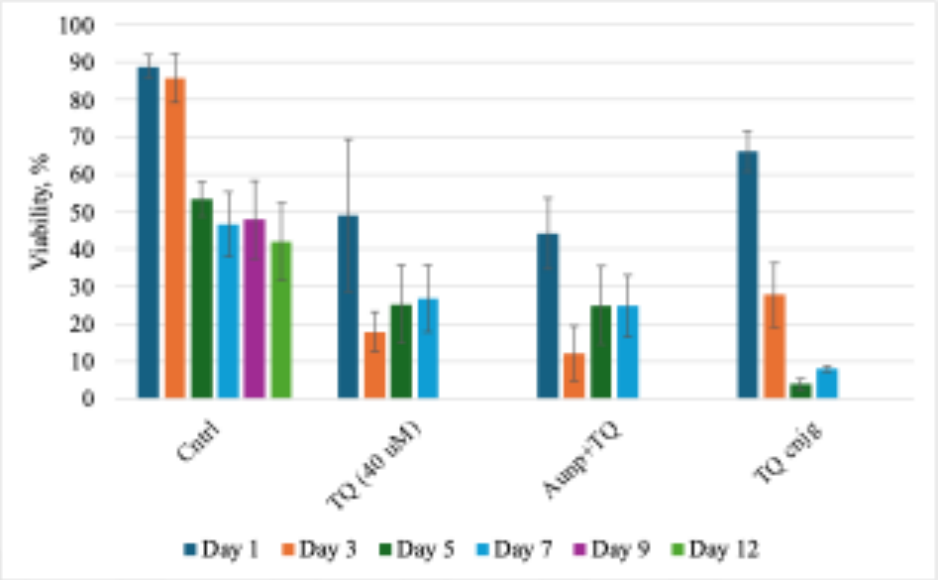


Figure 6.15. Viability of A375-WT cells with TQ-based treatments in 8G4A scaffold.

AuNP and TQ co-administered cells show a similar pattern to TQ alone, with a slight enhancement of early cytotoxicity by AuNPs, leading to similar persistent low viability (Figure 6.15). The AuNPs might improve TQ delivery and add to overall stress. They also show low ROS. This could suggest that the combined toxicity is not primarily driven by high levels of DCFDA-detectable ROS, or that cell death is so rapid that cells cannot maintain a ROS-generating capacity. A low number of cells have a rhodamine fluorescence signal, consistent with cell death and mitochondrial dysfunction (Figure 6.16).

TQ conjugated AuNPs cause drastic cell viability, having a potent cytotoxicity, indicating that the conjugation significantly enhances the cytotoxic effect compared to free TQ. This is a strong indicator of improved delivery, stability, or specific targeting of the conjugate. Cells show initial moderate ROS on day 1, then the ROS decreases. This suggests that while ROS might contribute, the primary driver of the conjugate's potent toxicity could be through other pathways or that cells die too quickly to maintain high ROS levels. Rhodamine signals are low in general, indicating that the overall high efficacy of the conjugate in killing cells is likely due to direct and severe cellular damage, including mitochondrial dysfunction.

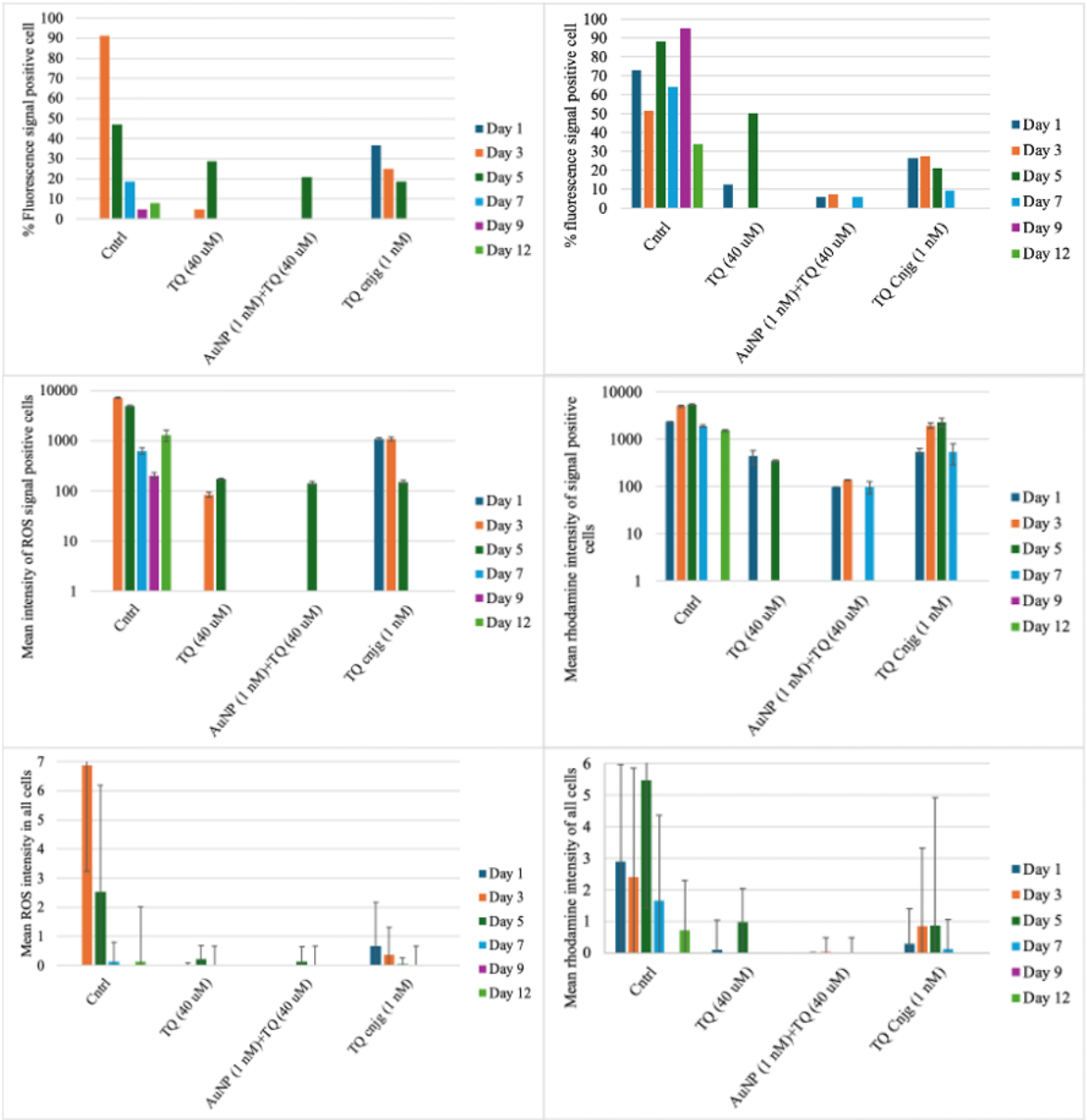


Figure 6.16. ROS and Rhodamine analysis of TQ-based treated A375-WT in 8G4A scaffold.

Untreated melanoma cells grown in gelatin-alginate displayed literature-consistent growth, thereby validating our control group and its alignment with studies reporting defined cellular phenotypes after 3D-bioprinting in multiple bioinks [138].

A summary of cytotoxic outcomes in response to drug and phytochemical applications is given in Table 6.1 based on ROS and rhodamine data. In ROS-driven

intrinsic apoptosis, the mitochondrial membrane potential loss (Rhodamine staining assay) follows ROS accumulation.

Table 6.1. Mechanistic effects of drug and phytochemical applications.

Treatment	**Type of cell**	**Reason for cytotoxicity / Cell death**
AuNPs	A375	Early oxidative stress-induced apoptosis
Temsirolimus	A375	mTOR inhibition
AuNP + Temsirolimus	A375	Severe mitochondrial dysfunction
Curcumin	A375	Substantial mitochondrial disruption and redox stress, mitochondrial depolarization, consistent with intrinsic (mitochondria-mediated) apoptosis
Cur + AuNPs	A375	Prolonged stress response and potentially slower apoptosis
Cur conjugated to AuNPs	A375	Minimized oxidative and mitochondrial damage, suggesting enhanced biocompatibility, controlled release, or reduced pro-apoptotic effect
Thymoquinone (TQ)	A375	Intrinsic apoptosis via strong oxidative stress, and mitochondrial depolarization
TQ + AuNPs	A375	Sustained oxidative stress, apoptosis over time
TQ conjugated to AuNPs	A375	Reduced apoptosis, possibly due to controlled drug release

6.2.2. A375-WT in Matrigel-Alginate Hydrogel

1.5 mL Matrigel is thawed on ice in a precooled Falcon tube. Precooled 0.5 mL of 1% w/w alginate is added onto the Matrigel. A375-WT cells (3.3×10^6 viable cells/mL, 84% viability) are gently mixed with Matrigel alginate hydrogel by using a precooled pipette and pipetting the bioink up and down to mix the cells. Then, the bioink is transferred to the bioprinter syringe and incubated at 37°C for 30 minutes to lead the gelation. Scaffolds are printed in petri dishes and subsequently crosslinked with $CaCl_2$ for 10 minutes in the incubator to crosslink alginate and provide stability to the scaffold. Following crosslinking, the scaffolds are transferred into 6-well plates to reduce the medium consumption. The medium containing various treatments is added to each well, directly onto the scaffold. Cell viability is assessed on the first, second, third, and fifth day of incubation using AO/PI staining, and fluorescence images are analyzed using ImageJ for quantitative evaluation. ROS and rhodamine analyses are done on the same days. The following treatments are administered to the cells, mixed with the DMEM complete medium.

- AuNP (1 nM)
- Temsirolimus (500 nM)
- Curcumin (40 uM)
- AuNP (1 nM) + Temsirolimus (500 nM)
- AuNP (1 nM) + Curcumin (40 uM)
- Control

The viability trends observed underscore distinct cytotoxic profiles associated with each intervention and highlight the potential of 3D culture systems to reveal time-dependent treatment effects. Also, the results align with the response of the cells on 2D systems.

Control samples exhibit high viability, with only moderate decline observed by day 5 (from 86% to 64% Figure 6.17). This behavior is consistent with the known

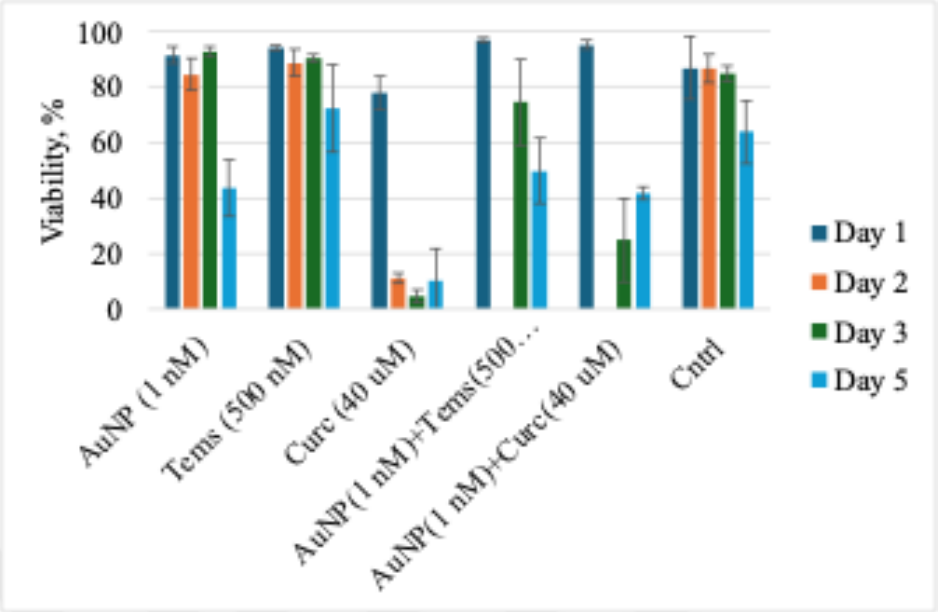


Figure 6.17. Viability results of A375-WT in Matrigel-alginate scaffold.

diffusion limitations and gradual scaffold degradation that commonly impact cell survival in 3D hydrogel systems. ROS analysis revealed a relatively high proportion of ROS-positive cells along with substantial mean ROS intensity across the population (Figure 6.18), indicating oxidative stress as a baseline feature of the 3D bioprinting process and 3D microenvironment. This is consistent with previous reports that 3D cultures impose. Hypoxic and nutrient-gradient-driven oxidative conditions compared to 2D monolayers [257]. Rhodamine anlysis results show stable mitochondrial function with 60-75% rhodamine+ cells throughout the experiment, suggesting that while oxidative stress is present, mitochondria retained sufficient integrity to support cell survival. This balance between ROS and mitochondrial potential may explain the relatively slow and steady reduction in viability.

Treatment with AuNPs alone maintains viability levels comparable to or slightly exceeding controls until day 3 (Figure 6.17), suggesting low cytotoxicity of the nanoparticles. However, a substantial reduction to 44% by the 5th day implies that prolonged AuNP exposure may generate cumulative cellular stress, potentially via increased oxidative stress or lysosomal disruption [265]. ROS analysis indicates a sharp oxidative burst on day 1 on ROS+ cells that dropped by day 5, likely due to the loss of highly

oxidative cells undergoing apoptosis. The rhodamine signal demonstrates moderate mitochondrial depolarization on day 3, followed by partial recovery on day 5 (35% rhodamine+ cells to 60%, Figure 6.18), suggesting that AuNP-induced oxidative stress is transient but capable of triggering downstream apoptotic pathways. The delayed decrease in viability aligns with a mechanism where early oxidative damage accumulates, leading to mitochondrial dysfunction and apoptotic cell death over time.

Curcumin elicited a rapid and pronounced cytotoxic response. Viability declines to 11% by day 2 and falls below 4% by day 3 (Figure 6.17), consistent with curcumin's well-established proapoptotic and oxidative stress-inducing properties in melanoma cells [266]. This rapid cytotoxicity is accompanied by high ROS generation early on (58% ROS+ cells with high intensity on day 1) and the collapse of mitochondrial potential by day 3, as indicated by the absence of rhodamine+ cells. Notably, this effect is not mitigated by the 3D hydrogel environment, suggesting that curcumin retains potent bioactivity even within scaffold-embedded cultures.

The combination of AuNP and curcumin demonstrated even greater potency, with viability plummeting from 90% to 5% by day 5. ROS profiles revealed a strong early oxidative response with enhanced mean ROS intensity compared to curcumin alone. Rhodamine data confirm rapid mitochondrial depolarization, indicating synergistic disruption of mitochondrial function. These findings suggest that AuNPs enhance curcumin's cellular uptake and ROS generation, resuşting in amplified mitochondrial damage and apoptosis, consistent with earlier reports [221].

Temsirolimus treatment results in relatively stable viability exceeding 90% until day 3 (Figure 6.17), which reflects the agent's cytostatic mode of action [267]. The decline to 70% by day 5 represents the progressive inhibition of mTOR-dependent survival pathways. However, temsirolimus treatment on A375 within a 3D printed scaffold responses contradict the results in Section 5.1.1-96 well plate experiments, where the viability dropped to less than 10% on 7th day of Temsirolimus (500nM) treatment. This pattern underscores that in short-term assays, temsirolimus may not

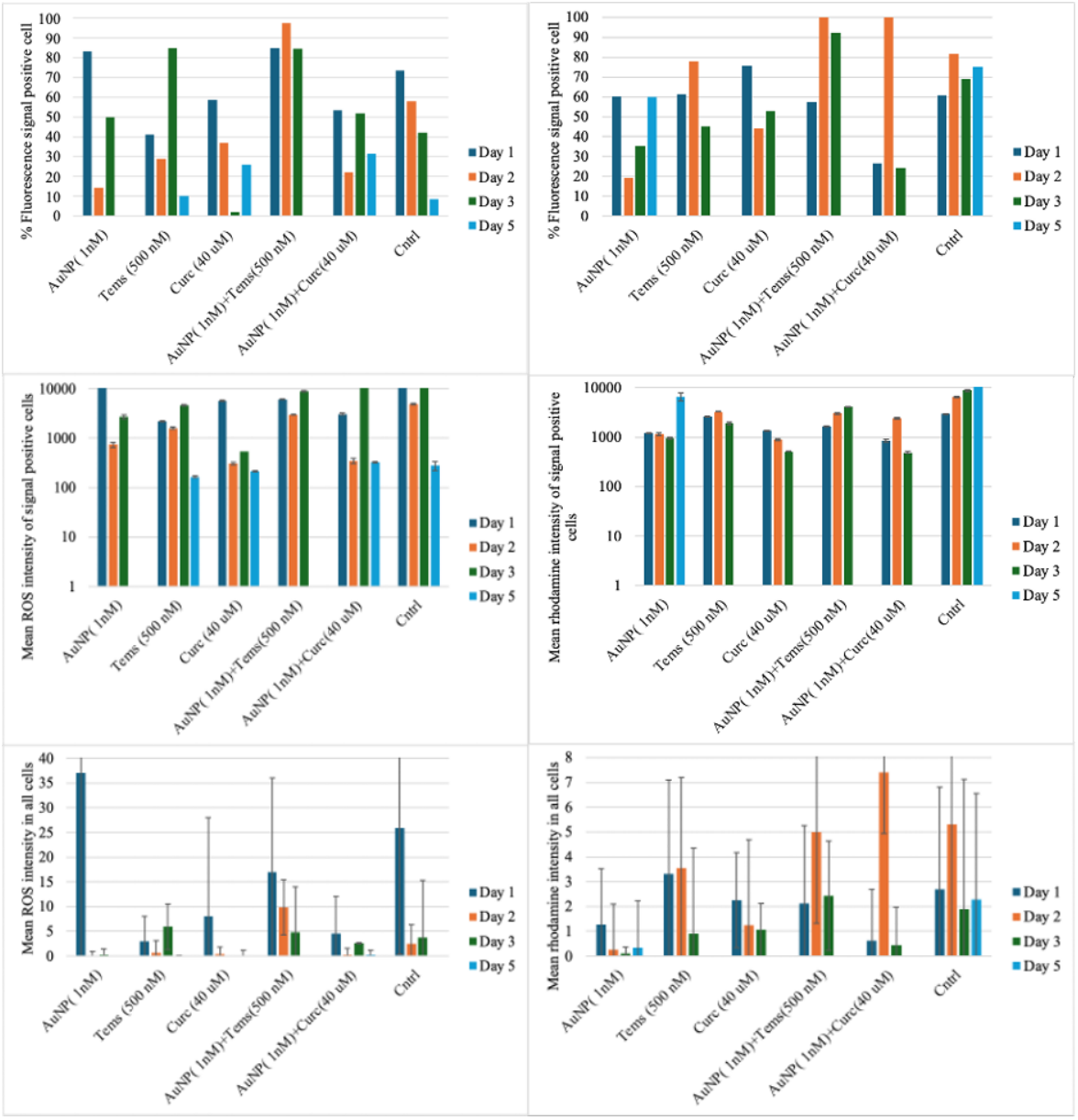


Figure 6.18. ROS and Rhodamine analysis of A375-WT in Matrigel-alginate scaffold.

appear overtly cytotoxic, necessitating longer-term studies to capture its antiproliferative potential and/or checking he efficacy of the agent. A bioprinted scaffold may be denser, delaying the reach of the drug to the cells and also delaying its action, or it may block the drug from reaching the cells. So, coadministration with nanoparticles or conjugation may improve the results. ROS measurements show moderate oxidative stress, with ROS+ cells ranging from 41% on day 1 to 84% on day 3, suggesting that metabolic stress induced by mTOR inhibition may indirectly enhance ROS generation.

Rhodamine analysis reveals high mitochondrial potential through day 2 but complete mitochondrial depolarization by day 5, indicating that prolonged metabolic inhibition triggers mitochondrial dysfunction.

When combined with AuNPs, temsirolimus exhibited a synergistic effect: initial viability is slightly enhanced, possibly due to stress adaptation, but declines more rapidly to 49% by day 5 (Figure 6.18). ROS profiles show pronounced oxidative stress and rhodamine data show faster mitochondrial collapse, suggesting AuNP-induced oxidative stress sensitizes cells to temsirolimus-mediated metabolic suppression, leading to amplified apoptotic responses [44].

Untreated melanoma cells grown in Matrigel displayed literature-consistent growth, thereby validating our control group and its alignment with studies reporting defined cellular phenotypes after 3D-bioprinting in multiple bioinks [268].

6.2.3. M0 in 8G4A Hydrogel - 3D Bioprinted

M0-WT cells (1.8×10^6 viable cells/mL, 68% viability) are mixed gently with 8G4A hydrogel as 1×10^6 cells per mL and loaded into a bioprinter syringe. Scaffolds are printed in petri dishes and subsequently crosslinked with $CaCl_2$ for 10 minutes in the incubator. Following crosslinking, the scaffolds are transferred into 6-well plates to reduce the medium consumption. The medium containing temsirolimus is added to each well, directly onto the scaffold. Cell viability is assessed on the first and seventh day of incubation using AO/PI staining, and fluorescence images are analyzed using ImageJ for quantitative evaluation.

The control group's viability trajectory shows an initial increase from 12% on day 1 to 30% on day 3, followed by a decline to 22% by day 5 (Figure 6.19). This pattern indicates an initial period of cellular adaptation or recovery within the 3D hydrogel environment, which is characteristic of cells adjusting to a new culture system. This is followed by a progressive decrease in the percentage of live cells over extended

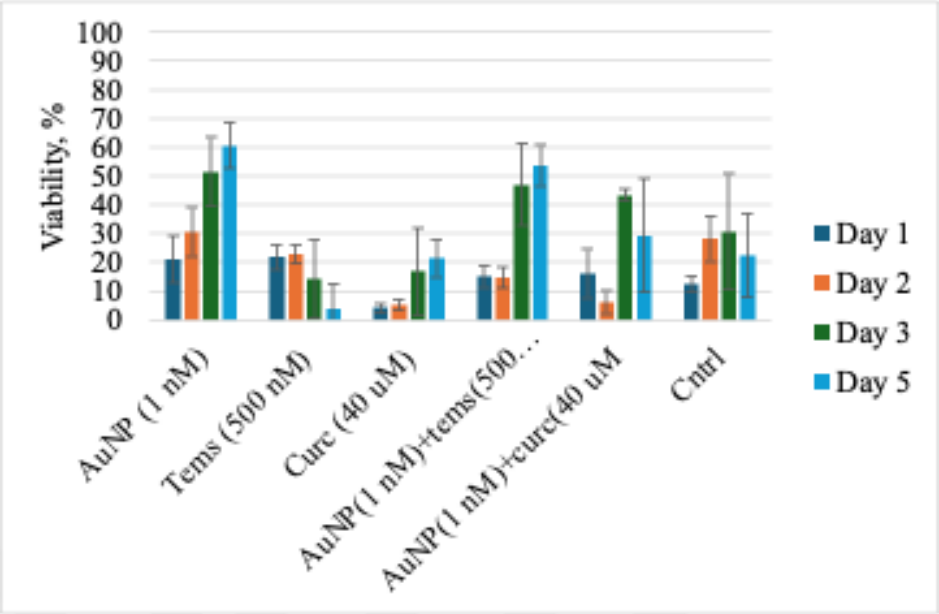


Figure 6.19. Viability results of M0-WT in 8G4A scaffold.

periods, as anticipated for non-proliferating cell populations. The control group shows a low percentage of ROS+ cells on day 11, with a complete absence of detectable ROS signal on day 3 (Figure 6.20), which is an interesting observation, may indicate a transient phase of low metabolic activity or efficient ROS scavenging. By day 5, a small percentage of cells exhibit ROS, suggesting a baseline level of oxidative activity or stress as the culture progresses. The control group shows a significant increase in mitochondrial activity from day 1 to day 3, with nearly 90% of cells exhibiting high MMP (mitochondrial membrane potential) and overall rhodamine intensity. This suggests that after an initial adaptation, the M0 macrophages in the 3D hydrogel become metabolically active. By day 5, there is a decline, but activity remains robust, indicating sustained mitochondrial function in the surviving population.

AuNP-treated cells show a continuous and substantial increase in viability, starting from 20% to up to 60%. For the non-proliferative M0 macrophages, it indicates a potent cytoprotective or cell-health-enhancing effect of the AuNPs. The observed trend suggests that AuNPs are actively preventing cell death and maintaining cellular integrity and survival over an extended period within the 3D bioprinted hydrogel. AuNPs are known for their superior biocompatibility and have been shown to exhibit

anti-inflammatory and antioxidant properties [269]. These properties can directly enhance cell survival by weakening oxidative stress and inflammation, which are often encountered in long-term cell cultures. Additionally, AuNPs have the potential to modulate macrophage polarization, possibly driving M0 macrophages towards a more resilient or anti-inflammatory (M2-like) phenotype that promotes cell survival [269], although this cannot be directly measured in this study. The 1 nM AuNP concentration appears to be highly biocompatible and cytoprotective in this specific 3D macrophage model, suggesting a strong therapeutic potential for AuNPs in maintaining cellular integrity and function in complex biological systems, especially where cell survival, rather than proliferation, is the primary goal. AuNP treatment initially shows a higher percentage of ROS+ cells and total intensity compared to the control on day 1 (Figure 6.20). Similar to control, day 3 shows no detectable ROS. By day 5, the percentage of ROS+ cells is significantly higher than the control (Figure 6.20), but the average intensity per signal+ cell is lower. This pattern suggests that while AuNPs may induce a transient increase in ROS+ cells, i.e., a broader population of cells with some ROS activity, the overall ROS burden per active cell might be reduced over time. This could indicate a hermetic effect, where initial low-level stress primes antioxidant defenses, or a shift in the type of ROS produced. AuNPs are known for antioxidant properties, typically functioning by directly neutralizing ROS or by upregulating endogenous antioxidant enzymes [270]. The increase in viability following AuNP treatment, despite the initial rise in ROS levels (Figure 6.20), indicates a cytoprotective effect. This effect may stem from favorable modulation of redox signaling rather than an ongoing harmful oxidative stress [269] [260].

AuNP treatment shows very low mitochondrial activity on day 1 (Figure 6.20), which contrasts with its relatively higher viability on day 1. However, by day 3, there is a substantial increase in mitochondrial activity, with a very high average intensity per positive cell, indicating highly active mitochondria in the responding population. On day 5, while the percentage of positive cells remains high, the average intensity per cell decreases. The initial low MMP might suggest a transient metabolic shift or adaptation induced by AuNPs or created by the bioprinting process, but the strong increase by day

3 aligns with the observed long-term viability enhancement. AuNPs have been shown to stimulate the respiratory activity of macrophages and the activity of mitochondrial enzymes [271], which directly supports mitochondrial health and function, and overall health. This suggests that AuNPs promote a metabolic state that supports long-term survival, possibly by optimizing mitochondrial efficiency or resilience [271].

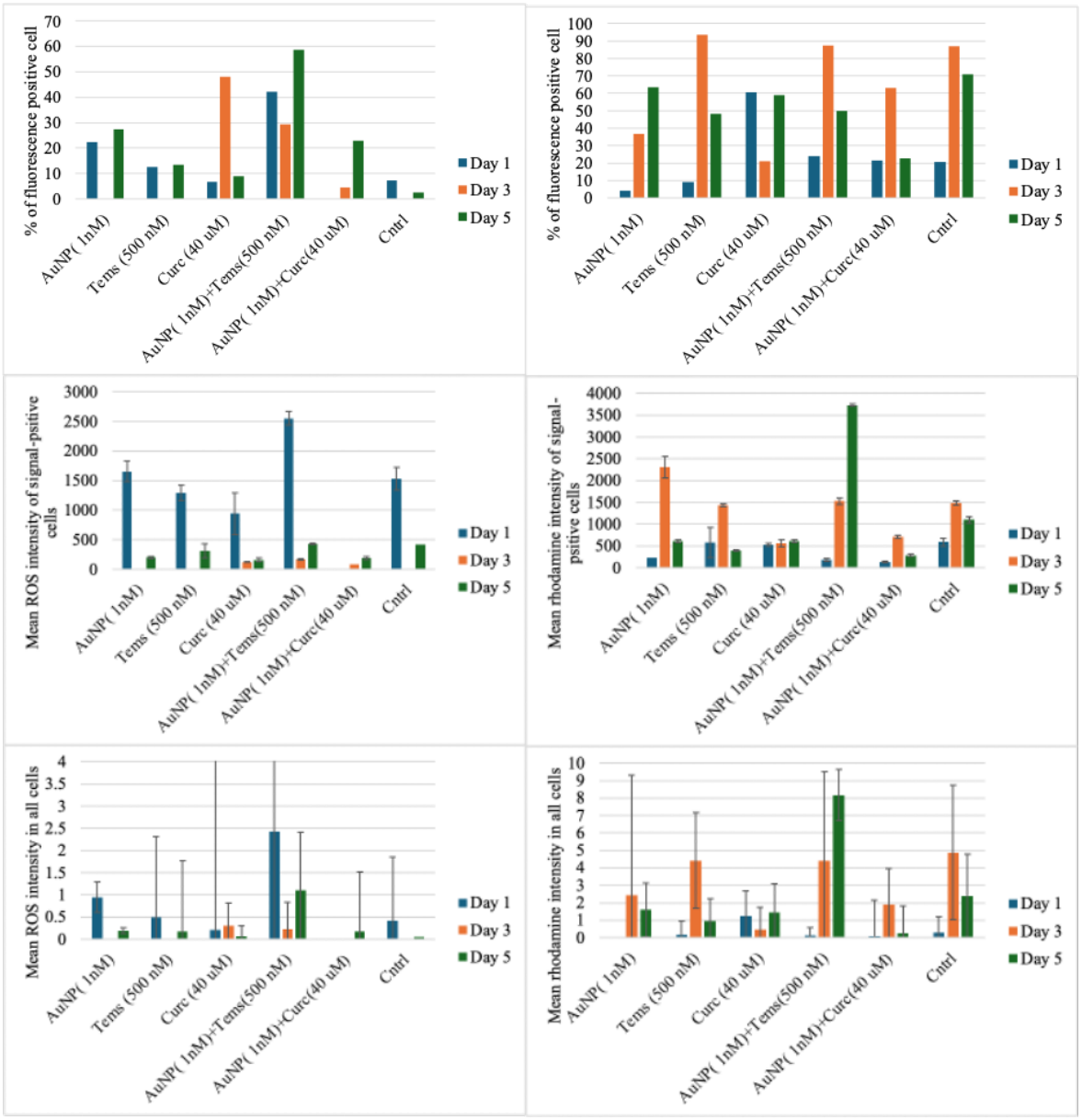


Figure 6.20. ROS and Rhodamine analysis of M0-WT in 8G4A scaffold.

The severe cytotoxicity observed in M0 macrophages suggests that temsirolimus induces significant metabolic disruption or other detrimental effects that override any potential protective mechanisms. While mTOR inhibition can attenuate lipotoxic cell death (Figure 6.19) in some macrophage contexts by reducing mitochondrial oxidative metabolism [272], it also plays a central role in regulating cell proliferation, survival, and metabolism [273]. In non-proliferating M0 macrophages, the inhibition of mTOR might lead to an unfavorable metabolic state, potentially by disrupting mitochondrial dynamics or energy production pathways that are essential for macrophage maintenance. Macrophages undergo significant metabolic reprogramming, and mitochondrial dysfunction can drive inflammatory responses and cell death [274, 275]. The high mitochondrial activity observed on day 3 in temsirolimus-treated cells (Figure 6.20), followed by a sharp decline in viability, could indicate a compensatory metabolic overdrive that ultimately becomes unsustainable or leads to cellular exhaustion and death. The specific concentration of 500 nM might be supra-therapeutic or inherently toxic to the metabolic machinery of M0 macrophages in this 3D environment, leading to a net negative impact on cell survival.

In AuNP and temsirolimus combination, AuNPs likely reduce the cytotoxicity of temsirolimus through several mechanisms. Firstly, AuNPs may directly counteract the metabolic disruption or oxidative stress induced by temsirolimus, leveraging their inherent antioxidant and anti-inflammatory properties [275]. Secondly, AuNPs could influence the cellular uptake, intracellular localization, or metabolic processing of temsirolimus within the macrophages, potentially reducing its off-target detrimental effects on non-cancerous cells. The exceptionally high mitochondrial activity observed on day 5 in this combination (Figure 6.20), despite high ROS levels, suggests that AuNPs enable a regulated ROS environment [270] that supports robust mitochondrial function and overall cell survival. This could involve the modulation of specific redox signaling pathways that promote cell resilience rather than damage [276]. The ability of AuNPs to rescue macrophage viability from temsirolimus toxicity is highly significant for developing combination therapies, as it suggests a potential to broaden the therapeutic window of mTOR inhibitors, making them safer for critical immune cells within the

tumor microenvironment.

Curcumin is well-documented for its dual nature as both an antioxidant and, at certain concentrations or conditions, a pro-oxidant [276]. The initial low viability (Figure 6.19) and low ROS on day 1 (Figure 6.20), followed by a spike in ROS on day 3, suggest an early cellular stress response where curcumin might initially act as a pro-oxidant, inducing a transient oxidative burden. This may be attributed to its capacity to modulate the cell's redox status, possibly through interactions with cellular thiols [255] or by affecting enzyme activities [255]. The observed recovery in cell viability and mitochondrial function by day 5 suggests that the surviving cells either adapt to this initial challenge or that curcumin's powerful anti-inflammatory and antioxidant properties take precedence. Curcumin can modulate macrophage polarization, shifting them from a pro-inflammatory. M1 to an anti-inflammatory M2 phenotype [277] , which could contribute to long-term cell health and survival. It also enhances mitochondrial function and autophagy, protecting against oxidative damage [278]. The recovery observed in viability and mitochondrial function suggests that these effects eventually outweigh the initial stress, allowing for cellular maintenance in the 3D environment.

The initial exacerbated dip in viability and complete absence of ROS on day 1 suggest a transient antagonistic effect or increased early cellular stress when AuNPs and curcumin are combined. Curcumin acts as a reducing and capping agent for AuNP synthesis [279], implying strong chemical interactions that might initially alter the bioavailability or immediate cellular impact of both compounds. The initial absence of ROS could indicate an immediate and potent quenching effect by the combination, which might paradoxically lead to a temporary disruption of essential redox signaling, contributing to early cellular stress. The subsequent recovery in viability and MMP by day 3 (Figures 6.19 and 6.20) suggests that the combined anti-inflammatory and antioxidant properties, potentially enhanced by AuNP's role as a delivery vehicle for curcumin [280], eventually provide some cytoprotection [281].

However, the decline in viability and MPP by day 5 suggests that the prolonged interaction might lead to persistent stress or a less favorable metabolic state compared to the AuNP and temsirolimus combination. This highlights a complex and time-dependent balance between synergistic and antagonistic effects, in which the combined impact on redox homeostasis and mitochondrial dynamics may not remain consistently beneficial over extended periods.

A summary of cytotoxic outcomes in response to drug and phytochemical applications is given in Table 6.2 based on ROS and rhodamine data. In ROS-driven intrinsic apoptosis, the mitochondrial membrane potential loss (Rhodamine staining assay) follows ROS accumulation.

Furthermore, M0-WT cells were also tested in Matrigel-alginate hydrogel in 3D bioprinted form. Temsirolimus (500 nM), AuNP (1 nM), and their combination were given to the cells as treatments. However, these experiments cannot be repeated and, therefore, are not discussed here.

6.3. Coculture Treatments (Viability/Rhodamine Analyses – Day 1,2,3)

In this section, the interplay between melanoma cells and macrophages under treatment conditions is investigated by establishing a coculture model using A375 melanoma cells and THP-1-derived M0 macrophage cells in transwell plates (8 μm pore size, polycarbonate membrane). A375-WT cells are embedded within 8G4A hydrogel (0.5×10^6 cells/mL, as in previous experiments) and deposited into the basal well of a 6-well transwell plate (300 μL hydrogel per well), supplemented with 2.5 mL of DMEM complete medium containing either curcumin (40 μM) or thymoquinone (40 μM), or no treatment as control. M0-WT macrophages (2×10^5 cells/well) are seeded into the upper insert wells with 1.5 mL of RPMI1640 complete medium, adjusted to mirror treatment conditions of the basal compartment. The inserts are then placed over the A375-containing wells, allowing paracrine communication between the two cell populations. Viability (AO/PI staining) and mitochondrial activity (Rhodamine

Table 6.2. Effect of treatments on cell death mechanism.

Treatment	**Type of cell**	**Reason for cytotoxicity / Cell death**
AuNPs	M0	Cell death prevention: Antioxidant properties (ROS scavenging, enzyme upregulation), enhanced mitochondrial function, anti-inflammatory / M2 polarization
Temsirolimus	M0	Direct cytotoxicity: mTOR inhibition
AuNP + Temsirolimus	M0	AuNP-mediated rescue via antioxidant effect, mitochondrial resilience, potential drug delivery / safety modulation
Curcumin	M0	Initial stress / pro-oxidant effect; later recovery with potent antioxidant and mitochondrial protective effects
Cur + AuNPs	M0	Complex interaction: early stress due to pro-oxidant effect; mid-term recovery due to combined antioxidant / anti-inflammatory effects; long-term decline from persistent stress

123) analysis are conducted on days 1, 2, and 3 to evaluate treatment effects and intercellular interactions.

The use of transwell plates is advantageous for modeling tumor-immune cell crosstalk, as it enables soluble factor exchange through a semipermeable membrane without direct cell-to-cell contact. This approach allows macrophages to respond to tumor-derived cytokines and secreted metabolites, while A375 cells are simultaneously

influenced by macrophage-conditioned media, while they are in a 3D environment. Thus, the system closely mimics paracrine signaling observed in the tumor microenvironment, making it suitable for studying the effects of bioactive compounds such as curcumin and TQ on melanoma-macrophage dynamics. The viability results of A375 melanoma cells and M0 macrophage cells are given in Figure 6.21.

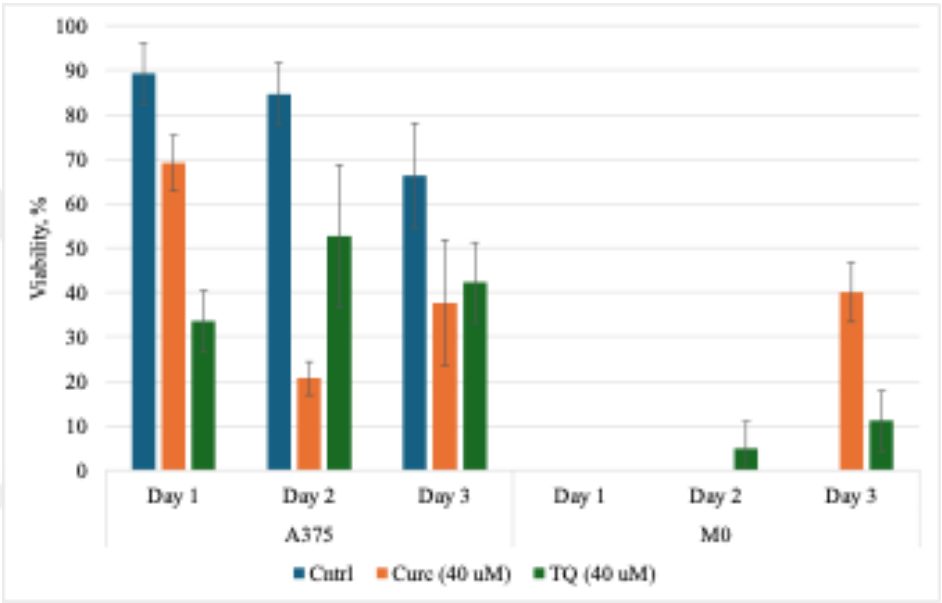


Figure 6.21. Viability results of A375-WT and M0-WT cells in coculture.

In the control group, A375 melanoma cells maintained a high initial viability of approximately 89% on day 1, which gradually decreased to 66% by day 3 (Figure 6.21), reflecting the natural decline associated with metabolic stress within the 3D environment. M0 macrophages, cultured in the inserts, showed no viability across all time points, indicating high environmental stress and/or experimental error. Rhodamine analysis of A375 cells revealed an initial increase in the proportion of mitochondrially active cells from day 1 (58%) to day 2 (77%), followed by a decrease to 59% by day 3 (Figure 6.22). This transient increase in mitochondrial signal may indicate early mitochondrial hyperpolarization, which often precedes apoptosis, whereas the subsequent decline suggests a shift toward mitochondrial depolarization as cells experience progressive stress. In M0 cells, mitochondrial activity remained high (92-100% rhodamine+ cells), and total fluorescence intensity is consistently elevated, indicating

preserved mitochondrial function and stable energy metabolism under untreated conditions. Viability and rhodamine analyses are performed in separate wells. No viable cells are observed in the wells used for viability assay (Figure 6.23); therefore, viability is recorded as zero. However, it is uncertain whether the cells in the wells used for rhodamine analysis are alive, meaning that the rhodamine signals may only represent a few surviving cells or residual signals within dead cells.

Upon curcumin treatment, A375 cells displayed a pronounced reduction in viability, declining from 69% on day 1 to 20% on day 2, with a partial recovery to 38% by day 3 (Figure 6.21). This biphasic response (which is also similar to the results of 8G4A scaffold in section 5.2.1) suggests an initial wave of apoptosis triggered by curcumin's pro-oxidant activity, followed by survival of a subset of resistant cells. Rhodamine analysis corroborated this trend, showing a drop in the fraction of rhodamine+ cells from 77% on day 1 to 46% by day 2, accompanied by a decline in total mitochondrial fluorescence intensity, indicating early mitochondrial depolarization and loss of mitochondrial membrane potential (Figure 6.22) [253, 261, 266, 282]. The M0 results have a contradiction between viability and rhodamine analysis, so it would be better to repeat the experiment.

Thymoquinone treatment elicits a more gradual but sustained cytotoxic effect on A375 cells, with viability changing from 33% on day 1 to 51% on day 2 and decreasing to 42% by day 3 (Figure 6.21), suggesting a slower induction of apoptosis compared to curcumin (Figure 6.21). Rhodamine analysis shows a pronounced decline in the proportion of mitochondrially active A375 cells, from 46% on day 1 to just 18% by day 3, along with a substantial reduction in total fluorescence intensity (Figure 6.22), indicating severe mitochondrial [264, 283] dysfunction and loss of bioenergetic capacity. In M0 macrophages, TQ induced a time-dependent reduction in viability and a marked decrease in mitochondrial signal (50% rhodamine+ cells by day 2), reflecting its oxidative and pro-apoptotic mechanisms of action. These results are in agreement with previous studies reporting that TQ induces ROS-mediated apoptosis and inhibits pro-survival signaling, including the mTOR and STAT3 pathways [283], in both cancer

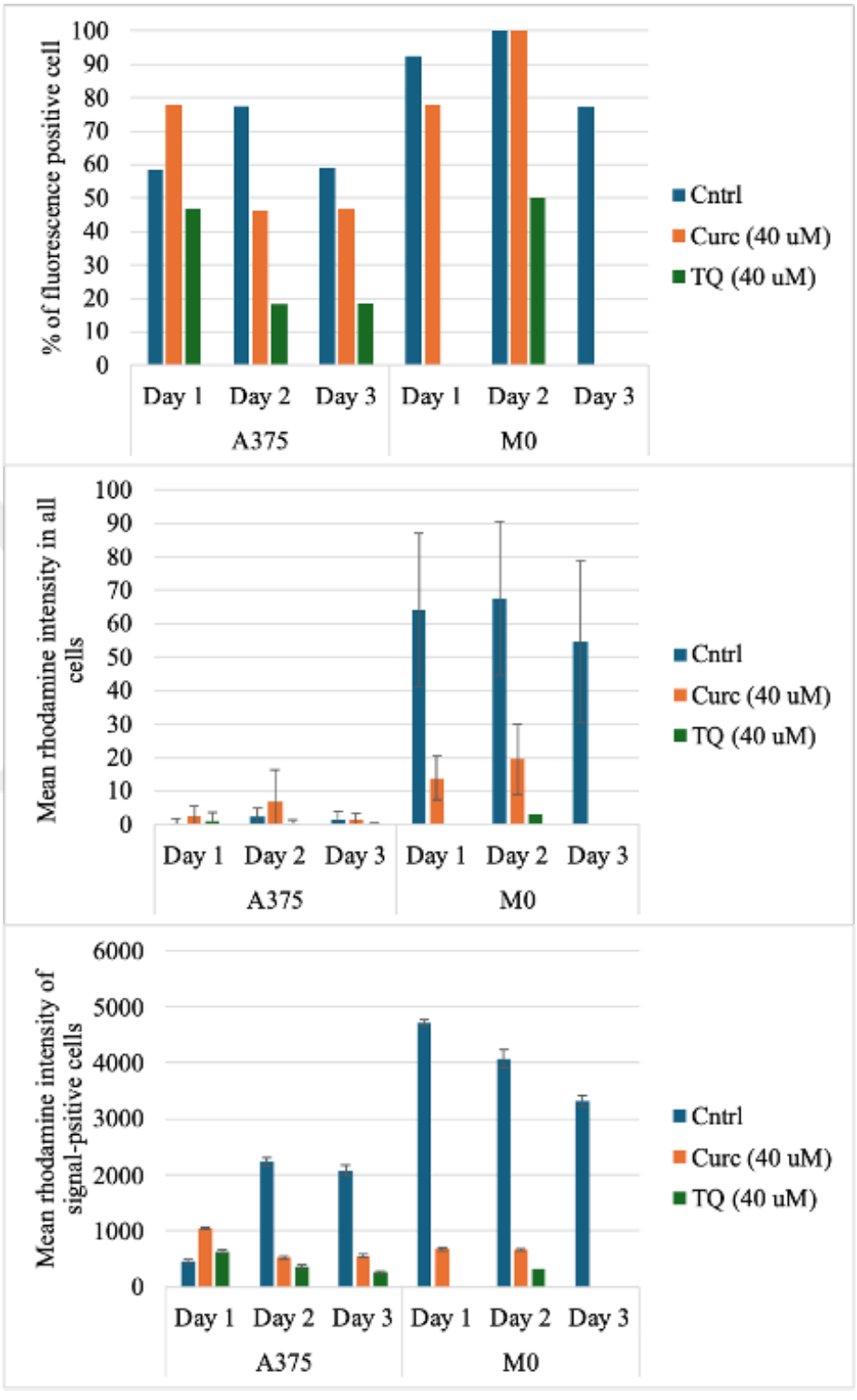


Figure 6.22. Rhodamine analysis of coculture.

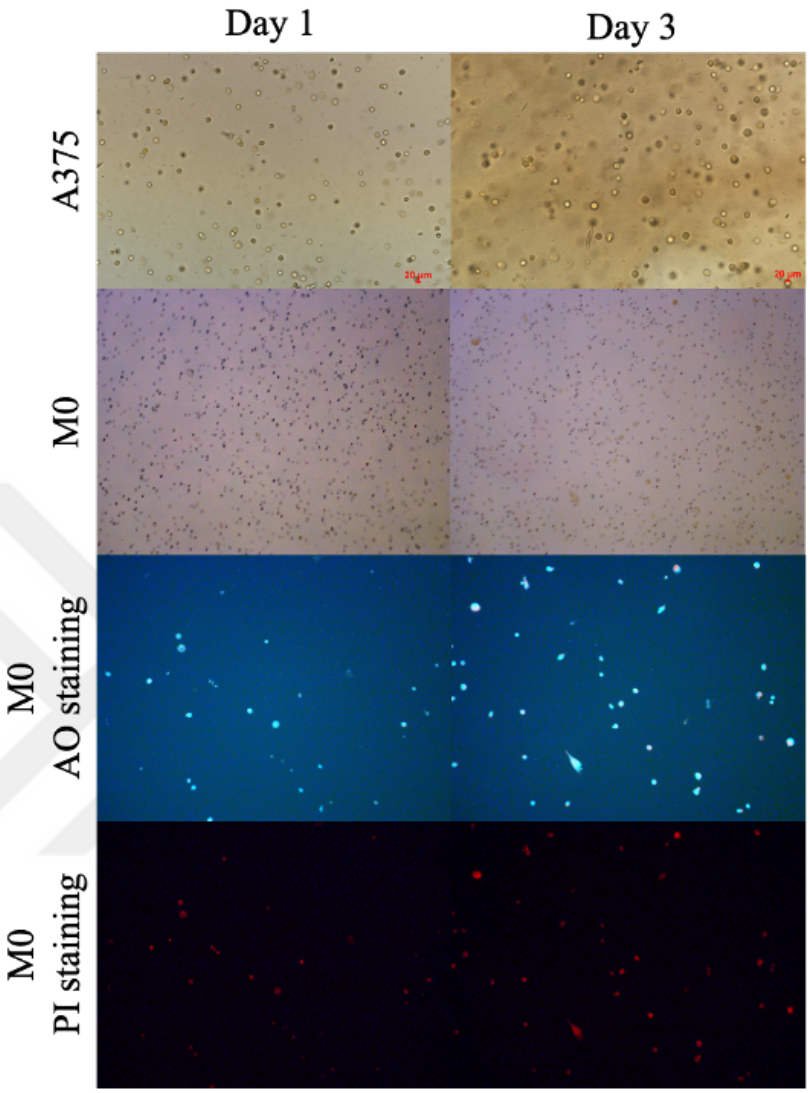


Figure 6.23. A375 and M0 of non-treated coculture.

and immune cells. Taken together, the data highlight distinct kinetic patterns of cytotoxicity: curcumin exerts acute mitochondrial stress leading to rapid apoptosis, while TQ causes a progressive collapse of mitochondrial function, affecting both melanoma cells and macrophages [284].

In this experimental setup, there are several technical issues that must be mentioned. First of all, and the most critical one is, M0 cells are transferred to the insert well by removing their differentiation plate. This creates a loss in viability and the number of cells since re-adhesion of M0 cells to the membrane is not definite. When

M0 cells are subjected to viability and rhodamine staining, most of the potentially viable but non-adherent cells are lost upon removal of the medium, resulting in loss of viability and rhodamine signaling data. Second, when spreading the A375-embedded 8G4A hydrogel into the basal well, it is crucial that the height of the hydrogel is lower than the bottom of the insert well (Figure 6.24a). If hydrogel contacts with the insert well, the risk of contamination increases. Third, the imaging of the cells in the basal well and insert well must be done in an inverted microscope and an upright microscope, respectively. The polycarbonate membrane makes it difficult to see the cells already, even when the cells are imaged with an upright microscope (Figure 6.24b).

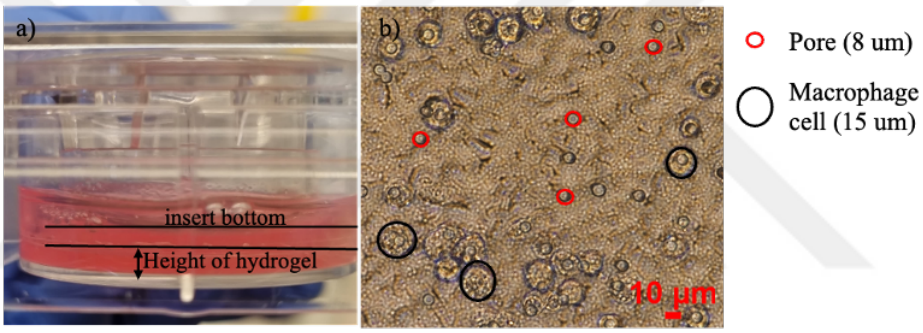


Figure 6.24. (a) Placement of the wells, (b) M0 cells on membrane.

7. PBPK MODELLING

Curcumin is a bioactive compound derived from Curcuma longa (turmeric), widely investigated for its therapeutic potential. Despite its promising potential, the clinical application of curcumin is hampered by its low oral bioavailability. This poor bioavailability stems from poor aqueous solubility, rapid intestinal metabolism, rapid systemic clearance, and extensive biliary excretion. Physiologically-based pharmacokinetic (PBPK) modeling provides a mechanistic framework to understand its absorption, distribution, metabolism, and elimination (ADME) processes, enabling the quantitative predictions of systemic exposure [285, 286].

This chapter describes the development of a PBPK model for curcumin, focusing on oral absorption characteristics and distribution. The model is built using a system of ordinary differential equations (ODEs), and it aims to stimulate the concentration-time profiles of curcumin in various physiological compartments. The model incorporates both the plasma and lymphatic absorption pathways, which are critical for understanding the disposition of lipophilic compounds like curcumin. The model's parameters are derived from a combination of literature data and publicly available databases. The model is implemented in MATLAB for numerical simulations.

7.1. Model Structure

The PBPK model developed for curcumin is a multicomponent system designed to represent the key physiological spaces involved in the drug's ADME processes. The model's structure is comprised of five interconnected compartments (Figure 7.1):

(i) Gut (V_{gut}): This compartment represents the gastrointestinal tract, where the orally administered curcumin is initially deposited. It is the site of drug dissolution and absorption into the systemic circulation.

(ii) Plasma (V_p): This compartment represents the central blood pool. Curcumin

enters the plasma from the gut and is then distributed to other tissues or cleared from the body.

(iii) Tight tissues (V_{tight}): This compartment represents tissues with low permeability, such as skeletal muscle, skin, adipose tissue, and the brain. The exchange of curcumin between plasma and these tissues is typically slower and more restricted.

(iv) Leaky tissues (V_{leaky}): This compartment represents tissues with high permeability and high blood flow, such as the liver, kidneys, and heart. These tissues are often involved in drug metabolism and elimination.

(v) Lymphatic system (V_{lymph}): This compartment represents the entire lymphatic network, which plays a crucial role in the absorption and transport of lipophilic compounds. Curcumin, being a lipophilic molecule, is absorbed from the gut into the lymph and also leaks from the interstitial fluid of other tissues back into the lymph, eventually returning to plasma.

The model assumes that curcumin, after oral administration, is absorbed from the gut into two primary pathways: directly into the plasma via the portal vein and into the lymphatic system [287]. These processes are modeled as first-order with absorption rate constants of $k_{a,\,blood}$, and $k_{a,\,lymph}$, respectively.

The distribution of curcumin from plasma to the tight and leaky tissues is governed by concentration gradients. A unique feature of this model is the inclusion of a lymphatic pathway for tissue leakage. Curcumin that has been distributed from the plasma into the interstitial fluid of the tissues (both tight and leaky) can then drain into the lymphatic system, which returns the drug to plasma, creating a recirculatory loop.

Systemic clearance is accounted for in the plasma compartment. This plasma clearance (CL_p) term represents the combined effects of hepatic metabolism and renal excretion, which are the primary routes of elimination for most drugs. The parameters of the model are set for a standard 70 kg human. The physiological volumes for the various compartments (V_p, V_{tight}, V_{leaky}, V_{lymph}) and lymphatic flow rates (L_1,

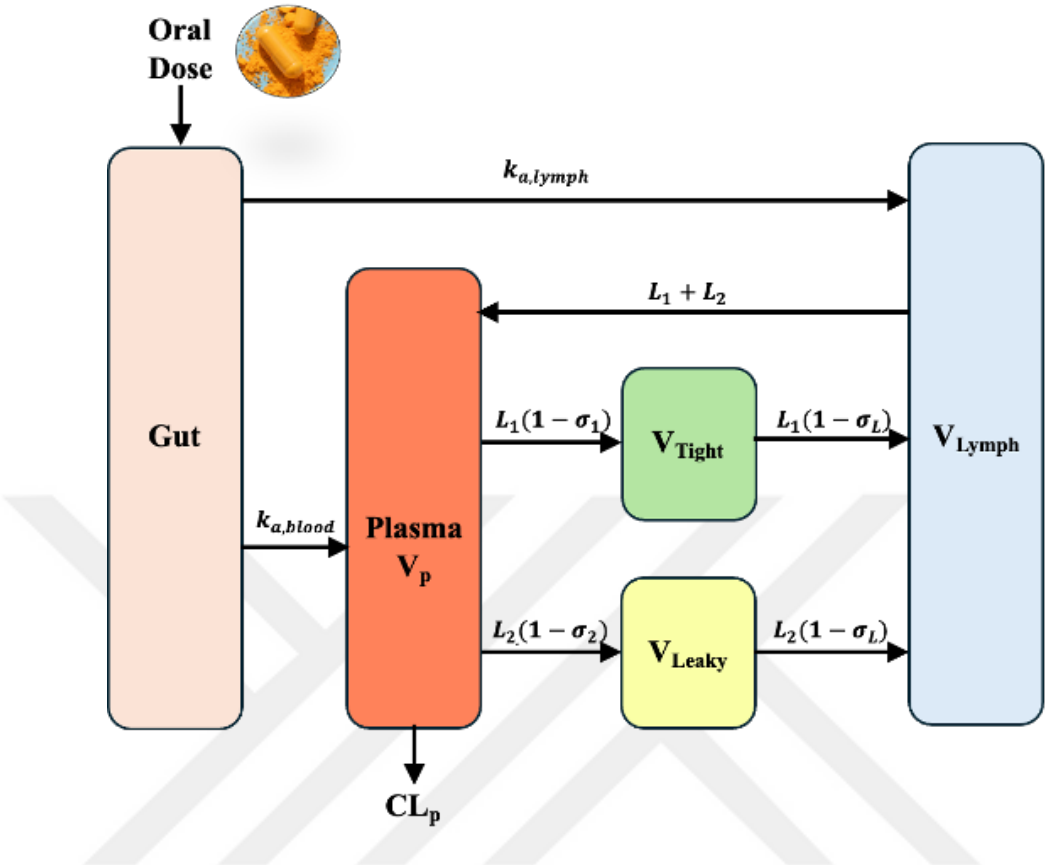


Figure 7.1. PBPK model for curcumin.

L_2) are sourced from established PBPK literature by Cao *et al.* [288, 289] to ensure physiological relevance. Pharmacokinetic parameters, such as bioavailability (F) and clearance (CL_p), are obtained from reliable databases like Admetlab 3.0 and DrugBank, respectively. The absorption rate constants, $k_{a,\,blood}$ and $k_{a,\,lymph}$, are derived from Vareed *et al.* (2008) and Yousef *et al.* (2023), respectively (Table 7.1) [290, 291]. The oral uptake amount of curcumin is selected as the highest reported in the literature, which is 12 g [290].

The dynamic behavior of curcumin within this system is described by a set of ordinary differential equations (ODEs), which track the change in the amount of drug over time in each compartment. Concentration vs time profiles are obtained by solving equations using MATLAB.

Table 7.1. Physiological and pharmacokinetic parameters used in the PBPK model.

Parameter	**Value**
Plasma volume, V_p	2.6 L
Interstitial fluid volume, ISF	15.6 L
Volume of tight tissues, V_{tight}	8.11 L
Volume of leaky tissues, V_{leaky}	4.36 L
Lymphatic volume, V_{lymph}	5.6 L
Lymphatic flow to tight tissues, L_1	0.04 L/h
Lymphatic flow to leaky tissues, L_2	0.08 L/h
Bioavailability, F	1%
Clearance, CL_p	40.467 L/h
$k_{a,\,blood}$	1.05 h^{-1}
$k_{a,\,lymph}$	0.131 h^{-1}

The ODEs for the model are defined as

$$\frac{dA_{\text{gut}}}{dt} = -\left(k_{a,\text{blood}} + k_{a,\text{lymph}}\right) A_{\text{gut}}, \tag{7.1}$$

$$\frac{dC_p}{dt} = \frac{k_{a,\text{blood}}\, A_{\text{gut}}}{V_p} + \frac{C_{\text{ly}}(L_1 + L_2) - C_p\, L_1(1-\sigma_1) - C_p\, L_2(1-\sigma_2) - CL_p\, C_p}{V_p}, \tag{7.2}$$

$$\frac{dC_t}{dt} = \frac{L_1(1-\sigma_1)\, C_p - L_1(1-\sigma_L)\, C_t}{V_{\text{tight}}}, \tag{7.3}$$

$$\frac{dC_l}{dt} = \frac{L_2(1-\sigma_2)\, C_p - L_2(1-\sigma_L)\, C_l}{V_{\text{leaky}}}, \tag{7.4}$$

$$\frac{dC_{\text{ly}}}{dt} = \frac{k_{a,\text{lymph}}\, A_{\text{gut}}}{V_{\text{lymph}}} + \frac{L_1(1-\sigma_L)\, C_t + L_2(1-\sigma_L)\, C_l - (L_1 + L_2)\, C_{\text{ly}}}{V_{\text{lymph}}} \tag{7.5}$$

where A_{gut} is the amount of curcumin in the gastrointestinal tract available for absorption, C_p is the curcumin concentration in plasma, C_t is the concentration in tight

tissues, C_l is the concentration in leaky tissues, and C_{ly} is the concentration in systemic lymph. σ_1, σ_2, and σ_L represent permeability limitations across tight and leaky tissues or lymphatic return. $k_{a,\,\text{blood}}$ and $k_{a,\,\text{lymph}}$ are the first-order absorption rate constants from the gut to plasma and lymph, respectively. L_1 and L_2 represent the lymph flow for V_{tight} and V_{leaky}, respectively.

In this specific model, it is assumed that the permeability between plasma and the tissues is very high, such that the exchange is essentially instantaneous. This is represented by setting σ_1 and σ_2 to 0.5 and 0.4, respectively. Although curcumin is a lipophilic compound (logP = 3.3 [292]), its poor aqueous solubility, extensive plasma protein binding, and low passive permeability justify the non-zero sigma values. A higher σ_1 (0.5) was assigned to tight tissues to reflect more restrictive barriers such as reduced capillary fenestration and limited interstitial diffusion, whereas a lower σ_2 (0.4) was used for leaky tissues, which are generally more permissive to drug transport. This setup helps to focus on the distribution kinetics, like L_1 and L_2. The lymphatic return from tissues to the plasma is considered to have a mild barrier, represented by σ_L as 0.05. This small value implies that while the lymphatic system does contribute to drug return, it is not a highly efficient process, reflecting the complex and slow nature of lymphatic circulation [290, 291, 293].

Figure 7.2 shows the amount of curcumin in the gut compartment over time. The curve starts at the initial dose amount (12 g oral take, 120 mg dose due to bioavailability) and decreases rapidly. This decline represents the combined rate of absorption into the blood and lymph.The curve flattens out around 5 hours, indicating that most of the curcumin has been absorbed or moved out of the gut. The rapid decrease is governed by the total absorption rate constant ($k_{a,\,\text{blood}} + k_{a,\,\text{lymph}}$).This rapid emptying of the gut is consistent with the fast-acting nature of the absorption process assumed in the model.

Figure 7.3 illustrates the simulated concentration–time profiles of curcumin in the different compartments of the PBPK model following gut absorption.

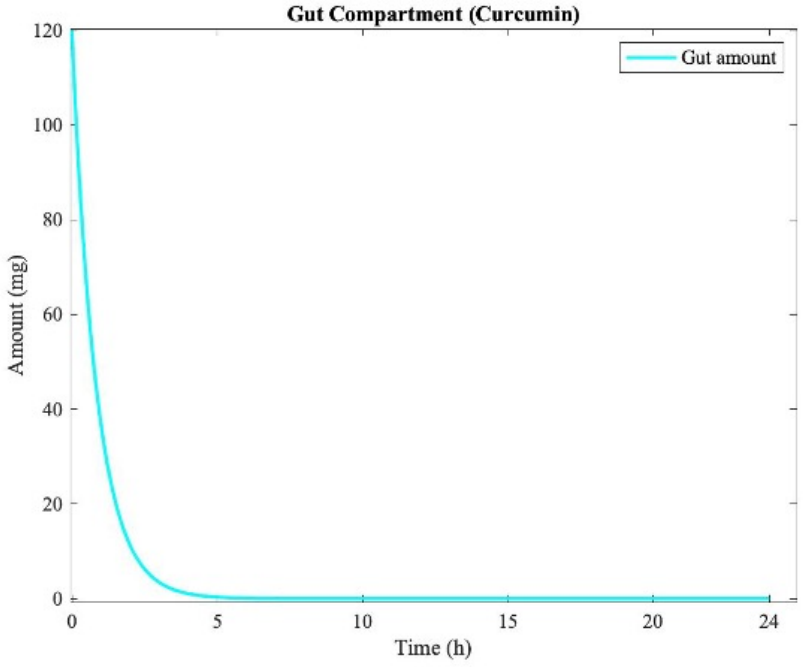


Figure 7.2. Amount of curcumin in the gut with respect to time.

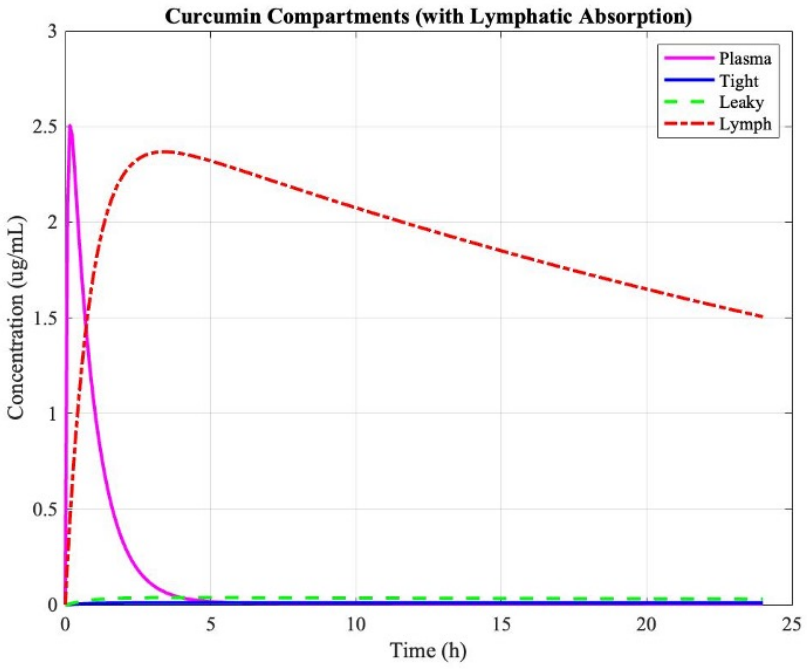


Figure 7.3. Curcumin concentration in all compartments.

The magenta line shows the plasma concentration of curcumin over time. The profile shows a sharp and rapid increase reaching its maximum concentration, $C_{\max}$, in less than an hour. This quick absorption is driven by $k_{a,\,\text{blood}}$ from the gut. The peak plasma concentration is relatively low, according to the dose, reaching about 2.5 μg/mL. This is a hallmark of the poor oral bioavailability of curcumin. It reflects the incomplete absorption, first-pass metabolism and rapid distribution. Following the peak, the plasma concentration declines very quickly and approaches zero within a few hours. This rapid decrease is due to the high clearance rate and the rapid distribution of curcumin into other compartments, especially the leaky tissues for metabolism and the lymphatic system.

The red dashed line shows the lymph concentration profile of curcumin over time. In contrast to plasma, the lymphatic compartment shows a much slower increase in concentration. The peak concentration is reached after 3–4 hours. This delayed peak is a direct result of the lower $k_{a,\,\text{lymph}}$ constant and the slow nature of lymphatic flow. The peak concentration in the lymph is similar to the plasma, 2.4 μg/mL, but the decline is much more gradual and prolonged (Figure 7.4a). This is a critical finding of the model. It suggests that a significant portion of the orally administered curcumin is absorbed via the lymphatic system, and it remains there for an extended period. This sustained exposure in the lymph could be relevant for therapeutic effects in the lymphatic system or for its role as a "depot" before slowly returning to the systemic circulation. Also, the high concentration and long residence time in the lymphatic system show that curcumin is preferentially absorbed via the lymphatic system when a low bioavailability formulation is used.

The blue line shows that the concentration in the tight tissue compartment remains very low throughout the entire simulation (Figure 7.4b). This result suggests that despite the assumption of free and rapid exchange between plasma and tissues, the overall low plasma concentration and rapid clearance prevent a significant amount of curcumin from distributing into and accumulating in these tissues. The drug simply does not stay in the plasma long enough to build up a concentration gradient to drive

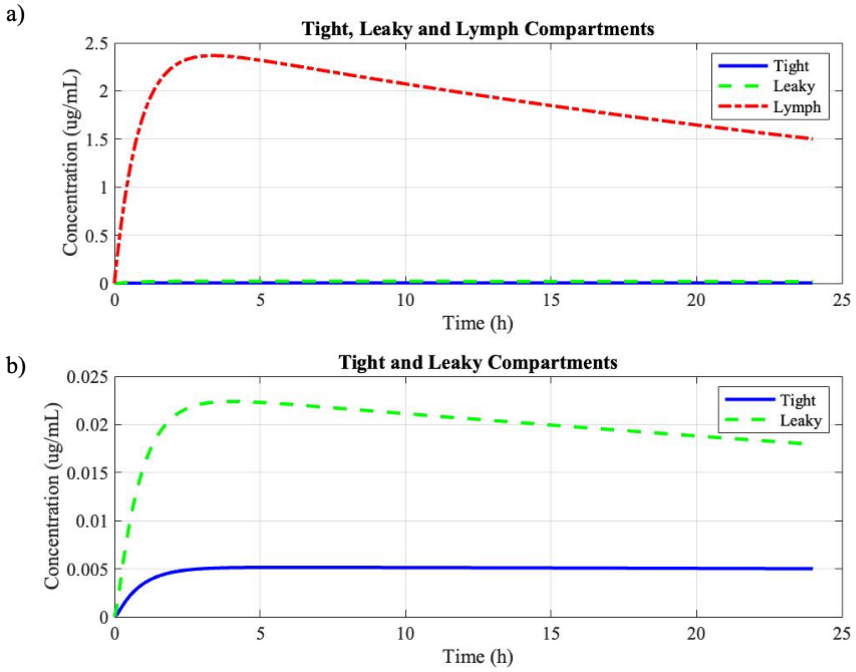


Figure 7.4. Curcumin concentration in (a) lymph, (b) tight and leaky compartments.

its distribution into these large-volume compartments. Similar to tight tissues, the leaky tissue concentration is also low, only it shows a slight rise. The low concentration in leaky tissues is expected since they are the primary sites of metabolism and elimination. Yet, being higher than the tight tissues is also expected because the flow rate to the leaky tissues, L_2, is higher than the flow rate to the tight tissues, L_1.

The simulation of these ODEs over a specified time period provides the concentration–time profiles for curcumin in each compartment. From the plasma concentration profile, the Area Under the Curve (AUC) can be calculated as

$$AUC_{\text{plasma}(0-24h)} = \int_0^{24} C_p \, dt \tag{7.6}$$

which is a key measure of systemic drug exposure.

The plasma AUC_{0-24h} was computed numerically using the trapezoidal rule by MATLAB. The calculated value of 2.74 μg·h/mL provides a quantitative measure of

the total systemic exposure of curcumin following oral administration under specified model conditions. This value is similar to the experimental studies [281] conducted by Vareed *et al.*, which used oral uptake of 12 mg.

Fança-Berthon studied with 30 healthy men and women who were administered 1500 mg standard turmeric extract. Their results show $C_{\max}$ is 0.3 μg/mL in plasma [294]. Our PBPK model, when the oral uptake is set to 1500 mg, gives the plasma $C_{\max}$ as 0.31 μg/mL (Figure 7.5), which aligns with the experimental data.

Cheng et al. developed a physiologically based pharmacokinetic (PBPK) model for curcumin and validated it against clinical data obtained from a study involving 15 healthy volunteers who received a single oral dose of 4 g of curcumin [295]. Their analysis employed a single one-compartment model to describe systemic disposition. When our model was adapted to simulate the same 4 g oral dose, the predicted maximum plasma concentration was higher than that reported by Cheng et al and the decline in plasma concentration was noticeably slower in their study. This discrepancy can be attributed primarily to differences in the assumed clearance values and the compartmental structure of the models. Nevertheless, the overall order of magnitude of the plasma concentration profiles was consistent between the two studies, supporting the general validity of our modeling approach.

To sum up, the plasma profile shows a fast, but very low systemic exposure, which is characteristic of curcumin's poor bioavailability. The lymphatic profile highlights the lymphatic system's role as a major absorption and distribution pathway for curcumin. The high and sustained concentration in the lymph compartment suggests that this pathway is essential for understanding curcumin's overall disposition and could be a key target for developing formulations to improve its therapeutic efficacy. The model provides a quantitative basis for the hypothesis that the lymphatic system is a major route of absorption for curcumin.

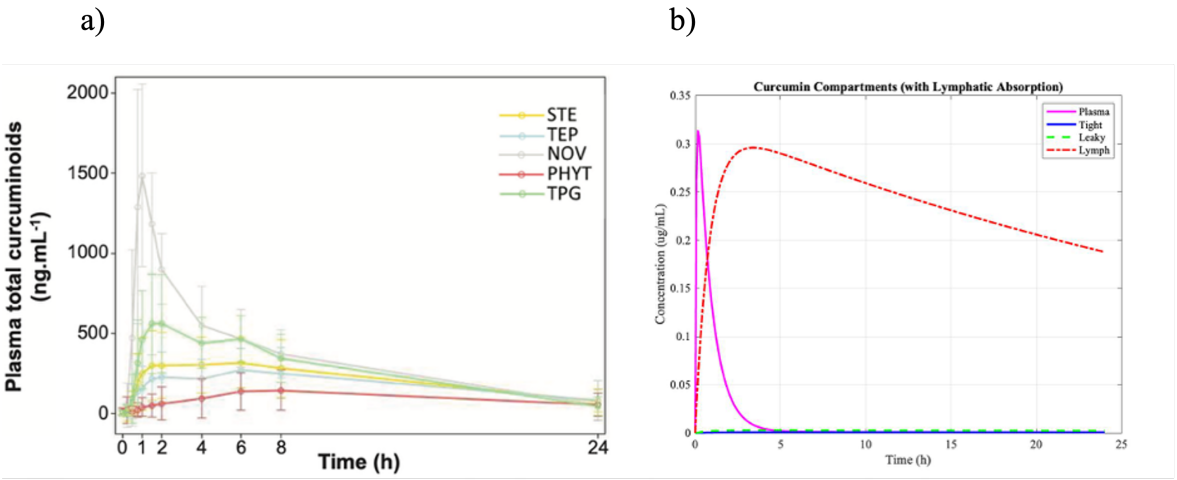


Figure 7.5. (a) Experimental vs (b) PBPK model curcumin plasma concentration (experimental figure is obtained from Fança-Berthon et al., and the standard turmeric extract (STE) is the yellow line.

Curcumin alone has many challenges, like low systemic availability due to poor water solubility, rapid metabolism, and low oral bioavailability. Conjugation or coadministration with AuNPs would be a promising solution to challenges. This approach can enhance the solubility of curcumin, protect it from degradation, and improve the transport through the lymphatic system. Consequently, conjugation or coadministration with AuNP may lead to more sustained tissue exposure. However, there is a challenge in integrating nanoformulations into PBPK models, requiring size-dependent permeability, cellular uptake, clearance pattern, etc., which are challenging to quantify. Since this information is lacking, predictive PBPK modeling for AuNP-based phytochemicals could not be achieved.

7.2. Sensitivity Analysis

To investigate the impact of input parameters on the pharmacokinetic behavior of curcumin, a sensitivity analysis is conducted. Given curcumin's known limitations in systemic bioavailability and its dual absorption via the blood and lymphatic routes, the analysis focused on two key absorption rate constants, $k_{a,blood}$ and $k_{a,lymph}$. These

parameters were individually varied over physiologically plausible ranges while keeping all other variables constant. The resulting concentration-time profiles were evaluated for the plasma, tight, leaky, and systemic lymph compartments to assess how changes in absorption kinetics influence the distribution and systemic exposure of curcumin. Key pharmacokinetic metrics such as C_{max}, T_{max}, and AUC were extracted to quantify the effect of parameter variation on curcumin's disposition (Table 7.2).

Increasing the rate of absorption into the blood causes a higher and earlier plasma peak (C_{max}) and a faster drop in concentration. However, the total systemic exposure (plasma AUC) remains unchanged (Figure 7.6). This is because the overall exposure is limited by the rapid clearance from the body, not how fast it enters the bloodstream. Crucially, a faster blood absorption rate leads to less drug being available for the lymphatic system, causing a significant drop in both the peak concentration and total exposure in the lymph.

Increasing the rate of lymphatic absorption has the opposite effect. It dramatically boosts the drug's concentration and total exposure in the lymph compartment while causing a slight decrease in plasma (Figure 7.7). This reinforces that the lymphatic system is the primary "sink" for curcumin, sequestering a large portion of the drug. The plasma concentration remains relatively stable (Table 7.3) because its kinetics are more dependent on the blood absorption rate and rapid clearance.

To evaluate the role of tissue permeability on the overall pharmacokinetics of curcumin, a sensitivity analysis was performed varying the reflection coefficients (σ_1 and σ_2) for the tight and leaky compartments. The analysis explores a range of values from 0 (no barrier to drug transfer) to 1 (complete permeability-limited barrier). This analysis aims to elucidate how the degree of permeability limitation affects the concentration–time profiles and key pharmacokinetic parameters ($C_{\max}$ and AUC) within plasma, lymph, tight, and leaky compartments.

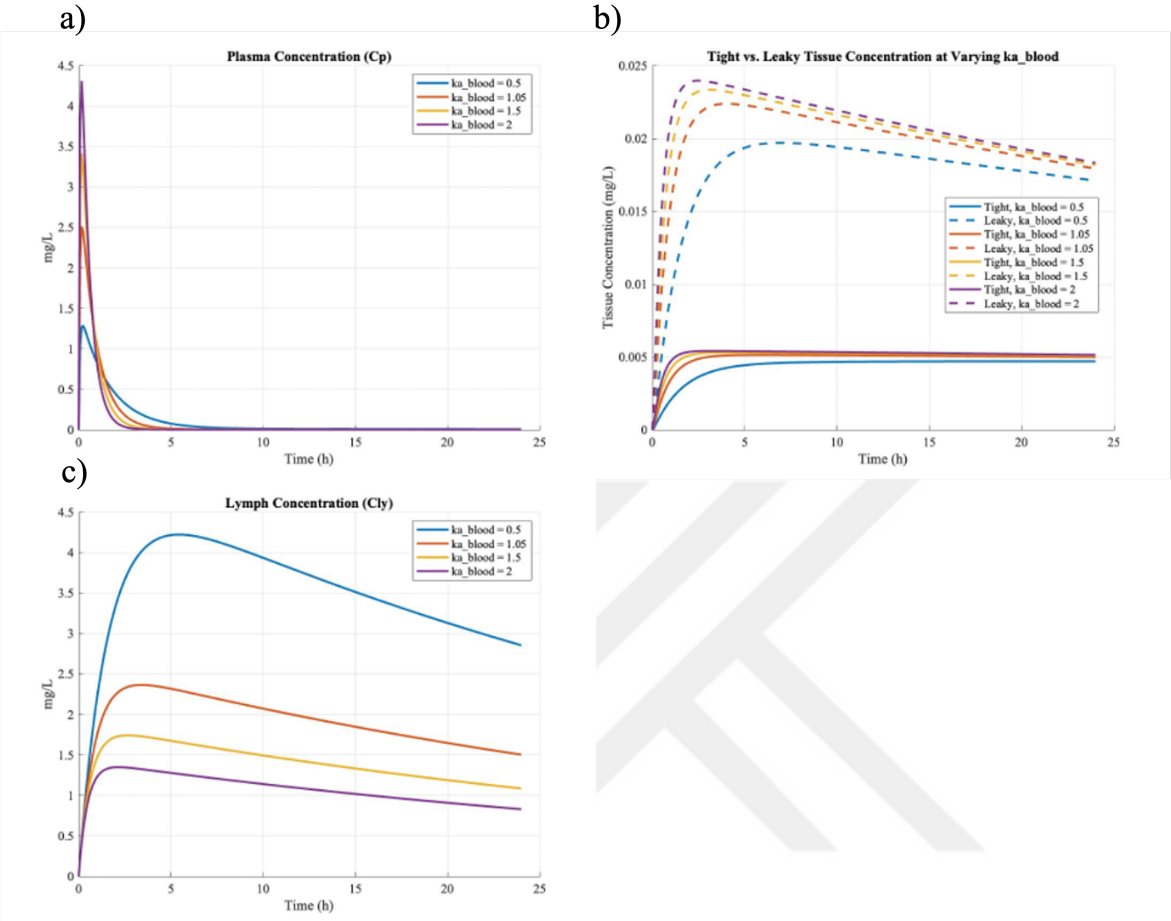


Figure 7.6. Concentration over time when varying $k_{a,\text{blood}}$, (a) plasma compartment, (b) tight and leaky compartments, (c) lymph compartment.

Based on these results, increasing the permeability barrier for drug transfer between the plasma and the peripheral tissues has a significant and direct impact on the tissue compartments but a negligible effect on the plasma and lymph compartments. As σ increases from 0 to 1, the total exposure (AUC) and peak concentration ($C_{\max}$) in both the tight and leaky tissues decrease dramatically, eventually dropping to zero when $\sigma = 1$, which represents a complete barrier to transfer (Figure 7.8). This suggests that σ is a key parameter controlling tissue distribution. In contrast, pharmacokinetic parameters for both the plasma and lymph compartments remain stable across all the varied σ values (Table 7.4). This suggests that for a fast-clearing drug like curcumin, the overall systemic exposure (plasma AUC) is limited by rapid clearance and extensive lymphatic absorption, not by the rate at which it distributes into peripheral tissues.

Table 7.2. $C_{\max}$, $T_{\max}$ and AUC when varied $k_{a,\text{blood}}$ and constant $k_{a,\text{lymph}} = 0.131$ h^{-1}.

$k_{a,\text{blood}}$ (h^{-1})	**Plasma**			$k_{a,\text{blood}}$ (h^{-1})	**Lymph**		
	$C_{\max}$ (μg/mL)	$T_{\max}$ (h)	AUC (μg·h/mL)		$C_{\max}$ (μg/mL)	$T_{\max}$ (h)	AUC (μg·h/mL)
0.50	1.291	0.24	2.58	0.50	4.225	5.46	83.74
1.05	2.508	0.16	2.74	1.05	2.367	3.37	45.96
1.50	3.412	0.16	2.79	1.50	1.744	2.65	33.58
2.00	4.311	0.16	2.81	2.00	1.351	2.17	25.86
$k_{a,\text{blood}}$ (h^{-1})	**Tight**			$k_{a,\text{blood}}$ (h^{-1})	**Leaky**		
	$C_{\max}$ (μg/mL)	$T_{\max}$ (h)	AUC (μg·h/mL)		$C_{\max}$ (μg/mL)	$T_{\max}$ (h)	AUC (μg·h/mL)
0.50	0.005	21.91	0.10	0.50	0.020	6.98	0.42
1.05	0.005	5.94	0.12	1.05	0.022	4.01	0.48
1.50	0.005	4.25	0.12	1.50	0.023	3.13	0.49
2.00	0.005	3.29	0.12	2.00	0.024	2.49	0.50

The stability of the lymphatic profile further validates its role as a primary absorption and storage compartment, largely independent of the kinetics of the tight and leaky tissues.

The extremely low oral bioavailability of curcumin significantly limits its therapeutic potential. As this PBPK model demonstrates, low systemic exposure is primarily due to systemic clearance and the diversion of a significant portion of the drug into the lymphatic system, which returns to the plasma very slowly. For this reason, delivering curcumin in a conjugated form to nanocarrier systems like gold nanoparticles (AuNPs) presents a promising approach to increase its systemic exposure. AuNPs can increase curcumin's solubility due to their lipophilic structure and enhance lymphatic absorption, allowing the drug to bypass metabolism in the gastrointestinal system. However, the complex biological interactions of curcumin conjugated to nanocarriers

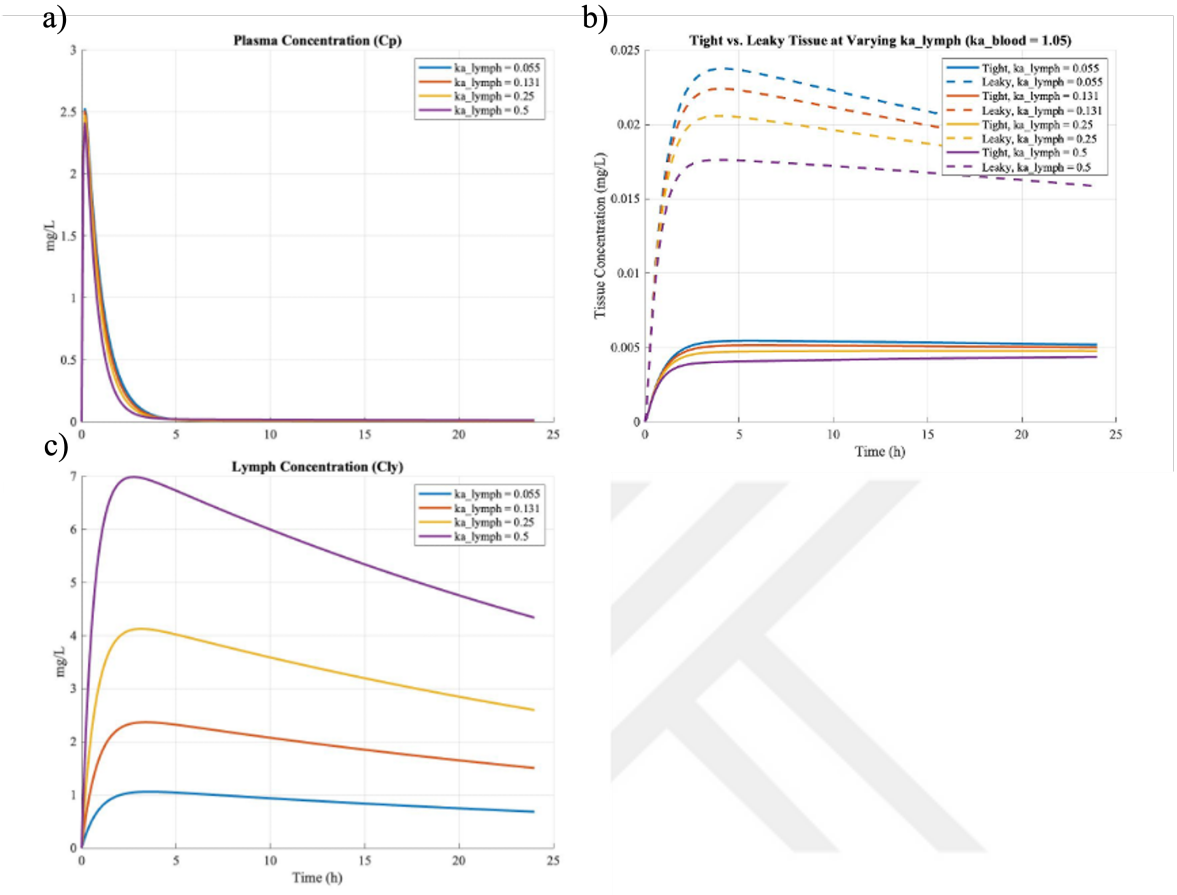


Figure 7.7. Concentration over time when varying $k_{a,\text{lymph}}$, (a) plasma compartment, (b) tight and leaky compartments, (c) lymph compartment.

like AuNPs require the inclusion of additional parameters, such as the nanoparticle's size, surface modification, and targeted tissue/cell types for integration into these types of PBPK models. These complexities make it challenging to consistently obtain reliable and comprehensive results using standard PBPK modeling approaches.

Table 7.3. $C_{\max}$, $T_{\max}$, and AUC when varied $k_{a,\text{lymph}}$, and constant $k_{a,\text{blood}} = 1.05\ \text{h}^{-1}$.

$k_{a,\text{lymph}}$ (h^{-1})	**Plasma**			$k_{a,\text{lymph}}$ (h^{-1})	**Lymph**		
	$C_{\max}$ **(μg/mL)**	$T_{\max}$ **(h)**	**AUC (μg·h/mL)**		$C_{\max}$ **(μg/mL)**	$T_{\max}$ **(h)**	**AUC (μg·h/mL)**
0.055	2.528	0.16	2.85	0.055	1.0598	3.61	20.61
0.131	2.508	0.16	2.74	0.131	2.367	3.37	45.96
0.25	2.474	0.16	2.60	0.25	4.126	3.13	79.77
0.50	2.409	0.16	2.38	0.50	6.984	2.17	134.3
$k_{a,\text{blood}}$ (h^{-1})	**Tight**			$k_{a,\text{blood}}$ (h^{-1})	**Leaky**		
	$C_{\max}$ **(μg/mL)**	$T_{\max}$ **(h)**	**AUC (μg·h/mL)**		$C_{\max}$ **(μg/mL)**	$T_{\max}$ **(h)**	**AUC (μg·h/mL)**
0.055	0.005	21.91	0.12	0.055	0.024	4.17	0.50
0.131	0.005	5.94	0.12	0.131	0.022	4.01	0.48
0.25	0.005	17.26	0.11	0.25	0.021	3.93	0.44
0.50	0.004	24.00	0.10	0.50	0.018	3.73	0.39

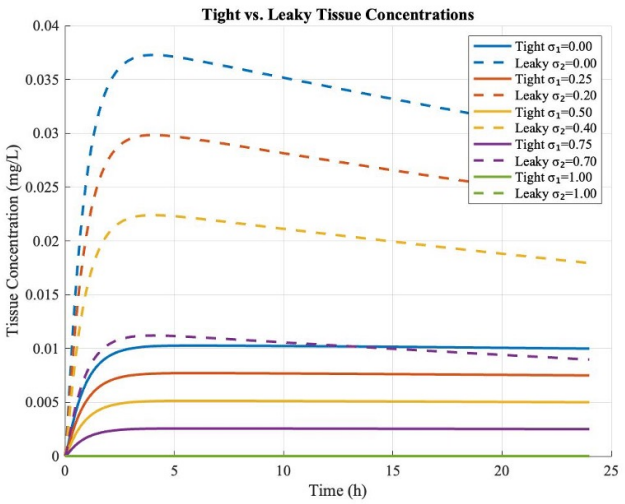


Figure 7.8. Concentration over time when varied σ_1 and σ_2

Table 7.4. $C_{\max}$, $T_{\max}$ and AUC when varied σ_1 and σ_2.

	Plasma				**Lymph**		
	$C_{\max}$ **(μg/mL)**	$T_{\max}$ **(h)**	**AUC (μg·h/mL)**		$C_{\max}$ **(μg/mL)**	$T_{\max}$ **(h)**	**AUC (μg·h/mL)**
$\sigma_1 = 0$ $\sigma_2 = 0$	2.505	0.16	2.74	$\sigma_1 = 0$ $\sigma_2 = 0$	2.367	3.37	45.96
$\sigma_1 = 0.25$ $\sigma_2 = 0.20$	2.506	0.16	2.74	$\sigma_1 = 0.25$ $\sigma_2 = 0.20$	2.367	3.37	45.93
$\sigma_1 = 0.50$ $\sigma_2 = 0.40$	2.508	0.16	2.74	$\sigma_1 = 0.50$ $\sigma_2 = 0.40$	2.367	3.37	45.90
$\sigma_1 = 0.75$ $\sigma_2 = 0.70$	2.509	0.16	2.75	$\sigma_1 = 0.75$ $\sigma_2 = 0.70$	2.366	3.37	45.86
$\sigma_1 = 1.0$ $\sigma_2 = 1.0$	2.511	0.16	2.75	$\sigma_1 = 1.0$ $\sigma_2 = 1.0$	2.366	3.37	45.82
	Tight				**Leaky**		
	$C_{\max}$ **(μg/mL)**	$T_{\max}$ **(h)**	**AUC (μg·h/mL)**		$C_{\max}$ **(μg/mL)**	$T_{\max}$ **(h)**	**AUC (μg·h/mL)**
$\sigma_1 = 0$ $\sigma_2 = 0$	0.010	5.94	0.24	$\sigma_1 = 0$ $\sigma_2 = 0$	0.037	4.01	0.79
$\sigma_1 = 0.25$ $\sigma_2 = 0.20$	0.008	5.94	0.18	$\sigma_1 = 0.25$ $\sigma_2 = 0.20$	0.030	4.01	0.63
$\sigma_1 = 0.50$ $\sigma_2 = 0.40$	0.005	5.94	0.12	$\sigma_1 = 0.50$ $\sigma_2 = 0.40$	0.022	4.01	0.48
$\sigma_1 = 0.75$ $\sigma_2 = 0.70$	0.003	5.94	0.06	$\sigma_1 = 0.75$ $\sigma_2 = 0.70$	0.011	4.01	0.24
$\sigma_1 = 1.0$ $\sigma_2 = 1.0$	0.000	0.00	0.00	$\sigma_1 = 1.0$ $\sigma_2 = 1.0$	0.000	0.00	0.00

8. CONCLUSIONS AND RECOMMENDATIONS

8.1. Conclusions

This thesis investigated the therapeutic potential and mechanistic effects of metallic nanoparticles (AuNPs), anti-cancer drug (temsirolimus), and phytochemicals against A375 melanoma cells in both conventional 2D and advanced 3D culture systems, with an emphasis on the role of cell-to-cell communication within the tumor microenvironment. In vivo, tumor progression and treatment resistance are profoundly shaped by dynamic interactions between cancer cells and surrounding stromal and immune cells, mediated by direct contact, extracellular matrix (ECM) cues, and the exchange of soluble factors and extracellular vesicles. Traditional 2D cultures fail to capture these interactions, whereas 3D systems incorporating multiple cell types and ECM-like scaffolds provide a more physiologically relevant context. Both gelatin–alginate and Matrigel–alginate hydrogels are used as hybrid biomaterials to mimic aspects of the extracellular matrix (ECM), but they differ significantly in composition, biological signaling, and application relevance. Gelatin–alginate (denatured collagen, rich in Arg–Gly–Asp (RGD) motifs) is better for defined, tunable, reproducible systems, while Matrigel–alginate is better for tumor-like, growth factor–rich (EGF, TGF-β, bFGF, VEGF, etc.) environments with adhesion ligands (laminin, collagen IV) to study invasion and drug response in cells. In this work, THP-1-derived M0 macrophages were integrated into melanoma cultures to model immune-tumor crosstalk and assess how these interactions influence treatment efficacy. Alongside experimental optimization of 3D bioprinted and hydrogel-based models, a PBPK model was developed for the phytochemical curcumin to contextualize in vitro findings within an in vivo pharmacokinetic framework.

8.1.1. Monoculture Studies (2D vs 3D)

8.1.1.1. Impact of AuNP and Temsirolimus Treatment on A375 Cell Viability.

- In 2D cultures, low concentrations of AuNPs generally showed minimal cytotoxicity, an effect that was highly dependent on both concentration and cell type. For A375-GFP cells, concentrations of AuNPs at 0.25 nM and above became toxic by day 3. This toxicity is likely an artifact of the measurement, as metal nanoparticles can quench nearby fluorophores through energy transfer or plasmonic effects, thus lowering the signal without actually inducing cell death. On the other hand, A375-WT cells tolerated AuNPs up to 2 nM without evident toxicity.
- In 3D systems with Matrigel-alginate hydrogels, control A375-WT cells (untreated) maintained high viability, underscoring the supportive ECM-like environment. After treatment with 1 nM AuNPs, A375-WT cells still remained unaffected, i.e., around 70% viability by day 5. AuNPs maintained high viability but also subtly modulated the hydrogel microenvironment via protein corona formation and ECM component interactions. In 3D-bioprinted A375-WT cells within 8G4A hydrogel, 1 nM AuNP showed toxicity by day 5. On the other hand, in 3D-bioprinted A375-WT cells within Matrigel-alginate, 1 nM AuNP decreased the viability only to 40% by day 5. The 3D system provides a more realistic and thus superior model; its ability to demonstrate treatment effects over a biologically relevant timeframe avoids the rapid and potentially misleading responses observed in 2D cultures.
- The anti-cancer drug temsirolimus is a kinase inhibitor and blocks cell division by inhibiting the activity of mTOR signaling. Inhibition of mTOR activity results in growth arrest in treated tumor cells. In a 2D system with A375-GFP cells, the anti-cancer drug temsirolimus (500 nM) alone was non-toxic, whereas with A375-WT cells, 500 nM temsirolimus caused significant viability loss by day 2. In 3D hydrogel cultures, 500 nM temsirolimus was toxic for A375-WT cells, whereas 4 nM temsirolimus was ineffective. However, in 3D Matrigel-alginate cultures, it took 5 days to achieve the same toxic effect of temsirolimus that is observed

in 2D cultures after 2 days. For A375-WT cells bioprinted with 8G4A hydrogel, 500 nM temsirolimus had a toxic effect by day 5. On the other hand, in A375-WT cells 3D-bioprinted within Matrigel-alginate, 500 nM temsirolimus showed a mildly toxic effect by day 5.

- When temsirolimus and AuNP were coadministered to A375-GFP cells at high concentrations in 2D system, they had a toxic effect on the cells. Similarly, coadministration of 500 nM temsirolimus and 1 nM AuNP on A375-WT cells decreased the viability by 50% by day 1, so the synergistic effect of AuNP and temsirolimus was greater than the single treatment. Possibly, the drug's bioavailability and uptake have changed. On the other hand, in 3D and 3D bioprinted systems, AuNP and temsirolimus coadministration decreased the viability to 50% by day 5, both in 8G4A and Matrigel-alginate, showing a slower cytotoxicity than the 2D systems.
- During 3D and 3D bioprinting treatment, ROS levels of AuNP and temsirolimus-treated cells were lower than those of the control cells; however, the ROS levels increased by day 5 in both. ROS levels in the case of coadministration of AuNPs and anti-cancer drug remained lower than the control cells in the 3D system, while it was much higher than the control cells in 3D bioprinted systems with 8G4A and Matrigel. Bioprinting may increase the stress levels of the cells. Also, the synergistic effects of AuNP and temsirolimus on A375 melanoma cells may also lead to apoptosis in 3D bioprinted systems that mimic the cells' natural environment.

8.1.1.2. Treatment of A375-WT Cells with Curcumin and Other Phytochemicals.

- Curcumin induced significant viability reduction in 2D A375-WT cell cultures, probably linked to inhibition of NF-κB, PI/3K/Akt, and MAPK pathways. The other phytochemicals EGCG, Betulin, and Thymoquinone showed dose-dependent cytotoxicity, where curcumin showed toxicity by day 1 at 40 μM on 2D cell cultures. When the A375-WT cells were bioprinted in Matrigel-alginate, their viability decreased to 10% by day 2 upon curcumin treatment, while it decreased to

35% by day 1 when the cells were bioprinted in 8G4A and administered with 40 μM curcumin.

- Matrigel–Alginate is a more supportive matrix for A375 cells under normal conditions (higher viability, higher mitochondrial potential-Rhodamine signaling). In treatment cases with phytochemicals, Curcumin cytotoxicity is stronger in Matrigel–Alginate (cells die faster, with only slight mitochondrial decrease which may indicate rapid necrosis or non-mitochondrial cell death). Gelatin-alginate (8G4A) hydrogel shows slower curcumin-induced death with clearer mitochondrial involvement (decreased rhodamine), suggesting apoptosis-like mechanisms.
- In 3D systems (3D hydrogels and 3D bioprinted scaffolds), with AuNP coadministration, curcumin sharply decreased the viability of A375-WT, the AuNPs amplifying the effect through improved solubility, uptake, and enhanced ROS generation.
- In 2D systems, the conjugated AuNP/Curc and AuNP/EGCG showed a significant increase in viability within a day for all concentrations. Thymoquinone conjugates had the lowest viability from the first day onwards and had the most toxic and rapid effect on A375-WT cells, indicating the kinetics of conjugated forms are independent of pure phytochemical effect on cells.
- In a 3D bioprinted system, AuNP/Curc conjugation maintained viability at 30% for 5 days. A high number of cells showed relatively high ROS levels starting from day 3. This corresponded to a decrease in the number of cells exhibiting high mitochondrial membrane potential, as measured by rhodamine 123 analysis, which directly correlated with a decline in overall cell viability. The sustained cytotoxicity is linked to increased ROS generation from day 3 onward and a corresponding decrease in mitochondrial membrane potential. This suggests the conjugate induces cell death through oxidative stress and mitochondrial damage. This mechanism contrasts with the initial proliferative effects observed in 2D systems and highlights the importance of the 3D environment in revealing the true cytotoxic potential of the conjugate.
- When curcumin was coadministered with the anti-cancer drug temsirolimus, this coadministration showed the most rapid and pronounced cytotoxicity, pointing

to strong pathway co-inhibition effects in both 2D and 3D systems.

- The phytochemicals curcumin and thymoquinone had antiproliferative effects on melanoma cells in single administration and synergistic effects when coadministered with AuNPs or anti-cancer drug temsirolimus, amplifying the desired drug response.

8.1.1.3. Treatment (AuNP, Temsirolimus and curcumin) Effects on M0 macrophages.

- M0 macrophages are known as naïve macrophages and are high-risk immune cell types linked to poor patient outcomes. They are essential components of the innate immune system that engulf and digest cancer cells. 1 nM AuNP-treated M0 macrophages showed similar viability to the control group when they were 3D bioprinted in 8G4A, so AuNPs were non-toxic to the M0 cells. M0 cells had a similar ratio of ROS+ cells and a similar membrane potential to control cells. Within the Matrigel-alginate hydrogel, M0 cells showed stable viability when administered 1 nM AuNP.
- Viability of M0 macrophages bioprinted in 8G4A was around 20% on the first day of 500 nM temsirolimus treatment and decreased further by day 3. On the other hand, M0 viability within 3D matrigel-alginate hydrogel started to decrease by day 5 when administered with 500 nM temsirolimus. This suggests that bioprinting M0 macrophages induces a more rapid cytotoxic effect, likely due to shear stress or other physical forces during the printing process.
- When the AuNPs and temsirolimus were coadministered, an additional effect of toxicity on M0 was observed in the 3D matrigel-alginate system. 40 μM curcumin only and coadministered with 1 nM AuNP increased the viability of M0, which was 3D bioprinted in 8G4A hydrogel. 500 nM curcumin on M0 cells within Matrigel-alginate hydrogel decreased the viability by day 3, while coadministration with 1 nM AuNP decreased the viability rapidly by day 1.
- In 3D matrigel-alginate system, control ROS levels increased by day 5, which may reflect baseline macrophage activation within the 3D ECM, independent of treatment. Single treatments (1 nM AuNP, 500 nM temsirolimus, 500 nM curcumin)

were not acutely cytotoxic to M0 cells, while they induced ROS levels. ROS intensity of M0 cells was particularly high when they were coadministered with AuNP and curcumin, and AuNP and temsirolimus, indicating a strong oxidative burst, while it drops by day 5, suggesting oxidative collapse due to cell death.

8.1.2. Impact of Coculture Compared to Monoculture Conditions

- In 2D coculture experiments, seeding M0-mCherry cells at a constant density of 2×10^6 per well with A375-GFP cells at 1×10^5 – 2×10^5 per well resulted in balanced co-cultures after two days, maintaining viability for both cell types. M0 cells exhibited reduced cell death in the 2D co-culture experiments, as evidenced by fluorescence imaging, likely due to the absence of external stressors such as reseeding into insert plates, which can impose mechanical and environmental disturbances.
- In 3D coculture experiments without any treatment, A375-WT cells in 8G4A hydrogel showed a decrease in viability to 70% by day 3, while it remained 90% when it was in monoculture. The slight decrease in viability in coculture may be due to the secretion of pro-inflammatory cytokines from M0 cells when they were faced with the tumor cells.
- When the 3D coculture was treated with 40 μM curcumin or thymoquinone, the viability of the A375-WT cells decreased to around 40% by day 3, which was double that of the monocultured A375-WT cells in 8G4A hydrogel for both curcumin and thymoquinone treatments. This result is interesting since it was expected to reduce the viability of tumor cells; however, macrophage involvement within the ECM changes the uptake or secretion of apoptotic mediators.
- A comparison of A375 cells alone vs. A375 cells co-cultured with M0 macrophages in gelatin–alginate hydrogel indicates that macrophages make melanoma cells less viable but raise mitochondrial activity, possibly reflecting a stress adaptation. However, curcumin restores some viability in the presence of macrophages but reduces mitochondrial activity in all contexts. This suggests curcumin may exert dual roles: directly cytotoxic to melanoma cells in monoculture, but immunomod-

ulatory in co-culture, altering macrophage–melanoma interactions.

- Due to their architectural similarity to in vivo tissues, 3D coculture systems, mimicking tumor microenvironment, offer a more physiologically relevant in vitro system for cancer research and provide opportunities for identifying therapeutic targets. Another benefit of this 3D co-culture condition is that it allows for the evaluation of cell-to-cell interactions in the cancer microenvironment.

8.1.3. PBPK Model

- Curcumin showed poor systemic exposure, with rapid plasma concentration increase and sharp decline, and tissue levels due to rapid clearance and limited absorption via the blood, and the plasma $C_{\max}$ values aligned with experimental results.
- Lymphatic absorption was the dominant route, providing sustained exposure and acting as a drug reservoir, especially at high absorption rate of lymph, $k_{a,\text{lymph}}$.
- Increasing absorption rate of plasma, $k_{a,\text{blood}}$, enhanced plasma peak levels but reduced lymphatic and tissue exposure, indicating competition between pathways.
- Tissue penetration was limited, especially in tight compartments, and highly dependent on permeability factors (σ_1, σ_2, σ_L).

In conclusion, this thesis work indicates the potential of nanoparticle-drug-phytochemical combinations in melanoma therapy and emphasizes the benefits of combining macrophage-tumor cocultures with 3D bioprinted models for more predictive drug testing.

8.2. Limitations and Recommendations

- THP-1-derived macrophages did not achieve strong M1/M2 polarization, limiting model fidelity for immune modulation studies. Rather than THP-1, peripheral blood mononuclear cells (PBMC) can be used to optimize the polarization protocols.

- In 2D cocultures, both A375-GFP and mCherry-M0 were cultured in the same well, and the viability was observed by fluorescence change. This analysis can be enhanced by coculturing them in insert–transwell plates, and ROS levels, cytokine, and chemokine secretions can be measured.
- 2D coculture experiments with drug administration could not be achieved since A375 cells overgrow quickly, disrupting the co-culture balance, and making it hard to distinguish cell types to analyze the drug effect. Using a transwell insert would enable the investigation of paracrine signaling and indirect drug effects, providing a more controlled environment.
- Correlation of immune and tumor signaling was not measured since secreted cytokines in 3D ECM could not be obtained. Extracting cells from ECM can be optimized, and ELISA arrays can be used to map changes in inflammatory and pro-tumorigenic signaling between macrophages and tumor cells. The analyses can be optimized and enhanced by following cytokine and chemokine secretions, thereby better understanding the cell-to-cell communication.
- 3D cocultures lacked fibroblasts or endothelial cells, so the ECM remodeling and migration inhibitory effects were underestimated. Fibroblasts can be introduced to the coculture to mimic early melanoma states and examine their influence on immune cell migration and tumor proliferation.
- AuNP distribution within the ECM and uptake by cells could not be visualized due to technical inadequacies. TEM and confocal microscope imaging, or ICP-MS analyses, can help to quantify AuNP internalization and distribution in both A375 and macrophage cells.
- Since the M0 cells did not adhere to the insert plate completely, there was a loss of M0 cells while ROS and viability assessments were conducted in coculture experiments. Also, co-culture duration was restricted, so the ability to model long-term tumor-immune dynamics was reduced. Culturing both A375 and M0 cells together within a single hydrogel scaffold, with the two cell populations seeded in distinct, adjacent regions, rather than in separate compartments like transwell plates or on a 2D surface, would create a more realistic co-culture model, providing more physiologically relevant results.

- Our static 3D ECM models did not fully replicate *in vivo* microenvironment changes over time. Thus, 4D bioprinting, which is a dynamic model, can be explored with stimuli-responsive hydrogels to simulate ECM stiffening, degradation, immune-driven modeling, or cell response monitoring.

REFERENCES

1. Connor, C., Q. L. Carr, A. Sweazy, K. McMasters and H. Hao, "Clinical Approaches for the Management of Skin Cancer: A Review of Current Progress in Diagnosis, Treatment, and Prognosis for Patients with Melanoma", *Cancers*, Vol. 17, No. 4, pp. 707–729, 2025.

2. Sung, H., J. Ferlay, R. L. Siegel, M. Laversanne, I. Soerjomataram, A. Jemal and F. Bray, "Global Cancer Statistics 2020: GLOBOCAN Estimates of Incidence and Mortality Worldwide for 36 Cancers in 185 Countries", *CA: A Cancer Journal for Clinicians*, Vol. 71, No. 3, pp. 209–249, 2021.

3. Dantonio, P., M. Klein, M. R. V. Freire, C. Araujo, A. Chiacetti and R. Correa, "Exploring Major Signaling Cascades in Melanomagenesis: A Rationale Route for Targetted Skin Cancer Therapy", *Bioscience Reports*, Vol. 38, No. 5, p. 20180511, 2018.

4. Luebker, S. A. and S. A. Koepsell, "Diverse Mechanisms of BRAF Inhibitor Resistance in Melanoma Identified in Clinical and Preclinical Studies", *Frontiers in Oncology*, Vol. 9, p. 268, 2019.

5. Smalley, K. S. M., Z. Eroglu and V. K. Sondak, "Combination Therapies for Melanoma: A New Standard of Care?", *American Journal of Clinical Dermatology*, Vol. 17, No. 2, pp. 99–105, 2016.

6. Castellani, G., M. Buccarelli, M. B. Arasi, S. Rossi, M. E. Pisanu, M. Bellenghi, C. Lintas and C. Tabolacci, "BRAF Mutations in Melanoma: Biological Aspects, Therapeutic Implications, and Circulating Biomarkers", *Cancers*, Vol. 15, No. 16, p. 4026, 2023.

7. Ott, P. A. and N. Bhardwaj, "Impact of MAPK Pathway Activation in

BRAFV600 Melanoma on T Cell and Dendritic Cell Function", *Frontiers in Immunology*, Vol. 4, 2013.

8. Tsuchiya, S., M. Yamabe, Y. Yamaguchi, Y. Kobayashi, T. Konno and K. Tada, "Establishment and Characterization of a Human Acute Monocytic Leukemia Cell Line (THP-1)", *International Journal of Cancer*, Vol. 26, No. 2, pp. 171–176, 1980.

9. Arora, S., S. Singh, A. Mittal, N. Desai, D. K. Khatri, D. Gugulothu, V. Lather, D. Pandita and L. K. Vora, "Spheroids in Cancer Research: Recent Advances and Opportunities", *Journal of Drug Delivery Science and Technology*, Vol. 100, No. 2024, p. 106033, 2024.

10. Fontoura, J. C., C. Viezzer, F. G. dos Santos, R. A. Ligabue, R. Weinlich, R. D. Puga, D. Antonow, P. Severino and C. Bonorino, "Comparison of 2D and 3D Cell Culture Models for Cell Growth, Gene Expression and Drug Resistance", *Materials Science and Engineering: C*, Vol. 107, No. 2020, p. 110264, 2020.

11. Kapałczyńska, M., T. Kolenda, W. Przybyła, M. Zajączkowska, A. Teresiak, V. Filas, M. Ibbs, R. Bliźniak, Łukasz Łuczewski and K. Lamperska, "2D and 3D Cell Cultures – a Comparison of Different Types of Cancer Cell Cultures", *Archives of Medical Science*, Vol. 14, No. 4, p. 18380, 2016.

12. Lovitt, C., T. Shelper and V. Avery, "Advanced Cell Culture Techniques for Cancer Drug Discovery", *Biology*, Vol. 3, No. 2, pp. 345–367, 2014.

13. D'Costa, K., M. Kosic, A. Lam, A. Moradipour, Y. Zhao and M. Radisic, "Biomaterials and Culture Systems for Development of Organoid and Organ-on-a-Chip Models", *Annals of Biomedical Engineering*, Vol. 48, No. 7, pp. 2002–2027, 2020.

14. Knight, E. and S. Przyborski, "Advances in 3D cell culture technologies enabling tissue-like structures to be created in vitro", *Journal of Anatomy*, Vol. 227, No. 6,

pp. 746–756, 2015.

15. Giuseppe, M. D., N. Law, B. Webb, R. A. Macrae, L. J. Liew, T. B. Sercombe, R. J. Dilley and B. J. Doyle, "Mechanical Behaviour of Alginate-Gelatin Hydrogels for 3D Bioprinting", *Journal of the Mechanical Behavior of Biomedical Materials*, Vol. 79, No. September 2017, pp. 150–157, 2018.

16. Parihar, A., D. S. Parihar, K. Gaur, N. Arya, V. K. Choubey and R. Khan, "3D Bioprinting for Drug Development and Screening: Recent Trends Towards Personalized Medicine", *Hybrid Advances*, Vol. 7, p. 100320, 2024.

17. Gao, G. and X. Cui, "Three-Dimensional Bioprinting in Tissue Engineering and Regenerative Medicine", *Biotechnology Letters*, Vol. 38, No. 2, pp. 203–211, 2016.

18. Murphy, S. V., P. D. Coppi and A. Atala, "Opportunities and Challenges of Translational 3D Bioprinting", *Nature Biomedical Engineering*, Vol. 4, No. 4, pp. 370–380, 2019.

19. Chatzinikolaidou, M., "Cell Spheroids: The New Frontiers in in Vitro Models for Cancer Drug Validation", *Drug Discovery Today*, Vol. 21, No. 9, pp. 1553–1560, 2016.

20. Mengus, C., M. G. Muraro, V. Mele, F. Amicarella, C. Manfredonia, F. Foglietta, S. Muenst, S. D. Soysal, G. Iezzi and G. C. Spagnoli, "In Vitro Modeling of Tumor–Immune System Interaction", *ACS Biomaterials Science & Engineering*, Vol. 4, No. 2, pp. 314–323, 2018.

21. Hirt, C., A. Papadimitropoulos, V. Mele, M. G. Muraro, C. Mengus, G. Iezzi, L. Terracciano, I. Martin and G. C. Spagnoli, "In Vitro 3D Models of Tumor-Immune System Interaction", *Advanced Drug Delivery Reviews*, Vol. 79-80, pp. 145–154, 2014.

22. Öztürk, S. E., E. K. Tilki, M. Dikmen and Z. Cantürk, "Comparison of the

Apoptotic Effects of Bortezomib Using 2D and 3D Co-Culture Models of THP-1 Derived Macrophage and A549 Lung Cancer", *Journal of Research in Pharmacy*, Vol. 25, No. 4, pp. 490–499, 2021.

23. Mostafa, M. A. H. and H. M. J. Khojah, "Nanoparticle-Based Delivery Systems for Phytochemicals in Cancer Therapy: Molecular Mechanisms, Clinical Evidence, and Emerging Trends", *Drug Development and Industrial Pharmacy*, Vol. 51, pp. 1–17, 2025.

24. Aljabali, A. A. A., M. A. Obeid, R. M. Bashatwah, E. Qnais, O. Gammoh, A. Alqudah, V. Mishra, Y. Mishra, M. A. Khan, S. Parvez, M. El-Tanani and T. Hatahet, "Phytochemicals in Cancer Therapy: A Structured Review of Mechanisms, Challenges, and Progress in Personalized Treatment", *Chemistry & Biodiversity*, Vol. 22, No. 8, p. e202402479, 2025.

25. Eiznhamer, D. A. and Z.-Q. Xu, "Betulinic Acid: A Promising Anticancer Candidate.", *IDrugs*, Vol. 7, No. 4, pp. 359–73, 2004.

26. Ilhan, S., F. Oguz and H. Atmaca, "Thymoquinone and Cancer: Mechanisms and Potential Therapeutic Applications", *Studies in Natural Products Chemistry*, Vol. 84, pp. 67–99, 2025.

27. Talib, W. H., M. M. Baban, M. F. Bulbul, E. Al-Zaidaneen, A. Allan, E. W. Al-Rousan, R. H. Y. Ahmad, H. K. Alshaeri, M. M. Alasmari and D. Law, "Natural Products and Altered Metabolism in Cancer: Therapeutic Targets and Mechanisms of Action", *International Journal of Molecular Sciences*, Vol. 25, No. 17, p. 9593, 2024.

28. Dykman, L., B. Khlebtsov and N. Khlebtsov, "Drug Delivery Using Gold Nanoparticles", *Advanced Drug Delivery Reviews*, Vol. 216, p. 115481, 2025.

29. Singh, P., S. Pandit, V. Mokkapati, A. Garg, V. Ravikumar and I. Mijakovic,

"Gold Nanoparticles in Diagnostics and Therapeutics for Human Cancer", *International Journal of Molecular Sciences*, Vol. 19, No. 7, p. 1979, 2018.

30. Kamiloglu, S., G. Sari, T. Ozdal and E. Capanoglu, "Guidelines for Cell Viability Assays", *Food Frontiers*, Vol. 1, No. 3, pp. 332–349, 2020.

31. Sakamuru, S., M. S. Attene-Ramos and M. Xia, "Mitochondrial Membrane Potential Assay", *Methods in Molecular Biology*, Vol. 1473, pp. 17–22, 2016.

32. Murphy, M. P., H. Bayir, V. Belousov, C. J. Chang, K. J. A. Davies, M. J. Davies, T. P. Dick, T. Finkel, H. J. Forman, Y. Janssen-Heininger, D. Gems, V. E. Kagan, B. Kalyanaraman, N.-G. Larsson, G. L. Milne, T. Nyström, H. E. Poulsen, R. Radi, H. V. Remmen, P. T. Schumacker, P. J. Thornalley, S. Toyokuni, C. C. Winterbourn, H. Yin and B. Halliwell, "Guidelines for Measuring Reactive Oxygen Species and Oxidative Damage in Cells and in Vivo", *Nature Metabolism*, Vol. 4, No. 6, pp. 651–662, 2022.

33. Zhuang, X. and C. Lu, "PBPK Modeling and Simulation in Drug Research and Development", *Acta Pharmaceutica Sinica B*, Vol. 6, No. 5, pp. 430–440, 2016.

34. Fisher, J. W., J. M. Gearhart and L. Zhoumeng (Editors), *Physiologically Based Pharmacokinetic (PBPK) Modeling*, Elsevier, 2020.

35. Hsieh, M.-Y., S.-K. Hsu, T.-Y. Liu, C.-Y. Wu and C.-C. Chiu, "Melanoma Biology and Treatment: A Review of Novel Regulated Cell Death-Based Approaches", *Cancer Cell International*, Vol. 24, No. 1, p. 63, 2024.

36. Siegel, R. L., K. D. Miller and A. Jemal, "Cancer statistics, 2020", *CA: A Cancer Journal for Clinicians*, Vol. 70, No. 1, pp. 7–30, 2020.

37. Occhi, G., S. Barollo, D. Regazzo, L. Bertazza, F. Galuppini, V. Guzzardo, M. L. Jaffrain-Rea, F. Vianello, D. Ciato, F. Ceccato, S. Watutantrige-Fernando, A. Bisognin, S. Bortoluzzi, G. Pennelli, M. Boscaro, C. Scaroni and C. Mian,

"A Constitutive Active MAPK/ERK Pathway Due to BRAFV600E Positively Regulates AHR Pathway in PTC.", *Oncotarget*, Vol. 6, No. 31, pp. 32104–14, 2015.

38. Cantwell-Dorris, E. R., J. J. O'Leary and O. M. Sheils, "BRAFV600E: Implications for Carcinogenesis and Molecular Therapy", *Molecular Cancer Therapeutics*, Vol. 10, No. 3, pp. 385–394, 2011.

39. Long, G. V., D. Stroyakovskiy, H. Gogas, E. Levchenko, F. de Braud, J. Larkin, C. Garbe, T. Jouary, A. Hauschild, J. J. Grob, V. C. Sileni, C. Lebbe, M. Mandalà, M. Millward, A. Arance, I. Bondarenko, J. B. Haanen, J. Hansson, J. Utikal, V. Ferraresi, N. Kovalenko, P. Mohr, V. Probachai, D. Schadendorf, P. Nathan, C. Robert, A. Ribas, D. J. DeMarini, J. G. Irani, M. Casey, D. Ouellet, A.-M. Martin, N. Le, K. Patel and K. Flaherty, "Combined BRAF and MEK Inhibition versus BRAF Inhibition Alone in Melanoma", *New England Journal of Medicine*, Vol. 371, No. 20, pp. 1877–1888, 2014.

40. Robert, C., B. Karaszewska, J. Schachter, P. Rutkowski, A. Mackiewicz, D. Stroiakovski, M. Lichinitser, R. Dummer, F. Grange, L. Mortier, V. Chiarion-Sileni, K. Drucis, I. Krajsova, A. Hauschild, P. Lorigan, P. Wolter, G. V. Long, K. Flaherty, P. Nathan, A. Ribas, A.-M. Martin, P. Sun, W. Crist, J. Legos, S. D. Rubin, S. M. Little and D. Schadendorf, "Improved Overall Survival in Melanoma with Combined Dabrafenib and Trametinib", *New England Journal of Medicine*, Vol. 372, No. 1, pp. 30–39, 2015.

41. Flaherty, K. T., J. R. Infante, A. Daud, R. Gonzalez, R. F. Kefford, J. Sosman, O. Hamid, L. Schuchter, J. Cebon, N. Ibrahim, R. Kudchadkar, H. A. Burris, G. Falchook, A. Algazi, K. Lewis, G. V. Long, I. Puzanov, P. Lebowitz, A. Singh, S. Little, P. Sun, A. Allred, D. Ouellet, K. B. Kim, K. Patel and J. Weber, "Combined BRAF and MEK Inhibition in Melanoma with BRAF V600 Mutations", *New England Journal of Medicine*, Vol. 367, No. 18, pp. 1694–1703, 2012.

42. Larkin, J., P. A. Ascierto, B. Dréno, V. Atkinson, G. Liszkay, M. Maio, M. Mandalà, L. Demidov, D. Stroyakovskiy, L. Thomas, L. de la Cruz-Merino, C. Dutriaux, C. Garbe, M. A. Sovak, I. Chang, N. Choong, S. P. Hack, G. A. McArthur and A. Ribas, "Combined Vemurafenib and Cobimetinib in BRAF - Mutated Melanoma", *New England Journal of Medicine*, Vol. 371, No. 20, pp. 1867–1876, 2014.

43. Wellbrock, C. and I. Arozarena, "The Complexity of the ERK/MAP-Kinase Pathway and the Treatment of Melanoma Skin Cancer", *Frontiers in Cell and Developmental Biology*, Vol. 4, p. 33, 2016.

44. Dancey, J. E., "Inhibitors of the Mammalian Target of Rapamycin", *Expert Opinion on Investigational Drugs*, Vol. 14, No. 3, pp. 313–328, 2005.

45. Margolin, K., J. Longmate, T. Baratta, T. Synold, S. Christensen, J. Weber, T. Gajewski, I. Quirt and J. H. Doroshow, "CCI-779 in Metastatic Melanoma", *Cancer*, Vol. 104, No. 5, pp. 1045–1048, 2005.

46. Tourneau, C. L., S. Faivre, M. Serova and E. Raymond, "mTORC1 Inhibitors: Is Temsirolimus in Renal Cancer Telling Us How They Really Work?", *British Journal of Cancer*, Vol. 99, No. 8, pp. 1197–1203, 2008.

47. Caporali, S., E. Alvino, P. M. Lacal, L. Levati, G. Giurato, D. Memoli, E. Caprini, G. C. A. Cappellini and S. D'atri, "Targeting the PI3K/AKT/mTOR Pathway Overcomes the Stimulating Effect of Dabrafenib on the Invasive Behavior of Melanoma Cells With Acquired Resistance to the BRAF Inhibitor", *International Journal of Oncology*, Vol. 49, No. 3, pp. 1164–1174, 2016.

48. Zeng, H., "mTOR Signaling in Immune Cells and Its Implications for Cancer Immunotherapy", *Cancer Letters*, Vol. 408, pp. 182–189, 2017.

49. Pal, H. C., K. M. Hunt, A. Diamond, C. A. Elmets and F. Afaq, "Phytochem-

icals for the Management of Melanoma", *Mini-Reviews in Medicinal Chemistry*, Vol. 16, No. 12, pp. 953–979, 2016.

50. Zheng, M., S. Ekmekcioglu, E. T. Walch, C.-H. Tang and E. A. Grimm, "Inhibition of Nuclear Factor-κB and Nitric Oxide by Curcumin Induces G2/M Cell Cycle Arrest and Apoptosis in Human Melanoma Cells", *Melanoma Research*, Vol. 14, No. 3, pp. 165–171, 2004.

51. Woo, J.-H., Y.-H. Kim, Y.-J. Choi, D.-G. Kim, K.-S. Lee, J. H. Bae, D. S. Min, J.-S. Chang, Y.-J. Jeong, Y. H. Lee, J.-W. Park and T. K. Kwon, "Molecular Mechanisms of Curcumin-Induced Cytotoxicity: Induction of Apoptosis Through Generation of Reactive Oxygen Species, Down-Regulation of Bcl-XL and IAP, the Release of Cytochrome C and Inhibition of Akt", *Carcinogenesis*, Vol. 24, No. 7, pp. 1199–1208, 2003.

52. Ghobadi, N. and A. Asoodeh, "Curcumin and Epigallocatechin-3-Gallate: Targeting Receptor Tyrosine Kinases and their Signaling Pathways in Cancer Therapy", *Current Pharmacology Reports*, Vol. 10, No. 12, pp. 297–311, 2024.

53. Singh, T. and S. K. Katiyar, "Green Tea Catechins Reduce Invasive Potential of Human Melanoma Cells by Targeting COX-2, PGE2 Receptors and Epithelial-to-Mesenchymal Transition", *PLoS ONE*, Vol. 6, No. 10, p. e25224, 2011.

54. Laszczyk, M., "Pentacyclic Triterpenes of the Lupane, Oleanane and Ursane Group as Tools in Cancer Therapy", *Planta Medica*, Vol. 75, No. 15, pp. 1549–1560, 2009.

55. Woo, C. C., A. P. Kumar, G. Sethi and K. H. B. Tan, "Thymoquinone: Potential Cure for Inflammatory Disorders and Cancer", *Biochemical Pharmacology*, Vol. 83, No. 4, pp. 443–451, 2012.

56. Liao, W., W. Xiang, F. F. Wang, R. Wang and Y. Ding, "Curcumin Inhib-

ited Growth of Human Melanoma A375 Cells via Inciting Oxidative Stress", *Biomedicine and Pharmacotherapy*, Vol. 95, pp. 1177–1186, 2017.

57. Chen, J., L. Li, J. Su, B. Li, T. Chen and Y.-S. Wong, "Synergistic Apoptosis-Inducing Effects on A375 Human Melanoma Cells of Natural Borneol and Curcumin.", *PloS One*, Vol. 9, No. 6, p. e101277, 2014.

58. Zhang, Y., Y. Li, Y. Lv and J. Wang, "Effect of Curcumin on the Proliferation, Apoptosis, Migration, and Invasion of Human Melanoma A375 Cells", *Genetics and Molecular Research*, Vol. 14, No. 1, pp. 1056–1067, 2015.

59. Liebscher, G., K. Vanchangiri, T. Mueller, K. Feige, J.-M. Cavalleri and R. Paschke, "In Vitro Anticancer Activity of Betulinic Acid and Derivatives Thereof on Equine Melanoma Cell Lines From Grey Horses and Invivo Safety Assessment of the Compound NVX-207 in Two Horses", *Chemico-Biological Interactions*, Vol. 246, pp. 20–29, 2016.

60. Coricovac, D., C. A. Dehelean, I. Pinzaru, A. Mioc, O.-M. Aburel, I. Macasoi, G. A. Draghici, C. Petean, C. Soica, M. Boruga, B. Vlaicu and M. D. Muntean, "Assessment of Betulinic Acid Cytotoxicity and Mitochondrial Metabolism Impairment in a Human Melanoma Cell Line", *International Journal of Molecular Sciences*, Vol. 22, No. 9, p. 4870, 2021.

61. Wróblewska-Łuczka, P., J. Cabaj, W. Bąk, J. Bargieł, A. Grabarska, A. Góralczyk and J. J. Łuszczki, "Additive Interactions Between Betulinic Acid and Two Taxanes in In Vitro Tests against Four Human Malignant Melanoma Cell Lines", *International Journal of Molecular Sciences*, Vol. 23, No. 17, p. 9641, 2022.

62. Coricovac, D., I. Pînzaru, Ștefana Avram, I. Macașoi, C. Șoica and C. Dehelean, "In Vitro and In Ovo Assessment of Betulinic Acid Antimelanoma Effect", *Timisoara Medical Journal*, Vol. 2020, No. 1, p. 6, 2020.

63. Chang, C. W., Y. H. Hsieh, W. E. Yang, S. F. Yang, Y. Chen and D. N. Hu, "Epigallocatechingallate Inhibits Migration of Human Uveal Melanoma Cells via Downregulation of Matrix Metalloproteinase-2 Activity and ERK1/2 Pathway", *BioMed Research International*, Vol. 2014, p. 141582, 2014.

64. Zhang, J., Z. Lei, Z. Huang, X. Zhang, Y. Zhou, Z. Luo, W. Zeng, J. Su, C. Peng and X. Chen, "Epigallocatechin-3-gallate(EGCG) Suppresses Melanoma Cell Growth and Metastasis by Targeting TRAF6 Activity.", *Oncotarget*, Vol. 7, No. 48, pp. 79557–79571, 2016.

65. Shen, Q., F. Tian, P. Jiang, Y. Li, L. Zhang, J. Lu and J. Li, "EGCG Enhances TRAIL-Mediated Apoptosis in Human Melanoma A375 Cell Line", *Journal of Huazhong University of Science and Technology - Medical Science*, Vol. 29, No. 6, pp. 771–775, 2009.

66. Wu, S., J. Han, D. Feskanich, E. Cho, M. J. Stampfer, W. C. Willett and A. A. Qureshi, "Citrus Consumption and Risk of Cutaneous Malignant Melanoma", *Journal of Clinical Oncology*, Vol. 33, No. 23, pp. 2500–2508, 2015.

67. Soriano-Lerma, A., V. Sánchez-Martín, J. Murciano-Calles, M. Ortiz-González, M. J. Tello-López, V. Pérez-Carrasco, Ángel Linde-Rodríguez, I. Ramírez-Macías, I. Gómez-Pìnto, I. López-Aliaga, M. Soriano and J. A. G. Salcedo, "In-Depth Analysis of the Mode of Action of Resveratrol: Genome-Wide Characterization of G-Quadruplex Binding Properties", *Cellular & Molecular Biology Letters*, Vol. 30, No. 1, p. 74, 2025.

68. Niles, R. M., M. McFarland, M. B. Weimer, A. Redkar, Y.-M. Fu and G. G. Meadows, "Resveratrol Is a Potent Inducer of Apoptosis in Human Melanoma Cells", *Cancer Letters*, Vol. 190, No. 2, pp. 157–163, 2003.

69. Zhao, J., Y. Liang, Z. Liu, K. Xu, H. Li, H. Zhang, A. Sui and J. Wang, "3d-printing Template Assisted 125I Seed Interstitial Brachytherapy for

Retroperitoneal Lymph Node Metastasis: Individual Template Design Method", *Brachytherapy*, Vol. 17, No. 4, p. S142, 2018.

70. Seo, S. Y., W. S. Ju, K. Kim, J. Kim, J. O. Yu, J.-S. Ryu, J.-S. Kim, H.-A. Lee, D.-B. Koo and Y.-K. Choo, "Quercetin Induces Mitochondrial Apoptosis and Downregulates Ganglioside GD3 Expression in Melanoma Cells", *International Journal of Molecular Sciences*, Vol. 25, No. 10, p. 5146, 2024.

71. Hussein, S. A., N. A. Ababneh, N. Tarawneh, M. A. Ismail, A. Awidi and S. Abdalla, "Antitumor Effects of Quercetin and Luteolin in A375 Cutaneous Melanoma Cell Line Are Mediated by Upregulation of P-ERK, c-Myc, and the Upstream GPER.", *Life (Basel, Switzerland)*, Vol. 15, No. 3, 2025.

72. Roman, A., A. Smeu, A. Lascu, C. A. Dehelean, I. A. Predescu, A. Motoc, C. Borza, G. A. Draghici, C. M. Trandafirescu, A. Anton and S. Ardelean, "Quercetin Enhances 5-Fluorouracil-Driven Cytotoxicity Dose-Dependently in A375 Human Melanoma Cells", *Life*, Vol. 14, No. 12, 2024.

73. Cao, H.-H., A. K.-W. Tse, H.-Y. Kwan, H. Yu, C.-Y. Cheng, T. Su, W.-F. Fong and Z.-L. Yu, "Quercetin Exerts Anti-Melanoma Activities and Inhibits STAT3 Signaling", *Biochemical Pharmacology*, Vol. 87, No. 3, pp. 424–434, 2014.

74. Arcidiacono, P., A. M. Stabile, F. Ragonese, A. Pistilli, S. Calvieri, U. Bottoni, A. Crisanti, R. Spaccapelo and M. Rende, "Anticarcinogenic Activities of Sulforaphane Are Influenced by Nerve Growth Factor in Human Melanoma A375 Cells", *Food and Chemical Toxicology*, Vol. 113, pp. 154–161, 2018.

75. Chiang, T.-C., B. Koss, L. J. Su, C. L. Washam, S. D. Byrum, A. Storey and A. J. Tackett, "Effect of Sulforaphane and 5-Aza-2'-Deoxycytidine on Melanoma Cell Growth.", *Medicines (Basel, Switzerland)*, Vol. 6, No. 3, 2019.

76. Kiani, B. H., W. K. Kayani, A. U. Khayam, E. Dilshad, H. Ismail and B. Mirza,

"Artemisinin and Its Derivatives: A Promising Cancer Therapy", *Molecular Biology Reports*, Vol. 47, No. 8, pp. 6321–6336, 2020.

77. Liu, W., H. Zhou, W. Lai, C. Hu, Q. Wang, C. Yuan, C. Luo, M. Yang, M. Hu, R. Zhang and G. Li, "Artesunate Induces Melanoma Cell Ferroptosis and Augments Antitumor Immunity Through Targeting Ido1", *Cell Communication and Signaling*, Vol. 22, No. 1, p. 378, 2024.

78. Wong, S. K., K. Y. Chin and S. Ima-Nirwana, "Quercetin as an Agent for Protecting the Bone: A Review of the Current Evidence", *International Journal of Molecular Sciences*, Vol. 21, No. 17, pp. 1–37, 2020.

79. Tuzimski, T., A. Petruczynik, B. Kaproń, T. Plech, A. Makuch-Kocka, D. Janiszewska, M. Sugajski, B. Buszewski and M. Szultka-Młyńska, "In Vitro and In Silico of Cholinesterases Inhibition and In Vitro and In Vivo Anti-Melanoma Activity Investigations of Extracts Obtained from Selected Berberis Species", *Molecules*, Vol. 29, No. 5, p. 1048, 2024.

80. Lin, S., S.-C. Tsai, C.-C. Lee, B.-W. Wang, J.-Y. Liou and K.-G. Shyu, "Berberine Inhibits HIF-1α Expression via Enhanced Proteolysis", *Molecular Pharmacology*, Vol. 66, No. 3, pp. 612–619, 2004.

81. Liu, Q., Q. Li, S. Xu, Q. Zheng and X. Cao, "Preparation and Properties of 3D Printed Alginate-Chitosan Polyion Complex Hydrogels for Tissue Engineering", *Polymers*, Vol. 10, No. 6, 2018.

82. Li, Q., H. Zhao, W. Chen and P. Huang, "Berberine Induces Apoptosis and Arrests the Cell Cycle in Multiple Cancer Cell Lines", *Archives of Medical Science*, Vol. 19, No. 5, pp. 1530–1537, 2023.

83. Dash, S. P., S. Gupta and P. P. Sarangi, "Monocytes and Macrophages: Origin, Homing, Differentiation, and Functionality During Inflammation", *Heliyon*,

Vol. 10, No. 8, p. e29686, 2024.

84. Austermann, J., J. Roth and K. Barczyk-Kahlert, "The Good and the Bad: Monocytes' and Macrophages' Diverse Functions in Inflammation", *Cells*, Vol. 11, No. 12, p. 1979, 2022.

85. Gordon, S. and A. Plüddemann, "Tissue Macrophages: Heterogeneity and Functions", *BMC Biology*, Vol. 15, No. 1, p. 53, 2017.

86. Italiani, P. and D. Boraschi, "From Monocytes to M1/M2 Macrophages: Phenotypical vs. Functional Differentiation", *Frontiers in Immunology*, Vol. 5, No. 514, pp. 1–22, 2014.

87. Murray, P. J. and T. A. Wynn, "Protective and Pathogenic Functions of Macrophage Subsets", *Nature Reviews Immunology*, Vol. 11, No. 11, pp. 723–737, 2011.

88. Su, J., Y. Song, Z. Zhu, X. Huang, J. Fan, J. Qiao and F. Mao, "Cell–cell Communication: New Insights and Clinical Implications", *Signal Transduction and Targeted Therapy*, Vol. 9, No. 1, p. 196, 2024.

89. Alberts, B., *Molecular Biology of the Cell*, Garland Science, 5th edn., 2008.

90. Hwang, I., "Cell-Cell Communication Via Extracellular Membrane Vesicles and Its Role in the Immune Response", *Molecules and Cells*, Vol. 36, No. 2, pp. 105–111, 2013.

91. Altan-Bonnet, G. and R. Mukherjee, "Cytokine-Mediated Communication: A Quantitative Appraisal of Immune Complexity", *Nature Reviews Immunology*, Vol. 19, No. 4, pp. 205–217, 2019.

92. Caligiuri, G. and D. A. Tuveson, "Activated Fibroblasts in Cancer: Perspectives and Challenges", *Cancer Cell*, Vol. 41, No. 3, pp. 434–449, 2023.

93. Lan, X., W. Li, K. Zhao, J. Wang, S. Li and H. Zhao, "Revisiting the Role of Cancer-Associated Fibroblasts in Tumor Microenvironment.", *Frontiers in immunology*, Vol. 16, p. 1582532, 2025.

94. Madsen, N. H., B. S. Nielsen, S. L. Nhat, S. Skov, M. Gad and J. Larsen, "Monocyte Infiltration and Differentiation in 3D Multicellular Spheroid Cancer Models", *Pathogens*, Vol. 10, No. 8, p. 969, 2021.

95. Kerneur, C., C. E. Cano and D. Olive, "Major Pathways Involved in Macrophage Polarization in Cancer", *Frontiers in Immunology*, Vol. 13, 2022.

96. Pieniazek, M., R. Matkowski and P. Donizy, "Macrophages in Skin Melanoma-the Key Element in Melanomagenesis", *Oncology Letters*, Vol. 15, No. 4, 2018.

97. Weagel, E. and C. Smith, "Macrophage Polarization and Its Role in Cancer", *Journal of Clinical & Cellular Immunology*, Vol. 06, No. 04, pp. 1–8, 2015.

98. Xiong, K., M. Qi, T. Stoeger, J. Zhang and S. Chen, "The Role of Tumor-Associated Macrophages and Soluble Mediators in Pulmonary Metastatic Melanoma", *Frontiers in Immunology*, Vol. 13, No. 3389, p. 1000927, 2022.

99. Staros, R., A. Michalak, K. Rusinek, K. Mucha, Z. Pojda and R. Zagożdżon, "Perspectives for 3D-Bioprinting in Modeling of Tumor Immune Evasion.", *Cancers*, Vol. 14, No. 13, p. 3126, 2022.

100. Mantovani, A., F. Marchesi, A. Malesci, L. Laghi and P. Allavena, "Tumour-Associated Macrophages as Treatment Targets in Oncology", *Nature Reviews Clinical Oncology*, Vol. 14, No. 7, pp. 399–416, 2017.

101. Xiang, X., A. Poliakov, C. Liu, Y. Liu, Z. Deng, J. Wang, Z. Cheng, S. V. Shah, G. Wang, L. Zhang, W. E. Grizzle, J. Mobley and H. Zhang, "Induction of Myeloid-derived Suppressor Cells by Tumor Exosomes", *International Journal of Cancer*, Vol. 124, No. 11, pp. 2621–2633, 2009.

102. Lu, J., X. Ye, F. Fan, L. Xia, R. Bhattacharya, S. Bellister, F. Tozzi, E. Sceusi, Y. Zhou, I. Tachibana, D. Maru, D. Hawke, J. Rak, S. A. Mani, P. Zweidler-McKay and L. Ellis, "Endothelial Cells Promote the Colorectal Cancer Stem Cell Phenotype through a Soluble Form of Jagged-1", *Cancer Cell*, Vol. 23, No. 2, pp. 171–185, 2013.

103. Lin, X., D. Bai, Z. Wei, Y. Zhang, Y. Huang, H. Deng and X. Huang, "Curcumin Attenuates Oxidative Stress in RAW264.7 Cells by Increasing the Activity of Antioxidant Enzymes and Activating the Nrf2-Keap1 Pathway", *PLoS ONE*, Vol. 14, No. 5, p. e0216711, 2019.

104. Noy, R. and J. Pollard, "Tumor-Associated Macrophages: From Mechanisms to Therapy", *Immunity*, Vol. 41, No. 1, pp. 49–61, 2014.

105. Deb, G., A. Cicala, A. Papadas and F. Asimakopoulos, "Matrix Proteoglycans in Tumor Inflammation and Immunity", *American Journal of Physiology-Cell Physiology*, Vol. 323, No. 3, pp. C678–C693, 2022.

106. Hussein, M. R., "Tumour-associated Macrophages and Melanoma Tumourigenesis: Integrating the Complexity", *International Journal of Experimental Pathology*, Vol. 87, No. 3, pp. 163–176, 2006.

107. Pizzurro, G. A., C. Liu, K. Bridges, A. F. Alexander, A. Huang, J. P. Baskaran, J. Ramseier, M. W. Bosenberg, M. Mak and K. Miller-Jensen, "3D Model of the Early Melanoma Microenvironment Captures Macrophage Transition into a Tumor-Promoting Phenotype", *Cancers*, Vol. 13, No. 18, p. 4579, 2021.

108. Klangprapan, J., G. R. Souza and J. N. Ferreira, "Bioprinting Salivary Gland Models and Their Regenerative Applications", *BDJ Open*, Vol. 10, No. 1, p. 39, 2024.

109. Murphy, S. V. and A. Atala, "3D Bioprinting of Tissues and Organs", *Nature*

Biotechnology, Vol. 32, No. 8, pp. 773–785, 2014.

110. Billiet, T., M. Vandenhaute, J. Schelfhout, S. V. Vlierberghe and P. Dubruel, "A Review of Trends and Limitations in Hydrogel-Rapid Prototyping for Tissue Engineering", *Biomaterials*, Vol. 33, No. 26, pp. 6020–6041, 2012.

111. Vanaei, S., M. Parizi, S. Vanaei, F. Salemizadehparizi and H. Vanaei, "An Overview on Materials and Techniques in 3D Bioprinting Toward Biomedical Application", *Engineered Regeneration*, Vol. 2, No. 11, pp. 1–18, 2021.

112. Ozbolat, I. T. and M. Hospodiuk, "Current Advances and Future Perspectives in Extrusion-Based Bioprinting", *Biomaterials*, Vol. 76, No. 1016, pp. 321–343, 2016.

113. Tian, S., H. Zhao and N. Lewinski, "Key Parameters and Applications of Extrusion-Based Bioprinting", *Bioprinting*, Vol. 23, No. 1016, p. e00156, 2021.

114. de Andrés, J. L., M. Ruiz-Toranzo, C. Antich, C. Chocarro-Wrona, E. López-Ruíz, G. Jiménez and J. A. Marchal, "Biofabrication of a Tri-Layered 3D-Bioprinted CSC-Based Malignant Melanoma Model for Personalized Cancer Treatment", *Biofabrication*, Vol. 15, No. 3, p. 035016, 2023.

115. Vázquez-Aristizabal, P., M. Henriksen-Lacey, C. García-Astrain, D. J. de Aberasturi, J. Langer, C. Epelde, L. Litti, L. M. Liz-Marzán and A. Izeta, "Biofabrication and Monitoring of a 3D Printed Skin Model for Melanoma", *Advanced Healthcare Materials*, Vol. 13, No. 27, p. 2401136, 2024.

116. Chae, S., D.-H. Ha and H. Lee, "3D Bioprinting Strategy for Engineering Vascularized Tissue Models.", *International journal of bioprinting*, Vol. 9, No. 5, p. 748, 2023.

117. Sánchez, E. M., J. C. Gómez-Blanco, E. L. Nieto, J. G. Casado, A. Macías-García, M. A. D. Díez, J. P. Carrasco-Amador, D. T. Martín, F. M. Sánchez-Margallo

and J. B. Pagador, "Hydrogels for Bioprinting: A Systematic Review of Hydrogels Synthesis, Bioprinting Parameters, and Bioprinted Structures Behavior", *Frontiers in Bioengineering and Biotechnology*, Vol. 8, No. 3389, p. 776, 2020.

118. Hospodiuk, M., M. Dey, D. Sosnoski and I. T. Ozbolat, "The Bioink: A Comprehensive Review on Bioprintable Materials", *Biotechnology Advances*, Vol. 35, No. 2, pp. 217–239, 2017.

119. Flores-Torres, S., O. Peza-Chavez, H. Kuasne, J. G. Munguia-Lopez, J. Kort-Mascort, L. Ferri, T. Jiang, C. V. Rajadurai, M. Park, V. Sangwan and J. M. Kinsella, "Alginate-Gelatin-Matrigel Hydrogels Enable the Development and Multigenerational Passaging of Patient-Derived 3D Bioprinted Cancer Spheroid Models", *Biofabrication*, Vol. 13, No. 2, p. 25001, 2021.

120. Hafeez, S., H. W. Ooi, F. L. Morgan, C. Mota, M. Dettin, C. van Blitterswijk, L. Moroni and M. B. Baker, "Viscoelastic Oxidized Alginates With Reversible Imine Type Crosslinks: Self-Healing, Injectable, and Bioprintable Hydrogels", *Gels*, Vol. 4, No. 4, p. 85, 2018.

121. Ji, S., E. Almeida and M. Guvendiren, "3D Bioprinting of Complex Channels Within Cell-Laden Hydrogels", *Acta Biomaterialia*, Vol. 95, pp. 214–224, 2019.

122. Sakai, S., K. Hirose, K. Taguchi, Y. Ogushi and K. Kawakami, "An Injectable, in Situ Enzymatically Gellable, Gelatin Derivative for Drug Delivery and Tissue Engineering", *Biomaterials*, Vol. 30, No. 20, pp. 3371–3377, 2009.

123. Ferjaoui, Z., R. López-Muñoz, S. Akbari, F. Chandad, D. Mantovani, M. Rouabhia and R. D. Fanganiello, "Design of Alginate/Gelatin Hydrogels for Biomedical Applications: Fine-Tuning Osteogenesis in Dental Pulp Stem Cells While Preserving Other Cell Behaviors", *Biomedicines*, Vol. 12, No. 7, p. 1510, 2024.

124. Billiet, T., E. Gevaert, T. D. Schryver, M. Cornelissen and P. Dubruel, "The

3D Printing of Gelatin Methacrylamide Cell-Laden Tissue-Engineered Constructs With High Cell Viability", *Biomaterials*, Vol. 35, No. 1, pp. 49–62, 2014.

125. Bertassoni, L. E., J. C. Cardoso, V. Manoharan, A. L. Cristino, N. S. Bhise, W. A. Araujo, P. Zorlutuna, N. E. Vrana, A. M. Ghaemmaghami, M. R. Dokmeci and A. Khademhosseini, "Direct-Write Bioprinting of Cell-Laden Methacrylated Gelatin Hydrogels", *Biofabrication*, Vol. 6, No. 2, 2014.

126. Gu, Y., L. Zhang, X. Du, Z. Fan, L. Wang, W. Sun, Y. Cheng, Y. Zhu and C. Chen, "Reversible physical crosslinking strategy with optimal temperature for 3D bioprinting of human chondrocyte-laden gelatin methacryloyl bioink", *Journal of Biomaterials Applications*, Vol. 33, No. 5, pp. 609–618, 2018.

127. Wang, L. L., C. B. Highley, Y. C. Yeh, J. H. Galarraga, S. Uman and J. A. Burdick, "Three-Dimensional Extrusion Bioprinting of Single- and Double-Network Hydrogels Containing Dynamic Covalent Crosslinks", *Journal of Biomedical Materials Research - Part A*, Vol. 106, No. 4, pp. 865–875, 2018.

128. Reyes-Furrer, A. A., S. D. Andrade, D. Bachmann, H. Jeker, M. Steinmann, N. Accart, A. Dunbar, M. Rausch, E. Bono, M. Rimann and H. Keller, "Matrigel 3D Bioprinting of Contractile Human Skeletal Muscle Models Recapitulating Exercise and Pharmacological responses.", *Communications biology*, Vol. 4, No. 1, p. 1183, 2021.

129. Fan, R., M. Piou, E. Darling, D. Cormier, J. Sun and J. Wan, "Bio-Printing Cell-Laden Matrigel–agarose Constructs", *Journal of Biomaterials Applications*, Vol. 31, No. 5, pp. 684–692, 2016.

130. Berg, J., T. Hiller, M. S. Kissner, T. H. Qazi, G. N. Duda, A. C. Hocke, S. Hippenstiel, L. Elomaa, M. Weinhart, C. Fahrenson and J. Kurreck, "Optimization of Cell-Laden Bioinks for 3D Bioprinting and Efficient Infection With Influenza a Virus", *Scientific Reports*, Vol. 8, No. 1, p. 3877, 2018.

131. Ding, H., F. Tourlomousis and R. C. Chang, "A Methodology for Quantifying Cell Density and Distribution in Multidimensional Bioprinted Gelatin-Alginate Constructs", *Journal of Manufacturing Science and Engineering, Transactions of the ASME*, Vol. 140, No. 5, p. 051014, 2018.

132. Krishnamoorthy, S., Z. Zhang and C. Xu, "Biofabrication of Three-Dimensional Cellular Structures Based on Gelatin Methacrylate–alginate Interpenetrating Network Hydrogel", *Journal of Biomaterials Applications*, Vol. 33, No. 8, pp. 1105–1117, 2019.

133. Gungor-Ozkerim, P. S., I. Inci, Y. S. Zhang, A. Khademhosseini and M. R. Dokmeci, "Bioinks for 3D Bioprinting: An Overview", *Biomaterials Science*, Vol. 6, No. 5, pp. 915–946, 2018.

134. Datta, P., M. Dey, Z. Ataie, D. Unutmaz and I. T. Ozbolat, "3D Bioprinting for Reconstituting the Cancer Microenvironment", *npj Precision Oncology*, Vol. 4, No. 1, p. 1, 2020.

135. Dai, X., L. Liu, J. Ouyang, X. Li, X. Zhang, Q. Lan and T. Xu, "Coaxial 3D Bioprinting of Self-Assembled Multicellular Heterogeneous Tumor Fibers", *Scientific Reports*, Vol. 7, No. 1, p. 1457, 2017.

136. Zhang, Y. S., A. Arneri, S. Bersini, S.-R. Shin, K. Zhu, Z. Goli-Malekabadi, J. Aleman, C. Colosi, F. Busignani, V. Dell'Erba, C. Bishop, T. Shupe, D. Demarchi, M. Moretti, M. Rasponi, M. R. Dokmeci, A. Atala and A. Khademhosseini, "Bioprinting 3D Microfibrous Scaffolds for Engineering Endothelialized Myocardium and Heart-on-a-Chip", *Biomaterials*, Vol. 110, pp. 45–59, 2016.

137. Nomdedeu-Sancho, G., A. Gorkun, N. Mahajan, K. Willson, C. R. Schaaf, K. I. Votanopoulos, A. Atala and S. Soker, "In Vitro Three-Dimensional (3D) Models for Melanoma Immunotherapy", *Cancers*, Vol. 15, No. 24, p. 5779, 2023.

138. Schmid, R., S. K. Schmidt, R. Detsch, H. Horder, T. Blunk, S. Schrüfer, D. W. Schubert, L. Fischer, I. Thievessen, S. Heltmann-Meyer, D. Steiner, D. Schneidereit, O. Friedrich, A. Grüneboom, H. Amouei, H. Wajant, R. E. Horch, A. K. Bosserhoff, A. Arkudas and A. Kengelbach-Weigand, "A New Printable Alginate/Hyaluronic Acid/Gelatin Hydrogel Suitable for Biofabrication of In Vitro and In Vivo Metastatic Melanoma Models", *Advanced Functional Materials*, Vol. 32, No. 2, p. 2107993, 2022.

139. Schmidt, S. K., S. Fischer, Z. E. Ahmad, R. Schmid, E. Metzger, R. Schüle, C. Hellerbrand, A. Arkudas, A. Kengelbach-Weigand, M. Kappelmann-Fenzl and A. K. Bosserhoff, "Modeling a Mesenchymal Cell State by Bioprinting for the Molecular Analysis of Dormancy in Melanoma", *Materials Today Bio*, Vol. 32, p. 101674, 2025.

140. Duan, J., Y. Cao, Z. Shen, Y. Cheng, Z. Ma, L. Wang, Y. Zhang, Y. An and S. Sang, "3D Bioprinted GelMA/PEGDA Hybrid Scaffold for Establishing an in Vitro Model of Melanoma", *Journal of Microbiology and Biotechnology*, Vol. 32, No. 4, pp. 531–540, 2022.

141. Barthes, J., C. Dollinger, C. B. Muller, U. Liivas, A. Dupret-Bories, H. Knopf-Marques and N. E. Vrana, "Immune Assisted Tissue Engineering via Incorporation of Macrophages in Cell-Laden Hydrogels Under Cytokine Stimulation", *Frontiers in Bioengineering and Biotechnology*, Vol. 6, No. 8, pp. 1–17, 2018.

142. Coburn, P. T., A. C. Herbay, M. Berrini and N. Y. Li-Jessen, "An in Vitro Assessment of the Response of THP-1 Macrophages to Varying Stiffness of a Glycol-Chitosan Hydrogel for Vocal Fold Tissue Engineering Applications", *Journal of Biomedical Materials Research - Part A*, Vol. 109, No. 8, pp. 1337–1352, 2021.

143. Raveendran, N., K. Vaswani, P. Han, S. Basu, C. S. Moran and S. Ivanovski, "Modeling Inflammatory Response Using 3D Bioprinting of Polarized Macrophages", *International Journal of Bioprinting*, Vol. 10, No. 2, pp.

398–412, 2024.

144. Aldrich, A., M. A. Kuss, B. Duan and T. Kielian, "3D Bioprinted Scaffolds Containing Viable Macrophages and Antibiotics Promote Clearance of Staphylococcus aureus Craniotomy-Associated Biofilm Infection", *ACS Applied Materials and Interfaces*, Vol. 11, No. 13, pp. 12298–12307, 2019.

145. Harjunpää, H., M. L. Asens, C. Guenther and S. C. Fagerholm, "Cell Adhesion Molecules and Their Roles and Regulation in the Immune and Tumor Microenvironment", *Frontiers in Immunology*, Vol. 10, p. 1078, 2019.

146. Zhou, M., M. Zheng, X. Zhou, S. Tian, X. Yang, Y. Ning, Y. Li and S. Zhang, "The Roles of Connexins and Gap Junctions in the Progression of Cancer", *Cell Communication and Signaling*, Vol. 21, No. 1, p. 8, 2023.

147. Zhang, S., X. Cai, G. J. Khan, J. Cheng, J. He, K. Zhai and Y. Mao, "Exploring the Molecular Mechanism of Artemisia Rupestris L. for the Treatment of Hepatocellular Carcinoma via PI3K/AKT Pathway", *Journal of Ethnopharmacology*, Vol. 322, p. 117572, 2024.

148. Melwani, P. K. and B. N. Pandey, "Tunneling Nanotubes: The Intercellular Conduits Contributing to Cancer Pathogenesis and Its Therapy", *Biochimica et Biophysica Acta (BBA) - Reviews on Cancer*, Vol. 1878, No. 6, p. 189028, 2023.

149. Desigaux, T., L. Comperat, N. Dusserre, M. L. Stachowicz, M. Lea, J. W. Dupuy, A. Vial, M. Molinari, J. C. Fricain, F. Paris and H. Oliveira, "3D Bioprinted Breast Cancer Model Reveals Stroma-Mediated Modulation of Extracellular Matrix and Radiosensitivity", *Bioactive Materials*, Vol. 42, pp. 316–327, 2024.

150. Liu, M. H., Y. F. Li and B. H. Chen, "Inhibition of Melanoma Cells A375 by Carotenoid Extract and Nanoemulsion Prepared From Pomelo Leaves", *Plants*, Vol. 10, No. 10, p. 2129, 2021.

151. Wang, Y., W. Shi, M. Kuss, S. Mirza, D. Qi, A. Krasnoslobodtsev, J. Zeng, H. Band, V. Band and B. Duan, "3D Bioprinting of Breast Cancer Models for Drug Resistance Study", *ACS Biomaterials Science and Engineering*, Vol. 4, No. 12, pp. 4401–4411, 2018.

152. Li, C., B. Jin, H. Sun, Y. Wang, H. Zhao, X. Sang, H. Yang and Y. Mao, "Exploring the Function of Stromal Cells in Cholangiocarcinoma by Three-Dimensional Bioprinting Immune Microenvironment Model", *Frontiers in Immunology*, Vol. 13, p. 941289, 2022.

153. Tang, M., Q. Xie, R. C. Gimple, Z. Zhong, T. Tam, J. Tian, R. L. Kidwell, Q. Wu, B. C. Prager, Z. Qiu, A. Yu, Z. Zhu, P. Mesci, H. Jing, J. Schimelman, P. Wang, D. Lee, M. H. Lorenzini, D. Dixit, L. Zhao, S. Bhargava, T. E. Miller, X. Wan, J. Tang, B. Sun, B. F. Cravatt, A. R. Muotri, S. Chen and J. N. Rich, "Three-Dimensional Bioprinted Glioblastoma Microenvironments Model Cellular Dependencies and Immune Interactions", *Cell Research*, Vol. 30, No. 10, pp. 833–853, 2020.

154. Niederalt, C., L. Kuepfer, J. Solodenko, T. Eissing, H. U. Siegmund, M. Block, S. Willmann and J. Lippert, "A Generic Whole Body Physiologically Based Pharmacokinetic Model for Therapeutic Proteins in PK-Sim", *Journal of Pharmacokinetics and Pharmacodynamics*, Vol. 45, No. 2, pp. 235–257, 2018.

155. Salgado, E. and Y. Cao, "Pharmacokinetics and Pharmacodynamics of Therapeutic Antibodies in Tumors and Tumor-Draining Lymph Nodes", *Mathematical Biosciences and Engineering*, Vol. 18, No. 1, pp. 112–131, 2020.

156. Kovar, L., C. Schräpel, D. Selzer, Y. Kohl, R. Bals, M. Schwab and T. Lehr, "Physiologically-Based Pharmacokinetic (PBPK) Modeling of Buprenorphine in Adults, Children and Preterm Neonates", *Pharmaceutics*, Vol. 12, No. 6, pp. 1–22, 2020.

157. Malik, P. R., A. Hamadeh, C. Phipps and A. N. Edginton, "Population PBPK Modelling of Trastuzumab: A Framework for Quantifying and Predicting Inter-Individual Variability", *Journal of Pharmacokinetics and Pharmacodynamics*, Vol. 44, No. 3, pp. 277–290, 2017.

158. Chang, H. Y., S. Wu, G. Meno-Tetang and D. K. Shah, "A Translational Platform PBPK Model for Antibody Disposition in the Brain", *Journal of Pharmacokinetics and Pharmacodynamics*, Vol. 46, No. 4, pp. 319–338, 2019.

159. Zhao, J., Y. Cao and W. J. Jusko, "Across-Species Scaling of Monoclonal Antibody Pharmacokinetics Using a Minimal PBPK Model", *Pharmaceutical Research*, Vol. 32, No. 10, pp. 3269–3281, 2015.

160. Mosser, D. M. and J. P. Edwards, "Exploring the Full Spectrum of Macrophage Activation", *Nature Reviews Immunology*, Vol. 8, No. 12, pp. 958–969, 2008.

161. Daigneault, M., J. A. Preston, H. M. Marriott, M. K. Whyte and D. H. Dockrell, "The Identification of Markers of Macrophage Differentiation in PMA-Stimulated THP-1 Cells and Monocyte-Derived Macrophages", *PLoS ONE*, Vol. 5, No. 1, p. e8668, 2010.

162. Mantovani, A., S. K. Biswas, M. R. Galdiero, A. Sica and M. Locati, "Macrophage Plasticity and Polarization in Tissue Repair and Remodelling", *Journal of Pathology*, Vol. 229, No. 2, pp. 176–185, 2013.

163. Sica, A. and A. Mantovani, "Macrophage Plasticity and Polarization: In Vivo Veritas", *Journal of Clinical Investigation*, Vol. 122, No. 3, pp. 787–795, 2012.

164. Martinez, F. O. and S. Gordon, "The M1 and M2 Paradigm of Macrophage Activation: Time for Reassessment", *F1000Prime Reports*, Vol. 6, No. 13, pp. 1–13, 2014.

165. Chanput, W., J. J. Mes and H. J. Wichers, "THP-1 Cell Line: An in Vitro Cell

Model for Immune Modulation Approach", *International Immunopharmacology*, Vol. 23, No. 1, pp. 37–45, 2014.

166. Vogel, D. Y., E. J. Vereyken, J. E. Glim, P. D. Heijnen, M. Moeton, P. V. D. Valk, S. Amor, C. E. Teunissen, J. V. Horssen and C. D. Dijkstra, "Macrophages in Inflammatory Multiple Sclerosis Lesions Have an Intermediate Activation Status", *Journal of Neuroinflammation*, Vol. 10, p. 809, 2013.

167. Rampersad, S. N., "Multiple Applications of Alamar Blue as an Indicator of Metabolic Function and Cellular Health in Cell Viability Bioassays", *Sensors (Switzerland)*, Vol. 12, No. 9, pp. 12347–12360, 2012.

168. Darzynkiewicz, Z., *Chapter 27 Differential Staining of DNA and RNA in Intact Cells and Isolated Cell Nuclei with Acridine Orange*, Vol. 33, pp. 285–298, Academic Press, 1990.

169. Cummings, B. S. and R. G. Schnellmann, "Measurement of Cell Death in Mammalian Cells", *Current Protocols in Pharmacology*, Vol. 25, No. 1, p. 1, 2004.

170. Casaburi, I., P. Avena, A. D. Luca, A. Chimento, R. Sirianni, R. Malivindi, V. Rago, M. Fiorillo, F. Domanico, C. Campana, A. R. Cappello, F. Sotgia, M. P. Lisanti and V. Pezzi, "Estrogen Related Receptor α (ERRα) a Promising Target for the Therapy of Adrenocortical Carcinoma (ACC)", *Oncotarget*, Vol. 6, No. 28, pp. 25135–48, 2015.

171. Namvar, F., R. Mohammad, J. Baharara, M. Mahdavi, E. Amini, S. K. Yeap, M. S. Chartrand and H. S. Rahman, "Cytotoxic Effect of Magnetic Iron Oxide Nanoparticles Synthesized via Seaweed Aqueous Extract", *International Journal of Nanomedicine*, Vol. 9, No. 1, p. 2479, 2014.

172. Lee, H. L., M. H. Park, J. K. Song, Y. Y. Jung, Y. Kim, K. B. Kim, D. Y. Hwang, D. Y. Yoon, M. J. Song, S. B. Han and J. T. Hong, "Tumor Growth

Suppressive Effect of IL-4 Through P21-Mediated Activation of STAT6 in IL-4Rα Overexpressed Melanoma Models", *Oncotarget*, Vol. 7, No. 17, pp. 23425–23438, 2016.

173. Todaro, M., M. P. Alea, A. Scopelliti, J. P. Medema and G. Stassi, "IL-4-Mediated Drug Resistance in Colon Cancer Stem Cells", *Cell Cycle*, Vol. 7, No. 3, pp. 309–313, 2008.

174. Cavo, M., M. Caria, I. Pulsoni, F. Beltrame, M. Fato and S. Scaglione, "A New Cell-Laden 3D Alginate-Matrigel Hydrogel Resembles Human Breast Cancer Cell Malignant Morphology, Spread and Invasion Capability Observed "In Vivo"", *Scientific Reports*, Vol. 8, No. 1, pp. 1–12, 2018.

175. Tomić, S. L., J. Nikodinović-Runić, M. Vukomanović, M. M. Babić and J. S. Vuković, "Novel Hydrogel Scaffolds Based on Alginate, Gelatin, 2-Hydroxyethyl Methacrylate, and Hydroxyapatite", *Polymers*, Vol. 13, No. 6, p. 932, 2021.

176. Cooke, M. E. and D. H. Rosenzweig, "The Rheology of Direct and Suspended Extrusion Bioprinting", *APL Bioengineering*, Vol. 5, No. 1, p. 11502, 2021.

177. Gregory, T., P. Benhal, A. Scutte, D. Quashie, K. Harrison, C. Cargill, S. Grandison, M. J. Savitsky, S. Ramakrishnan and J. Ali, "Rheological Characterization of Cell-Laden Alginate-Gelatin Hydrogels for 3D Biofabrication", *Journal of the Mechanical Behavior of Biomedical Materials*, Vol. 136, p. 105474, 2022.

178. Gao, T., G. J. Gillispie, J. S. Copus, A. P. Kumar, Y. J. Seol, A. Atala, J. J. Yoo and S. J. Lee, "Optimization of Gelatin-Alginate Composite Bioink Printability Using Rheological Parameters: A Systematic Approach", *Biofabrication*, Vol. 10, No. 3, p. 034106, 2018.

179. Northcutt, L. A., A. M. Questell, J. Rhoades and M. Rafat, "Development of an Alginate-Matrigel Hydrogel System to Evaluate Cancer Cell Behavior in the

Stiffness Range of the Bone Marrow", *Frontiers in Biomaterials Science*, Vol. 2, p. 1140641, 2023.

180. Elango, J. and C. Zamora-Ledezma, "Rheological, Structural, and Biological Trade-Offs in Bioink Design for 3D Bioprinting", *Gels*, Vol. 11, No. 8, p. 659, 2025.

181. Deng, B., Z. Zhao, W. Kong, C. Han, X. Shen and C. Zhou, "Biological Role of Matrix Stiffness in Tumor Growth and Treatment", *Journal of Translational Medicine*, Vol. 20, No. 1, p. 540, 2022.

182. Chopin-Doroteo, M., E. A. Mandujano-Tinoco and E. Krötzsch, "Tailoring of the Rheological Properties of Bioinks to Improve Bioprinting and Bioassembly for Tissue Replacement", *Biochimica et Biophysica Acta - General Subjects*, Vol. 1865, No. 2, p. 129782, 2021.

183. Davies, L. C., M. Rosas, S. J. Jenkins, Chia-Te, M. J. Scurr, F. Brombacher, D. J. Fraser, J. E. Allen, S. A. Jones and P. R. Taylor, "Distinct Bone Marrow-Derived and Tissue-Resident Macrophage Lineages Proliferate at Key Stages During Inflammation", *Nature Communications*, Vol. 4, No. 1, p. 1886, 2013.

184. Ushach, I. and A. Zlotnik, "Biological Role of Granulocyte Macrophage Colony-Stimulating Factor (GM-CSF) and Macrophage Colony-Stimulating Factor (M-CSF) on Cells of the Myeloid Lineage", *Journal of Leukocyte Biology*, Vol. 100, No. 3, pp. 481–489, 2016.

185. Hume, D. A. and K. P. A. MacDonald, "Therapeutic Applications of Macrophage Colony-Stimulating Factor-1 (CSF-1) and Antagonists of CSF-1 Receptor (CSF-1R) Signaling", *Blood*, Vol. 119, No. 8, pp. 1810–1820, 2012.

186. Draijer, C., L. R. K. Penke and M. Peters-Golden, "Distinctive Effects of GM-CSF and M-CSF on Proliferation and Polarization of Two Major Pulmonary

Macrophage Populations", *The Journal of Immunology*, Vol. 202, No. 9, pp. 2700–2709, 2019.

187. Hamilton, J. A., "CSF-1 Signal Transduction", *Journal of Leukocyte Biology*, Vol. 62, No. 2, pp. 145–155, 1997.

188. Fleetwood, A. J., T. Lawrence, J. A. Hamilton and A. D. Cook, "Granulocyte-Macrophage Colony-Stimulating Factor (CSF) and Macrophage CSF-Dependent Macrophage Phenotypes Display Differences in Cytokine Profiles and Transcription Factor Activities: Implications for CSF Blockade in Inflammation", *The Journal of Immunology*, Vol. 178, No. 8, pp. 5245–5252, 2007.

189. Minotti, G., P. Menna, E. Salvatorelli, G. Cairo and L. Gianni, "Anthracyclines: Molecular Advances and Pharmacologic Developments in Antitumor Activity and Cardiotoxicity", *Pharmacological Reviews*, Vol. 56, No. 2, pp. 185–229, 2004.

190. Xu, M., M. Duan, M. Chen, A. Mahal, L. Yang, C. Meng, Z. Zhang, J. Ren, A. J. Obaidullah, S. Li and C. Wang, "Study on the Activity of Targeted Delivery of DOX Against Melanoma by Exosome-Like Nanovesicles of Rhodiola Rosea", *Biochimica et Biophysica Acta (BBA) - General Subjects*, Vol. 1869, No. 5, p. 130776, 2025.

191. Changenet-Barret, P., T. Gustavsson, D. Markovitsi, I. Manet and S. Monti, "Unravelling Molecular Mechanisms in the Fluorescence Spectra of Doxorubicin in Aqueous Solution by Femtosecond Fluorescence Spectroscopy", *Physical Chemistry Chemical Physics*, Vol. 15, No. 8, pp. 2937–2944, 2013.

192. Bundscherer, A., C. Hafner, T. Maisch, B. Becker, M. Landthaler and T. Vogt, "Antiproliferative and Proapoptotic Effects of Rapamycin and Celecoxib in Malignant Melanoma Cell Lines.", *Oncology reports*, Vol. 19, No. 2, pp. 547–53, 2008.

193. Swierczewska, M., S. Lee and X. Chen, "The Design and Application of Flu-

orophore–gold Nanoparticle Activatable Probes", *Physical Chemistry Chemical Physics*, Vol. 13, No. 21, p. 9929, 2011.

194. Zhang, M., C. Wang, R. Zhang, Y. Chen, C. Zhang, H. Heidi and M. Li, "Comparison of the Guidelines on Good Agricultural and Collection Practices in Herbal Medicine of the European Union, China, the WHO, and the United States of America", *Pharmacological Research*, Vol. 167, p. 105533, 2021.

195. Cordani, M. and Álvaro Somoza, "Targeting Autophagy Using Metallic Nanoparticles: A Promising Strategy for Cancer Treatment", *Cellular and Molecular Life Sciences*, Vol. 76, No. 7, pp. 1215–1242, 2019.

196. Li, Y., J. Yang and X. Sun, "Reactive Oxygen Species-Based Nanomaterials for Cancer Therapy", *Frontiers in Chemistry*, Vol. 9, p. 650587, 2021.

197. Zhou, J., S. Geng, W. Ye, Q. Wang, R. Lou, Q. Yin, B. Du and H. Yao, "ROS-Boosted Photodynamic Therapy Against Metastatic Melanoma by Inhibiting the Activity of Antioxidase and Oxygen-Producing Nano-Dopants", *Pharmacological Research*, Vol. 158, p. 104885, 2020.

198. Dastgheib, Z. S., S. S. Abolmaali, G. Farahavar, M. Salmanpour and A. M. Tamaddon, "Gold Nanostructures in Melanoma: Advances in Treatment, Diagnosis, and Theranostic Applications", *Heliyon*, Vol. 10, No. 15, p. e35655, 2024.

199. Piktel, E., I. Ościłowska, Łukasz Suprewicz, J. Depciuch, N. Marcińczyk, E. Chabielska, P. Wolak, T. Wollny, M. Janion, M. Parlinska-Wojtan and R. Bucki, "ROS-Mediated Apoptosis and Autophagy in Ovarian Cancer Cells Treated with Peanut-Shaped Gold Nanoparticles", *International Journal of Nanomedicine*, Vol. Volume 16, pp. 1993–2011, 2021.

200. Catalani, E., M. Giovarelli, S. Zecchini, C. Perrotta and D. Cervia, "Oxidative Stress and Autophagy as Key Targets in Melanoma Cell Fate", *Cancers*, Vol. 13,

No. 22, p. 5791, 2021.

201. Xia, Q., J. Huang, Q. Feng, X. Chen, X. Liu, X. Li, T. Zhang, S. Xiao, H. Li, Z. Zhong and K. Xiao, "Size- and Cell Type-Dependent Cellular Uptake, Cytotoxicity and in Vivo Distribution of Gold Nanoparticles", *International Journal of Nanomedicine*, Vol. Volume 14, No. 2019, pp. 6957–6970, 2019.

202. Al-Khedhairy, A. A. and R. Wahab, "Size-Dependent Cytotoxic and Molecular Study of the Use of Gold Nanoparticles against Liver Cancer Cells", *Applied Sciences*, Vol. 12, No. 2, p. 901, 2022.

203. Pan, Y., S. Neuss, A. Leifert, M. Fischler, F. Wen, U. Simon, G. Schmid, W. Brandau and W. Jahnen-Dechent, "Size-Dependent Cytotoxicity of Gold Nanoparticles", *Small*, Vol. 3, No. 11, pp. 1941–1949, 2007.

204. Sztandera, K., M. Gorzkiewicz and B. Klajnert-Maculewicz, "Gold Nanoparticles in Cancer Treatment", *Molecular Pharmaceutics*, Vol. 16, No. 1, pp. 1–23, 2019.

205. Iavicoli, I., E. J. Calabrese and M. A. Nascarella, "Exposure to Nanoparticles and Hormesis", *Dose-Response*, Vol. 8, No. 4, pp. 501–517, 2010.

206. Hoon, D. S., M. Banez, E. Okun, D. L. Morton and R. F. Irie, "Modulation of Human Melanoma Cells by Interleukin-4 and in Combination with γ-Interferon or α-Tumor Necrosis Factor", *Cancer Research*, Vol. 51, No. 8, pp. 2002–2008, 1991.

207. Garbe, C. and K. Krasagakis, "Effects of Interferons and Cytokines on Melanoma Cells", *Journal of Investigative Dermatology*, Vol. 100, No. 2 SUPPL., pp. S239–S244, 1993.

208. Yano, S., S. Sone, Y. Nishioka, N. Mukaida, K. Matsushima and T. Ogura, "Differential Effects of Anti-Inflammatory Cytokines (IL-4, IL-10 and IL-13) on Tumoricidal and Chemotactic Properties of Human Monocytes Induced by Monocyte

Chemotactic and Activating Factor", *Journal of Leukocyte Biology*, Vol. 57, No. 2, pp. 303–309, 1995.

209. Setrerrahmane, S. and H. Xu, "Tumor-Related Interleukins: Old Validated Targets for New Anti-Cancer Drug Development", *Molecular Cancer*, Vol. 16, No. 1, p. 153, 2017.

210. Calimeri, T. and A. J. M. Ferreri, *mTOR Inhibitors, with Special Focus on Temsirolimus and Similar Agents*, pp. 85–105, Springer International Publishing, Cham, 2018.

211. Maity, N. and M. Sengupta, *Targeting Macrophages Through Gold Nanoparticle-Induced Immunomodulation: A Therapeutic Approach in Inflammation and Cancer*, pp. 161–175, Springer Nature Singapore, 2023.

212. Bekić, M., S. Tomić, R. Rudolf, M. Milanović, D. Vučević, I. Anžel and M. Čolić, "The Effect of Stabilisation Agents on the Immunomodulatory Properties of Gold Nanoparticles Obtained by Ultrasonic Spray Pyrolysis", *Materials*, Vol. 12, No. 24, p. 4121, 2019.

213. Duan, X. and Y. Li, "Physicochemical Characteristics of Nanoparticles Affect Circulation, Biodistribution, Cellular Internalization, and Trafficking", *Small*, Vol. 9, No. 9-10, pp. 1521–1532, 2013.

214. Powell, J. D., K. N. Pollizzi, E. B. Heikamp and M. R. Horton, "Regulation of Immune Responses by mTOR", *Annual Review of Immunology*, Vol. 30, No. 1, pp. 39–68, 2012.

215. Ibrahim, W. N., L. M. B. M. Rosli and A. A. Doolaanea, "Formulation, Cellular Uptake and Cytotoxicity of Thymoquinone-Loaded Plga Nanoparticles in Malignant Melanoma Cancer Cells", *International Journal of Nanomedicine*, Vol. 15, No. 2020, pp. 8059–8074, 2020.

216. Prodea, A., A. Milan, M. Mioc, A. Mioc, C. Oprean, R. Racoviceanu, R. Negrea-Ghiulai, G. Mardale, Ștefana Avram, M. Balan-Porcărașu, S. Rotunjanu, C. Trandafirescu, I. Şoica and C. Șoica, "Novel Betulin-1,2,4-Triazole Derivatives Promote In Vitro Dose-Dependent Anticancer Cytotoxicity", *Processes*, Vol. 12, No. 1, p. 24, 2024.

217. Petiti, J., L. Revel and C. Divieto, "Standard Operating Procedure to Optimize Resazurin-Based Viability Assays", *Biosensors*, Vol. 14, No. 4, p. 156, 2024.

218. Neufeld, B. H., J. B. Tapia, A. Lutzke and M. M. Reynolds, "Small Molecule Interferences in Resazurin and MTT-Based Metabolic Assays in the Absence of Cells", *Analytical Chemistry*, Vol. 90, No. 11, pp. 6867–6876, 2018.

219. Wang, X. and S.-Y. Sun, "Enhancing mTOR-Targeted Cancer Therapy", *Expert Opinion on Therapeutic Targets*, Vol. 13, No. 10, pp. 1193–1203, 2009.

220. Wang, P., S. M. Henning and D. Heber, "Limitations of MTT and MTS-Based Assays for Measurement of Antiproliferative Activity of Green Tea Polyphenols", *PLoS ONE*, Vol. 5, No. 4, p. e10202, 2010.

221. Kunnumakkara, A. B., D. Bordoloi, C. Harsha, K. Banik, S. C. Gupta and B. B. Aggarwal, "Curcumin Mediates Anticancer Effects by Modulating Multiple Cell Signaling Pathways", *Clinical Science*, Vol. 131, No. 15, pp. 1781–1799, 2017.

222. Min, K.-J. and T. K. Kwon, "Anticancer Effects and Molecular Mechanisms of Epigallocatechin-3-Gallate", *Integrative Medicine Research*, Vol. 3, No. 1, pp. 16–24, 2014.

223. Yogeeswari, P. and D. Sriram, "Betulinic Acid and Its Derivatives: A Review on their Biological Properties", *Current Medicinal Chemistry*, Vol. 12, No. 6, pp. 657–666, 2005.

224. Almajali, B., H. A. N. Al-Jamal, W. R. W. Taib, I. Ismail, M. F. Johan, A. A.

Doolaanea and W. N. Ibrahim, "Thymoquinone, as a Novel Therapeutic Candidate of Cancers", *Pharmaceuticals*, Vol. 14, No. 4, p. 369, 2021.

225. Wahab, S. I. A., A. B. Abdul, A. S. Alzubairi, M. M. Elhassan and S. Mohan, "In Vitro Ultramorphological Assessment of Apoptosis Induced by Zerumbone on (HeLa)", *Journal of Biomedicine and Biotechnology*, Vol. 2009, No. 1, p. 769568, 2009.

226. Mioc, M., I. Z. Pavel, R. Ghiulai, D. E. Coricovac, C. Farcas, C. V. Mihali, C. Oprean, V. Serafim, R. A. Popovici, C. A. Dehelean, M. I. Shtilman, A. M. Tsatsakis and C. Soica, "The Cytotoxic Effects of Betulin-Conjugated Gold Nanoparticles as Stable Formulations in Normal and Melanoma Cells", *Frontiers in Pharmacology*, Vol. 9, No. 5, p. 429, 2018.

227. Monopoli, M. P., C. Åberg, A. Salvati and K. A. Dawson, "Biomolecular Coronas Provide the Biological Identity of Nanosized Materials", *Nature Nanotechnology*, Vol. 7, No. 12, pp. 779–786, 2012.

228. Hadjidemetriou, M. and K. Kostarelos, "Nanomedicine: Evolution of the Nanoparticle Corona", *Nature Nanotechnology*, Vol. 12, No. 4, pp. 288–290, 2017.

229. Nandakumar, A., W. Wei, G. Siddiqui, H. Tang, Y. Li, A. Kakinen, X. Wan, K. Koppel, S. Lin, T. P. Davis, D. T. Leong, D. J. Creek, F. Ding, Y. Song and P. C. Ke, "Dynamic Protein Corona of Gold Nanoparticles with an Evolving Morphology", *ACS Applied Materials and Interfaces*, Vol. 13, No. 48, pp. 58238–58251, 2021.

230. Dvir, T., B. P. Timko, D. S. Kohane and R. Langer, "Nanotechnological Strategies for Engineering Complex Tissues", *Nature Nanotechnology*, Vol. 6, No. 1, pp. 13–22, 2011.

231. Chithrani, B. D., A. A. Ghazani and W. C. Chan, "Determining the Size and

Shape Dependence of Gold Nanoparticle Uptake Into Mammalian Cells", *Nano Letters*, Vol. 6, No. 4, pp. 662–668, 2006.

232. Connor, E. E., J. Mwamuka, A. Gole, C. J. Murphy and M. D. Wyatt, "Gold Nanoparticles Are Taken Up by Human Cells but Do Not Cause Acute Cytotoxicity", *Small*, Vol. 1, No. 3, pp. 325–327, 2005.

233. Shukla, R., V. Bansal, M. Chaudhary, A. Basu, R. R. Bhonde and M. Sastry, "Biocompatibility of Gold Nanoparticles and Their Endocytotic Fate Inside the Cellular Compartment: A Microscopic Overview", *Langmuir*, Vol. 21, No. 23, pp. 10644–10654, 2005.

234. Edmondson, R., J. J. Broglie, A. F. Adcock and L. Yang, "Three-Dimensional Cell Culture Systems and Their Applications in Drug Discovery and Cell-Based Biosensors", *Assay and Drug Development Technologies*, Vol. 12, No. 4, pp. 207–218, 2014.

235. Vinci, M., S. Gowan, F. Boxall, L. Patterson, M. Zimmermann, W. Court, C. Lomas, M. Mendiola, D. Hardisson and S. A. Eccles, "Advances in establishment and analysis of three-dimensional tumor spheroid-based functional assays for target validation and drug evaluation", *BMC Biology*, Vol. 10, No. 29, pp. 1–20, 2012.

236. Chiarini, F., A. Lonetti, G. Teti, E. Orsini, D. Bressanin, A. Cappellini, F. Ricci, P. L. Tazzari, A. Ognibene, M. Falconi, P. Pagliaro, I. Iacobucci, G. Martinelli, S. Amadori, J. A. McCubrey and A. M. Martelli, "A Combination of Temsirolimus, an Allosteric mTOR Inhibitor, With Clofarabine as a New Therapeutic Option for Patients With Acute Myeloid Leukemia", *Oncotarget*, Vol. 3, No. 12, pp. 1615–1628, 2012.

237. Ballou, L. M. and R. Z. Lin, "Rapamycin and mTOR Kinase Inhibitors", *Journal of Chemical Biology*, Vol. 1, No. 1-4, pp. 27–36, 2008.

238. Shrestha, B., L. Wang, H. Zhang, C. Y. Hung and L. Tang, "Gold Nanoparticles Mediated Drug-Gene Combinational Therapy for Breast Cancer Treatment.", *International journal of nanomedicine*, Vol. 15, No. 2020, pp. 8109–8119, 2020.

239. Wahnou, H., R. E. Kebbaj, B. Liagre, V. Sol, Y. Limami and R. E. Duval, "Curcumin-Based Nanoparticles: Advancements and Challenges in Tumor Therapy.", *Pharmaceutics*, Vol. 17, No. 1, p. 114, 2025.

240. Aggarwal, B. B. and B. Sung, "Pharmacological Basis for the Role of Curcumin in Chronic Diseases: An Age-Old Spice With Modern Targets", *Trends in Pharmacological Sciences*, Vol. 30, No. 2, pp. 85–94, 2009.

241. Thangapazham, R. L., A. Sharma and R. K. Maheshwari, "Multiple Molecular Targets in Cancer Chemoprevention by Curcumin", *The AAPS Journal*, Vol. 8, No. 3, p. E443, 2006.

242. Lotempio, M. M., M. S. Veena, H. L. Steele, B. Ramamurthy, T. S. Ramalingam, A. N. Cohen, R. Chakrabarti, E. S. Srivatsan and M. B. Wang, "Curcumin Suppresses Growth of Head and Neck Squamous Cell Carcinoma", *Clinical Cancer Research*, Vol. 11, No. 19 I, pp. 6994–7002, 2005.

243. Arvapalli, D. M., A. T. Sheardy, K. Allado, H. Chevva, Z. Yin and J. Wei, "Design of Curcumin Loaded Carbon Nanodots Delivery System: Enhanced Bioavailability, Release Kinetics, and Anticancer Activity", *ACS Applied Bio Materials*, Vol. 3, No. 12, pp. 8776–8785, 2020.

244. Seo, B. R., K. J. Min, I. J. Cho, S. C. Kim and T. K. Kwon, "Curcumin Significantly Enhances Dual PI3K/Akt and mTOR Inhibitor NVP-BEZ235-Induced Apoptosis in Human Renal Carcinoma Caki Cells Through Down-Regulation of P53-Dependent Bcl-2 Expression and Inhibition of Mcl-1 Protein Stability", *PLoS ONE*, Vol. 9, No. 4, p. e0151886, 2014.

245. Aggarwal, S., H. Ichikawa, Y. Takada, S. K. Sandur, S. Shishodia and B. B. Aggarwal, "Curcumin (Diferuloylmethane) Down-Regulates Expression of Cell Proliferation and Antiapoptotic and Metastatic Gene Products through Suppression of IκBα Kinase and Akt Activation", *Molecular Pharmacology*, Vol. 69, No. 1, pp. 195–206, 2006.

246. Weichhart, T., G. Costantino, M. Poglitsch, M. Rosner, M. Zeyda, K. M. Stuhlmeier, T. Kolbe, T. M. Stulnig, W. H. Hörl, M. Hengstschläger, M. Müller and M. D. Säemann, "The TSC-mTOR Signaling Pathway Regulates the Innate Inflammatory Response", *Immunity*, Vol. 29, No. 4, pp. 565–577, 2008.

247. Matteis, V. D., M. Cascione, L. Rizzello, D. E. Manno, C. D. Guglielmo and R. Rinaldi, "Synergistic Effect Induced by Gold Nanoparticles with Polyphenols Shell during Thermal Therapy: Macrophage Inflammatory Response and Cancer Cell Death Assessment", *Cancers*, Vol. 13, No. 14, p. 3610, 2021.

248. Lee, Y. J., N. Y. Kim, Y. A. Suh and C. H. Lee, "Involvement of ROS in Curcumin-Induced Autophagic Cell Death", *Korean Journal of Physiology and Pharmacology*, Vol. 15, No. 1, pp. 1–7, 2011.

249. Teixeira, B. H., K. de Oliveira Gonçalves, D. P. Vieira and L. C. Courrol, "Synergizing Immune Balance: Curcumin Gold Nanoparticles and Ultrasound Irradiation for Macrophage Down-Regulation", *AppliedChem*, Vol. 4, No. 1, pp. 70–85, 2024.

250. Alkilany, A. M. and C. J. Murphy, "Toxicity and Cellular Uptake of Gold Nanoparticles: What We Have Learned So Far?", *Journal of Nanoparticle Research*, Vol. 12, No. 7, pp. 2313–2333, 2010.

251. Xu, Y., O. K. Sung, Y. Li and J. Han, "Autophagy Contributes to Caspase-Independent Macrophage Cell Death", *Journal of Biological Chemistry*, Vol. 281, No. 28, pp. 19179–19187, 2006.

252. Villalpando-Rodriguez, G. E. and S. B. Gibson, "Reactive Oxygen Species (ROS) Regulates Different Types of Cell Death by Acting as a Rheostat", *Oxidative Medicine and Cellular Longevity*, Vol. 2021, No. 1, p. 9912436, 2021.

253. Aggarwal, B. B., M. E. V. Kuiken, L. H. Iyer, K. B. Harikumar and B. Sung, "Molecular Targets of Nutraceuticals Derived From Dietary Spices: Potential Role in Suppression of Inflammation and Tumorigenesis", *Experimental Biology and Medicine*, Vol. 234, No. 8, pp. 825–849, 2009.

254. Trachootham, D., J. Alexandre and P. Huang, "Targeting Cancer Cells by ROS-Mediated Mechanisms: A Radical Therapeutic Approach?", *Nature Reviews Drug Discovery*, Vol. 8, No. 7, pp. 579–591, 2009.

255. Sandur, S. K., H. Ichikawa, M. K. Pandey, A. B. Kunnumakkara, B. Sung, G. Sethi and B. B. Aggarwal, "Role of Pro-Oxidants and Antioxidants in the Anti-Inflammatory and Apoptotic Effects of Curcumin (Diferuloylmethane)", *Free Radical Biology and Medicine*, Vol. 43, No. 4, pp. 568–580, 2007.

256. Hu, Y., L. Cheng, S. Du, K. Wang and S. Liu, "Antioxidant Curcumin Induces Oxidative Stress to Kill Tumor Cells (Review)", *Oncology Letters*, Vol. 27, No. 2, p. 67, 2024.

257. Ravi, M., V. Paramesh, S. R. Kaviya, E. Anuradha and F. D. P. Solomon, "3D Cell Culture Systems: Advantages and Applications", *Journal of Cellular Physiology*, Vol. 230, No. 1, pp. 16–26, 2015.

258. Chueh, P. J., R. Y. Liang, Y. H. Lee, Z. M. Zeng and S. M. Chuang, "Differential Cytotoxic Effects of Gold Nanoparticles in Different Mammalian Cell Lines", *Journal of Hazardous Materials*, Vol. 264, pp. 303–312, 2014.

259. Manke, A., L. Wang and Y. Rojanasakul, "Mechanisms of Nanoparticle-Induced Oxidative Stress and Toxicity", *BioMed Research International*, Vol. 2013, No. 1,

pp. 1–15, 2013.

260. Qian, X., J. Zhang, Z. Gu and Y. Chen, "Nanocatalysts-Augmented Fenton Chemical Reaction for Nanocatalytic Tumor Therapy", *Biomaterials*, Vol. 211, pp. 1–13, 2019.

261. Bush, J. A., K. J. J. Cheung and G. Li, "Curcumin Induces Apoptosis in Human Melanoma Cells Through a Fas Receptor/caspase-8 Pathway Independent of p53", *Experimental Cell Research*, Vol. 271, No. 2, pp. 305–314, 2001.

262. Dreaden, E. C., M. A. M. key, X. Huang, B. Kang and M. A. El-Sayed, "Beating Cancer in Multiple Ways Using Nanogold", *Chemical Society Reviews*, Vol. 40, No. 7, pp. 3391–3404, 2011.

263. Hua, H., Q. Kong, H. Zhang, J. Wang, T. Luo and Y. Jiang, "Targeting mTOR for Cancer Therapy", *Journal of Hematology & Oncology*, Vol. 12, No. 1, p. 71, 2019.

264. Ahmad, I., K. M. Muneer, I. A. Tamimi, M. E. Chang, M. O. Ata and N. Yusuf, "THymoquinone Suppresses Metastasis of Melanoma Cells by Inhibition of NLRP3 Inflammasome", *Toxicology and Applied Pharmacology*, Vol. 270, No. 1, pp. 70–76, 2013.

265. Chithrani, B. D. and W. C. W. Chan, "Elucidating the Mechanism of Cellular Uptake and Removal of Protein-Coated Gold Nanoparticles of Different Sizes and Shapes", *Nano Letters*, Vol. 7, No. 6, pp. 1542–1550, 2007.

266. Aggarwal, B. B. and K. B. Harikumar, "Potential Therapeutic Effects of Curcumin, the Anti-Inflammatory Agent, Against Neurodegenerative, Cardiovascular, Pulmonary, Metabolic, Autoimmune and Neoplastic Diseases", *The International Journal of Biochemistry & Cell Biology*, Vol. 41, No. 1, pp. 40–59, 2009.

267. Faivre, S., G. Kroemer and E. Raymond, "Current Development of mTOR In-

hibitors as Anticancer Agents", *Nature Reviews Drug Discovery*, Vol. 5, No. 8, pp. 671–688, 2006.

268. Schmidt, S. K., R. Schmid, A. Arkudas, A. Kengelbach-Weigand and A. K. Bosserhoff, "Tumor Cells Develop Defined Cellular Phenotypes After 3D-Bioprinting in Different Bioinks", *Cells*, Vol. 8, No. 10, p. 1295, 2019.

269. Koushki, K., S. K. Shahbaz, M. Keshavarz, E. E. Bezsonov, T. Sathyapalan and A. Sahebkar, "Gold Nanoparticles: Multifaceted Roles in the Management of Autoimmune Disorders", *Biomolecules*, Vol. 11, No. 9, p. 1289, 2021.

270. Pinho, R. A., D. P. Haupenthal, P. E. Fauser, A. Thirupathi and P. C. Silveira, "Gold Nanoparticle-Based Therapy for Muscle Inflammation and Oxidative Stress", *Journal of Inflammation Research*, Vol. 15, No. 12, pp. 3219–3234, 2022.

271. Staroverov, S. A., N. M. Aksinenko, K. P. Gabalov, O. A. Vasilenko, I. V. Vidyasheva, S. Y. Shchyogolev and L. A. Dykman, "Effect of Gold Nanoparticles on the Respiratory Activity of Peritoneal Macrophages", *Gold Bulletin*, Vol. 42, No. 2, pp. 153–156, 2009.

272. He, L., K. J. Weber, A. Diwan and J. D. Schilling, "Inhibition of mTOR Reduces Lipotoxic Cell Death in Primary Macrophages Through an Autophagy-Independent Mechanism", *Journal of Leukocyte Biology*, Vol. 100, No. 5, pp. 1113–1124, 2016.

273. Zhan, J. and M. Jücker, "The Role of PI3K/AKT/mTOR Signaling in Tumor Radioresistance and Advances in Inhibitor Research", *International Journal of Molecular Sciences*, Vol. 26, No. 14, p. 6853, 2025.

274. Li, P., Z. Fan, Y. Huang, L. Luo and X. Wu, "Mitochondrial Dynamics at the Intersection of Macrophage Polarization and Metabolism", *Frontiers in Immunology*, Vol. 16, 2025.

275. Alalmaie, A., H. T. Alshahrani, M. Alqahtani, Z. Alshahrani, S. Alahmari, A. Asiri, B. Alqadi, A. Alshahrani, S. Alshahrani and M. H. Akhter, "Integrating Computational Insights in Gold Nanoparticle-Mediated Drug Delivery: Enhancing Efficacy and Precision", *Frontiers in Medical Technology*, Vol. 7, p. 1528826, 2025.

276. Siddique, S. and J. C. Chow, "Gold Nanoparticles for Drug Delivery and Cancer Therapy", *Applied Sciences (Switzerland)*, Vol. 10, No. 11, p. 3824, 2020.

277. Chen, Q., W. Lin, Y. Tang, F. He, B. Liang, J. Chen, H. Li and H. Zhu, "Curcumin Targets YAP1 to Enhance Mitochondrial Function and Autophagy, Protecting Against UVB-Induced Photodamage", *Frontiers in Immunology*, Vol. 16, p. 1566287, 2025.

278. Sathyabhama, M., L. C. P. Dharshini, A. Karthikeyan, S. Kalaiselvi and T. Min, "The Credible Role of Curcumin in Oxidative Stress-Mediated Mitochondrial Dysfunction in Mammals", *Biomolecules*, Vol. 12, No. 10, p. 1405, 2022.

279. Dharman, S., G. Maragathavalli, R. Shanmugam and K. Shanmugasundaram, "Curcumin Mediated Gold Nanoparticles and Analysis of its Antioxidant, Anti-inflammatory, Antimicrobial Activity Against Oral Pathogens", *Pesquisa Brasileira em Odontopediatria e Clinica Integrada*, Vol. 23, p. e220068, 2023.

280. Al-Ani, L. A., W. A. Yehye, F. A. Kadir, N. M. Hashim, M. A. AlSaadi, N. M. Julkapli and V. K. Hsiao, "Hybrid Nanocomposite Curcumin-Capped Gold Nanoparticle-Reduced Graphene Oxide: Antioxidant Potency and Selective Cancer Cytotoxicity", *PLoS ONE*, Vol. 14, No. 5, p. e0216725, 2019.

281. Jenie, R. I., A. N. Artanti, R. Rumiyati, D. Novitasari, Y. Kusumastuti and M. Toriyama, "Cytoprotective Properties of Turmeric Oil (Curcuma longa L.) on Fibroblast Cells", *Asian Pacific Journal of Cancer Prevention*, Vol. 25, No. 11, pp. 4005–4012, 2024.

282. Kocyigit, A. and E. M. Guler, "Curcumin Induce DNA Damage and Apoptosis Through Generation of Reactive Oxygen Species and Reducing Mitochondrial Membrane Potential in Melanoma Cancer Cells", *Cellular and Molecular Biology*, Vol. 63, No. 11, pp. 97–105, 2017.

283. Farooqi, A. A., R. Attar and B. Xu, "Anticancer and Anti-Metastatic Role of Thymoquinone: Regulation of Oncogenic Signaling Cascades by Thymoquinone", *International Journal of Molecular Sciences*, Vol. 23, No. 11, p. 6311, 2022.

284. Mohd, H. and B. Michniak-Kohn, "Synergistic Anti-Cancer Effects of Curcumin and Thymoquinone Against Melanoma", *Antioxidants*, Vol. 13, No. 12, p. 1573, 2024.

285. Khalil, F. and S. Läer, "Physiologically Based Pharmacokinetic Modeling: Methodology, Applications, and Limitations with a Focus on Its Role in Pediatric Drug Development", *BioMed Research International*, Vol. 2011, No. 1, p. 907461, 2011.

286. Upton, R. N., D. J. Foster and A. Y. Abuhelwa, "An Introduction to Physiologically-based Pharmacokinetic Models", *Pediatric Anesthesia*, Vol. 26, No. 11, pp. 1036–1046, 2016.

287. Miao, Y.-B., T. Xu, Y. Gong, A. Chen, L. Zou, T. Jiang and Y. Shi, "Cracking the Intestinal Lymphatic System Window Utilizing Oral Delivery Vehicles for Precise Therapy", *Journal of Nanobiotechnology*, Vol. 21, No. 1, p. 263, 2023.

288. Cao, Y. and W. J. Jusko, "Survey of Monoclonal Antibody Disposition in Man Utilizing a Minimal Physiologically-Based Pharmacokinetic Model", *Journal of Pharmacokinetics and Pharmacodynamics*, Vol. 41, No. 6, pp. 571–580, 2014.

289. Cao, Y., J. P. Balthasar and W. J. Jusko, "Second-Generation Minimal Physiologically-Based Pharmacokinetic Model for Monoclonal Antibodies", *Jour-*

nal of Pharmacokinetics and Pharmacodynamics, Vol. 40, No. 5, pp. 597–607, 2013.

290. Vareed, S. K., M. Kakarala, M. T. Ruffin, J. A. Crowell, D. P. Normolle, Z. Djuric and D. E. Brenner, "Pharmacokinetics of Curcumin Conjugate Metabolites in Healthy Human Subjects", *Cancer Epidemiology Biomarkers and Prevention*, Vol. 17, No. 6, pp. 1411–1417, 2008.

291. Yousef, M., C. Park, M. Henostroza, N. B. Chacra, N. M. Davies and R. Löbenberg, "Development of a Novel In Vitro Model to Study Lymphatic Uptake of Drugs via Artificial Chylomicrons", *Pharmaceutics*, Vol. 15, No. 11, p. 2532, 2023.

292. Tabanelli, R., S. Brogi and V. Calderone, "Improving Curcumin Bioavailability: Current Strategies and Future Perspectives", *Pharmaceutics*, Vol. 13, No. 10, p. 1715, 2021.

293. Yáñez, J. A., S. W. Wang, I. W. Knemeyer, M. A. Wirth and K. B. Alton, "Intestinal Lymphatic Transport for Drug Delivery", *Advanced Drug Delivery Reviews*, Vol. 63, No. 10-11, pp. 923–942, 2011.

294. Fança-Berthon, P., M. Tenon, S. L. Bouter-Banon, A. Manfré, C. Maudet, A. Dion, H. Chevallier, J. Laval and R. B. V. Breemen, "Pharmacokinetics of a Single Dose of Turmeric Curcuminoids Depends on Formulation: Results of a Human Crossover Study", *Journal of Nutrition*, Vol. 151, No. 7, pp. 1802–1816, 2021.

295. Cheng, D., W. Li, L. Wang, T. Lin, G. Poiani, A. Wassef, R. Hudlikar, P. Ondar, L. Brunetti and A. N. Kong, "Pharmacokinetics, Pharmacodynamics, and PKPD Modeling of Curcumin in Regulating Antioxidant and Epigenetic Gene Expression in Healthy Human Volunteers", *Molecular Pharmaceutics*, Vol. 16, No. 5, pp. 1881–1889, 2019.

APPENDIX A: BIOPRINTING OPTIMIZATION

Contents are given on CD.

APPENDIX B: PERMISSIONS FOR REUSED FIGURES

Permission for Figure 2.3

Figure reproduced from: Klangprapan, J., Souza, G. R., & Ferreira, J. N. "Bioprinting salivary gland models and their regenerative applications." BDJ Open, Vol. 10, p. 39, 2024. ©2024 The Authors. This is an open access article distributed under the Creative Commons Attribution 4.0 International License (CC BY 4.0). Reproduced without modification (See Figure B.1).

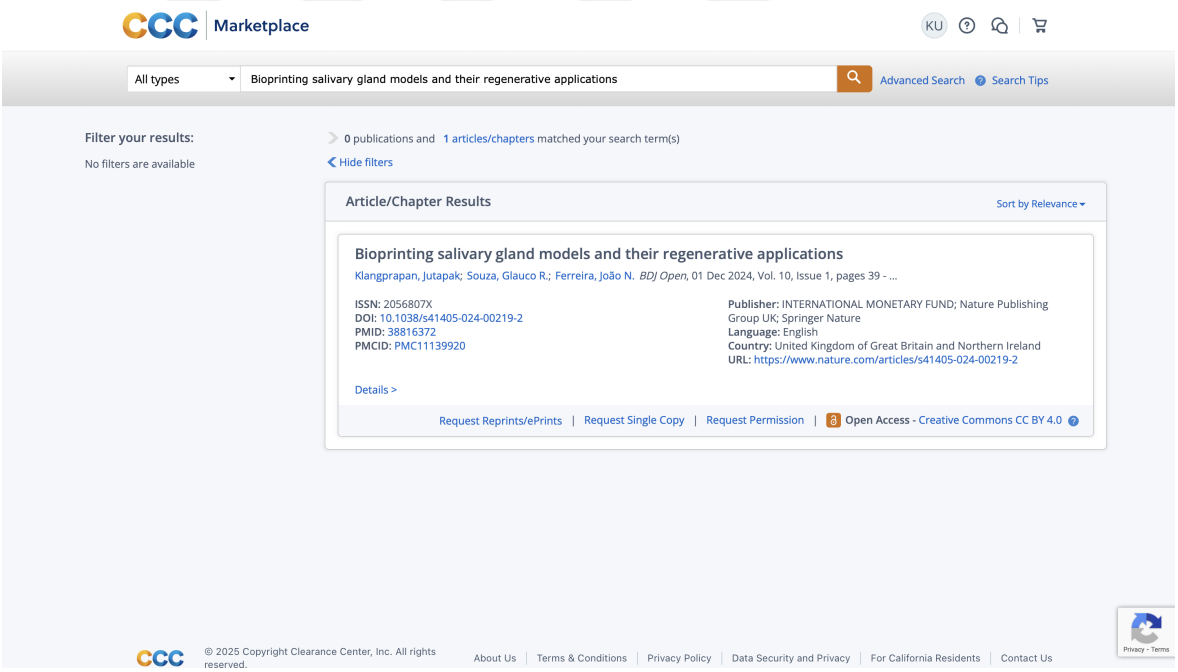


Figure B.1. Permission for Figure 2.3

Permission for Figures 2.4 to 2.7

Figures reproduced from: Vanaei, S., Parizi, M., Vanaei, S., Salemizadehparizi, F., & Vanaei, H. "An Overview on Materials and Techniques in 3D Bioprinting Toward Biomedical Application." Engineered Regeneration, Vol. 2, pp. 1–18, 2021. ©2021 The

Authors. Published by Elsevier B.V. This is an open access article under the Creative Commons Attribution 4.0 International License (CC BY 4.0). Reproduced without modification (See Figure B.2).

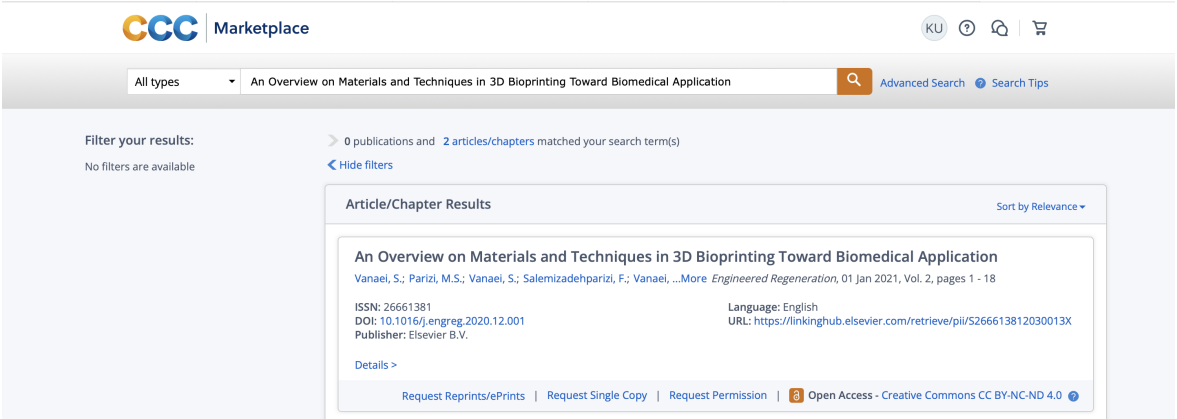


Figure B.2. Permission for Figures 2.4 to 2.7

Permission for Figure 2.8

Figure reproduced from: Vázquez-Aristizabal, P., Henriksen-Lacey, M., García-Astrain, C., de Aberasturi, D. J., Langer, J., Epelde, C., Litti, L., Liz-Marzán, L. M., & Izeta, A. "Biofabrication and Monitoring of a 3D Printed Skin Model for Melanoma." Advanced Healthcare Materials, Vol. 13, 2024. ©2024 The Authors. Published by Wiley-VCH GmbH. This is an open access article under the Creative Commons Attribution 4.0 International License (CC BY 4.0). Reproduced without modification (See Figure B.3).

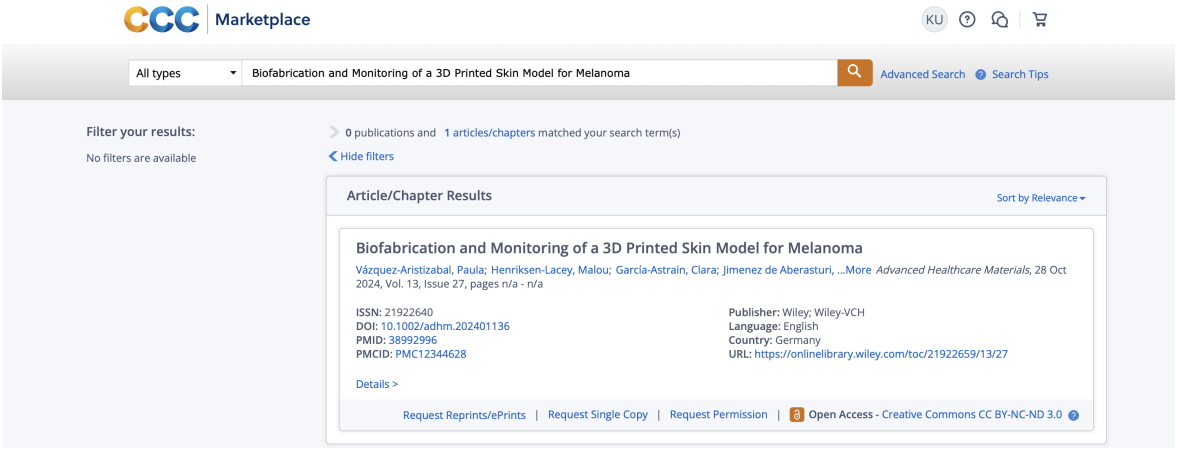


Figure B.3. Permission for Figure 2.8

Permission for Figure 2.13

Figure reproduced from: Kovar, L., Schröpel, C., Selzer, D., Kohl, Y., Bals, R., Schwab, M., & Lehr, T. "Physiologically-based pharmacokinetic (PBPK) modeling of buprenorphine in adults, children and preterm neonates." Pharmaceutics, Vol. 12, pp. 1–22, 2020. ©2020 The Authors. This is an open access article distributed under the Creative Commons Attribution 4.0 International License (CC BY 4.0). Reproduced without modification (See Figure B.4).

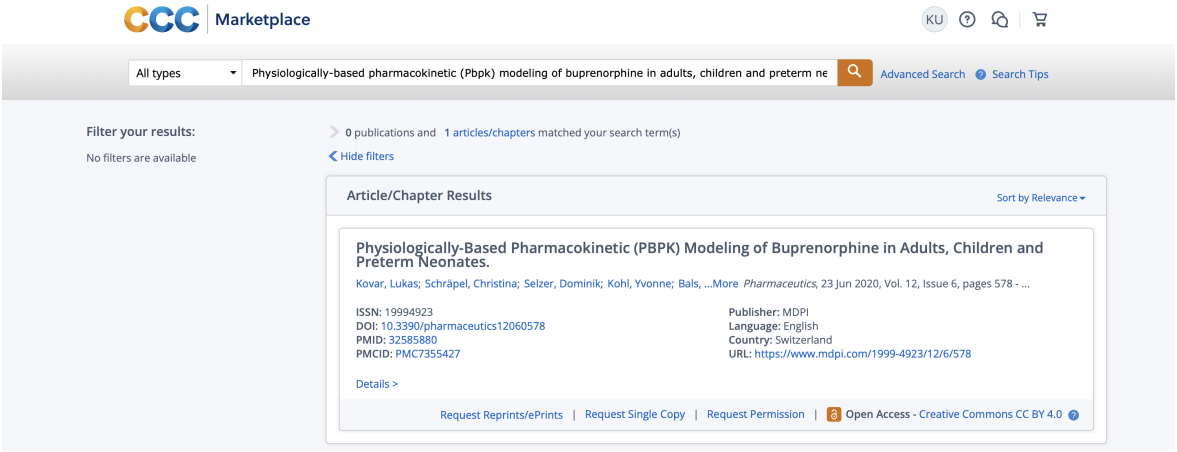


Figure B.4. Permission for Figure 2.13

Permission for Figure 2.14

Figure 2.14 is reproduced from: Malik, P. R., Hamadeh, A., Phipps, C. & Edginton, A. N. (2017). Population PBPK modelling of trastuzumab: a framework for quantifying and predicting interindividual variability. Journal of Pharmacokinetics and Pharmacodynamics, 44, 277–290. ©Springer Nature 2017. Reproduced with permission from Springer Nature. All rights reserved.



CCC Marketplace

This is a License Agreement between Muge Kasim Kirac ("User") and Copyright Clearance Center, Inc. ("CCC") on behalf of the Rightsholder identified in the order details below. The license consists of the order details, the Marketplace Permissions General Terms and Conditions below, and any Rightsholder Terms and Conditions which are included below.

All payments must be made in full to CCC in accordance with the Marketplace Permissions General Terms and Conditions below.

Order Date	29-Sep-2025	Type of Use	Republish in a thesis/dissertation
Order License ID	1656608-1	Publisher	PLENUM PUBLISHERS (JOURNALS)
ISSN	1573-8744	Portion	Image/photo/illustration

LICENSED CONTENT

Publication Title	Journal of pharmacokinetics and pharmacodynamics	Publication Type	e-Journal
Article Title	Population PBPK modelling of trastuzumab: a framework for quantifying and predicting inter-individual variability.	Start Page	277
		End Page	290
		Issue	3
Author / Editor	Springer Science+Business Media	Volume	44
Date	01/01/2001	URL	http://link.springer.com/journal/volumes...
Language	English		
Country	United States of America		
Rightsholder	Springer Nature BV		

REQUEST DETAILS

Portion Type	Image/photo/illustration	Distribution	Worldwide
Number of Images / Photos / Illustrations	1	Translation	Original language of publication
Format (select all that apply)	Print, Electronic	Copies for the Disabled?	No
Who Will Republish the Content?	Academic institution	Minor Editing Privileges?	No
Duration of Use	Life of current edition	Incidental Promotional Use?	No
Lifetime Unit Quantity	Up to 999	Currency	USD
Rights Requested	Main product		

NEW WORK DETAILS

Title	PBPK model with lymphatic system	Institution Name	Bogazici University
Instructor Name	Prof.. Kutlu Ulgen	Expected Presentation Date	2025-10-15

ADDITIONAL DETAILS

The Requesting Person / Organization to Appear on the License	Muge Kasim Kirac

REQUESTED CONTENT DETAILS

Title, Description or Numeric Reference of the Portion(s)	A schematic for the whole body PBPK model showing the connection of anatomical compartments by blood flow (solid line) and lymph flow (dashed line)	Title of the Article / Chapter the Portion Is From	Population PBPK modelling of trastuzumab: a framework for quantifying and predicting inter-individual variability.
		Author of Portion(s)	Malik, Paul R. V.; Hamadeh, Abdullah; Phipps, Colin; Edginton, Andrea N.
Editor of Portion(s)	Malik, Paul R. V.; Hamadeh, Abdullah; Phipps, Colin; Edginton, Andrea N.	Publication Date of Portion	2017-06-01
Volume / Edition	44		
Page or Page Range of Portion	277-290		

Figure B.5. Permission for Figure 2.14

Permission for Figure 2.15

Figure 2.15 is reproduced from: Zhao, J., Cao, Y. & Jusko, W. J. (2015). Across-Species Scaling of Monoclonal Antibody Pharmacokinetics Using a Minimal PBPK Model. Pharmaceutical Research, 32, 3269–3281. ©Springer Nature 2015. Reproduced with permission from Springer Nature. All rights reserved.



CCC Marketplace

This is a License Agreement between Muge Kasim Kirac ("User") and Copyright Clearance Center, Inc. ("CCC") on behalf of the Rightsholder identified in the order details below. The license consists of the order details, the Marketplace Permissions General Terms and Conditions below, and any Rightsholder Terms and Conditions which are included below.

All payments must be made in full to CCC in accordance with the Marketplace Permissions General Terms and Conditions below.

Order Date	29-Sep-2025	Type of Use	Republish in a thesis/dissertation
Order License ID	1656608-2	Publisher	PLENUM PUBLISHERS (JOURNALS)
ISSN	1573-904X	Portion	Image/photo/illustration

LICENSED CONTENT

Publication Title	Pharmaceutical research	Publication Type	e-Journal
Article Title	Across-Species Scaling of Monoclonal Antibody Pharmacokinetics Using a Minimal PBPK Model.	Start Page	3269
		End Page	3281
Author / Editor	American Association of Pharmaceutical Scientists.	Issue	10
		Volume	32
Date	01/01/1984	URL	http://www.kluweronline.com/issn/0724-...
Language	English		
Country	United States of America		
Rightsholder	Springer Nature BV		

REQUEST DETAILS

Portion Type	Image/photo/illustration	Distribution	Worldwide
Number of Images / Photos / Illustrations	1	Translation	Original language of publication
Format (select all that apply)	Print, Electronic	Copies for the Disabled?	No
Who Will Republish the Content?	Academic institution	Minor Editing Privileges?	No
Duration of Use	Life of current edition	Incidental Promotional Use?	No
Lifetime Unit Quantity	Up to 999	Currency	USD
Rights Requested	Main product		

NEW WORK DETAILS

Title	Minimal PBPK model	Institution Name	Bogazici University
Instructor Name	Prof. Kutlu Ulgen	Expected Presentation Date	2025-10-15

ADDITIONAL DETAILS

The Requesting Person / Organization to Appear on the License	Muge Kasim Kirac

REQUESTED CONTENT DETAILS

Title, Description or Numeric Reference of the Portion(s)	The mAb minimal PBPK model with allometric scaling of systemic clearance (CLp). Symbols and physiological restrictions are defined with Eq (1-4). The left box represents the venous plasma as in full PBPK models, but is not applied in the present model.	Title of the Article / Chapter the Portion Is From	Across-Species Scaling of Monoclonal Antibody Pharmacokinetics Using a Minimal PBPK Model.
		Author of Portion(s)	Zhao, Jie; Cao, Yanguang; Jusko, William J.
		Publication Date of Portion	2016-10-01
Editor of Portion(s)	Zhao, Jie; Cao, Yanguang; Jusko, William J.		
Volume / Edition	32		
Page or Page Range of Portion	3269-3281		

Figure B.6. Permission for Figure 2.15